Title

Computationally guided engineering of cell-selective cytokines

Author

Orcutt-Jahns, Brian Thomas

Publication Date

2024

Peer reviewed|Thesis/dissertation

UNIVERSITY OF CALIFORNIA

Los Angeles

Computationally guided engineering of cell-selective cytokines

A dissertation submitted in partial satisfaction of the requirements for the degree Doctor of Philosophy in Bioengineering

by

Brian Thomas Orcutt-Jahns

2024

ABSTRACT OF THE DISSERTATION

Computationally guided engineering of

cell-selective cytokines

by

Brian Thomas Orcutt-Jahns

Doctor of Philosophy in Bioengineering

University of California, Los Angeles, 2024

Professor Aaron S. Meyer, Chair

Cytokine signaling a core mechanism by which immune activity is regulated in both health and disease. Cytokine-mediated signaling regulates the proliferation, differentiation, and activity of cells in both the innate and adaptive immune systems. Due to their powerful regulatory capacity, cytokines have been leveraged as immunotherapies in a wide range of disease indications; for example, interleukin-2 (IL-2) has been explored as a potential immunostimulant for the treatment for cancer, as well as an immunosuppressant for the treatment of autoimmune diseases. However, in many such cases, the pleiotropic nature of cytokine signaling has stymied the development of efficacious and safe therapies due to the induction of signaling in off-target populations. To overcome this limitation and bias cytokines towards signaling in target populations, engineered cytokines with a variety of alterations, such as mutations affecting their binding interactions with their cognate receptors, fusion to antibody fragments, or co-formulation with antibodies to that cytokine have been developed. However, without a quantitative model of signaling the effects of such mutations and alterations are often difficult to anticipate, leading to inefficient cytokine

engineering efforts. To address this lack of quantitative understanding, we conducted a battery of computational studies. First, using a mechanistic binding model, we developed a general, quantitative understanding of the landscape of cell-selective cytokine signaling, and found that affinity, valency, and multi-specificity must be simultaneously optimized to engineer optimally selective cytokines. We then specifically studied the IL-2 signaling pathway, and used both ordinary differential equation models and our mechanistic binding model to study the signaling characteristics of wild-type and engineered IL-2 mutants. Leveraging our newfound quantitative of how affinity and valency interact to determine a cytokine's selectivity profile both generally and in the specific context of IL-2, we developed affinity-optimized tetravalent IL-2 mutants with superior regulatory cell selectivity. Using these models of IL-2 signaling, we also elucidated the mechanism by which engineered antibody-IL-2 fusions induced regulatory cell-selective signaling and conferred protection against autoimmunity. In total, this body of work demonstrates the critical role that computational modeling plays in potentiating the engineering of superior cytokine-based immunotherapies.

The dissertation of Brian Orcutt-Jahns is approved:

Jamie Spangler

Alexander Hoffmann

Dino Di Carlo

Aaron S. Meyer, Committee Chair

University of California, Los Angeles

2024

This thesis is dedicated to my parents, Peg Orcutt and Thomas Jahns, my sister, Anna Orcutt-Jahns, to my dear friends, Ruth Foley and Alexander Flemming, and to all those who have supported me during my nine years at UCLA.

TABLE OF CONTENTS

List of Figures

Chapter 1: A quantitative view of strategies to engineer cell-selective binding

Chapter 2: Modeling cell-specific dynamics and regulation of the common gamma chain cytokines

Chapter 3: Multivalent, asymmetric IL-2-FC fusions show enhanced selectivity for regulatory T cells

Chapter 4: Engineered human cytokine/antibody fusion proteins expand regulatory T cells and confer autoimmune disease protection

Acknowledgments

It would unfortunately be an impossible task to list and properly thank all of the people who have been instrumental in helping me arrive to this point in my scientific career, and so I will instead focus my attention here on my advisor, Dr. Meyer, my family, Peg Orcutt, Thomas Jahns, and Anna Orcutt-Jahns, and my friends, Ruth Foley and Alexander Flemming.

When I first committed to joining the lab of Dr. Aaron Meyer, I knew that I was lucky to have been given an opportunity to study computational biology, a passion which I discovered late in my academic journey; however, I now know that I was completely unaware of exactly how lucky I truly was. As an investigator, Dr. Meyer is clever and dedicated, as a mentor he is supportive and diligent, and as a person he is compassionate and caring. From him, I have learned to think critically, how to conduct impactful science, how to communicate that science effectively, how to support mentees, and how to be a leader who can be relied upon. He is someone who gave me my career and the tools to exceed in it, and for that I am eternally grateful.

I would also like to sincerely thank my parents and sister, whose support of me as a person and as an academic has been unwavering and unconditional. Their steadfast belief in me has been the foundation upon which I've stood in all of my pursuits, and the reason why I've never questioned my ability or drive to pursue things larger than myself.

Finally, I would like to direct thanks to my roommates and friends Ruth Foley and Alex Flemming, who have helped make this journey something I never thought it would be; an absolute ton of fun. They have taught me the value of taking life exactly as seriously as it needs to be taken (often not very seriously) and have been there to help me make the best out of both the highs and lows throughout the last five years.

Chapter 1 is a reproduction of the publication led by Brian Orcutt-Jahns and supervised by Aaron S Meyer:

Tan, Z. C.*, **Orcutt-Jahns, B. T.*,** & Meyer, A. S. (2021). A quantitative view of strategies to engineer cell-selective ligand binding. *Integrative Biology*

Chapter 2 is a reproduction of the publication led by Ali Farhat and Adam Weiner, contributed to by Brian Orcutt-Jahns, and supervised by Aaron S Meyer:

Farhat, A. M., Weiner**.,** A. C., Posner, C., Kim, Z. S., **Orcutt-Jahns, B**., Carlson, S. M., & Meyer, A. S. (2021). Modeling cell-specific dynamics and regulation of the common gamma chain cytokines. *Cell Reports*

Chapter 3 is a reproduction of the publication led by Brian Orcutt-Jahns and supervised by Aaron S Meyer:

Orcutt-Jahns, B., Emmel, P. C., Snyder, E. M., Posner, C., Carlson, S. M., & Meyer, A. S. (2023). Multivalent, asymmetric IL-2-Fc fusions provide optimally enhanced T regulatory cell selectivity. *Science Signaling*

Chapter 4 is a reproduction of the publication led by Derek VanDyke, contributed to by Brian Orcutt-Jahns, and supervised by Jamie Spangler and Aaron S Meyer:

Van Dyke, D., Iglesias, M., Tomala, J., Young, A., Smith, J., Perry, P. A., Gebara, E., Cross, A., Cheung, L. S., Dykema, A. G., **Orcutt-Jahns, B. T.,** Henclova, T., Golias, J., Balolong, J., Tomasovic, L., Funda, D., Meyer, A. S., Pardoll, D. M., Hester, J., Issa, F., Hunter, C. A., Anderson, M. S., Bluestone, J. A., Raimondi, G., & Spangler, J. S. (2022). Engineered human cytokine/antibody fusion proteins elicit targeted expansion of regulatory T cells and confer protection against autoimmune diseases, *Cell Reports*

VITA

ENGINEERING RESEARCH

Graduate Student Researcher, Department of Bioengineering, PI: Aaron Meyer **2019 – Present**

Researcher, UCLA Department of Bioengineering, PI: Andrea Kasko **2017 – 2019**

Research Assistant, UCLA Department of Radiological Sciences, PI: Daniel Ennis **2016– 2017**

PROFESSIONAL EXPERIENCE

Computational Biology Intern, *Genentech, South San Francisco, CA* **2023**

R&D Intern, Global Patient Safety and Labeling, *Amgen, Thousand Oaks, CA* **2018**

EDUCATION

Ph.D. Bioengineering **2019 – 2024 (expected May)**

University of California, Los Angeles (UCLA)

Advisor: Dr. Aaron Meyer

B.S. Bioengineering **2015 - 2019**

University of California, Los Angeles (UCLA)

PUBLICATIONS (In chronological order)

Farhat, A. M., Weiner**.,** A. C., Posner, C., Kim, Z. S., **Orcutt-Jahns, B**., Carlson, S. M., & Meyer, A. S. (2021). Modeling cell-specific dynamics and regulation of the common gamma chain cytokines. *Cell Reports*, *35*(4), 109044

Tan, Z. C.*, **Orcutt-Jahns, B. T.*,** & Meyer, A. S. (2021). A quantitative view of strategies to engineer cell-selective ligand binding. *Integrative Biology*, *13*(11), 269-282

Van Dyke, D., Iglesias, M., Tomala, J., Young, A., Smith, J., Perry, P. A., Gebara, E., Cross, A., Cheung, L. S., Dykema, A. G., **Orcutt-Jahns, B. T.,** Henclova, T., Golias, J., Balolong, J., Tomasovic, L., Funda, D., Meyer, A. S., Pardoll, D. M., Hester, J., Issa, F., Hunter, C. A., Anderson, M. S., Bluestone, J. A., Raimondi, G., & Spangler, J. S. (2022) Engineered human cytokine/antibody fusion proteins elicit targeted expansion of regulatory T cells and confer protection against autoimmune diseases, *Cell Reports, 41*(3), 111478

Yang, H., Ulge, U. Y., Quijano-Rubio, A., Bernsetein, Z. J., Maestas, D. R., Chun, J., Wang, W., Lin, J., Jude, K. M., Singh, S., **Orcutt-Jahns, B. T.,** Li, P., Mou, J., Chung, L., Kuo, Y., Ali, Y, Meyer, A. S., Grayson, W. L., Heller, N. M., Garcia, K. C., Leonard, W. J., Silva, D., Elisseef, J. H., Baker, D., & Spangler, J. B. (2023) Design of hyper-stable cell type-specific IL-4 cytokine mimetics using a modular *de novo* cytokine scaffold, *Nature Chemical Biology*, *11*(1)

Orcutt-Jahns, B., Emmel, P. C., Snyder, E. M., Posner, C., Carlson, S. M., & Meyer, A. S. (2023). Multivalent, asymmetric IL-2-Fc fusions provide optimally enhanced T regulatory cell selectivity. *Science Signaling, 16*(807), eadg0699p

Orcutt-Jahns, B. T.*, Rodrigues Lima Junior, J.*, Rockne, R. C., Matache, A., Branciamore, S., Hung, E., Rodin, A. S., Lee, P. L., & Meyer, A. S. (2023) Systems profiling reveals recurrently dysregulated cytokine signaling responses in ER+ breast cancer patients' blood *bioRxiv, in review*

* = *co-first authors*

HONORS

Dissertation Year Fellowship **2023**

UCLA Graduate Division, Los Angeles, CA

Oral Presentation Award (1st Place) **2023**

UCLA Bioengineering Research Day, Los Angeles, CA

Poster Award (1st Place) **2022**

Pearl Cohen Poster Competition, Los Angeles, CA

Best Short Talk Award **2021**

Systems Biology of Human Disease Conference, Berlin, Germany

Magna Cum Laude Graduation Honors **2019**

University of California, Los Angeles

Phi Beta Kappa Member **2019 – Present**

University of California, Los Angeles

TEACHING EXPERIENCE

Teaching Assistant, University of California, Los Angeles **2020, 2022**

Data driven modeling and machine learning in Bioengineering

Chapter 1:

A quantitative view of strategies to engineer cell-selective ligand binding

Zhixin Cyrillus Tan[1,†], **Brian T. Orcutt-Jahns [2,†],** and Aaron S. Meyer[1,2,3,4]

[1]Bioinformatics Interdepartmental Program, University of California, Los Angeles, CA 90024, USA

2 Department of Bioengineering, University of California, Los Angeles, CA 90024, USA

3 Jonsson Comprehensive Cancer Center, University of California, Los Angeles, CA 90024, USA

4 Eli and Edythe Broad Center of Regenerative Medicine and Stem Cell Research, University of California, Los Angeles, CA 90024, USA

† These authors contributed equally

Integrative Biology, 2021, **13**, 269–282
https://doi.org/10.1093/intbio/zyab019
Advance access publication date 21 December 2021
Original Article

A quantitative view of strategies to engineer cell-selective ligand binding

Zhixin Cyrillus Tan [1,†], Brian T. Orcutt-Jahns [2,†] and Aaron S. Meyer [1,2,3,4,*]

[1]Bioinformatics Interdepartmental Program, University of California, Los Angeles, CA 90024, USA
[2]Department of Bioengineering, University of California, Los Angeles, CA 90024, USA
[3]Jonsson Comprehensive Cancer Center, University of California, Los Angeles, CA 90024, USA
[4]Eli and Edythe Broad Center of Regenerative Medicine and Stem Cell Research, University of California, Los Angeles, CA 90024, USA
*Corresponding author. E-mail: ameyer@ucla.edu

†These authors contributed equally.

Abstract

A critical property of many therapies is their selective binding to target populations. Exceptional specificity can arise from high-affinity binding to surface targets expressed exclusively on target cell types. In many cases, however, therapeutic targets are only expressed at subtly different levels relative to off-target cells. More complex binding strategies have been developed to overcome this limitation, including multi-specific and multivalent molecules, creating a combinatorial explosion of design possibilities. Guiding strategies for developing cell-specific binding are critical to employ these tools. Here, we employ a uniquely general multivalent binding model to dissect multi-ligand and multi-receptor interactions. This model allows us to analyze and explore a series of mechanisms to engineer cell selectivity, including mixtures of molecules, affinity adjustments, valency changes, multi-specific molecules and ligand competition. Each of these strategies can optimize selectivity in distinct cases, leading to enhanced selectivity when employed together. The proposed model, therefore, provides a comprehensive toolkit for the model-driven design of selectively binding therapies.

Insight Window

Selective binding to specific target cells is a critical property of many therapies. To enhance selectivity, a series of strategies have been proposed in the drug development literature, including affinity, valency, multi-specificity and other alterations to target cell binding. We employ a simple yet general multivalent ligand–receptor binding model that can help to direct therapeutic engineering. Using this model, we provide generalized and quantitative analyses of the effectiveness and limitations of each strategy. We also demonstrate that combining strategies can offer enhanced selectivity. This work therefore provides guidance for future therapeutic development.

INTRODUCTION

The intricacies of both inter-population expression differences and intrapopulation expression heterogeneity present significant challenges that limit the selectivity of therapies within the body. Many drugs both derive their therapeutic benefit and avoid toxicity through selective binding to specific cells within the body. Often, target cells differ from off-target populations only subtly in surface receptor expression, making selective binding to or activation of target cells difficult to achieve. This can result in reduced effectiveness and increased toxicity. Even with a drug of very specific molecular binding, genetic and non-genetic heterogeneity can create a wide distribution of cell responses. For example, in cancer, resistance to anti-tumor antibodies [1], targeted inhibitors [2], chemotherapies [3] and chimeric antigen receptor T cells [4, 5] all can arise through the selection of poorly targeted cells among heterogeneous cell populations.

Numerous engineering efforts have tried to develop new selective targeting strategies. Engineering therapies to have high-affinity, monomeric binding to antigens uniquely expressed on target cell populations has been used extensively, but only works to the degree that the surface marker is uniquely expressed [6]. More commonly, target and off-target cells express the same collection of receptors and differ only in their magnitude of receptor expression. In such situations, developing selectivity is an area of ongoing research and has inspired a myriad of drug designs [7–9]. There are also extensive efforts to program complex logic into cellular therapies to recognize target cells more specifically, but they suffer from shortcomings in drug access, manufacture and reliability [10–13]. Many cell selectivity engineering

Received: September 2, 2021. **Revised:** November 17, 2021. **Editorial decision:** November 18, 2021. **Accepted:** November 23, 2021

strategies have been proposed. A remaining challenge, however, is to consolidate these scattered efforts into a holistic picture. A quantitative, unified cell targeting framework would not only elucidate how each strategy achieves better cell type-selectivity, but also guide the discovery of new strategies and their synergistic combination.

Here, we systematically enumerate a suite of molecular approaches for engineering binding to specific cells and analyze their quantitative characteristics using a multivalent, multi-receptor, multi-ligand binding model. The generality of this model enables a unified approach toward exploration of many different therapeutic formats. We show that strategies including affinity, valency, binding competition, ligand mixtures and hetero-valent complexes provide improvements in cell-specific targeting in distinct situations and through unique mechanisms. We then demonstrate how these strategies can be used in combination to enhance target cell binding specificity. In summary, our work demonstrates that simple, passive binding-based therapies can usually offer selective targeting without the need to engineer complex cellular therapies, and that their design can be guided using a unified computational framework.

RESULTS

A model system to explore the factors contributing to cell selectivity

Virtually any therapy can be thought of as a ligand for cognate receptors expressed on target cells. To investigate ligand binding quantitatively, we employed a general multivalent, multi-ligand equilibrium binding model [14]. This model can accurately account for the interactions between a mixture of multivalent ligands and cells expressing various types of receptors. The amount of binding is predicted given the monomer binding affinities and cell receptor expression (see Materials and Methods). Monovalent binding interactions are simple and governed by both the affinity with which the ligand binds to surface receptor and the abundance of those receptors. Behavior is more complicated when the ligands are multivalent complexes consisting of multiple units, each of which can bind to a receptor (Fig. 1a). To model this behavior, we assume that the complex's first receptor–ligand interaction proceeds according to the same dynamics that govern monovalent binding during initial association. Subsequent binding events exhibit different behavior, however, due to the increased local concentration of the complex and steric effects. We assume that the effective association constant for the subsequent binding is proportional to that of the free binding, scaled by a crosslinking constant, K_x^*. The mathematical details and accompanying assumptions of the model are described in previous work [14]. In comparison to previous models, the current formulation is distinguished in its ability to predict the binding of multiple ligand, multiple receptor interactions with higher valency efficiently (Table 1). The assumptions of this model have been successfully applied to a variety of signaling pathways where multivalent interactions play a key role, such as the interaction between T cell receptors and oligomeric major histocompatibility complexes or the interaction between Fcγ receptors and IgG antibodies [15, 16]. In this work, we define cell population selectivity as the ratio of the number of ligands bound to target cell populations divided by the average number of ligands bound to off-target cell populations. We will use the quantitative binding estimation for each cell population to examine each selectivity strategy.

As a simplification, we will consider theoretical cell populations that express only two receptors capable of binding ligand, uniformly distributed across the cell surface (Fig. 1b), ranging in abundance from 100 to 1 000 000 per cell. Figure 1c shows the log-scaled predicted amount of binding of a monovalent ligand (L_0, 1 **nM**) given the abundance of two receptors with dissociation constants of 10 μ**M** and 100 **nM**, respectively. Because all axes are log-scaled, the contour lines intuitively indicate the ratio of ligand binding between populations. For instance, in Figure 1c, cell populations at points 1 and 2 are on the same contour line and thus have the same amount of ligand bound; the cell populations at points 1 and 3 are separated by multiple contour lines, indicating that cells at point 3 bind more ligand. (In fact, the ratio can be read as the exponent of the contour line difference. For point 3 to point 1, the ratio is $e^{9.4-4.6} \approx 121.5$.) Alternatively, moving from one point to another represents a change in a cell population's expression profile. This situation might correspond to a cue inducing expression of a receptor, such as interferon-induced upregulation of MHC or the interleukin-induced upregulation of IL-2Rα in helper T cell populations [17]. If the amount of receptor 1 (R_1) increased (moving rightward, e.g. from 1 to 2), the amount of binding would not increase significantly. In contrast, increased expression of R_2 (moving upward, e.g. from 1 to 3) would lead to significantly more binding. These trends are governed by the ligand's high affinity for R_2 and relatively low affinity for R_1 which leads to binding varying more strongly with changes to R_2 expression than R_1.

To analyze more general cases, we arbitrarily defined eight theoretical cell populations according to their expression of two receptor types (R_1 and R_2 plotted on x and y axes). As shown in Figure 1d, they either have high (10^6), medium (10^4) or low (10^2) expression of R_1 and R_2. We chose to exclude $R_1^{lo}R_2^{med}$ from our analysis to introduce asymmetry between R_1 and R_2; however, any finding pertaining to $R_1^{med}R_2^{lo}$ can also be generalized to $R_1^{lo}R_2^{med}$ by swapping R_1 and R_2. The receptor expression profile within each cell population can also vary widely. To represent cell-to-cell heterogeneity, we arbitrarily defined intrapopulation variability for each population and computationally accounted for this heterogeneity

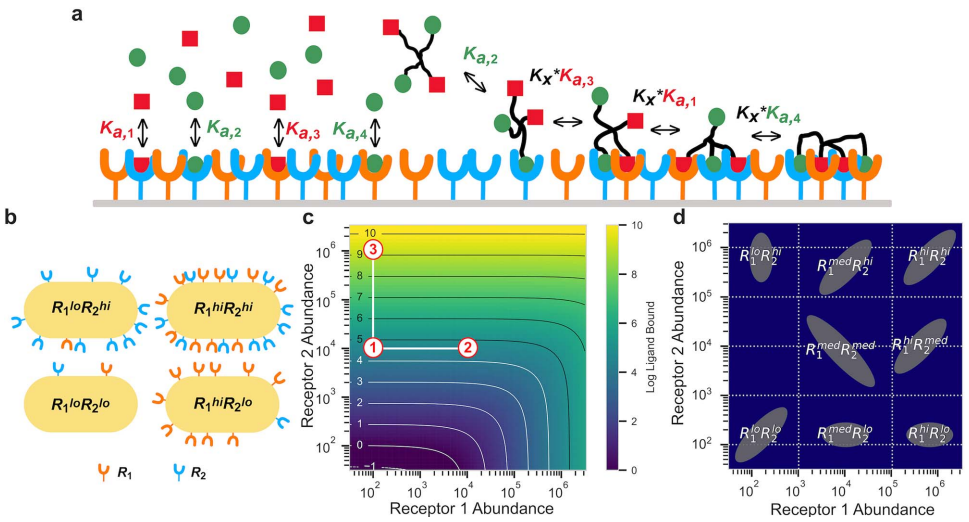

Figure 1. A model system for exploring the factors contributing to cell selectivity. (a) A simplified schematic of the binding model. In this example, there are two types of receptors and two types of ligand monomers that form a tetravalent complex. The two ligands (represented by red squares and green circles), initially interact with the surface receptors (blue and orange) with various association constants ($K_{a,1}$, $K_{a,2}$, $K_{a,3}$ and $K_{a,4}$). (b) A cartoon for four-cell populations expressing two different receptors at low or high amounts. (c) A sample heat/contour map for the model-predicted log ligand bound given the expression of two types of receptors. (d) Eight arbitrary theoretical cell populations with various receptor expression profiles.

Table 1. Comparison of selected modeling approaches and their capacity in cell-selective binding analysis

Model	Multiple receptors	Multiple ligands	Valency	Flexibility	Scalability	Dynamics
Context-specific ODE model	Possible	Possible	Possible	No	No	Yes
[49]	No	No	Yes	Yes	Yes	No
Rule-based [50]	Yes	Yes	Yes	Yes	No	Yes
[51]	Yes	Yes	Yes	No	No	Yes
Our model [14]	Yes	Yes	Yes	Yes	Yes	No

[18]. For instance, the expression profile of $R_1^{med}R_2^{med}$ has a wider range. We will use this binding model to examine how engineering a ligand using various strategies can improve cell-specific targeting. Although we will only consider two receptor and ligand subunit types, the principles we present can generalize to more complex cases.

Quantitative model grants insights to existing selectivity engineering strategies

To demonstrate that our model provides a unified but flexible platform to examine selectivity strategies, we first applied it to some more commonly explored ligand-engineering techniques, including affinity modification, multivalency and ligand mixtures (Fig. 2a). While these strategies have been investigated experimentally or modeled separately, here we propose that our model provides a unified framework to examine each of these strategies simultaneously. This not only allows us to quantitatively match known trends but also provide novel insight to how they each impart specificity when combined.

We first altered the receptor-binding affinity of a monovalent ligand as a cell population targeting strategy (Fig. S1). Affinity modulation is the most intuitive strategy to change the binding profile of a ligand: by enhancing a ligand's affinity to the receptors target cells express, the ligand will bind more tightly and in higher number to them. Heat/contour maps predicted by the model clearly illustrate this effect (Fig. S1a). To explain how affinity modulation can enhance selectivity, we created four cases of target vs. off-target population pairs (Fig. S1b–e). Unsurprisingly, we found that when a target cell population expresses a receptor not expressed by off-target cell populations, enhancing the affinity to this receptor is a clear and effective strategy to increase selective binding to this population. For example, when $R_1^{hi}R_2^{lo}$ only significantly expresses R_1, whereas $R_1^{lo}R_2^{hi}$ only significantly expresses R_2, enhancing the affinity to R_1 and reducing the affinity to R_2 is a strategy to increase $R_1^{hi}R_2^{lo}$ selectivity (Fig. S1b). However, the benefit of this strategy is reduced when both on- and off-target cell populations express the same set of receptors and

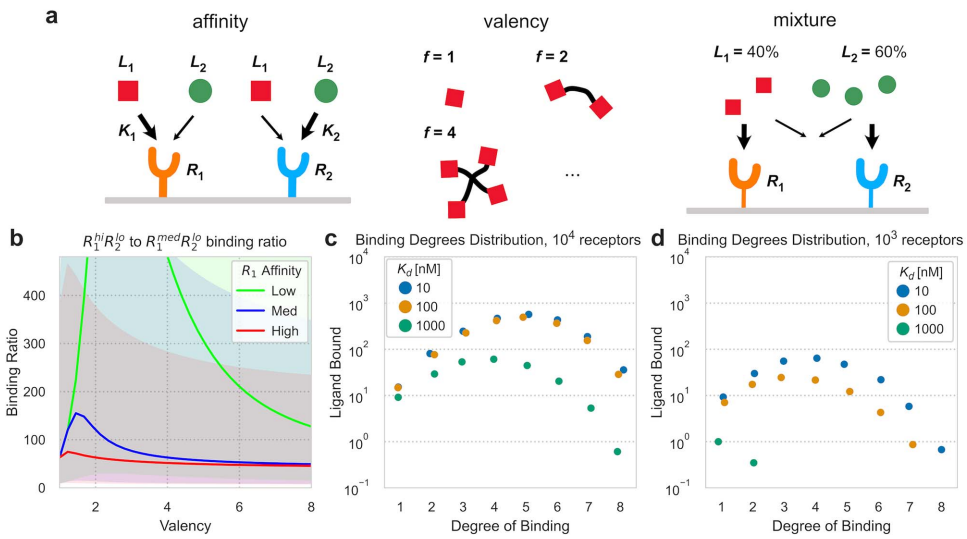

Figure 2. Our model recapitulates known engineering strategies. (a) Schematics of cell selective engineering strategies. (b) The ligand binding ratio between $R_1^{hi}R_2^{lo}$ and $R_1^{med}R_2^{lo}$ for ligands of valency ranging from 1 to 8. The shaded areas indicate the variance of binding ratios caused by the intrapopulation heterogeneity. (c, d) Number of ligands bound to each possible number of receptors for cells exposed to octavalent ligand complexes composed of subunits with dissociation constants of 1000, 100 or 10 **nM** for receptor 1. Number of octavalent complexes bound at each degree for a cell with 10^4 receptors (c) or 10^3 receptors (d).

differ only in their magnitude of expression, such as the selective binding to $R_1^{med}R_2^{hi}$ over $R_1^{hi}R_2^{med}$ and $R_1^{hi}R_2^{lo}$ over $R_1^{med}R_2^{lo}$ (Fig. S1c and d). The model also showed that affinity tuning fails when both receptors have identical relative abundance in target and off-target populations, such as when comparing $R_1^{hi}R_2^{hi}$ to $R_1^{med}R_2^{med}$ (Fig. S1e). These results thus mirror previous findings and intuition about ligand affinity engineering in a mathematically rigorous fashion.

Next, we sought to recapitulate the effect of multivalency within our model (Fig. S2). Multivalent ligand binds differently than monovalent ligand due to its nonlinear relationship with receptor density, allowing targeting based on receptor abundance [19]. This effect of valency engineering has been well corroborated [20–22]. Our analysis scheme can intuitively illustrate this relationship: in the heat/contour plot, there are roughly the same amount of contour lines between $R_1^{lo}R_2^{lo}$ and $R_1^{med}R_2^{lo}$ as there are between $R_1^{med}R_2^{lo}$ and $R_1^{hi}R_2^{lo}$ in the monovalent case, whereas in the tetravalent case, there are comparatively more contour lines between $R_1^{med}R_2^{lo}$ and $R_1^{hi}R_2^{lo}$ (Fig. S2a). Moreover, the model confirmed that multivalency-derived selectivity to high receptor expression population requires coordinate changes in lower affinity, as many previous studies suggest [20–23]. It shows that the binding ratio between $R_1^{hi}R_2^{lo}$ and $R_1^{med}R_2^{lo}$ is maximized by low-affinity ligands but requires greater valency to achieve peak binding selectivity (Fig. 2b). Similar effects were seen in other population pairs (Fig. S2b and c).

We used the model to explore the underlying mechanism of this 'high-valency, low-affinity' selectivity effect. We examined the distribution of binding degrees, defined as the number of receptors bound to each complex, achieved by octavalent ligands of differing affinities on cells with differing receptor abundances. Cells expressing 10^4 receptors displayed similar amounts of binding at each binding degree for ligands with high and low affinities (Fig. 2c). However, cells expressing 10^3 receptors exhibit extremely low amounts of higher-degree binding with low binding affinity (Fig. 2d). This finding illustrates the 'Velcro'-like binding behavior of multivalent ligands. Cells with higher receptor abundances can form stable, high-degree binding due to the proximity of receptors upon initial binding. They accumulate multivalent binding as the forward rate of secondary binding events is greater than that of receptor–ligand disassociation (Fig. S2d). This effect becomes particularly apparent when the affinity is low and cells must compensate with higher receptor availability to maintain stable interactions, where cells with lower receptor abundances cannot. Therefore, multivalent low-affinity ligands can selectively target cells with high receptor abundances. The model is thus able to recapitulate the known effects and benefits of valency, its dependence on affinity and elucidate the mechanism by which that relationship is governed.

Table 2. Summary of engineering strategies examined in this work

Strategy	Examples	Characteristics
Affinity	IL-2 Muteins [10, 35, 36] IgG Muteins [43, 44]	Ligands with strong affinities for a particular receptor selectively bind to cells expressing that receptor uniquely when compared with off-target populations.
Valency	Multivalent fibronectin nanorings [22] Anti-Gal small molecules [9] Antimicrobial peptides [45]	Ligands in higher valency formats can preferentially bind populations with higher receptor abundances. Requires coordinated change in affinity to achieve optimum (high-valency, low-affinity effect).
Mixture	MET targeted antibodies [26] IFN-α/IFN-γ co-formulations [27] Bronchodilator co-formulations [46]	Mixtures of monovalent ligands may enhance selectivity slightly when considering two or more off-target cell populations. Most therapeutic benefits come from complementary signaling responses.
Hetero-specificity	Bispecific antibodies [47] Angiogenesis inhibitors [48]	Multispecific complexes can provide unique benefits to selectivity only when simultaneous binding of multiple units is required for therapeutic efficacy.
Monovalent agonist with multivalent antagonist	None	Mixtures of monovalent receptor agonists and multivalent receptor antagonists allow agonists to bind preferentially to cells expressing fewer receptors than off-target populations.

Finally, we explored the effects of ligand mixture engineering (Fig. S3). Mixtures may enhance selectivity through synergistic combinations of actions [24]; therefore, many co-formulations of monoclonal antibodies or cytokine cocktails are undergoing development and clinical trials for efficacy in the treatment of solid tumors, blood disease and immunodeficiencies, among others [25–27]. Here, we specifically evaluated model-predicted binding while varying the composition between two distinct monovalent ligands, each exhibiting preferential binding to either R_1 or R_2 (Fig. S3a). Selectivity varies monotonically with composition, such that any mixture combination is no better than simply using the more specific ligand (Fig. S3b). Our model did show that when considering multiple populations and defining selectivity as the amount of ligand bound by target cells divided by the amount of ligand bound by the off-target cell with the greatest amount of binding, there are unique situations where mixtures provide enhanced selectivity, but only modestly (Fig. S3c). While our model confirms that mixtures can rarely enact selectivity through simple binding, ligands can have non-overlapping signaling effects even with identical amounts of binding where the effect of combinations can be distinct from either individual ligand, and therapeutic advantages are conferred by signaling or therapeutic synergy [16, 28].

In total, we showed that our model can accurately model previously studied strategies for selective binding. While previous models have been used to individually identify and characterize these strategies (Table 2), our modeling approach allows us to flexibly explore these trends within a unified framework.

Heterovalent bispecific ligands exhibit unique characteristics when activity is tied to dual receptor engagement

Constructing multispecific drugs has become a promising new strategy for finer target cell specificity with the advancement of expanded protein engineering techniques [29]. The number of possible configurations of multispecific drugs is combinatorially large and impossible to enumerate, however, creating a challenge when optimizing drug design. Therefore, a computational approach is needed to explore the general principles of multispecificity-induced cell specificity and identify the most effective constructions. We use bivalent bispecific ligands as examples to explore the unique benefit of multispecificity distinct from the previous strategies. We compared a bispecific ligand with a 50–50% mixture of two monovalent ligands and a 50–50% mixture of two different homogeneous bivalent ligands (Fig. 3a). These two strategies both have some similarities to bispecific therapeutics. First, they contain two different ligand monomers with equal proportion. By comparing a bispecific with a 50–50% mixture of monovalent ligands we can determine the benefit of tethering these two monomers into one complex. Second, bispecific molecules are also naturally bivalent; by comparing them to homogeneous bivalent drugs, we see how having two different subunits in the same complex modify the behavior of a drug. By examining any unique behavior exhibited by bispecific ligands when compared with these two basic cases, we sought to explore the potential therapeutic benefits conferred by multispecificity.

We first applied the binding model to predict the amount of ligand bound in bispecific drugs (Fig. 3b), a 50–50% mixture of two monomers (Fig. 3c), and a 50–50% mixture of two different homogeneous bivalents (Fig. 3d), with the same set of parameters in ligand concentration and affinities. Surprisingly, the patterns of ligand binding in these three cases are almost identical, and bispecificity appeared to offer no unique properties. However, many bispecifics only impart their therapeutic action when both of their subunits bind to the target population [30]. For example, in the design of bispecific antibodies, it is common to require binding from both subunits for the desired effect [31, 32]. We therefore investigated whether bispecific ligands that

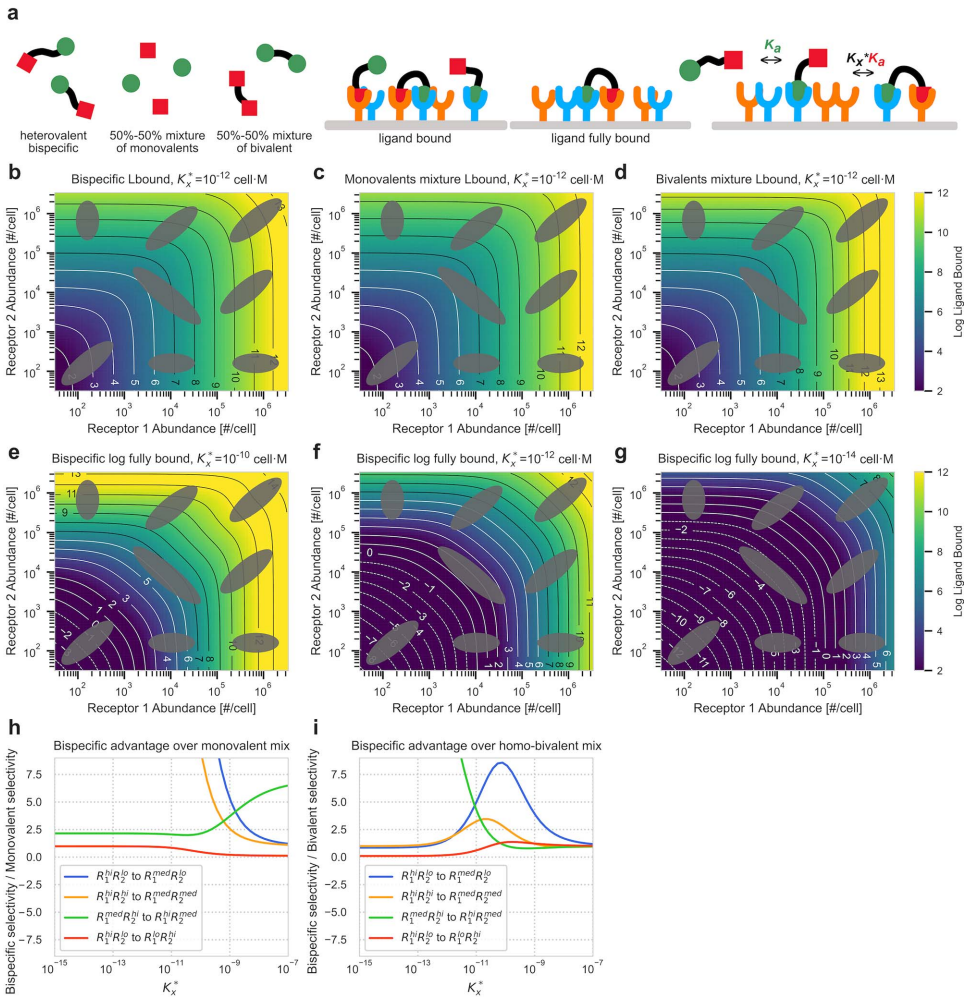

Figure 3. Bispecific ligands exhibit unique selectivity when their effect requires both subunits bound. (a) Schematic of bispecific ligands and fully bound ligand. (b–d) Comparing the total bispecific ligand binding (b) with the amount of binding achieved by a 50–50% mixture of monovalent ligands (c) or a 50–50% mixture of bivalent ligands (d). Total bound ligand is dominated by monovalently bound ligands and so the bispecific ligand lacks unique advantages. Here, the ligand concentration (L_0) was set to 10 **nM**; binding affinities $K_{d11}, K_{d22}, K_{d12}$ **and** K_{d21} were 100 nM, 1 **μM**, 10 **μM** and 10 **μM**, respectively. (e–g) The amount of fully bound bispecific ligand depends on the tendency for multimerization, encapsulated by K_x^*. Crosslinking constants (K_x^*) were set to 10^{-10} **cell· M** (e), 10^{-12} **cell· M** (f) and 10^{-14} **cell· M** (g), respectively. (h, i) Comparing bispecific with mixture selectivity, varying K_x^*, the crosslinking constant. When the ratios are larger, bispecific ligands bind to target populations more specifically. (h) Bispecific divided by monovalent 50–50% mixture selectivity. (i) Bispecific divided by a 50–50% homogeneous bivalent mixture selectivity.

must be doubly bound display any special cell population selectivity characteristics.

We used the model to calculate the amount of ligand fully bound (Fig. 3a). With the same set of parameters, the predictions made for bispecific fully bound show a very distinct pattern from general ligand bound (Fig. 3f). The contour plot of fully bound bispecific ligands has more convex contour lines: $R_1^{hi}R_2^{hi}$ has about the same level of general ligand bound as $R_1^{hi}R_2^{med}$ (Fig. 3b), but it has significantly more ligands fully bound than $R_1^{hi}R_2^{med}$ (Fig. 3f). This convexity of contour lines indicates that for bispecific complexes, double-positive cells bind more ligands fully.

The specific amount of fully bound ligand is dependent on the ligand's propensity for crosslinking captured

by the constant K_x^* (Fig. 3a). Less steric hindrance among the subunits of a multivalent drug molecule (e.g., longer/more flexible tether and smaller subunit size) or local receptor clustering on the target cell corresponds to greater secondary binding and a larger K_x^* [33]. We plotted the pattern of bispecific fully bound with $K_x^* = 10^{-10}$, 10^{-12} and 10^{-14} **cell·M** (Fig. 3e–g). In general, when K_x^* was larger, there were more fully bound units. To demonstrate how this characteristic of fully bound bispecific ligand imparts cell population specificity, we compared the selectivity conferred by bispecific ligands via fully bound interactions to the selectivity conferred by other ligand mixtures for two chosen target and off-target cell population pairs drug given a range of K_x^* (Fig. 3h and i). These plotted numbers are the selectivity imparted by a bispecific drug divided by the selectivity from a drug mixture of either monovalent (Fig. 3h) or homogeneous bivalent (Fig. 3i). When these quotients are larger, it implies that bispecific ligands with both subunits bound have a greater selectivity advantage than its counterpart. Figure 3h compares the selectivity under bispecific ligands with a 50–50% mixture of monovalent ligands. The results show that a fully bound bispecific can grant enhanced binding selectivity when K_x^* is small enough. This fits with the expectation that when K_x^* is small and cross-linking is rarer, most ligands will bind monovalently and fully bound bispecifics will especially favor cell populations with higher dual receptor expression. However, when we compared fully bound bispecific to fully bound homogeneous bivalent mixtures (Fig. 3i), the advantage of bispecific drugs does not increase monotonically with smaller K_x^* except for $R_1^{med}R_2^{hi}$ to $R_1^{hi}R_2^{med}$ selectivity. In cases where the target populations always have equal or more receptor abundance in every type than the off-target ones, such as $R_1^{hi}R_2^{lo}$ to $R_1^{med}R_2^{lo}$, or $R_1^{hi}R_2^{hi}$ to $R_1^{med}R_2^{med}$, an optimal K_x^* exists. This indicates that in these situations, the linker optimization may be an important consideration. Together, we show that bispecific ligands only exhibit unique advantages in inducing selective binding when they are only active upon binding of both subunits and highlight the role of crosslinking in their design.

Using binding competition to invert receptor targeting

While the strategies above provided selectivity in many cases, we recognized that they are all limited to a positive relationship between receptor abundance and binding. Therefore, we wondered if binding competition with a signaling/effect deficient multivalent receptor antagonist could invert this relationship and explored its effect with the model.

To investigate the effect of ligand competition with an antagonist, we modeled mixtures of ligands but only quantified the amount of binding for the active ligand (the agonist). We chose to start by only considering a monovalent agonist and tetravalent antagonist for simplicity's sake (Fig. 4a). We found that combinations of monovalent agonistic ligands and multivalent antagonistic ligands were able to uniquely target populations expressing small or intermediate amounts of receptors, which is demonstrated by comparing ligand binding ratios between $R_1^{med}R_2^{lo}$ to $R_1^{hi}R_2^{lo}$ (Fig. 4b). Here, nearly 16-fold more monovalent agonist can be bound to the target population than the off-target population when combined with a tetravalent antagonist (Fig. 4c). This is striking as $R_1^{med}R_2^{lo}$ expresses either equal or lesser abundances of either receptors when compared with $R_1^{hi}R_2^{lo}$. This phenomenon, which could not be achieved without multivalent antagonists (Fig. 4e), occurs due to the preferential binding of multivalent antagonist to populations expressing more R_1 (Figs 2b and 4d). Thus, in cases where previously discussed ligand engineering strategies and approaches fail to achieve selective binding to cells expressing smaller or similar amounts of receptors to off-target populations, combinations of agonistic and antagonistic ligands may provide unique benefits.

We next explored whether the potential selectivity benefits derived from using mixtures of multivalent antagonists with monovalent agonists could be further enhanced by changing the antagonist valency (Fig. 4f). Here, we again optimized the amount of agonist binding to $R_1^{med}R_2^{lo}$ when compared with $R_1^{hi}R_2^{lo}$ and allowed the affinity of both agonist and antagonist ligands to vary. We found that antagonists of greater valency could confer even greater selectivity. For example, an optimized octavalent antagonist could allow 25 times more agonist binding to $R_1^{med}R_2^{lo}$ when compared with $R_1^{hi}R_2^{lo}$. These selectivity increases required coordinate changes in affinity of the antagonist: when the valency of the antagonist is higher, its affinity to both receptors should be reduced to achieve optimal selectivity (Fig. 4g). Here, preferential binding of low-affinity, high-valency antagonists to off-target populations with greater abundances of receptors allows for agonists to achieve selective binding to target cells with lower receptor abundances. The optimal agonist affinity does not change with antagonist valency and achieved optimal selectivity via weak interaction with the off-target population, in this case weak binding to R_1 and strong binding to R_2 (Fig. 4g).

Finally, we wondered whether modulating the amount of agonist and antagonist in a therapeutic cocktail could increase selectivity (Fig. 4h). Here, we kept the concentration of agonist at 1 nM and varied the concentration of antagonist ligand, which effectively changed the mixture profile of the combination. We optimized the affinity of a tetravalent antagonist-monovalent agonist pair in each case. This analysis found that selectivity was only weakly dependent on concentration (Fig. 4h). Unlike when changing valency, optimal agonist affinities to R_2 vary with different mixtures (Fig. 4i). However, the optimal agonists maintain weak interaction with the target population with a low R_1 affinity, and the antagonist still binds to both receptors with intermediate

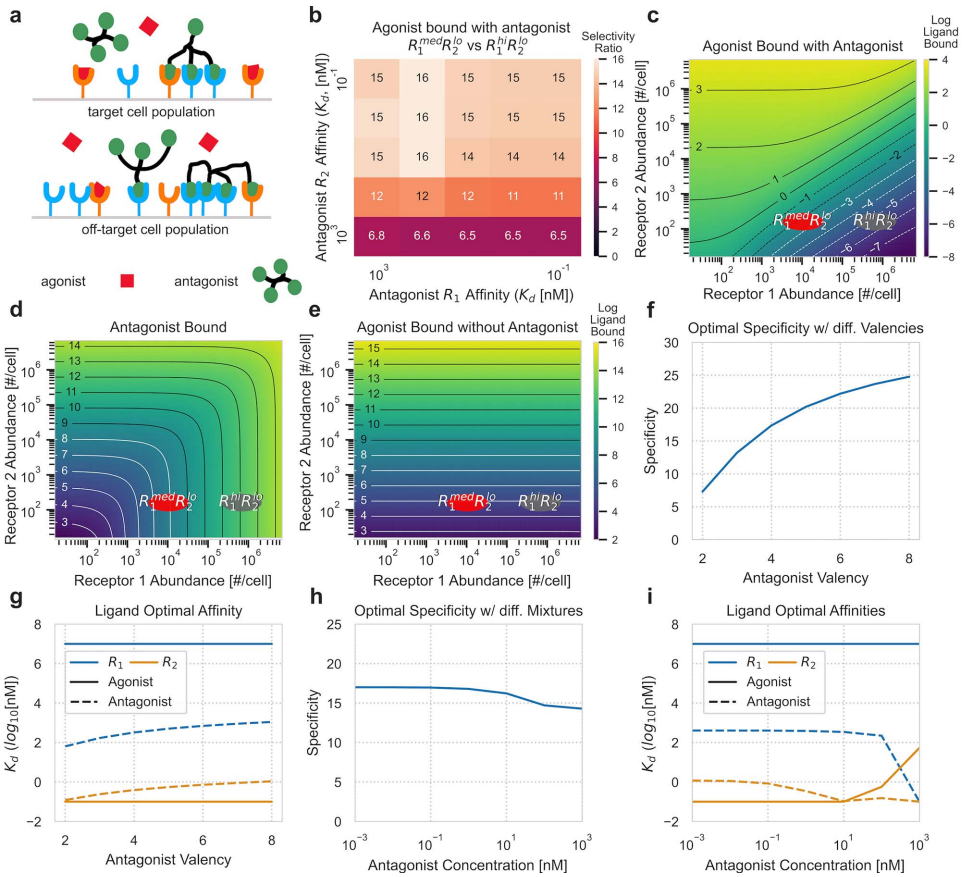

Figure 4. Mixtures of receptor agonists and antagonists allow for unique population targeting activity. Ligand concentration (L_0) was set to 1 **nM**. (a) Schematics of the binding activity of monovalent agonist and multivalent antagonist mixtures. (b) Selectivity for $R_1^{med}R_2^{lo}$ against $R_1^{hi}R_2^{lo}$ when exposed to a tetravalent antagonist with varying affinities for receptors 1 and 2, and a monovalent therapeutic receptor agonist with affinities optimized for selectivity. Only the amount of agonist bound is considered in determination of the optimal selectivity. (c–d) Heatmap of agonist (c) and antagonist (d) ligand bound for antagonist and agonist ligand combination shown to impart greatest selectivity improvement in (b). (e) Heatmap of agonist bound with the same parameters when no antagonist is present. (f) Optimal selectivity for $R_1^{med}R_2^{lo}$ against $R_1^{hi}R_2^{lo}$ achieved when using antagonists of varying valency with an equal concentration of agonist ligand. The affinity (K_d) for receptors 1 and 2 for both the agonist and antagonist ligand were allowed to vary between 0.1 nM and 10 mM in addition to K_x^*. (g) Affinities at which optimal selectivity was achieved for agonist and antagonist ligand for each antagonist valency. (h) Optimal selectivity for $R_1^{med}R_2^{lo}$ against $R_1^{hi}R_2^{lo}$ achieved using combining concentration of a tetravalent antagonist ligand with 1 nM monovalent agonist. Agonist and antagonist affinities for receptors 1 and 2 were allowed to vary as above along with K_x^*. (i) Affinities at which optimal selectivity was achieved for agonist and antagonist ligand for each agonist/antagonist mixture.

or high affinities. Together, these results suggest that high valency antagonists may offer unique benefits for increasing ligand selectivity in cases where off-target populations express more receptors than target population. For optimal effect, high valency of the antagonist is critical.

While previous work has explored multivalent antagonists to decrease pathway activation [34], the benefit of combining multivalent antagonists and monovalent agonists to enhance cell type-selective binding has yet to be explored. Our model outlines the potential of this novel approach, which further demonstrates how a unified model can facilitate the discovery of new selectivity strategies.

Combining strategies for superior selectivity

Each strategy described above provided selectivity benefits in distinct situations, suggesting that they might synergistically improve selectivity when combined. With

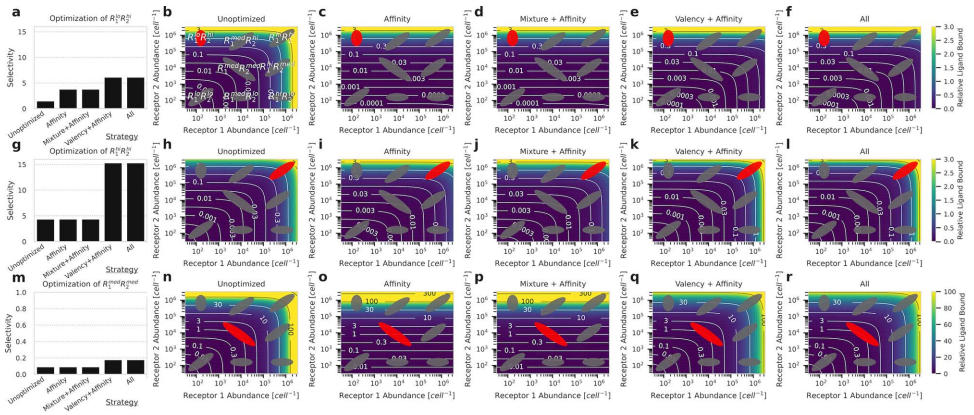

Figure 5. Combinations of strategies provide superior selectivity. Optimization was performed to target $R_1^{lo}R_2^{hi}$ (a–f), $R_1^{hi}R_2^{hi}$ (g–l) and $R_1^{med}R_2^{med}$ (m–r). (a, g, m) Optimal selectivity levels (ligand bound on target population divided by average ligand bound by all other populations) achieved using various ligand engineering techniques. Ligand concentration (L_0) was set to 1 **nM**. 'Unoptimized' ligands are monovalent ligands with affinities of 1 **μM** for both receptor 1 and 2. The dissociation constant was allowed to vary between 10 **mM** and 0.1 **nM** for both receptors using the 'affinity' approach. Valency was allowed to vary from 1 to 16 for the 'valency' approach in addition to affinities varying. Mixtures were assumed to be composed of two monovalent ligands, and affinities were allowed to vary in the 'mixture' approach. The combined 'all' approach allowed all these quantities to vary simultaneously. The cross-linking constant K_x^* was allowed to vary between 10^{-15} **cell·M** and 10^{-9} **cell·M** for all approaches. (b–f, h–l, n–f) Heatmap of magnitude of ligand bound for ligand with optimized characteristics according to various ligand engineering strategies. The target population is shown in red.

binding affinities, valency, mixture and subunit composition all considered as variables, the search space is enormous, and experimentally examining the selectivity of every possible ligand is unrealistic. Some theoretical guidance on the most promising direction can greatly reduce the workload. Here, we explored mathematical optimization to determine the ligand design that provided optimal selectivity for one of our theoretical cell populations when combining strategies. We started with an 'unoptimized' ligand, a monovalent ligand with plausible initial affinities, prior to selectivity engineering. Then, we elected one population as the target while considering all others to be off-target. The optimization algorithm allowed ligand characteristics to vary within biologically plausible bounds (see Materials and Methods). We examined optimizing affinity alone ('affinity'), mixture along with affinity ('mixture + affinity') and valency along with affinity ('valency + affinity') and finally combined all three strategies ('all') (Fig. 5). We elected to simultaneously vary valency and mixture effects with affinity due to affinity's critical role in modulating the effects that valency and mixture engineering have in determining binding selectivity. It should be noted that the parameter space is not convex, and initial parameters were selected manually for strategies where valency and affinity were allowed to vary simultaneously to locate the global maximum selectivity. To examine the efficacy and benefits of each approach, we compared the results of these strategies with the selectivity of an 'unoptimized' monovalent ligand. The heatmaps and contour lines here are normalized by the amount of ligand bound to the target population to compare target and off-target binding activity more effectively (Fig. 5).

Optimizing a ligand for selectivity to $R_1^{lo}R_2^{hi}$ highlights a situation in which affinity imparts greater specificity, and optimal selectivity is achieved by combining affinity and valency modulation (Fig. 5a–f). Here selectivity is optimized by ligands with selective binding to receptor 2 and higher valency, which allow the ligands to selectively bind to cells with more abundant receptor. One case contradictory to this trend is shown during the optimization for selectivity toward the $R_1^{hi}R_2^{hi}$ population (Fig. 5g–l). Affinity engineering is unable to impart selectivity and significant improvement is only achieved when using valency modulation. A more difficult design problem is featured in the optimization of $R_1^{med}R_2^{med}$ (Fig. 5m–r). Since it lies amid the other populations in receptor expression space, any modulation of affinity, valency or combining it with mixture-based strategies seems ineffective. Engineering the mixture composition was ineffective at imparting selectivity in all cases when the ligand's design specifications were flexible and is likely only efficacious when using ligands with static properties and considering multiple off-target populations.

Our results highlight that both in singular and combined strategies for therapeutic manipulation, the target and off-target populations dictate the optimal approach. It is also clear that combined approaches do offer context-dependent synergies that can be harnessed.

DISCUSSION

In this work, we analyzed a suite of ligand engineering strategies for population-selective binding with a multivalent, multi-ligand, multi-receptor binding model

(Fig. 1). Using a representative set of theoretical cell populations defined by their distinct expression of two receptors, we examined the efficacy of several potential ligand engineering strategies, including changes to affinity, ligand valency, mixtures of species, multi-specificity, antagonist competition and these in combination. Most importantly, this framework provides a unified approach for analyzing all selectivity strategies.

The computational model reveals the general patterns of each strategy's contribution (Table 2). We found that affinity changes were most effective when the target and off-target populations expressed distinct combinations of receptors (Fig. S1). When target and off-target populations expressed the same pattern of receptors and only differed in receptor abundances, modulations in valency, but not affinity, were effective (Figs 2 and S2). A key determinant of valency's effectiveness was the secondary binding and unbinding rate, which is dependent on both the kinetics of the receptor–ligand interaction and receptor abundance. Ligand mixtures were mostly ineffective for imparting binding selectivity, and only had modest benefits when considering two or more off-target populations (Fig. S3). Heterovalent bispecific ligands only showed unique advantages over mixtures of monovalent ligands or bivalent ligands if activity required dual receptor binding (Fig. 3). These ligands exhibit preferential binding to target populations that have high expression of both receptors over those with high expression of only a single receptor, with the propensity for secondary binding acting as a key determinant for selectivity. Using this model, we also found that combinations of monovalent therapeutic ligands with multivalent antagonistic ligands uniquely allow for the selection of target populations expressing relatively fewer receptors than off-target populations (Fig. 4). We investigated how the antagonist effect can be maximally harnessed by optimizing valency, affinity and mixture composition. Finally, we found that, while a single ligand engineering strategy dominated in its contributions to cell type selectivity, synergies between these strategies existed in some cases to derive even greater specificity (Fig. 5).

While the multivalent binding model we applied in this work provides both generality and computational efficiency, it relies on several assumptions. For example, it assumes that receptors are uniformly distributed on the surface of the cell and that no pre-association or colocalization of receptors occurs. While the effects of receptor colocalization may be captured to some degree by the K_x^* parameter in the model, it is not explicitly accounted for by our approach. The model also assumes that an equilibrium ligand concentration is roughly known. These details and possible adjustment for alternative assumptions are discussed in our previous work [14]. However, for any exception, the absolute and relative abundances of available receptors still play a governing role in determining cell type selectivity of ligand binding; thus, we believe our model's findings remain pertinent in most selectivity engineering efforts.

While our multivalent binding model identified strategies for selective targeting in many cases, it also identified situations for which selective binding is challenging. For example, selectively targeting populations based on their absence of receptor expression remains elusive. While we computationally show the potential of using multivalent antagonists with monovalent agonists to selectively target such populations, implementing this may be challenging in practice. In cases where a target population expresses fewer receptors of any kind than an off-target population, our analysis suggests that targeting other receptors should be considered. However, in cases where target populations express more of any type of receptor than an off-target population, we show that one or more of our formulated ligand engineering strategies can be employed to improve binding selectivity. While we expect the same patterns to apply with greater than two receptors, still other emergent behaviors may exist with trispecific and more complex ligand binding.

A few of the strategies that we explored have been utilized in existing engineered therapies. For example, affinity changes to the cytokine IL-2 have been used to bias its effects toward either effector or regulatory immune populations [35, 36]. Varying the valency of tumor-targeted antibodies leads to selective cell clearance based upon the levels of expressed antigen [23]. Manipulating of the affinities of the fibronectin domains on octavalent nanorings was shown to enhance the selectivity of binding to cancerous cells displaying relatively higher densities of fibronectin receptors compared with native tissue [22]. The tendency of low-affinity, multivalent interactions to target cells expressing high receptor abundances was also described in a study describing the selectivity of multivalent antibody binding to tumor cells bound by a bispecific therapeutic ligand [13]. These examples lend support to the accuracy and translational value of our model. At the same time, recognizing these previously described ligand engineering approaches as separable strategies provides clearer guidance for future engineering.

Some of the optimization strategies described here have not been exploited in part due to the complexity of real biological applications. It may be difficult to achieve the precise affinity indicated by the model. This problem may be exacerbated in cases where specificity is derived through binding to multiple receptors as binding reagents must be designed for each. Potential dynamic changes in the receptor expression profile of a target population also complicate the matter. It is well documented that cancer cells can escape therapeutic targeting by upregulating [37, 38] or downregulating [39] the expression of certain receptors. In this case, both the current and potential abundance of each receptor must be considered. While this work does not address these issues, we propose that using a computational binding model can analyze these strategies quantitatively and collectively from a mechanistic perspective. Even when the absolute mathematically optimal ligand

characteristics cannot be achieved biochemically, the model can provide guidance within the bounds of what is attainable and how to approach the optimum, accounting for implementation feasibility and facilitating the implementation of strategy combinations.

In many therapeutic applications where selective engagement of target cell populations is an important performance metric, such as the treatment of cancer, cellular therapies are becoming increasingly popular [40]. Human engineered chimeric antigen receptor (CAR) T cells have enhanced the potential to selectively recognize and attack malignant tissues [41]. These technologies bypass ligand–receptor binding restrictions by allowing recognition in signaling response. However, we have shown here that high selectivity can often be attained with relatively simple therapeutic ligands. This study lays a general framework for how ligand engineering can be directed using computational modeling. It should be noted that the application of this logic is reliant on knowledge of the target and off-target cell population receptor expression levels. Future application of the ligand binding logic described in this study could be guided using high-throughput single-cell profiling techniques, such as RNA-seq or high-parameter flow cytometry. A computational tool that could directly translate such datasets into ligand design criteria, selecting among potential receptor targets, may represent a potential avenue for the translation of our analyses into a more broadly applicable ligand engineering tool.

MATERIALS AND METHODS

Data and software availability

All analysis was implemented in Python v3.9 and can be found at https://github.com/meyer-lab/cell-selective-ligands.

Generalized multi-ligand, multi-receptor multivalent binding model

To model multivalent ligand complexes, we employed a binding model we previously developed to account the multi-ligand case [14]. In this model, we define N_L as the number of distinct monomer ligands and N_R the number of distinct receptors. For the binding between monomer ligand i and receptor j, their affinity can be described by the association constant, $K_{a,ij}$, or its reciprocal, the dissociation constant $K_{d,ij}$. During initial association, we assume that the linker portion of the complex does not sterically inhibit binding, and thus, the first subunit on a ligand complex binds according to the same dynamics that govern monovalent binding. For subsequent binding events, we assume that the effective association constant for the subsequent bindings is proportional to that of the free binding, but scaled by a crosslinking constant, K_x^*, which describes how easily a multivalent ligand bound to a cell monovalently can attain secondary binding. Therefore, multivalent binding interactions after the initial interaction have an association constant of $K_x^* K_{a,ij}$. The concentration of complexes at equilibrium is L_0, and the complexes consist of random ligand monomer assortments according to their relative proportion. For exogenously administered drugs and *in vitro* experiments, usually the number of ligand complexes in the solution is much greater than that of the receptors, so it is reasonable to assume binding does not deplete the ligand concentration significantly, and we can use the initial concentration as L_0. Otherwise, we need to estimate L_0 from the initial concentration (see section 4.3 in our previous work [14] for details). The model implicitly assumes that all receptors are uniformly mixed on the cell surface. Should different receptors be organized in discrete domains, the model would have to be updated to account for different K_x^* values for crosslinking within and among various domains. The proportion of ligand i in all monomers is C_i. By this setup, we know $\sum_{i=1}^{N_L} C_i = 1$. $R_{\mathbf{tot},i}$ is the total number of receptors i expressed on the cell surface, and $R_{\mathbf{eq},i}$ the number of unbound receptors i on a cell at the equilibrium state during the ligand complex–receptor interaction.

The binding configuration at the equilibrium state between an individual complex and a cell expressing various receptors can be described as a vector $\mathbf{q} = (q_{10}, q_{11}, \ldots, q_{1N_R}, q_{20}, \ldots, q_{2N_R}, q_{30}, \ldots, q_{N_L N_R})$ of length $N_L(N_R + 1)$, where q_{ij} is the number of ligand i bound to receptor j, and $q_{i,0}$ is the number of unbound ligand i on that complex in this configuration. The sum of elements in $\mathbf{q}$ is equal to f, the effective avidity. For all i in $\{1, 2, \ldots, N_L\}$, let $\varphi_{ij} = R_{\mathbf{eq},j} K_{a,ij} K_x^* C_i$ when j is in $\{1, 2, \ldots, N_R\}$, and $\varphi_{i0} = C_i$. The relative number of complexes in the configuration described by $\mathbf{q}$ at equilibrium is

$$v_{\mathbf{q},eq} = \binom{f}{\mathbf{q}} \frac{L_0}{K_x^*} \prod_{\substack{i=1 \\ j=0}}^{\substack{i=N_L \\ j=N_R}} \varphi_{ij}^{q_{ij}},$$

with $\binom{f}{\mathbf{q}}$ being the multinomial coefficient. Then, the total relative amount of bound receptor type n at equilibrium is

$$R_{\mathbf{bound},n} = \frac{L_0 f}{K_x^*} \sum_{m=0}^{N_L} \varphi_{mn} \left(\sum_{\substack{i=1 \\ j=0}}^{\substack{i=N_L \\ j=N_R}} \varphi_{ij}^{q_{ij}} \right)^{f-1}.$$

By conservation of mass, we know that $R_{\mathbf{tot},n} = R_{\mathbf{eq},n} + R_{\mathbf{bound},n}$ for each receptor type n, whereas $R_{\mathbf{bound},n}$ is a function of $R_{\mathbf{eq},n}$. Therefore, each $R_{\mathbf{eq},n}$ can be solved numerically using $R_{\mathbf{tot},n}$. Similarly, the total relative number of complexes bound to at least one receptor on the

cell is

$$L_{\text{bound}} = \frac{L_0}{K_x^*}\left[\left(\sum_{\substack{i=1\\ j=0}}^{\substack{i=N_L\\ j=N_R}} \varphi_{ij}^{q_{ij}}\right)^f - 1\right].$$

Generalized multivalent binding model with defined complexes

When complexes are engineered and ligands are not randomly sorted into multivalent complexes, such as with the Fabs of bispecific antibodies, the proportions of each kind of complex become exogenous variables and are no longer decided by the monomer composition C_i's. The monomer composition of a ligand complex can be represented by a vector $\boldsymbol{\theta} = (\theta_1, \theta_2, \ldots, \theta_{N_L})$, where each θ_i is the number of monomer ligand type i on that complex. Let $C_{\boldsymbol{\theta}}$ be the proportion of the $\boldsymbol{\theta}$ complexes in all ligand complexes, and Θ be the set of all possible $\boldsymbol{\theta}$'s. By this definition $\sum_{\boldsymbol{\theta}\in\Theta} C_{\boldsymbol{\theta}} = 1$.

The binding between a ligand complex and a cell expressing several types of receptors can still be represented by a series of q_{ij}. The relationship between q_{ij}'s and θ_i is given by $\theta_i = q_{i0} + q_{i1} + \cdots + q_{iN_R}$. Let the vector $\mathbf{q}_i = (q_{i0}, q_{i1}, \ldots, q_{iN_R})$, and the corresponding $\boldsymbol{\theta}$ of a binding configuration $\mathbf{q}$ be $\boldsymbol{\theta}(\mathbf{q})$. For all i in $\{1, 2, \ldots, N_L\}$, we define $\psi_{ij} = R_{\text{eq},j} K_{a,ij} K_x^*$ where $j = \{1, 2, \ldots, N_R\}$ and $\psi_{i0} = 1$. The relative number of complexes bound to a cell with configuration $\mathbf{q}$ at equilibrium is

$$v_{\mathbf{q},eq} = \frac{L_0 C_{\boldsymbol{\theta}(\mathbf{q})}}{K_x^*} \prod_{\substack{i=1\\ j=0}}^{\substack{i=N_L\\ j=N_R}} \psi_{ij}^{q_{ij}} \prod_{i=1}^{N_L} \binom{\theta_i}{\mathbf{q}_i}.$$

Then, we can calculate the relative amount of bound receptor n as

$$R_{\text{bound},n} = \frac{L_0}{K_x^*} \sum_{\boldsymbol{\theta}\in\Theta} C_{\boldsymbol{\theta}} \left[\sum_{i=1}^{N_L} \frac{\psi_{in}\theta_i}{\sum_{j=0}^{N_R}\psi_{ij}}\right] \prod_{i=1}^{N_L}\left(\sum_{j=0}^{N_R}\psi_{ij}\right)^{\theta_i}.$$

By $R_{\text{tot},n} = R_{\text{eq},n} + R_{\text{bound},n}$, we can solve $R_{\text{eq},n}$ numerically for each type of receptor. The total relative amount of ligand binding at equilibrium is

$$L_{\text{bound}} = \frac{L_0}{K_x^*} \sum_{\boldsymbol{\theta}\in\Theta} C_{\boldsymbol{\theta}} \left[\prod_{i=1}^{N_L}\left(\sum_{j=0}^{N_R}\psi_{ij}\right)^{\theta_i} - 1\right].$$

Mathematical optimization

We used the limited-memory Broyden–Fletcher–Goldfarb–Shanno algorithm as implemented in SciPy to perform selectivity optimization combining several strategies [42]. Unless specified otherwise, the initial values for optimization were 10^{-12} **cell·M** for crosslinking coefficient K_x^*, 1 for valency f, 100% ligand 1 for mixture composition and 1 **μM** for the affinity dissociation constants, K_x^*. A previous study of IgG–Fc receptor interactions used a reduced form of this binding model and fit it to *in vitro* immune complex binding measurements, deriving a similar value for K_x^* [17]. To optimize ligand characteristics for cell type specificity, we defined different ligand engineering strategies and allowed various ligand characteristics to vary accordingly. For all optimization strategies, K_x^* was allowed to vary 1000-fold from 10^{-12} **cell·M**, thus 10^{-15} to 10^{-9} **cell·M**. In the 'affinity' approach, we allowed the dissociation constant for ligands to vary between 10 **mM** and 0.1 **nM** for both receptors. We then allowed the valency of the ligand to vary between 1 and 16 when considering the 'valency + affinity' engineering approach. In the 'affinity + mixture' approach, the content of a mixture of two ligands was allowed to vary between 100% of each ligand, and the receptor affinities of both ligands were allowed to vary as previously described. Finally, all ligand characteristics were allowed to vary simultaneously to model the 'all' approach. Local optimal selectivity was reliant on the initial point as the optimization space was non-convex. Initialization points were manually selected based on their propensity to result in large improvements during optimization. A variety of starting points were tried within the bounds.

Sigma point filter

To consider the intrapopulation variance of a cell population in the optimization, we implemented the sigma point filter [18], a computationally efficient method to approximate the variance propagated through models. It should be noted that while we found that modulating the magnitude or shape of intrapopulation heterogeneity did affect the inter-population variabilities predicted by our model, it only marginally changed the mean selectivity and did not reverse or alter the qualitative trends that any ligand engineering strategy would have on cell type selectivity.

Author contributions statement

A.S.M. conceived of the work. All authors implemented the analysis and wrote the paper.

Supplementary data

Supplementary data are available at *INTBIO* Journal online.

Funding

National Institutes of Allergy and Infectious Disease at the National Institutes of Health [U01-AI148119 to A.S.M.].

Conflict of interest statement

None declared.

References

1. Mittendorf EA, Wu Y, Scaltriti M et al. Loss of HER2 amplification following trastuzumab-based neoadjuvant systemic therapy and survival outcomes. *Clin Cancer Res* 2009;**15**:7381–8.
2. Turke AB, Zejnullahu K, Wu Y-L et al. Preexistence and clonal selection of MET amplification in EGFR mutant NSCLC. *Cancer Cell* 2010;**17**:77–88.
3. Paek AL, Liu JC, Loewer A et al. Cell-to-cell variation in p53 dynamics leads to fractional killing. *Cell* 2016;**165**:631–42.
4. Maude SL, Frey N, Shaw PA et al. Chimeric antigen receptor T cells for sustained remissions in leukemia. *N Engl J Med* 2014;**371**:1507–17.
5. O'Rourke DM, Nasrallah MP, Desai A et al. A single dose of peripherally infused EGFRvIII-directed CAR T cells mediates antigen loss and induces adaptive resistance in patients with recurrent glioblastoma. *Sci Transl Med* 2017;**9**:eaaa0984.
6. Shalek AK, Satija R, Shuga J et al. Single-cell RNA-seq reveals dynamic paracrine control of cellular variation. *Nature* 2014;**510**:363–9.
7. Mitra S, Leonard WJ. Biology of IL-2 and its therapeutic modulation: mechanisms and strategies. *J Leukoc Biol* 2018;**103**:643–55.
8. Robinson MK, Hodge KM, Horak E et al. Targeting ErbB2 and ErbB3 with a bispecific single-chain Fv enhances targeting selectivity and induces a therapeutic effect in vitro. *Br J Cancer* 2008;**99**:1415–25.
9. Carlson CB, Mowery P, Owen RM. Selective tumor cell targeting using low-affinity, multivalent interactions. *ACS Chem Biol* 20 February 2007;**2**. 10.1021/cb6003788.
10. Silva D-A, Yu S, Ulge UY et al. De novo design of potent and selective mimics of IL-2 and IL-15. *Nature* 2019;**565**:186–91.
11. Chen Z, Kibler RD, Hunt A et al. De novo design of protein logic gates. *Science* 2020;**368**:78–84.
12. Srivastava S, Salter AI, Liggitt D et al. Logic-gated ROR1 chimeric antigen receptor expression rescues T cell-mediated toxicity to normal tissues and enables selective tumor targeting. *Cancer Cell* 2019;**35**:489–503.e8.
13. Cho JH, Collins JJ, Wong WW. Universal chimeric antigen receptors for multiplexed and logical control of T cell responses. *Cell* 2018;**173**:1426–1438.e11.
14. Tan ZC, Meyer AS. A general model of multivalent binding with ligands of heterotypic subunits and multiple surface receptors. *Math Biosci* 2021;108714.
15. Stone JD, Cochran JR, Stern LJ. T-cell activation by soluble MHC oligomers can be described by a two-parameter binding model. *Biophys J* 2001;**81**:2547–57.
16. Robinett RA, Guan N, Lux A et al. Dissecting FcγR regulation through a multivalent binding model. *Cell Syst* 2018;**7**:41–48.e5.
17. Busse D, de la Rosa M, Hobiger K et al. Competing feedback loops shape IL-2 signaling between helper and regulatory T lymphocytes in cellular microenvironments. *Proc Natl Acad Sci U S A* 2010;**107**:3058–63.
18. van der Merwe R. *Sigma-point Kalman filters for probabilistic inference in dynamic state-space models. Ph.D.*, Oregon Health & Science University, https://www.proquest.com/docview/305048474/abstract/A7AA5C0CEEBF4CB6PQ/1 (accessed 21 October 2021).
19. Chittasupho C, Siahaan TJ, Vines CM et al. Autoimmune therapies targeting costimulation and emerging trends in multivalent therapeutics. *Ther Deliv* 2011;**2**:873–89.
20. Liu SP, Zhou L, Lakshminarayanan R et al. Multivalent antimicrobial peptides as therapeutics: design principles and structural diversities. *Int J Pept Res Ther* 2010;**16**:199–213.
21. Liu CJ, Cochran JR. Engineering multivalent and multispecific protein therapeutics. In: Cai W (ed.). *Engineering in Translational Medicine*. London, Springer, 2014, 365–96.
22. Csizmar CM, Petersburg JR, Perry TJ et al. Multivalent ligand binding to cell membrane antigens: defining the interplay of affinity, valency, and expression density. *J Am Chem Soc* 2019;**141**:251–61.
23. Mazor Y, Sachsenmeier KF, Yang C et al. Enhanced tumor-targeting selectivity by modulating bispecific antibody binding affinity and format valence. *Sci Rep* 2017;**7**:40098.
24. Lehár J, Krueger AS, Avery W et al. Synergistic drug combinations tend to improve therapeutically relevant selectivity. *Nat Biotechnol* 2009;**27**:659–66.
25. Chauhan VM, Zhang H, Dalby PA et al. Advancements in the co-formulation of biologic therapeutics. *J Control Release* 2020;**327**:397–405.
26. Poulsen TT, Grandal MM, Skartved NJØ et al. Sym015: a highly efficacious antibody mixture against MET-amplified tumors. *Clin Cancer Res* 2017;**23**:5923–35.
27. Bello C, Vazquez-Blomquist D, Miranda J et al. Regulation by IFN-α/IFN-γ co-formulation (HerberPAG®) of genes involved in interferon-STAT-pathways and apoptosis in U87MG. *Curr Top Med Chem* 2014;**14**:351–8.
28. Antebi YE, Linton JM, Klumpe H et al. Combinatorial signal perception in the BMP pathway. *Cell* 2017;**170**:1184–1196.e24.
29. Deshaies RJ. Multispecific drugs herald a new era of biopharmaceutical innovation. *Nature* 2020;**580**:329–38.
30. Stefanick JF, Omstead DT, Kiziltepe T et al. Dual-receptor targeted strategy in nanoparticle design achieves tumor cell selectivity through cooperativity. *Nanoscale* 2019;**11**:4414–27.
31. Piccione EC, Juarez S, Liu J et al. A bispecific antibody targeting CD47 and CD20 selectively binds and eliminates dual antigen expressing lymphoma cells. *MAbs* 2015;**7**:946–56.
32. Qi J, Chen S-S, Chiorazzi N et al. An IgG1-like bispecific antibody targeting CD52 and CD20 for the treatment of B-cell malignancies. *Methods* 2019;**154**:70–6.
33. Hlavacek WS, Posner RG, Perelson AS. Steric effects on multivalent ligand-receptor binding: exclusion of ligand sites by bound cell surface receptors. *Biophys J* 1999;**76**:3031–43.
34. Altiok EI, Santiago-Ortiz JL, Svedlund FL et al. Multivalent hyaluronic acid bioconjugates improves Flt-1 activity in vitro. *Biomaterials* 2016;**93**:95–105.
35. Bentebibel S-E, Hurwitz ME, Bernatchez C et al. A first-in-human study and biomarker analysis of NKTR-214, a novel IL2R$\beta\gamma$-biased cytokine, in patients with advanced or metastatic solid tumors. *Cancer Discov* June 2019;**9**. 10.1158/2159-8290.CD-18-1495.
36. Peterson LB, Bell CJM, Howlett SK et al. A long-lived IL-2 mutein that selectively activates and expands regulatory T cells as a therapy for autoimmune disease. *J Autoimmun* 2018;**95**:1–14.

37. Towers CG, Fitzwalter BE, Regan D et al. Cancer cells upregulate NRF2 Signaling to adapt to autophagy inhibition. *Dev Cell* 2019;**50**:690–703.e6.
38. Knowles LM, Gurski LA, Engel C et al. Integrin $\alpha v\beta 3$ and fibronectin upregulate slug in cancer cells to promote clot invasion and metastasis. *Cancer Res* 2013;**73**:6175–84.
39. Bubeník J. Tumour MHC class I downregulation and immunotherapy (review). *Oncol Rep* 2003;**10**:2005–8.
40. Guedan S, Ruella M, June CH. Emerging cellular therapies for cancer. *Annu Rev Immunol* 2019;**37**:145–71.
41. Rezvani K, Rouce R, Liu E et al. Engineering natural killer cells for cancer immunotherapy. *Mol Ther* 2017;**25**:1769–81.
42. Virtanen P, Gommers R, Oliphant TE et al. SciPy 1.0: fundamental algorithms for scientific computing in Python. *Nat Methods* 2020;**17**:261–72.
43. Yeung YA, Leabman MK, Marvin JS et al. Engineering human IgG1 affinity to human neonatal Fc receptor: impact of affinity improvement on pharmacokinetics in primates. *J Immunol* 2009;**182**:7663–71.
44. Chao G, Lau WL, Hackel BJ et al. Isolating and engineering human antibodies using yeast surface display. *Nat Protoc* 2006;**1**:755–68.
45. Liu Z, Young AW, Hu P et al. Tuning the membrane selectivity of antimicrobial peptides by using multivalent design. *Chembiochem* 2007;**8**:2063–5.
46. Pelaia G, Maselli R, Matera MG. Treatment of chronic obstructive pulmonary disease by dual bronchodilation with coformulation of indacaterol/glycopyrronium. *Pharmacology* 2014;**94**:249–58.
47. Kontermann RE, Brinkmann U. Bispecific antibodies. *Drug Discov Today* 2015;**20**:838–47.
48. Martiniani R, Di Loreto V, Di Sano C et al. Biological activity of lenalidomide and its underlying therapeutic effects in multiple myeloma. *Adv Hematol* 2012;**2012**:842945.
49. Perelson AS Receptor clustering on a cell surface. III. Theory of receptor cross-linking by multivalent ligands: description by ligand states. *Mathematical Biosciences* 1981;**53**:1–39.
50. Harris LA, Hogg JS, Tapia JJ et al. BioNetGen 2.2: advances in rule-based modeling. *Bioinformatics* 2016;**32**:3366–8.
51. Errington WJ, Bruncsics B, Sarkar CA. Mechanisms of noncanonical binding dynamics in multivalent protein–protein interactions. *Proceedings of the National Academy of Sciences* 2019;**116**:25659–67.

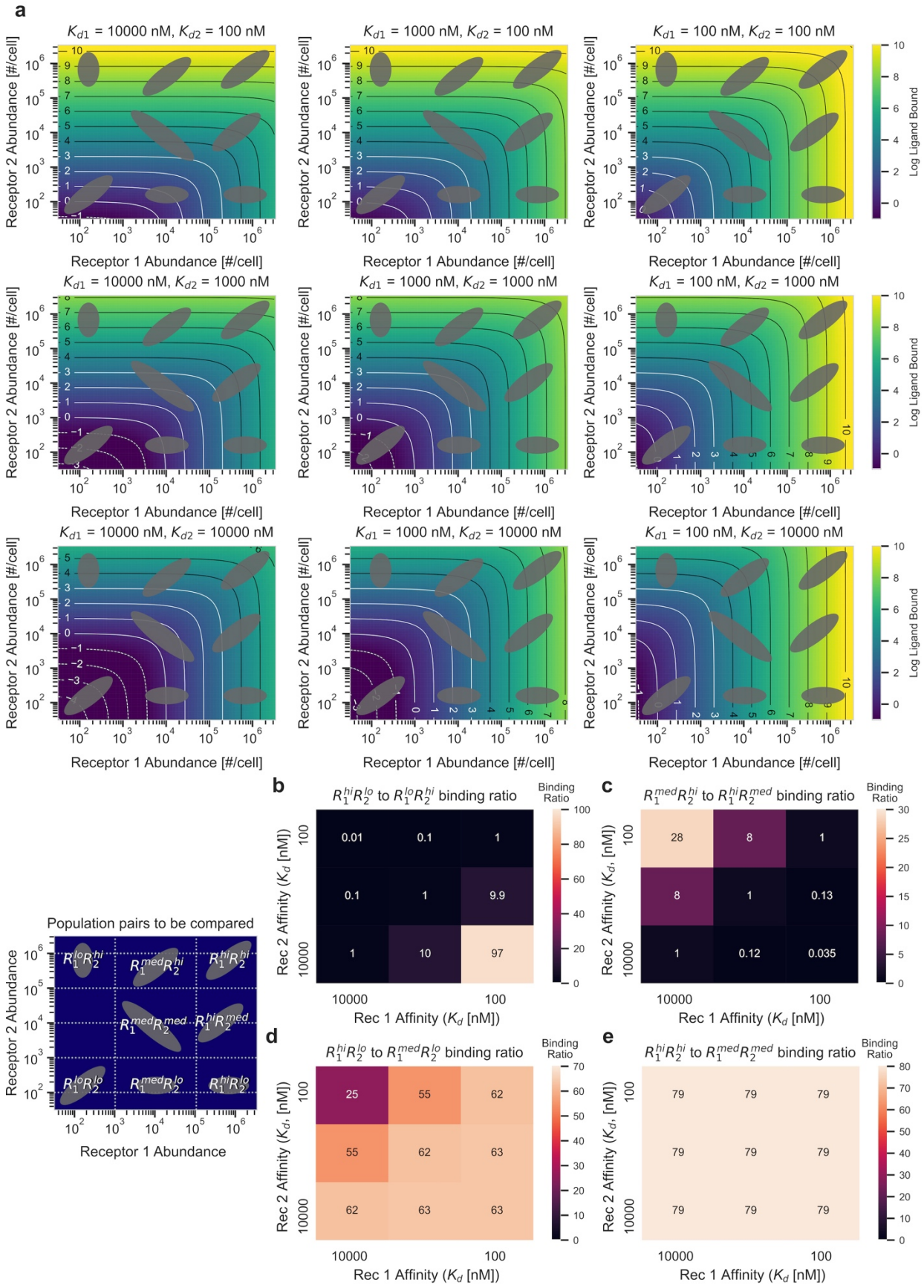
a
K_{d1} = 10000 nM, K_{d2} = 100 nM
K_{d1} = 1000 nM, K_{d2} = 100 nM
K_{d1} = 100 nM, K_{d2} = 100 nM
K_{d1} = 10000 nM, K_{d2} = 1000 nM
K_{d1} = 1000 nM, K_{d2} = 1000 nM
K_{d1} = 100 nM, K_{d2} = 1000 nM
K_{d1} = 10000 nM, K_{d2} = 10000 nM
K_{d1} = 1000 nM, K_{d2} = 10000 nM
K_{d1} = 100 nM, K_{d2} = 10000 nM
Receptor 2 Abundance [#/cell]
Receptor 1 Abundance [#/cell]
Log Ligand Bound
Population pairs to be compared
$R_1^{lo}R_2^{hi}$
$R_1^{med}R_2^{hi}$
$R_1^{hi}R_2^{hi}$
$R_1^{med}R_2^{med}$
$R_1^{hi}R_2^{med}$
$R_1^{lo}R_2^{lo}$
$R_1^{med}R_2^{lo}$
$R_1^{hi}R_2^{lo}$
Receptor 2 Abundance
Receptor 1 Abundance
b
$R_1^{hi}R_2^{lo}$ to $R_1^{lo}R_2^{hi}$ binding ratio
0.01 0.1 1
0.1 1 9.9
1 10 97
c
$R_1^{med}R_2^{hi}$ to $R_1^{hi}R_2^{med}$ binding ratio
28 8 1
8 1 0.13
1 0.12 0.035
d
$R_1^{hi}R_2^{lo}$ to $R_1^{med}R_2^{lo}$ binding ratio
25 55 62
55 62 63
62 63 63
e
$R_1^{hi}R_2^{hi}$ to $R_1^{med}R_2^{med}$ binding ratio
79 79 79
79 79 79
79 79 79
Binding Ratio
Rec 2 Affinity (K_d, [nM])
Rec 1 Affinity (K_d [nM])
10000
100

Figure 1: Affinity provides selectivity to cell populations with divergent receptor expression. a) Heat/contour maps of monovalent ligand binding to cell populations given the surface abundance of two receptors. Ligand dissociation constants to these receptors range from 10μM ~ 100nM. Ligand concentration L_0 = 1nM. **b-e)** Heatmap of binding ratio of cell populations exposed to a monovalent ligand with dissociation constants to receptor 1 and 2 ranging from 10^4 ~ 10^2nM, at a concentration L_0 = 1nM. Ligand bound ratio of (b) $R_1^{hi}R_2^{lo}$ to $R_1^{lo}R_2^{hi}$, (c) $R_1^{med}R_2^{hi}$ to $R_1^{hi}R_2^{med}$, (d) $R_1^{hi}R_2^{lo}$ to $R_1^{med}R_2^{hi}$, and (e) $R_1^{hi}R_2^{hi}$ to $R_1^{med}R_2^{med}$.

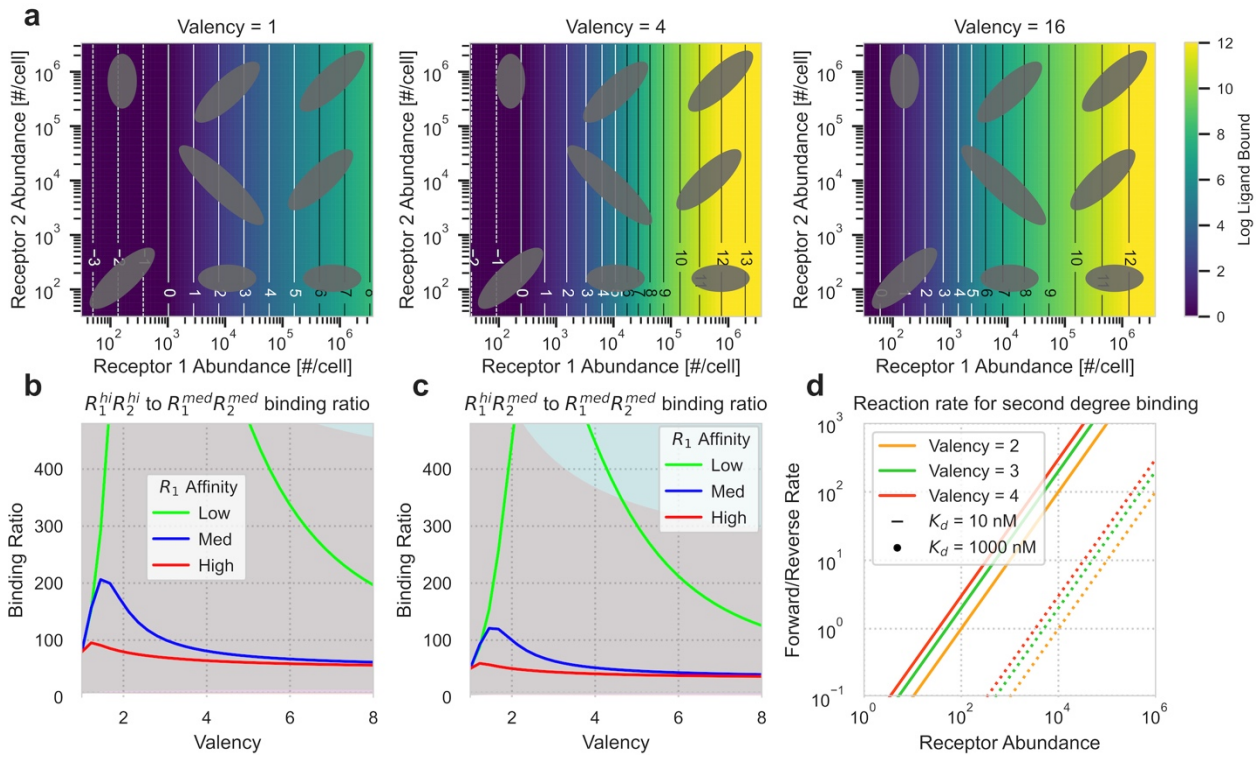

Figure S2: Valency provides selectivity based on receptor expression levels. a) Heat/contour maps of multivalent ligands bound to cell populations given their expression profiles of two receptors. Multivalent ligand subunits bind to only R_1 with an dissociation constant of 100 nM, and do not bind to R_2. Complexes vary in valency from 1 to 16. Ligand concentration L_0 = 1 nM; crosslinking constant $K_x^* = 10^{-10}$. **b-d)** Ligand binding ratio between various cell populations for ligands of valency ranging from 1 to 16. The shaded areas indicate the variance of binding ratios caused by the intrapopulation heterogeneity and estimated by sigma point filters. b) Ligand bound ratio $R_1^{hi}R_2^{lo}$ to $R_1^{med}R_2^{lo}$, and (c) $R_1^{hi}R_2^{hi}$ to $R_1^{med}R_2^{med}$. d) Ratio of forward to reverse binding rate for secondary binding events for multivalent ligands to cells expressing variable amounts of receptors.

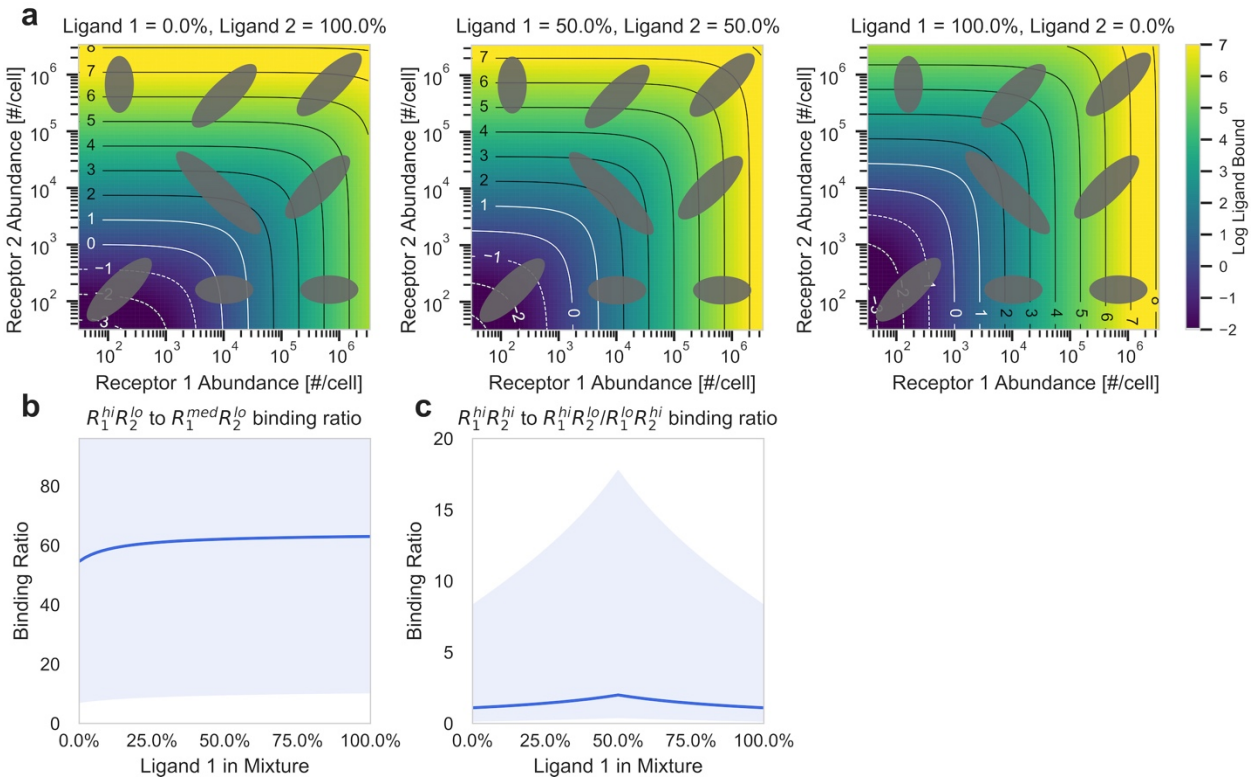

Figure S3: Ligand mixtures with non-overlapping responses can enhance selectivity. a) Heat/contour maps of multivalent ligands bound to cell populations given their expression profiles of two receptors. A mixture of monovalent ligands is used, with ligand 1 binding to receptor 1 and 2 with dissociation constants of 1 μM and 10 μM respectively, and ligand 2 binding to receptors 1 and 2 with dissociation constants of 10 μM and 1 μM respectively. Ligand concentration L_0 = 1 nM; crosslinking constant $K_X^* = 10^{-10}$. **b,c)** Ratio of ligand bound to cell populations exposed to monovalent mixtures of ligand 1 and 2. The ratio of the target population to the single off target population with the greatest ligand bound is plotted. The shaded areas indicate the variance caused by intrapopulation heterogeneity, of $R_1^{hi}R_2^{lo}$ to $R_1^{med}R_2^{lo}$, and c) $R_1^{hi}R_2^{hi}$ to $R_1^{hi}R_2^{lo}$ and $R_1^{lo}R_2^{hi}$.

Chapter 2:

Modeling cell-specific dynamics and regulation of the common gamma chain cytokines

Farhat, A. M.[1], Weiner**.,** A. C. [1], Posner, C. [2], Kim, Z. S.[1], **Orcutt-Jahns, B**.[1], Carlson, S. M.[2], & Meyer, A. S.[1]

[1] Department of Bioengineering, Jonsson Comprehensive Cancer Center, Eli and Edythe Broad Center of Regenerative Medicine and Stem Cell Research, University of California, Los Angeles, Los Angeles, CA 90024, USA

[2] Visterra Inc., Waltham, MA 02451

Cell Reports

Article

Modeling cell-specific dynamics and regulation of the common gamma chain cytokines

Graphical abstract

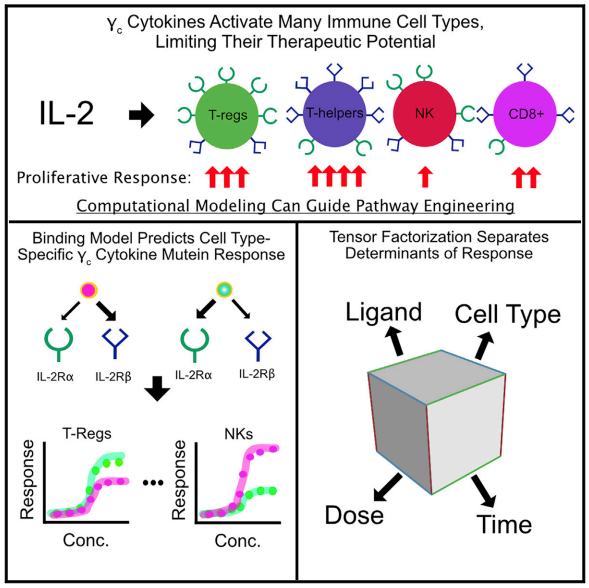

Highlights

- A dynamical model of the common γ-chain cytokines accurately predicts response
- Receptor trafficking is necessary for predicting ligand response in new contexts
- Tensor factorization maps responses across cell populations, receptors, and cytokines
- Pathway model provides design criteria for ligands with greater cell type selectivity

Authors

Ali M. Farhat, Adam C. Weiner, Cori Posner, Zoe S. Kim, Brian Orcutt-Jahns, Scott M. Carlson, Aaron S. Meyer

Correspondence

a@asmlab.org

In brief

Farhat et al. develop a mechanistic model of the common γ-chain receptor cytokines incorporating the structure of receptor-ligand interaction and trafficking. This model can predict the response to these cytokines, alone and in combination, and changes in binding affinity, enabling more rational cytokine engineering.

Farhat et al., 2021, Cell Reports *35*, 109044
April 27, 2021
https://doi.org/10.1016/j.celrep.2021.109044

Cell Reports

CellPress
OPEN ACCESS

Article

Modeling cell-specific dynamics and regulation of the common gamma chain cytokines

Ali M. Farhat,[1,3] Adam C. Weiner,[1,3] Cori Posner,[2] Zoe S. Kim,[1] Brian Orcutt-Jahns,[1] Scott M. Carlson,[2] and Aaron S. Meyer[1,4,*]

[1]Department of Bioengineering, Jonsson Comprehensive Cancer Center, Eli and Edythe Broad Center of Regenerative Medicine and Stem Cell Research, University of California, Los Angeles, Los Angeles, CA 90024, USA
[2]Visterra, Inc., Waltham, MA 02451, USA
[3]These authors contributed equally
[4]Lead contact
*Correspondence: a@asmlab.org
https://doi.org/10.1016/j.celrep.2021.109044

SUMMARY

The γ-chain receptor dimerizes with complexes of the cytokines interleukin-2 (IL-2), IL-4, IL-7, IL-9, IL-15, and IL-21 and their corresponding "private" receptors. These cytokines have existing uses and future potential as immune therapies because of their ability to regulate the abundance and function of specific immune cell populations. Here, we build a binding reaction model for the ligand-receptor interactions of common γ-chain cytokines, which includes receptor trafficking dynamics, enabling quantitative predictions of cell-type-specific response to natural and engineered cytokines. We then show that tensor factorization is a powerful tool to visualize changes in the input-output behavior of the family across time, cell types, ligands, and concentrations. These results present a more accurate model of ligand response validated across a panel of immune cell types as well as a general approach for generating interpretable guidelines for manipulation of cell-type-specific targeting of engineered ligands.

INTRODUCTION

Cytokines are cell signaling proteins responsible for cellular communication within the immune system. The common γ-chain (γ_c) receptor cytokines, including interleukin-2 (IL-2), IL-4, IL-7, IL-9, IL-15, and IL-21, are integral for modulating innate and adaptive immune responses. Therefore, they have existing uses and future potential as immune therapies (Leonard et al., 2019; Rochman et al., 2009). Each ligand binds to its specific private receptors before interacting with the common γ_c receptor to induce signaling (Walsh, 2010). γ_c receptor signaling induces lymphoproliferation, offering a mechanism for selectively expanding or repressing immune cell types (Amorosi et al., 2009; Vigliano et al., 2012). Consequently, loss-of-function or reduced-activity mutations in the γ_c receptor can cause severe combined immunodeficiency (SCID) because of insufficient T and natural killer (NK) cell maturation (Wang et al., 2011). Deletion or inactivating mutations in IL-2 or its private receptors leads to more selective effects, including diminished regulatory T cell (T_{reg}) proliferation and loss of self-tolerance (Horak, 1995; Sharfe et al., 1997; Sharma et al., 2007). Deficiency in the IL-2 receptor IL-2Rα also causes hyperproliferation in CD8+ T cells but a diminished antigen response (Goudy et al., 2013). These examples show how γ_c receptor cytokines coordinate a dynamic balance of immune cell abundance and function.

The γ_c cytokines' ability to regulate lymphocytes can affect solid and hematological tumors (Pulliam et al., 2016). IL-2 is an approved, effective therapy for metastatic melanoma, and the antitumor effects of IL-2 and IL-15 have been explored in combination with other treatments (Bentebibel et al., 2019; Zhu et al., 2015). Nonetheless, understanding these cytokines' regulation is stymied by their complex binding and activation mechanism (Walsh, 2010). Any intervention imparts effects across multiple distinct cell populations, with each population having a unique response defined by its receptor expression (Cotari et al., 2013; Ring et al., 2012). These cytokines' potency is largely limited by severe toxicity, such as deadly vascular leakage with IL-2 (Krieg et al., 2010). Finally, IL-2 and IL-15 are cleared rapidly renally and by receptor-mediated endocytosis, limiting their half-life *in vivo* (Bernett et al., 2017; Donohue and Rosenberg, 1983; Konrad et al., 1990).

To address the limitations of natural ligands, engineered proteins with potentially beneficial properties have been produced (Leonard et al., 2019). The most common approach has been to develop mutant ligands by modulating the binding kinetics of specific receptors (Berndt et al., 1994; Collins et al., 1988). For example, mutant IL-2 forms with a higher binding affinity for IL-2Rβ or reduced binding to IL-2Rα and induces greater cytotoxic T cell proliferation, antitumor responses, and proportionally less T_{reg} expansion (Bentebibel et al., 2019; Levin et al., 2012). This behavior can be understood through IL-2's typical mode of action, in which T_{reg} cells are sensitized to IL-2 by expression of IL-2Rα (Ring et al., 2012). Bypassing this sensitization mechanism shifts cell specificity (Levin et al., 2012).

Conversely, mutants skewed toward IL-2Rα over IL-2Rβ binding selectively expand T_{reg} cell populations over cytotoxic T cells and NK cells compared with native IL-2 (Bell et al., 2015; Peterson et al., 2018).

The therapeutic potential and complexity of this family make computational models especially valuable for rational engineering. Early attempts to mathematically model the synergy between IL-2 and IL-4 in B and T cells successfully identified a phenomenological model that could capture the synergy between the two cytokines (Burke et al., 1997). A cell population model has explained how T_{reg} cell IL-2 consumption suppresses effector T cell signaling (Feinerman et al., 2010). However, any model needs to incorporate the key regulatory features of a pathway to accurately predict cell response. With structural information that clarified the mechanism of cytokine binding, for example, a model of IL-4, IL-7, and IL-21 binding revealed pathway crosstalk depending on the relative γ_c receptor affinities (Gonnord et al., 2018). Nevertheless, these models have not accounted for endosomal trafficking and have not been constructed to model multiple immune cell types. The crucial role receptor-mediated endocytosis has been shown to play in signaling and drug delivery processes has led to development of many mathematical models incorporating its effects (Lao et al., 2007; Byun and Jung, 2020). IL-2 induces rapid endocytosis-mediated IL-2Rα and IL-2Rβ downregulation (Duprez et al., 1988; Ring et al., 2012), and trafficking is known to be a potent regulatory mechanism for all members of the γ_c family (Lamaze et al., 2001). Indeed, recent IL-15 engineering observed that attenuated cytokine potency can lead to a greater therapeutic effect via reduced receptor-mediated clearance (Bernett et al., 2017). Non-intuitive properties such as this can be better understood and optimized through models incorporating trafficking.

Here we assemble a predictive model and tools to visualize γ_c cytokine family regulation. We first built a family-wide mathematical model that incorporates binding and trafficking kinetics. This more comprehensive model allows us to investigate emergent behavior, such as competition between cytokines. This cytokine family is inherently highly dimensional, with multiple ligands, cognate receptors, and cells with distinct expression. Therefore, we use tensor factorization to visualize the family-wide regulation. This map helps us to identify how native or engineered ligands are targeted to specific immune cell populations based on their receptor expression levels. The methods used here can be used similarly in experimental and computational efforts of decoding other complex signaling pathways, such as Wnt, Hedgehog, Notch, and bone morphogenic protein (BMP)/transforming growth factor β (TGF-β) (Antebi et al., 2017a, 2017b; Eubelen et al., 2018; Li et al., 2018).

RESULTS

A model including trafficking captures IL-2 and IL-15 dose response and the effect of IL-2Rα expression

To model how individual binding events give rise to cell response, we built a differential equation model representing the relevant binding and regulatory mechanisms in the γ_c receptor cytokine family (Figure 1A). The differential equations and corresponding rate parameters that define our model are described in the STAR Methods (Table 1). Binding interactions were modeled based on their known structural components and led to formation of receptor complexes capable of Janus kinase (JAK)/signal transducer and activator of transcription (STAT) signaling (Rochman et al., 2009). Endocytic trafficking of cell surface receptors is a critical mechanism of regulatory feedback (Basquin et al., 2013; Fallon and Lauffenburger, 2000; Fallon et al., 2000; Volkó et al., 2019). Therefore, we extended earlier modeling efforts by including trafficking of receptors and their complexes (Feinerman et al., 2010; Ring et al., 2012). We assumed that species trafficked into an endosomal compartment while continuing to produce JAK/STAT signaling and participating in binding events.

Rate parameters for IL-2 and IL-15 binding events were parameterized by previous experimental measurements and detailed balance or estimated by model fitting to existing experimental measurements (Figures 1B–1E). Fitting was performed to measurements of STAT5 phosphorylation and surface IL-2Rβ/γ_c, upon IL-2 or IL-15 stimulation, in wild-type YT-1 human NK cells or YT-1 cells selected for expression of IL-2Rα. The experimental data were collected from previous studies (Mitra et al., 2015; Ring et al., 2012). The posterior parameter distributions from these fits (Figure 1F–1I) were plugged back into our model and showed quantitative agreement with the data, including differential sensitivity with IL-2Rα expression (Figures 1B–1E; Mitra et al., 2015; Ring et al., 2012). To evaluate the effect of including trafficking, we fit a version of the model without trafficking to the same pSTAT5 measurements. Surprisingly, the model without trafficking was able to fit the data equally well with small changes to some inferred rate constants (Figure S1). Although the model with trafficking inferred cell receptor expression of ~1 receptor/cell/min, corresponding to 500–5,000 receptors/cell, the model without trafficking inferred that YT-1 cells have receptor abundances of 1–10/cell. We elected to use the model including trafficking for the duration of the study because γ_c receptors have known trafficking regulation. We also show that endocytic signaling can uniquely affect the cell-type-specific response to γ_c cytokines (Figure 6C) and that trafficking improves model correspondence to our validation measurements (Figures S5 and S6). Depletion of surface IL-2Rβ and γ_c occurs through rapid endocytosis of active complexes, and indeed, depletion occurred faster at higher cytokine doses (Figures 1C–1E). Correspondingly, active complex internalization was inferred to be ~10× greater than that for inactive species (Figure 1G). These data suggest that trafficking and binding can be integrated in a model of IL-2 and IL-15 signaling response.

Because IL-2 and IL-15 drive formation of analogous active complexes with IL-2Rβ, γ_c, and a signaling-deficient high-affinity receptor (IL-2Rα/IL-15Rα), comparing their inferred binding rates gave insight into how IL-2 and IL-15 differ from one another (Figure 1I). The two ligands have nearly the same direct binding affinity to IL-2Rβ; however, IL-15 has a higher affinity than IL-2 for its α chain. Consequently, IL-15's complexes were inferred to more readily dimerize with a free α chain than IL-2's complexes. The other dimerization affinities were generally similar between IL-2 and IL-15. The unbinding rate constants were consistent with the literature indicating that IL-2 has a higher affinity for IL-2Rβ when bound to its α chain

CellPress
OPEN ACCESS

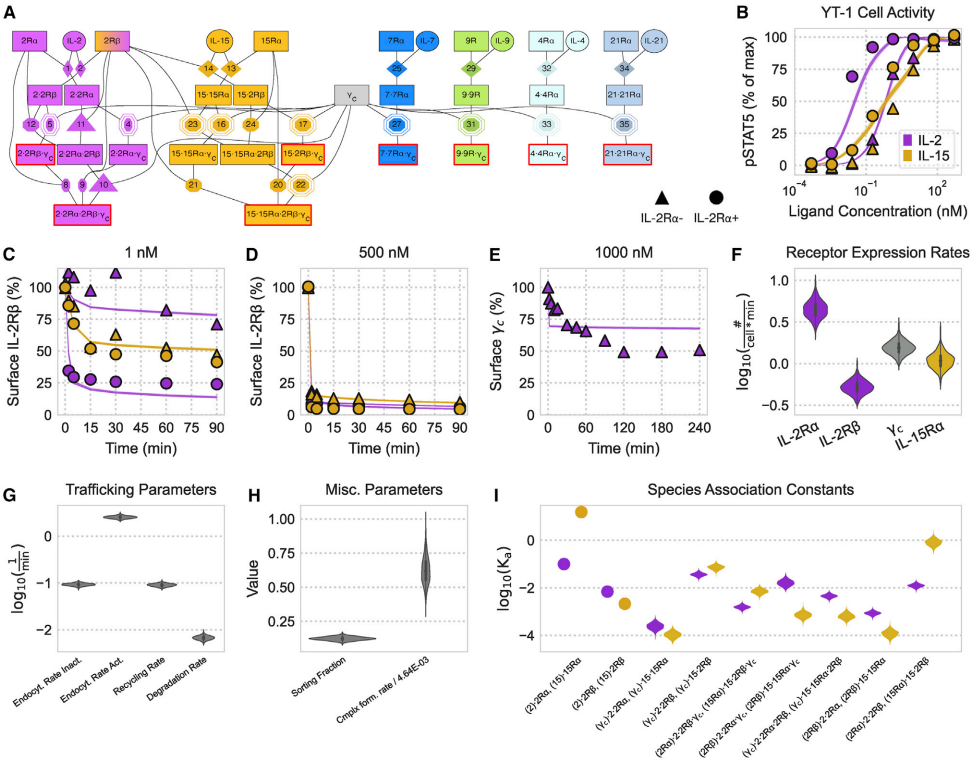

Figure 1. Unifying receptor binding and trafficking provides an accurate model of IL-2 and IL-15 response

Experimental data were collected in previous studies (Mitra et al., 2015; Ring et al., 2012).

(A) Schematic of all receptor (boxes)-ligand (circles) complexes and binding events. Active (pSTAT signaling; containing two signaling-competent receptors) complexes are outlined in red. Rate constants obtained from the literature, detailed balance, and fitting are denoted by diamonds, octagons, and octagons with a double outline, respectively. Rate constants that were measured experimentally relative to other rates are denoted by triangles. A scalar factor scales active receptor complexes to pSTAT predictions. See STAR Methods for full model equations.

(B–E) Model fit to experimental results, represented by shaded regions and shapes respectively, for (B) pSTAT5 in YT-1 cells under various concentrations of ligand stimulation for 500 min and (C–E) the percent of initial IL-2Rβ (C and D) and γ_c (E) on the cell surface for various ligand stimulation concentrations. The 25%–75% and 10%–90% confidence intervals of the model's fit are shaded dark and light, respectively. Note that only the 25%–75% interval is visible.

(F–H) Posterior distributions after data fitting. The forward receptor dimerization rate k_{fwd} has units of $cell \times \#^{-1} \times min^{-1}$, and the sorting fraction (f_{sort}) is unitless.

(I) Posterior distributions for the analogous association constants of IL-2 and IL-15. Association constants measured in the literature are represented by dots. Association constants are shown for species in parentheses complexing with the following species. K_as for (2)·2Rα, (15)·15Rα, (2)·2Rβ, and (15)·2Rβ have nanomolar units; all other K_as have units of $\# \times cell^{-1}$.

See also Figures S1 and S2.

(Spangler et al., 2015). A model of IL-2 and IL-15 incorporating trafficking is consistent with known biophysical and cell response measurements.

The family model correctly captures IL-4/IL-7 dose response and cross-inhibition

To further test our model incorporating trafficking, we evaluated its performance in a series of experiments involving IL-4 and IL-7. IL-2 and IL-15 involve the same signaling-competent receptors, and so the signaling activity of each cytokine cannot be distinguished. IL-4 and IL-7 activity, in contrast, can be distinguished when both cytokines are co-administered to cells by measuring STAT6 and STAT5 phosphorylation, respectively (Leonard et al., 2019). Using this phenomenon, we explored previously published cross-inhibition data where IL-4 and IL-7 doses were administered to human peripheral blood mononuclear cell

Table 1. Cytokine reverse binding constants

Rate/Role Description	IL-2	IL-15	IL-4	IL-7
α receptor	IL-2Rα	IL-15Rα	–	–
β receptor	IL-2Rβ	IL-2Rβ	IL-4Rα	IL-7Rα
Rate of ligand dissociation from α receptor	$k_{1,rev}$	$k_{13,rev}$	$k_{32,rev}$	$k_{25,rev}$
Rate of ligand dissociation from β receptor	$k_{2,rev}$	$k_{14,rev}$	–	–
Rate of γ_c dissociation from ligand· α· γ_c complex	$k_{4,rev}$	$k_{16,rev}$	$k_{33,rev}$	$k_{27,rev}$
Rate of γ_c dissociation from ligand· β· γ_c complex	$k_{5,rev}$	$k_{17,rev}$	–	–
Rate of α dissociation from ligand· α· β· γ_c complex	$k_{8,rev}$	$k_{20,rev}$	–	–
Rate of β dissociation from ligand· α· β· γ_c complex	$k_{9,rev}$	$k_{21,rev}$	–	–
Rate of γ_c dissociation from ligand· α· β· γ_c complex	$k_{10,rev}$	$k_{22,rev}$	–	–
Rate of β dissociation from ligand· α· β complex	$k_{11,rev}$	$k_{23,rev}$	–	–
Rate of α dissociation from ligand· α· β complex	$k_{12,rev}$	$k_{24,rev}$	–	–

(PBMC)-derived $CD4^+TCR^+CCR7^{high}$ T cells individually and together (Gonnord et al., 2018).

Using surface abundance measurements of IL-4Rα, IL-7Rα, and γ_c, we applied a steady-state assumption in the absence of ligand to solve each receptor expression rate (Gonnord et al., 2018). Our model fit single and dual cytokine dose-response data with reasonable accuracy. Fits to the IL-4 and IL-7 dose response had systematic deviation toward higher half maximal effective concentration (EC_{50}) values (Figure 2B), but the model captured the difference in response between IL-4 and IL-7 as well as the effects of cross-inhibition (Figures 2B–2C). Some systematic error in the model can be expected, given our focus on receptor binding features and subsequent choice to not model the JAK-STAT pathway in total. The fitting process identifiably constrained the reaction rates and trafficking parameters (Figure 2F–2I). Although surface abundance was constrained, the receptor expression rates still formed distributions dependent on trafficking parameters (Figures 2G–2I).

The experimental data and model fits showed that IL-7 inhibited IL-4 signaling response more than vice versa (Figure 2C; Gonnord et al., 2018). Consistent with the experimentally derived mechanism (Gonnord et al., 2018), this inhibitory behavior was explained by the competition of ligand·α chain complexes for the common γ_c. The inferred association constant (K_a) value of this dimerization process for IL-7 was larger than the K_a value for IL-4, indicating that there was tighter dimerization of IL-7·IL-7Rα to γ_c than of IL-4·IL-4Rα to γ_c (Figure 2F). The competition for γ_c was determined to play a larger role in signaling inhibition than receptor internalization because our model showed that the same inhibitory relationships hold when active complexes were set to internalize at the same rate as other species (Figure 2D). Internalization was also dismissed because much of the γ_c remained on the cell surface after ligand stimulation in model simulations and experimental measurements (Figure 2E; Gonnord et al., 2018).

Tensor factorization maps the γ_c family response space

Because response to ligand is mostly defined by receptor expression, we quantitatively profiled the abundance of each IL-2, IL-15, and IL-7 receptor across 10 PBMC subpopulations (Figure 3A). PBMCs gathered from a single donor were stained using receptor-specific fluorescent antibodies and analyzed by flow cytometry; their subpopulations were separated using canonical markers (Figure S3; Table S1). These data recapitulated known variation in these receptors, including high IL-7Rα or IL-2Rα expression in helper and T_{reg} cells, respectively (Hassan and Reen, 1998; Rochman et al., 2009). Principal-component analysis (PCA) helped to further visualize variation in these receptor abundance data. The 10 PBMC cell types were mapped in the scores plot (Figure 3B) using two principal components, each of which was defined by a linear combination of the cell's receptor expression abundance, as described in the loadings plot (Figure 3C). Principal component 1, which explained 50% of the receptor expression data's variance, most prominently separated NK cells from all others because of their distinct receptor expression, featuring high levels of IL-2Rβ and relatively lower levels of γ_c compared with other cell types, which are strongly correlated positively and negatively with principal component 1, respectively. Principal component 2, which explained 36% of the receptor expression data's variance, then separated effector and T_{reg} cell populations based on their high IL-7Rα or IL-2Rα abundance, respectively. PCA also helped to highlight the subtly higher γ_c levels in T_{reg} cells and the slightly more T_{reg} cell-like profile of memory CD8+ cells.

Even with an accurate model, exploring how dynamic responses vary across responding cell types and ligand treatments remains challenging. Considering only a single time point, cell type, or ligand concentration provides only a slice of the picture. Therefore, we sought to apply factorization as a method to globally visualize ligand response.

To build a tensor of model predictions, we assembled simulation predictions across cell types, ligand conditions, and time.

CellPress
OPEN ACCESS

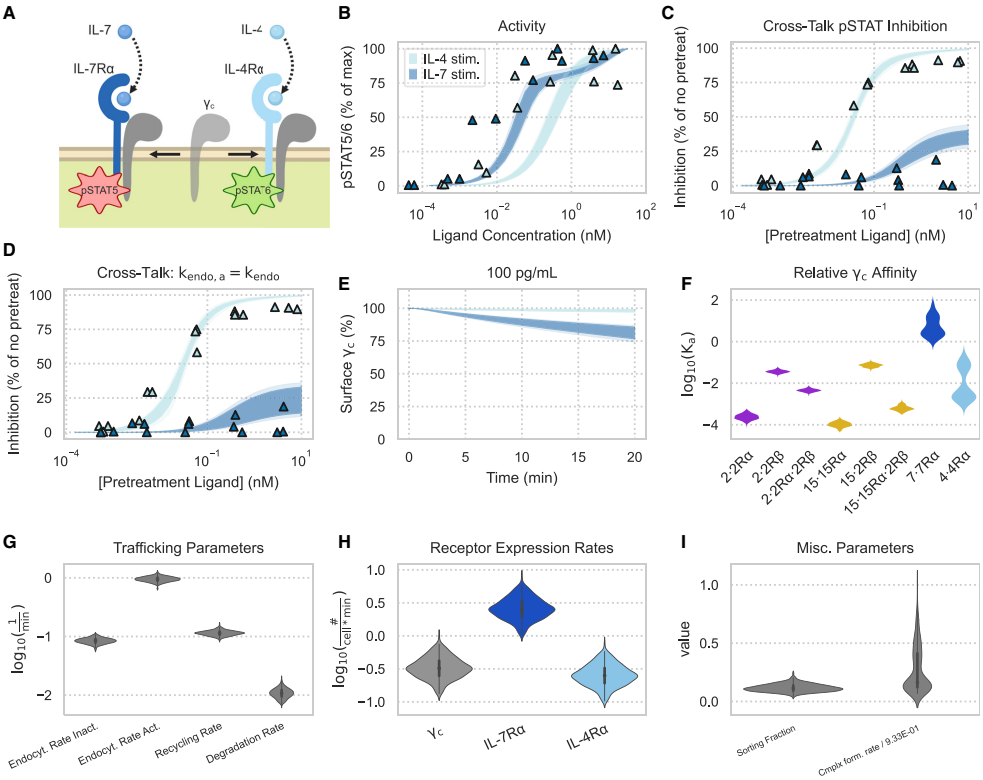

Figure 2. A reaction model captures cytokine-cytokine interactions

Experimental data were collected in previous studies (Gonnord et al., 2018).

(A) Schematic of IL-4 and IL-7 receptor complexes competing for γ_c and generating distinct pSTAT signals.

(B and C) Model fits to experimental data. Experimental measurements are denoted by triangles. Shaded areas represent the 25%–75% and 10%–90% confidence intervals of the model fit. pSTAT5 and pSTAT6 were measured for IL-7 and IL-4 experiments, respectively.

(B) Single-cytokine pSTAT dose-response measurements for 10 min of exposure to IL-4 and IL-7. The experiment was performed in duplicate (n = 2).

(C) Percent inhibition of the second cytokine's pSTAT response in a dual-cytokine dose-response experiment. Human PBMC-derived T cells ($CD4^+TCR^+CCR7^{high}$) were pretreated with various concentrations of one cytokine for 10 min before being stimulated with a fixed concentration (2 pM IL-7 or 6.25 pM IL-4) of the other cytokine for an additional 10 min.

(D) Model inference for percent inhibition of the second cytokine's pSTAT response in a dual-cytokine dose-response experiment after setting active species to be endocytosed at the same rate as inactive species.

(C and D) Experiments were performed in triplicate (n = 3).

(E) Model predictions for the percentage of γ_c on the cell surface when exposed to 100 pg/mL of IL-7 or IL-4 for 20 min.

(F) Violin plot of K_a values (units of $\#\times cell^{-1}$) for complexes with γ_c obtained via the posterior distribution of the forward and reverse binding rate parameters.

(G–I) Posterior parameter distributions from fitting to data. The forward dimerization rate k_{fwd} has units of $cell\times\#^{-1}\times min^{-1}$.

This three-dimensional (time, cell type, and ligand) tensor was then decomposed with non-negative canonical polyadic (CP) decomposition (Figure 3D). We selected three components during decomposition because this number captured 95% of the variance in our original data tensor (Figure 3E). To show the relationships among the tensor's three dimensions, the component plots of each dimension were plotted alongside each other.

CP decomposition can be interpreted by matching a single component's effects across factor plots for each dimension, allowing us to interpret its relationship to time, to a profile of cell responses, and a pattern of stimulation conditions (Figures 3F–3I). For example, component 2 is greatest at roughly 50 min (Figure 3F) for helper and CD8+ T cells (Figure 3G) and occurs almost exclusively with IL-7 stimulation (Figure 3I). This

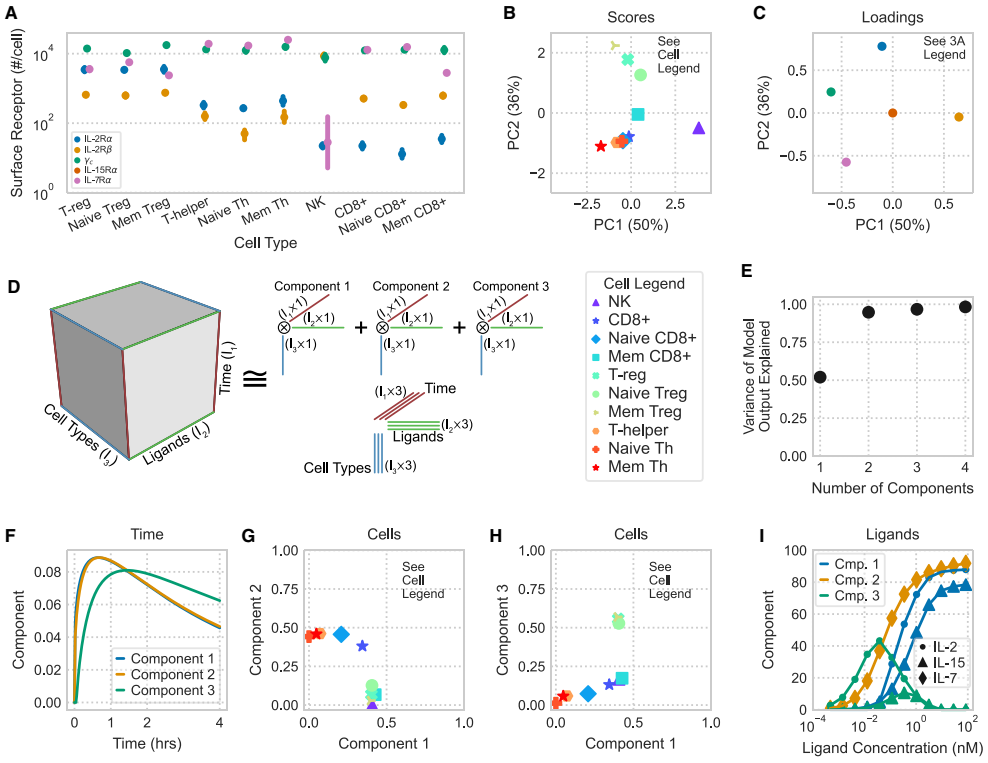

Figure 3. Tensor factorization map model-predicted cytokine responses

(A) Measured receptor abundance for 10 PBMC-derived subpopulations gathered from a single donor, measured by flow cytometry. Points and error bars show geometric mean and standard error, respectively (n = 4). Error bars for some points are too small to display.

(B and C) PCA scores (B) and loading (C) of receptor abundance. Axis label percentages indicate percent variance explained.

(D) Schematic representation of CP decomposition. Model predictions are arranged in a cube depending on the time, ligand treatment, and cell type being modeled. CP decomposition then helps to visualize this space.

(E) Percent variance reconstructed (R2X) versus the number of components used in non-negative CP decomposition.

(F–I) Component values versus time (F), cell type (G and H), and ligand stimulation (I). The variation explained by each component is the product of the component's time, ligand, and cell type factorization. Ligand components with only negligible values (<15% max) are not shown.

See also Figures S3 and S4.

indicates that this variation in the data occurs with IL-7 stimulation, leads to a response in helper and CD8+ T cells, and peaks at 50 min. In this way, different contributory factors in cell response are separated.

All components showed similar variation with time, peaking quickly and then decreasing after roughly 50 min (Figure 3F). This can be understood as two phases: one dominated by receptor activation and a second with trafficking-mediated downregulation of the receptors (Figure 1). Comparing the cells and ligand decomposition plots showed the expected effects. IL-7 response was separated by component 2, which showed a dose-dependent increase, and correlated with IL-7Rα expression levels (Figures 3A, 3G, and 3I). Interestingly, IL-2/15 response separated by concentration rather than ligand (Figure 3I). Low concentrations of IL-2 were represented by component 3, and preferentially activated T_{reg} over effector T cells (Figures 3H and 3I). High concentrations of IL-2/15 were represented by component 1 and similarly activated effector and T_{reg} cells (Figures 3G and 3I). This known dichotomy occurs through higher IL-2Rα expression in T_{reg} cells (Figure 3A). Importantly, although PCA can help to distinguish cells based on distinct receptor expression profiles, cells separated differently based on their predicted ligand stimulation response (Figures 3B, 3G, and 3H). This demonstrates the unique benefit of

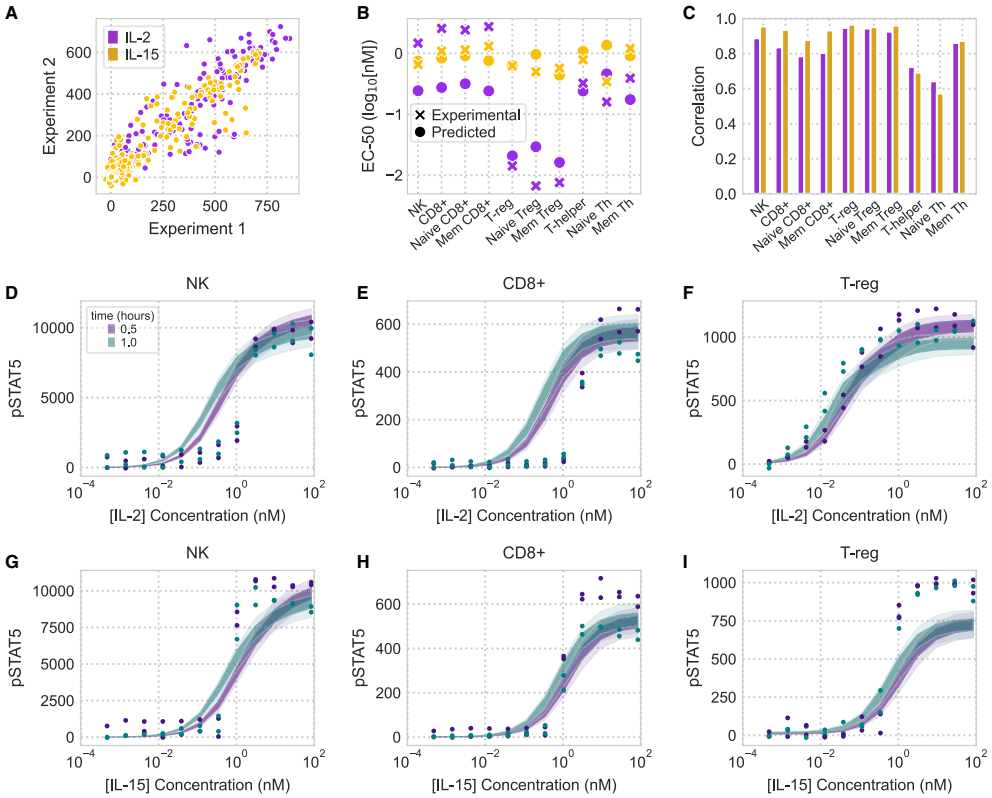

Figure 4. The model accurately predicts cell-type-specific response across a panel of PBMC-derived cell types

(A) Comparison of two experimental replicates measuring the pSTAT5 response of PBMC-derived cells to cytokine stimulation. Points represent flow cytometry measurements from each cell type to a dose response of IL-2 or IL-15 at multiple time points and have units of median fluorescence intensity.

(B) Experimentally derived and model-predicted EC_{50} values of dose response across IL-2/15 and all 10 cell types. EC_{50} values are shown for the 1-h time point.

(C) Pearson correlation coefficients between model prediction and experimental measurements for all 10 cell populations (full data are shown in Figure S5).

(D–I) pSTAT5 response to IL-2 (D–F) and IL-15 (G–I) dose responses in NK, CD8+, and T_{reg} cells. Experiments were performed in duplicate (n = 2).

See also Figure S5.

tensor- and model-based factorization to distinguish cells based on their predicted response profiles.

Other tensor decomposition methods exist and can be applied similarly to visualize response. For example, non-negative Tucker decomposition relaxes CP decomposition by employing a core tensor that provides interaction terms between components (Figure S4; Tucker, 1966). However, this flexibility comes at the cost of interpretability because visualizing the core tensor's effect is challenging. In total, factorization methods are effective means of visualizing the high-dimensional regulation of complex receptor families and separating the influence of time, ligand stimulation, and receptor expression.

An accurately predicted response across a panel of PBMC-derived cell types

We evaluated whether our model accurately predicts cell-type-specific differences in ligand response by comparing its predictions for IL-2/15 responses across a panel of 10 PBMC-derived cell populations. We measured and used our model to predict PBMC response to cytokine stimulation at 12 concentrations (0.5 pM–84 nM) and 4 time points (30 min, 1 h, 2 h, and 4 h). Individual cell types displayed reproducible responses to IL-2/15 treatment (Figure 4A). Overall, our model predictions of ligand pSTAT5 response closely matched experimental measurements (Figure 4; Figure S5). The differences between cell types largely matched known differences in cytokine response. For example,

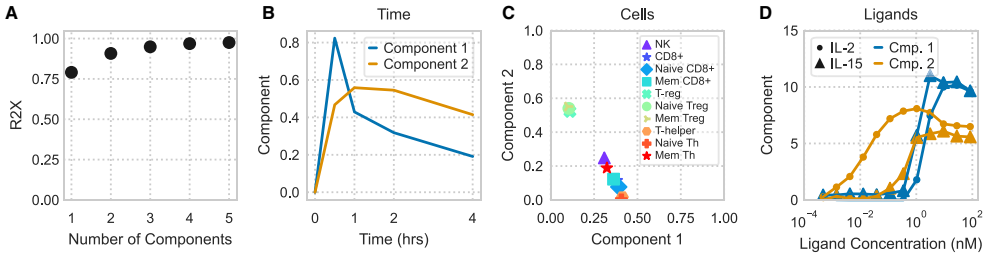

Figure 5. Non-negative CP decomposition applied to experimental pSTAT5 measurements

(A) R2X of non-negative CP decomposition versus number of components used.

(B–D) Decomposition plots with respect to time (B), cell type (C), or ligand treatment (D).

See also Figure S4.

T_{reg} cells were markedly sensitive to IL-2 (Figures 4B and 4F), but not IL-15 (Figures 4B and 4I), at low concentrations of the cytokine (Bell et al., 2015; Peterson et al., 2018). Small amounts of IL-2Rα in helper T cells (Figure 3A) partially sensitized them to IL-2 (Figure 4B; Figures S5H–S5J). The model was also able to partly predict downregulation of pSTAT response at 2 and 4 h by including receptor trafficking (Figure S5). Although our model was slightly less accurate in predicting T helper response to cytokine stimulation, it was able to broadly and accurately capture differences in sensitivity and response across all the cell populations (Figure 4C).

To further evaluate the importance of receptor trafficking, we also predicted PBMC response using our model without trafficking included (Figure S1). This model completely failed to predict PBMC cytokine responses across all populations (Figure S6). We expect this arose from the large difference in inferred receptor abundance when fitting the two models. The model without trafficking required very small amounts of receptor abundance to fit the YT-1 responses and therefore failed with the PBMC case, where we experimentally measured the receptor amounts. This difference in performance clearly demonstrates that incorporating trafficking is necessary to develop a model that generalizes to new contexts.

Although the model accurately predicted experimentally measured responses overall, we noticed some larger discrepancies specifically at high ligand concentrations and after 2 h in specific cell populations (Figure 4; Figure S5). For example, although CD8+ cells almost exactly matched model predictions at 1 h, by 4 h we experimentally observed a biphasic response with respect to IL-2 concentration and a plateau with IL-15 that decreased over time. This decrease in signaling was most pronounced with CD8+ cells but could be observed to lesser extents in some other cell populations such as NK cells (Figure S5). We hypothesize two possible explanations for this discrepancy. First, CD8+ populations are known to proteolytically shed IL-2Rα in an activity-responsive manner (Junghans and Waldmann, 1996). Second, our model does not encompass the JAK-STAT pathway, whose components surely influence dynamic response (Kuwabara et al., 2016). Our model also had a quantitative difference from experimental results for the pSTAT5 EC_{50} variation between effector and regulatory cells (Figures 4B, 4D, and 4E). However, overall, the model presented here remains useful for exploring the determinants of cell-type-specific response, which originate at the receptor expression profile on the cell surface. The broad experimental profiling here will also enable future model refinement.

Tensor factorization of experimental measurements distinguishes the cell-type-specific response

Given that tensor factorization helped to visualize model predictions of IL-2, IL-7, and IL-15 response, we wished to evaluate whether it could similarly help visualize experimental measurements. We structured our experimental pSTAT5 measurements in an identical format as the model simulation tensor (Figure 3). Two components explained roughly 90% of the variance in the original data (Figure 5A), which we then interpreted using similar factor plots (Figures 5B–5D).

Interestingly, as seen with the model prediction factorization, factors were distinguished by their concentration more than being tied to a specific ligand (Figure 5D). Component 2 increases with low concentrations of IL-2, whereas component 1 only increases at high concentrations of either ligand. As expected, effector and T_{reg} cells are most strongly associated with components 1 and 2, respectively, matching their known dose-response profiles (Figure 4). However, component 2 is also distinct from component 1 in its sustained signaling (Figure 5B; Figure S5). This can be expected from rapid endocytosis-mediated downregulation of IL-2Rβ at high IL-2/-15 concentrations (Figure 1). Thus, tensor factorization helps to separate these differences in dose- and cell-type-specific responses. Furthermore, there was clear, quantitative correspondence between the model and experimental factorization. For example, both components from the experimental measurement factorization (Figure 5C) correlated strongly in their cell type weighting with their analogous pairs in the model factorization (cosine similarity of 0.98 and 0.89; Figure 3H).

The model accurately captures the cell-type-specific response to IL-2 muteins

Using the model, we sought to identify strategies for selectively targeting T_{reg} cells. To quantify the effectiveness of selectively

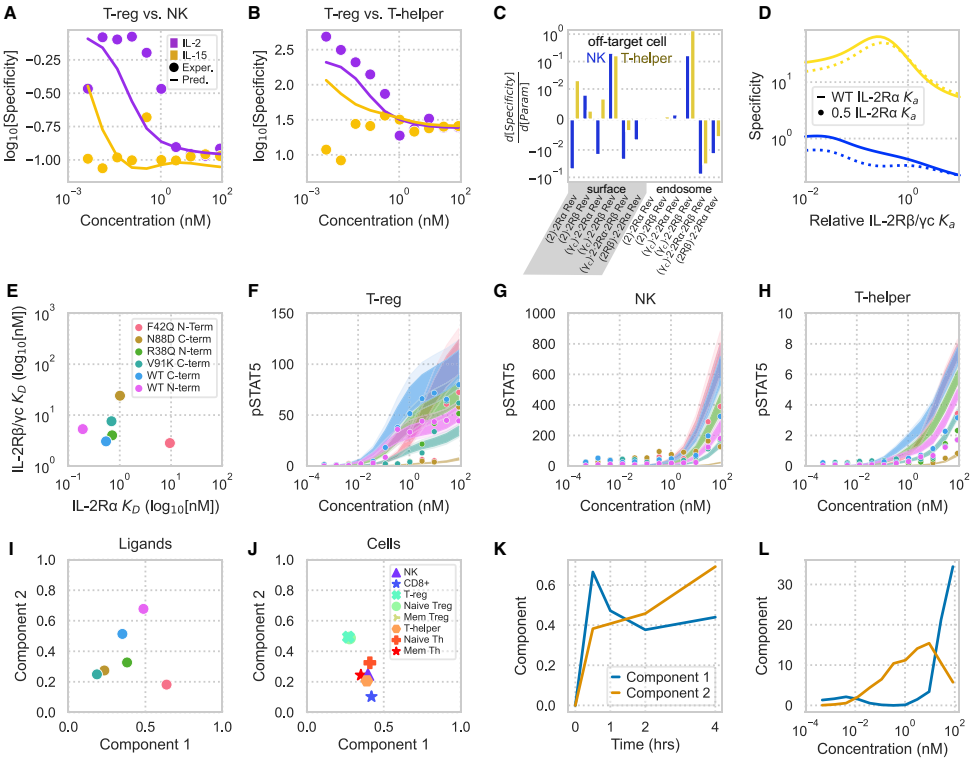

Figure 6. Model and tensor factorization predicts and decodes cell-type-specific responses to IL-2 muteins

(A and B) Predicted and measured T_{reg} cell signaling specificity compared with NK (A) and T helper (B) cells at 1 h. Specificity is defined here as the ratio of two cell types' pSTAT5. Experimental measures are average of two flow cytometry replicates (n = 2).

(C) Partial derivatives of T_{reg} cell signaling specificity compared with NK and T helper cells with respect to each surface and endosomal reverse binding rate constant.

(D) T_{reg} signaling specificity with respect to NK and T helper cells as a function of IL-2Rβ/γc binding affinity for ligands with wild-type and reduced IL-2Rα affinity. (C and D) Specificity values are shown for cells exposed to 38 pM of cytokine for 1 h.

(E) IL-2Rα and IL-2Rβ/γ_c dissociation constants for our panel of IL-2 muteins, determined using bio-layer interferometry.

(F–H) Predicted versus experimental immune cell responses to IL-2 muteins for T_{reg} cells (F), NK cells (G), and T-helper cells (H) for 1-h stimulation. Dots represent experimental flow cytometry measurements, and shaded regions represent the 10%–90% confidence interval for model predictions. Mutein stimulants are denoted by color.

(I–L) Tensor factorization of experimentally measured cellular signaling values for IL-2 muteins. Shown are component values versus ligand (I), cell type (J), time (K), and cytokine concentration (L).

See also Figures S7 and S8.

activating T_{reg} cells, we defined a specificity metric as the normalized pSTAT5 response of T_{reg} cells divided by the pSTAT5 response of T helper or NK cells. As expected, the model prediction and experimental values of this specificity increased with lower concentrations of IL-2 and had a lesser concentration-dependent relationship with IL-15 (Figures 6A and 6B). Our model was unable to quantitatively predict the specificity of T_{reg} cell signaling with respect to T helper cells, particularly for IL-15 stimulation. However, it was able to recapitulate the relationship of the quantity with IL-2 stimulation. With this quantity, we then examined the sensitivity of the specificity metric with respect to surface and endosomal binding. Increasing the dissociation rate of IL-2 from IL-2Rβ/γ_c, particularly in the endosome, provided the largest and most consistent specificity increase (Figure 6C). Changes in endosomal binding rates have been shown to have important effects on a protein therapy's half-life

(Sarkar et al., 2002). To the extent this binding can be manipulated separately, the model indicates that it might help to improve specificity as well. Although IL-2Rβ/γ_c affinity was identified as most sensitive, the model predicted that ligands with reduced IL-2Rα affinity had decreased T_{reg} cell specificity regardless of their IL-2Rβ/γ_c affinity (Figure 6D). Therefore, reducing IL-2Rβ/γ_c affinity can help modulate the potency of these cytokines, but maintaining IL-2Rα affinity is still critical. These results demonstrate this model's ability to predict immune cell response to wild-type or engineered cytokines, particularly for engineering cell-specific responses.

To evaluate these predictions, we measured the PBMC response to several Fc-fused IL-2 monomers. Wild-type and mutant forms of IL-2 were produced as fusions with a monomeric human antibody Fc domain. Targeted mutations were introduced to IL-2 in regions known to be instrumental for IL-2Rα or IL-2Rβ/γ_c binding. In particular, mutations at V91 and N88 are present in molecules being developed to treat autoimmune disease through selective IL-2 signaling in T_{reg} cells (Peterson et al., 2018, Ghelani et al., 2020, Gavin et al., 2017).

Cytokines are often Fc fused to increase the drug's *in vivo* half-life and can be placed in either orientation. We quantified the effect of our engineered mutations and Fc fusion on IL-2Rα and IL-2Rβ/γ_c binding kinetics using bio-layer inferometry (Figure S7). Surprisingly, we found that Fc fusion to the N terminus selectively lowered IL-2Rβ/γ_c affinity, whereas fusion to the C terminus selectively lowered IL-2Rα affinity (Data S1; Figure 6E). Therefore, Fc fusion can have either complementary or counterproductive effects on mutation-mediated changes in receptor affinity, and affinity must be assessed in a clinical format. The observed changes in receptor-ligand kinetics caused by Fc-fusion were assessed for ligands fused using a 20-amino-acid linker; linkers of different lengths or flexibility likely also affect cytokine binding kinetics.

Using these altered affinities, we were able to accurately predict the cell-type-specific pSTAT5 response to our modified ligands (Figure S8; Figures 6F–6H). The model widely captured the cell-type-specific response to the muteins and especially the signaling response in the first 2 h. However, accuracy varied according to ligand and cell type and was noticeably reduced for NK cells and T_{reg} cell variants at higher concentrations and in predicting most responses to N88D. The model's inaccuracy in predicting the N88D response is potentially to be expected because the N88D affinity for IL-2Rα and IL-2Rβ/γ_c is among the most drastically divergent from the wild-type IL-2 and IL-15 responses to which the model was fit (Figure 6E). Ligands with decreased IL-2Rα or IL-2Rβ/γ_c affinity had a decreased T_{reg} or T helper cell pSTAT5 response, respectively, as expected. As before, visualizing the effect of altered binding kinetics on cellular response is complicated by the contributions of cell type, concentration, and time (Figure 3). To visualize our results, we performed tensor factorization using the experimentally determined pSTAT5 response of PBMCs exposed to wild-type and modified IL-2 ligands (Figures 6I–6L). Two components explained 80% of the variance in the new combined data tensor. The two components matched those patterns from the model (Figures 3F–3I) and wild-type cytokines (Figure 5), with separation by cell type (Figure 6J) and concentration (Figure 6L) rather than ligand identity (Figure 6I) and a more sustained response by the T_{reg} cell-specific component (Figure 6K). Among the ligands, wild-type N-terminally conjugated IL-2 was the most potent inducer of T_{reg} cell response, as shown by its strong component 2 weighting (Figures 6I and 6J). The difference in signaling with Fc fusion orientation is likely due to the opposing effects on the cytokine's IL-2Rα affinity (Figure 6I) because these different responses were matched by the model (Figure 6F).

DISCUSSION

Here we built a mass action kinetic binding model for the common γ_c receptor family and used factorization methods to explore its cell-type-dependent behavior. This approach provided insights into its high-dimensional regulation. Our binding reaction model combined the structure of ligand interaction with endosomal trafficking, which allowed us to accurately model response (Figure 1). After fitting our model to previously published cytokine response data, we were able to predict IL-2, IL-2 mutein, and IL-15 response across a wide panel of PBMC-derived cell types (Figure 4; Figure S5). Mass action models can help to explain counterintuitive features of ligand response and identify specific strategies for optimizing therapeutically desired properties (Haugh, 2004; Meyer et al., 2015). In the case of the γ_c receptor cytokines, a therapeutic goal has been to specifically modulate subpopulations of cells based on their unique receptor expression profiles (Bell et al., 2015; Bentebibel et al., 2019; Levin et al., 2012; Peterson et al., 2018). To visualize these possibilities, we employed tensor factorization to map the signaling response space. This map provided a clearer picture of differential responsiveness between ligands, with selective and increased signaling for certain cells and ligands (Figures 5 and 6). For example, we could clearly identify the selectivity of IL-7 for T helper cells and low concentrations of IL-2 for T_{reg} cells (Figure 3).

The model described here serves as an effective tool for cell-type-selective rational cytokine design. In addition to the natural ligands, many cytokine muteins have been designed with altered binding affinities for specific receptors (Berndt et al., 1994; Collins et al., 1988). Our model serves as a computational tool for comparing these muteins as immunotherapeutic drugs that selectively activate certain cell populations. For example, our model helped to identify that high IL-2Rα affinity is essential to preserve T_{reg} cell specificity regardless of the affinity for IL-2Rβ/γ_c (Figure 6). The orientation of Fc fusion can significantly influence receptor affinity (including reducing IL-2Rα affinity), and so this step of drug design needs to be incorporated into ligand optimization (Figure 6E). Incorporating trafficking with the binding events of the cytokines allowed us to distinguish surface and endosomal binding, which is an unexplored axis for further engineering cell-specific responses. Indeed, endosomal IL-2Rα affinity is predicted to be more critical for T_{reg} cell specificity than binding on the surface, which agrees with the distinct temporal profiles of ligand response between cell types on the timescale of trafficking (Figures 6C and 6K).

Models incorporating the full panel of responding cell populations will enable further refinement of these engineered ligands (León et al., 2013). IL-2 and IL-15 have extremely short half-lives

in vivo, in part because of endocytosis-mediated clearance (Bernett et al., 2017; Konrad et al., 1990). Including endocytic trafficking of ligands will enable future work modeling ligand clearance *in vitro* and *in vivo*. Changes in receptor binding may therefore be selected based on optimized selectivity and pharmacokinetic properties. Although cell types were defined here by their average receptor expression, cell-to-cell variability within these populations leads to variation in stimulus response (Cotari et al., 2013). Incorporating single-cell variation will provide a more complete picture of population response and may help to further refine cell type selectivity.

Although the model was able to capture many of the overall differences and dynamics in cytokine response between cell populations and engineered ligands, we noted some systematic errors. In particular, predictions were generally worse for helper T cells (Figure 4C), longer and higher-concentration treatments (Figure S5), and engineered muteins with the largest changes in their receptor binding kinetics (Figure S8; N88D). We expect that there are three explanations for these errors that provide opportunities for further model refinement. First, we set a high bar for performance of the model by only fitting to cell line measurements and then trying to predict PBMC response as our validation. Any systematic differences between the YT-1 cell line and primary cultures would show up as an error in our model, and directly training the model on PBMC responses would reveal these. Second, we treat populations as overall averages, when cell-to-cell variation certainly exists (Cotari et al., 2013). As described above, modeling the variation in these populations could help correct for skewed responses that arise because of this heterogeneity. Finally, we elected to only model receptor-level regulatory events because these are most available for therapeutic engineering. However, the JAK-STAT pathway is dynamically regulated and certainly contributes to our measured responses (Kuwabara et al., 2016). Incorporating this pathway is sure to further improve our model's correspondence to the data. Each of these improvements will, in turn, reveal other useful points to engineer this pathway.

Receptor families with many receptors and ligands are often made up of a dense web of connections, making the role of individual components non-intuitive (Antebi et al., 2017b; Eubelen et al., 2018). Interconnected, cross-reactive components may have evolved as a tradeoff between transmitting ligand-mediated information and expanding the repertoire of cell-surface proteins (Komorowski and Tawfik, 2019). The methods detailed in this paper can be applied to many signaling systems characterized by pleiotropy and high dimensionality. The combination of dynamic, mechanistic models and statistical exploration methods is particularly powerful to provide actionable directions for how to optimize therapeutic response. Detailed biophysical and structural characterization, animal disease models, and evidence from human genetic studies make this engineering possible for therapeutically targeting other complex signaling pathways, including FcγR, Wnt, Hedgehog, Notch, and BMP/TGF-β (Antebi et al., 2017a, 2017b; Eubelen et al., 2018; Li et al., 2018; Robinett et al., 2018).

STAR★METHODS

Detailed methods are provided in the online version of this paper and include the following:

SUPPLEMENTAL INFORMATION

Supplemental information can be found online at https://doi.org/10.1016/j.celrep.2021.109044.

ACKNOWLEDGMENTS

This work was supported by National Institutes of Health DP5-OD019815 (to A.S.M.) and a research agreement with Visterra, Inc.

AUTHOR CONTRIBUTIONS

A.S.M. and S.M.C. conceived the study. S.M.C. and C.P. performed the PBMC experiments and engineered the IL-2 fusion proteins. A.C.W., A.M.F., A.S.M., B.O.-J., and Z.S.K. performed the computational analysis. All authors helped to design experiments and/or analyze the data.

DECLARATION OF INTERESTS

S.M.C. and C.P. are employees of Visterra, Inc.

INCLUSION AND DIVERSITY

One or more of the authors of this paper self-identifies as a member of the LGBTQ+ community.

Received: July 1, 2020
Revised: December 1, 2020
Accepted: April 6, 2021
Published: April 27, 2021

REFERENCES

Amorosi, S., Russo, I., Amodio, G., Garbi, C., Vitiello, L., Palamaro, L., Adriani, M., Vigliano, I., and Pignata, C. (2009). The cellular amount of the common γ-chain influences spontaneous or induced cell proliferation. J. Immunol. *182*, 3304–3309.

Antebi, Y.E., Nandagopal, N., and Elowitz, M.B. (2017a). An operational view of intercellular signaling pathways. Curr. Opin. Syst. Biol. *1*, 16–24.

Antebi, Y.E., Linton, J.M., Klumpe, H., Bintu, B., Gong, M., Su, C., McCardell, R., and Elowitz, M.B. (2017b). Combinatorial signal perception in the BMP pathway. Cell *170*, 1184–1196.e24.

Basquin, C., Malardé, V., Mellor, P., Anderson, D.H., Meas-Yedid, V., Olivo-Marin, J.-C., Dautry-Varsat, A., and Sauvonnet, N. (2013). The signalling factor PI3K is a specific regulator of the clathrin-independent dynamin-dependent endocytosis of IL-2 receptors. J. Cell Sci. *126*, 1099–1108.

Bell, C.J.M., Sun, Y., Nowak, U.M., Clark, J., Howlett, S., Pekalski, M.L., Yang, X., Ast, O., Waldhauer, I., Freimoser-Grundschober, A., et al. (2015). Sustained *in vivo* signaling by long-lived IL-2 induces prolonged increases of regulatory T cells. J. Autoimmun. *56*, 66–80.

Bentebibel, S.-E., Hurwitz, M.E., Bernatchez, C., Haymaker, C., Hudgens, C.W., Kluger, H.M., Tetzlaff, M.T., Tagliaferri, M.A., Zalevsky, J., Hoch, U., et al. (2019). A first-in-human study and biomarker analysis of NKTR-214, a novel IL-2-receptor beta/gamma (βγ)-biased cytokine, in patients with advanced or metastatic solid tumors. Cancer Discov. *9*, 711–721.

Berndt, W.G., Chang, D.Z., Smith, K.A., and Ciardelli, T.L. (1994). Mutagenic analysis of a receptor contact site on interleukin-2: preparation of an IL-2 analog with increased potency. Biochemistry *33*, 6571–6577.

Bernett, M.J., Bonzon, C., Rashid, R., Varma, R., Avery, K.N., Leung, I.W., Chu, S.Y., Muchhal, U.S., Moore, G.L., and Desjarlais, J.R. (2017). Abstract 1595: IL-15/IL-15Rα heterodimeric Fc-fusions with extended half-lives. Cancer Res. *77*, 1595, 1595.

Burke, M.A., Morel, B.F., Oriss, T.B., Bray, J., McCarthy, S.A., and Morel, P.A. (1997). Modeling the proliferative response of T cells to IL-2 and IL-4. Cell. Immunol. *178*, 42–52.

Byun, J.H., and Jung, I.H. (2020). Mathematical modeling of the receptor-mediated endocytosis process of targeted therapeutic agents in drug delivery systems. Appl. Math. Model. *79*, 300–313.

Cao, Y., Li, S., and Petzold, L. (2002). Adjoint sensitivity analysis for differential-algebraic equations: Algorithms and software. J. Comput. Appl. Math. *149*, 171–191.

Collins, L., Tsien, W.H., Seals, C., Hakimi, J., Weber, D., Bailon, P., Hoskings, J., Greene, W.C., Toome, V., and Ju, G. (1988). Identification of specific residues of human interleukin 2 that affect binding to the 70-kDa subunit (p70) of the interleukin 2 receptor. Proc. Natl. Acad. Sci. USA *85*, 7709–7713.

Cotari, J.W., Voisinne, G., Dar, O.E., Karabacak, V., and Altan-Bonnet, G. (2013). Cell-to-cell variability analysis dissects the plasticity of signaling of common γ chain cytokines in T cells. Sci. Signal. *6*, ra17.

Donohue, J.H., and Rosenberg, S.A. (1983). The fate of interleukin-2 after in vivo administration. J. Immunol. *130*, 2203–2208.

Dubois, S., Mariner, J., Waldmann, T.A., and Tagaya, Y. (2002). IL-15Ralpha recycles and presents IL-15 In trans to neighboring cells. Immunity *17*, 537–547.

Duprez, V., Cornet, V., and Dautry-Varsat, A. (1988). Down-regulation of high affinity interleukin 2 receptors in a human tumor T cell line. Interleukin 2 increases the rate of surface receptor decay. J. Biol. Chem. *263*, 12860–12865.

Eubelen, M., Bostaille, N., Cabochette, P., Gauquier, A., Tebabi, P., Dumitru, A.C., Koehler, M., Gut, P., Alsteens, D., Stainier, D.Y.R., et al. (2018). A molecular mechanism for Wnt ligand-specific signaling. Science *361*, eaat1178.

Fallon, E.M., and Lauffenburger, D.A. (2000). Computational model for effects of ligand/receptor binding properties on interleukin-2 trafficking dynamics and T cell proliferation response. Biotechnol. Prog. *16*, 905–916.

Fallon, E.M., Liparoto, S.F., Lee, K.J., Ciardelli, T.L., and Lauffenburger, D.A. (2000). Increased endosomal sorting of ligand to recycling enhances potency of an interleukin-2 analog. J. Biol. Chem. *275*, 6790–6797.

Feinerman, O., Jentsch, G., Tkach, K.E., Coward, J.W., Hathorn, M.M., Sneddon, M.W., Emonet, T., Smith, K.A., and Altan-Bonnet, G. (2010). Single-cell quantification of IL-2 response by effector and regulatory T cells reveals critical plasticity in immune response. Mol. Syst. Biol. *6*, 437.

Gavin, M.A., Kannan, G., Li, L., Pearson, J.T., and Karow, M. (2017). Interleukin-2 muteins for the expansion of T-regulatory cells. US patent US20140286898A1, filed March 13, 2014, and published September 25, 2014.

Geweke, J. (1992). Evaluating the accuracy of sampling-based approaches to the calculation of posterior moments. In Bayesian Statistics 4, J.M. Bernardo, J.O. Berger, A.P. Dawid, and A.F.M. Smith, eds. (University Press), pp. 169–193.

Ghelani, A., Bates, D., Conner, K., Wu, M.Z., Lu, J., Hu, Y.L., Li, C.M., Chaudhry, A., and Sohn, S.J. (2020). Defining the Threshold IL-2 Signal Required for Induction of Selective Treg Cell Responses Using Engineered IL-2 Muteins. Front. Immunol. *11*, 1106.

Gonnord, P., Angermann, B.R., Sadtler, K., Gombos, E., Chappert, P., Meier-Schellersheim, M., and Varma, R. (2018). A hierarchy of affinities between cytokine receptors and the common gamma chain leads to pathway cross-talk. Sci. Signal. *11*, eaal1253.

Goudy, K., Aydin, D., Barzaghi, F., Gambineri, E., Vignoli, M., Ciullini Mannurita, S., Doglioni, C., Ponzoni, M., Cicalese, M.P., Assanelli, A., et al. (2013). Human IL2RA null mutation mediates immunodeficiency with lymphoproliferation and autoimmunity. Clin. Immunol. *146*, 248–261.

Hassan, J., and Reen, D.J. (1998). IL-7 promotes the survival and maturation but not differentiation of human post-thymic CD4+ T cells. Eur. J. Immunol. *28*, 3057–3065.

Haugh, J.M. (2004). Mathematical model of human growth hormone (hGH)-stimulated cell proliferation explains the efficacy of hGH variants as receptor agonists or antagonists. Biotechnol. Prog. *20*, 1337–1344.

Hindmarsh, A.C., Brown, P.N., Grant, K.E., Lee, S.L., Serban, R., Shumaker, D.E., and Woodward, C.S. (2005). SUNDIALS: Suite of nonlinear and differential/algebraic equation solvers. ACM Trans. Math. Softw. *31*, 363–396.

Hogan, R.J. (2017). Adept 2.0: a combined automatic differentiation and array library for C++. http://www.met.reading.ac.uk/clouds/adept/.

Horak, I. (1995). Immunodeficiency in IL-2-knockout mice. Clin. Immunol. Immunopathol. *76*, S172–S173.

Ishino, T., Wang, M., Mosyak, L., Tam, A., Duan, W., Svenson, K., Joyce, A., O'Hara, D.M., Lin, L., Somers, W.S., and Kriz, R. (2013). Engineering a monomeric Fc domain modality by N-glycosylation for the half-life extension of biotherapeutics. J. Biol. Chem. *288*, 16529–16537.

Junghans, R.P., and Waldmann, T.A. (1996). Metabolism of Tac (IL2Ralpha): physiology of cell surface shedding and renal catabolism, and suppression of catabolism by antibody binding. J. Exp. Med. *183*, 1587–1602.

Komorowski, M., and Tawfik, D.S. (2019). The limited information capacity of cross-reactive sensors drives the evolutionary expansion of signaling. Cell Syst. *8*, 76–85.e6.

Konrad, M.W., Hemstreet, G., Hersh, E.M., Mansell, P.W.A., Mertelsmann, R., Kolitz, J.E., and Bradley, E.C. (1990). Pharmacokinetics of recombinant interleukin 2 in humans. Cancer Res. *50*, 2009–2017.

Kossaifi, J., Panagakis, Y., and Pantic, M. (2019). TensorLy: Tensor learning in Python. Journal of Machine Learning Research *20*, 1–6.

Krieg, C., Létourneau, S., Pantaleo, G., and Boyman, O. (2010). Improved IL-2 immunotherapy by selective stimulation of IL-2 receptors on lymphocytes and endothelial cells. Proc. Natl. Acad. Sci. USA *107*, 11906–11911.

Kuwabara, T., Kasai, H., and Kondo, M. (2016). Acetylation modulates IL-2 receptor signaling in T cells. J. Immunol. *197*, 4334–4343.

Lamaze, C., Dujeancourt, A., Baba, T., Lo, C.G., Benmerah, A., and Dautry-Varsat, A. (2001). Interleukin 2 receptors and detergent-resistant membrane domains define a clathrin-independent endocytic pathway. Mol. Cell *7*, 661–671.

Lao, B.J., Tsai, W.L.P., Mashayekhi, F., Pham, E.A., Mason, A.B., and Kamei, D.T. (2007). Inhibition of transferrin iron release increases in vitro drug carrier efficacy. J. Control. Release *117*, 403–412.

León, K., García-Martínez, K., and Carmenate, T. (2013). Mathematical models of the impact of IL2 modulation therapies on T cell dynamics. Front. Immunol. *4*, 439.

Leonard, W.J., Lin, J.-X., and O'Shea, J.J. (2019). The γc family of cytokines: Basic biology to therapeutic ramifications. Immunity *50*, 832–850.

Levin, A.M., Bates, D.L., Ring, A.M., Krieg, C., Lin, J.T., Su, L., Moraga, I., Raeber, M.E., Bowman, G.R., Novick, P., et al. (2012). Exploiting a natural conformational switch to engineer an interleukin-2 'superkine'. Nature *484*, 529–533.

Li, P., Markson, J.S., Wang, S., Chen, S., Vachharajani, V., and Elowitz, M.B. (2018). Morphogen gradient reconstitution reveals Hedgehog pathway design principles. Science *360*, 543–548.

Meyer, A.S., Zweemer, A.J.M., and Lauffenburger, D.A. (2015). The AXL receptor is a sensor of ligand spatial heterogeneity. Cell Syst. *1*, 25–36.

Mitra, S., Ring, A.M., Amarnath, S., Spangler, J.B., Li, P., Ju, W., Fischer, S., Oh, J., Spolski, R., Weiskopf, K., et al. (2015). Interleukin-2 activity can be fine tuned with engineered receptor signaling clamps. Immunity *42*, 826–838.

Mortier, E., Quéméner, A., Vusio, P., Lorenzen, I., Boublik, Y., Grötzinger, J., Plet, A., and Jacques, Y. (2006). Soluble interleukin-15 receptor α (IL-15R α)-sushi as a selective and potent agonist of IL-15 action through IL-15R β/γ. Hyperagonist IL-15 x IL-15R α fusion proteins. J. Biol. Chem. *281*, 1612–1619.

Peterson, L.B., Bell, C.J.M., Howlett, S.K., Pekalski, M.L., Brady, K., Hinton, H., Sauter, D., Todd, J.A., Umana, P., Ast, O., et al. (2018). A long-lived IL-2 mutein that selectively activates and expands regulatory T cells as a therapy for autoimmune disease. J. Autoimmun. *95*, 1–14.

Pulliam, S.R., Uzhachenko, R.V., Adunyah, S.E., and Shanker, A. (2016). Common gamma chain cytokines in combinatorial immune strategies against cancer. Immunol. Lett. *169*, 61–72.

Renauld, J.C., Druez, C., Kermouni, A., Houssiau, F., Uyttenhove, C., Van Roost, E., and Van Snick, J. (1992). Expression cloning of the murine and human interleukin 9 receptor cDNAs. Proc. Natl. Acad. Sci. USA *89*, 5690–5694.

Rickert, M., Boulanger, M.J., Goriatcheva, N., and Garcia, K.C. (2004). Compensatory energetic mechanisms mediating the assembly of signaling complexes between interleukin-2 and its α, β, and γ(c) receptors. J. Mol. Biol. *339*, 1115–1128.

Ring, A.M., Lin, J.-X., Feng, D., Mitra, S., Rickert, M., Bowman, G.R., Pande, V.S., Li, P., Moraga, I., Spolski, R., et al. (2012). Mechanistic and structural insight into the functional dichotomy between IL-2 and IL-15. Nat. Immunol. *13*, 1187–1195.

Robinett, R.A., Guan, N., Lux, A., Biburger, M., Nimmerjahn, F., and Meyer, A.S. (2018). Dissecting FcγR regulation through a multivalent binding model. Cell Syst. *7*, 41–48.e5.

Rochman, Y., Spolski, R., and Leonard, W.J. (2009). New insights into the regulation of T cells by γ(c) family cytokines. Nat. Rev. Immunol. *9*, 480–490.

Salvatier, J., Wiecki, T.V., and Fonnesbeck, C. (2016). Probabilistic programming in Python using PyMC3. PeerJ Comput. Sci. *2*, e55.

Sarkar, C.A., Lowenhaupt, K., Horan, T., Boone, T.C., Tidor, B., and Lauffenburger, D.A. (2002). Rational cytokine design for increased lifetime and enhanced potency using pH-activated "histidine switching". Nat. Biotechnol. *20*, 908–913.

Sharfe, N., Dadi, H.K., Shahar, M., and Roifman, C.M. (1997). Human immune disorder arising from mutation of the α chain of the interleukin-2 receptor. Proc. Natl. Acad. Sci. USA *94*, 3168–3171.

Sharma, R., Zheng, L., Deshmukh, U.S., Jarjour, W.N., Sung, S.S., Fu, S.M., and Ju, S.-T. (2007). A regulatory T cell-dependent novel function of CD25 (IL-2Ralpha) controlling memory CD8(+) T cell homeostasis. J. Immunol. *178*, 1251–1255.

Spangler, J.B., Tomala, J., Luca, V.C., Jude, K.M., Dong, S., Ring, A.M., Votavova, P., Pepper, M., Kovar, M., and Garcia, K.C. (2015). Antibodies to interleukin-2 elicit selective T cell subset potentiation through distinct conformational mechanisms. Immunity *42*, 815–825.

Tucker, L.R. (1966). Some mathematical notes on three-mode factor analysis. Psychometrika *31*, 279–311.

Vigliano, I., Palamaro, L., Bianchino, G., Fusco, A., Vitiello, L., Grieco, V., Romano, R., Salvatore, M., and Pignata, C. (2012). Role of the common γ chain in cell cycle progression of human malignant cell lines. Int. Immunol. *24*, 159–167.

Volkó, J., Kenesei, Á., Zhang, M., Várnai, P., Mocsár, G., Petrus, M.N., Jambrovics, K., Balajthy, Z., Müller, G., Bodnár, A., et al. (2019). IL-2 receptors preassemble and signal in the ER/Golgi causing resistance to antiproliferative anti-IL-2Rα therapies. Proc. Natl. Acad. Sci. USA *116*, 21120–21130.

Voss, S.D., Leary, T.P., Sondel, P.M., and Robb, R.J. (1993). Identification of a direct interaction between interleukin 2 and the p64 interleukin 2 receptor gamma chain. Proc. Natl. Acad. Sci. USA *90*, 2428–2432.

Walsh, S.T.R. (2010). A biosensor study indicating that entropy, electrostatics, and receptor glycosylation drive the binding interaction between interleukin-7 and its receptor. Biochemistry *49*, 8766–8778.

Walsh, S.T.R. (2012). Structural insights into the common γ-chain family of cytokines and receptors from the interleukin-7 pathway. Immunol. Rev. *250*, 303–316.

Wang, L., Yu, C.-R., Kim, H.-P., Liao, W., Telford, W.G., Egwuagu, C.E., and Leonard, W.J. (2011). Key role for IL-21 in experimental autoimmune uveitis. Proc. Natl. Acad. Sci. USA *108*, 9542–9547.

Zhu, E.F., Gai, S.A., Opel, C.F., Kwan, B.H., Surana, R., Mihm, M.C., Kauke, M.J., Moynihan, K.D., Angelini, A., Williams, R.T., et al. (2015). Synergistic innate and adaptive immune response to combination immunotherapy with anti-tumor antigen antibodies and extended serum half-life IL-2. Cancer Cell *27*, 489–501.

STAR★METHODS

KEY RESOURCES TABLE

REAGENT or RESOURCE	SOURCE	IDENTIFIER
Antibodies		
Anti-CD25, Brilliant Violet 421	BioLegend	Cat #356114; Clone #M-A251; RRID: AB_2562164
Anti-CD122, PE/Cy7	BioLegend	Cat #339014; Clone #TU27; RRID: AB_2562597
Anti-CD132, APC	BioLegend	Cat #338607; Clone #TUGh4; RRID: AB_2123585
Anti-CD215 1st mAb, APC	BioLegend	Cat #330210; Clone #JM7A4; RRID: AB_2561440
Anti-CD215 2nd mAb, APC	R&D Systems	Cat #FAB1471A; Clone #151303; RRID: AB_10890735
Anti-CD127, Alexa Fluor 488	BioLegend	Cat #351313; Clone #A019D5; RRID: AB_10895911
Anti-Ms IgG1κ, Brilliant Violet 421	BioLegend	Cat #400158; Clone #MOPC-21; RRID: AB_11150232
Anti-Md IgG1κ, PE/Cy7	BioLegend	Cat #400126; Clone #MOPC-21; RRID: AB_326448
Anti-Rat IgG2Bκ, APC	BioLegend	Cat #400612; Clone #RTK4530; RRID: AB_326556
Anti-Ms IgG2Bκ, APC	BioLegend	Cat #400320; Clone #MPC-11
Anti-Ms IgG2B, APC	R&D Systems	Cat #IC0041A; RRID: AB_357246
Anti-Ms IgG1κ, Alexa Fluor 488	BioLegend	Cat #400129; Clone #MOPC-21; RRID: AB_2890263
Anti-CD3, Brilliant Violet 605	BioLegend	Cat #300460; Clone #UCHT1; RRID: AB_2564380
Anti-CD8, Brilliant Violet 785	BioLegend	Cat #301046; Clone #RPA-T8; RRID: AB_2563264
Anti-CD45RA, PE/Dazzle 594	BioLegend	Cat #304146; Clone #HI100; RRID: AB_2564079
Anti-CD4, Brilliant Violet 785	BioLegend	Cat #300554; Clone #RPA-T4; RRID: AB_2564382
Anti-CD56, PE/Cy7	BioLegend	Cat #362510; Clone #5.1H11; RRID: AB_2563927
Anti-CD8, Alexa Fluor 647	BioLegend	Cat #301062; Clone #RPA-T8; RRID: AB_2564166
Anti-Foxp3, Alexa Fluor 488	BioLegend	Cat #320212; Clone #259D; RRID: AB_430887
Anti-CD4, Brilliant Violet 605	BioLegend	Cat #344646; Clone #SK3; RRID: AB_2734348
Anti-pSTAT5, Alexa Fluor 647	Cell Signaling Technology	Cat #9365; Clone #C71E5; RRID: AB_1904151
Anti-CD56, Alexa Fluor 488	BioLegend	Cat #362518; Clone #5.1H11; RRID: AB_2564093
Anti-pSTAT5, PE	Cell Signaling Technology	Cat #14603; Clone #D4737; RRID: AB_2798533
Chemicals, peptides, and recombinant proteins		
Simply Cellular Compensation Standard Beads	Bangs Labs	Cat #550

(*Continued on next page*)

Continued

REAGENT or RESOURCE	SOURCE	IDENTIFIER
Quantum Simply Cellular anti-Mouse IgG	Bangs Labs	Cat #815
Quantum Simply Cellular anti-Rat IgG	Bangs Labs	Cat #817
MabSelect Resin	GE Healthcare	Cat #17519901
BirA enzyme	BPS Biosciences	Cat #70030
Interleukin-2 (IL-2)	R&D Systems	Cat #202-IL-010
Interleukin-15 (IL-15)	R&D Systems	Cat #247-ILB-025
Interleukin-2 muteins	This Paper	N/A
Critical commercial assays		
Octet RED384 Biolayer Interferometer	ForteBio	N/A
Deposited data		
All raw and processed cellular response data	This paper; Gonnord et al., 2018; Ring et al., 2012	https://github.com/meyer-lab/gc-cytokines
Experimental models: Cell lines		
Cryopreserved PBMCs	ATCC	Cat #PCS-800-011
Expi293F Cells	ThermoFisher Scientific	Cat #A14527
Software and algorithms		
Python3	Python Software Foundation	https://python.org/
C++	Standard C++ Foundation	https://isocpp.org/
SUNDIALS	Hindmarsh et al., 2005	https://computing.llnl.gov/projects/sundials
PyMC3	Salvatier et al., 2016	https://docs.pymc.io/
Adept-2	Hogan, 2017	https://github.com/rjhogan/Adept-2
TensorLy	Kossaifi et al., 2019	https://github.com/tensorly/tensorly
γ_c Mechanistic Binding Model	This paper	https://github.com/meyer-lab/gc-cytokines

RESOURCE AVAILABILITY

Lead contact

Further information and requests for resources and reagents should be directed to and will be fulfilled by the Lead Contact, Aaron Meyer (a@asmlab.org).

Materials availability

Materials generated in this study are available upon reasonable request from the lead contact.

Data and code availability

All datasets generated during and/or analyzed during the current study and all custom scripts and functions generated or used during the current study are available from https://github.com/meyer-lab/gc-cytokines.

EXPERIMENTAL MODEL AND SUBJECT DETAILS

Cell lines

Cryopreserved PBMCs (ATCC, PCS-800-011, lot#81115172) were harvested from a single adult human subject.

METHOD DETAILS

Base model

Cytokine (IL-2, −4, −7, −9, −15, & −21) binding to receptors was modeled using ordinary differential equations (ODEs). IL-2 and −15 each had two private receptors, one being a signaling-deficient α chain (IL-2Rα & −15Rα) and the other being signaling-competent IL-2Rβ. The other four cytokines each had one signaling-competent private receptor (IL-7Rα, −9R, −4Rα, & −21Rα). JAK-STAT signaling is initiated when JAK-binding motifs are brought together. JAK binding sites are found on the intracellular regions of the γ_c, IL-2Rβ, IL-4Rα, IL-7Rα, IL-9R, and IL-21Rα receptors; therefore, all complexes which contained two signaling-competent

receptors were deemed to be active species. Ligands were assumed to first bind a receptor other than γ_c and then can dimerize with other receptors or γ_c thereafter. Direct binding of ligand to γ_c was not included due to its very weak or absent binding (Voss et al., 1993). Our model's output was defined by the number of active signaling complexes; experimental STAT phosphorylation measurements were scaled to model predictions by use of a fit scalar factor.

In addition to binding interactions, our model incorporated receptor-ligand trafficking. Receptor synthesis was assumed to occur at a constant rate. The endocytosis rate was defined separately for active ($k_{endo,a}$) and inactive (k_{endo}) receptors. f_{sort} defined the fraction of endosomal species that ultimately traffic to the lysosome; active species in the endosome had a sorting fraction of 1.0. All endosomal species not sent to lysosomes were recycled back to the cell surface. The lysosomal degradation and recycling rate constants were defined as k_{deg} and k_{rec}, respectively. We assumed no autocrine ligand was produced by the cells. We assumed an endosomal volume of 10 fL and endosomal surface area half that of the plasma membrane (Meyer et al., 2015). We assumed no fluid uptake of ligand and calculated the rate of change in endosomal ligand was derived by a mass balance of endosomal reactions. Endosomal ligand was assumed to completely sort into the lysosome from the endosome. All binding events were assumed to occur with 5-fold greater disassociation rate in the endosome due to its acidic pH (Fallon and Lauffenburger, 2000). Trafficking was therefore accounted for as:

$$\frac{dE}{dt} = -E \times k_{endo} + k_{rec} \times (1 - f_{sort}) \times I \times \varphi$$

$$\frac{dI}{dt} = \frac{E \times k_{endo}}{\varphi} - k_{rec} \times (1 - f_{sort}) \times I - k_{deg} \times f_{sort} \times I$$

where E and I indicate the abundance of the intracellular and extracellular forms, respectively. φ is the fractional membrane area of the endosomal compartment scaled to that of the surface membrane, and was assumed to be 0.5.

Free receptors and complexes were measured in units of number per cell and soluble ligands were measured in units of concentration (nM). Due to these unit choices for our species, the rate constants for ligand binding to free receptors had units of $nM^{-1}\ min^{-1}$. Rate constants for the forward dimerization of free receptor to complex had units of cell min^{-1} $number^{-1}$. Dissociation rates had units of min^{-1}. All ligand-receptor binding processes had an assumed forward rate (k_{bnd}) of $10^7\ M^{-1}\ sec^{-1}$. All forward dimerization reaction rates were assumed to be identical, represented by k_{fwd}. Reverse reaction rates were unique. Experimentally-derived affinities of 1.0 (Gonnord et al., 2018), 59 (Walsh, 2012), 0.1 (Renauld et al., 1992), and 0.07 nM (Gonnord et al., 2018) were used for IL-4, −7, −9, and −21 binding to their cognate private receptors, respectively. IL-2 and −15 were assumed to have affinities of 10 nM and 0.065 nM for their respective α chains (Dubois et al., 2002; Mortier et al., 2006; Rickert et al., 2004), and affinities of 144 nM and 438 nM for their respective β-chains (Rickert et al., 2004). Rates $k_{5,rev}$, $k_{10,rev}$, and $k_{11,rev}$ were set to their experimentally determined disassociation constants of 1.5, 12, and 63 min^{-1} (Rickert et al., 2004). Below are the ODEs pertaining to IL-2 binding and unbinding events, where L, α, and β signify IL-2, IL-2Rα, IL-2Rβ respectively:

$$\frac{d\alpha}{dt} = -k_{fbnd}\,\alpha\,L + k_{1,rev}\,[L\cdot\alpha] + k_{8,rev}\,[L\cdot\alpha\cdot\beta\cdot\gamma_c] - k_{fwd} \times (\alpha\,[L\cdot\beta] + a\,[L\cdot\beta\cdot\gamma_c]) + k_{12,rev}\,[L\cdot\alpha\cdot\beta]$$

$$\frac{d\beta}{dt} = -k_{fbnd}\,\beta\,L + k_{2,rev}\,[L\cdot\beta] + k_{9,rev}\,[L\cdot\alpha\cdot\beta\cdot\gamma_c] - k_{fwd}\,(\beta\,[L\cdot\alpha] + \beta\,[L\cdot\alpha\cdot\gamma_c]) + k_{11,rev}\,[L\cdot\alpha\cdot\beta]$$

$$\frac{d\gamma_c}{dt} = -k_{fwd}\,([L\cdot\beta]\,\gamma_c + [L\cdot\alpha]\,\gamma_c + [L\cdot\alpha\cdot\beta]\,\gamma_c) + k_{5,rev}\,[L\cdot\beta\cdot\gamma_c] + k_{4,rev}\,[L\cdot\alpha\cdot\gamma_c] + k_{10,rev}\,[L\cdot\alpha\cdot\beta\cdot\gamma_c]$$

$$\frac{d[L\cdot\alpha]}{dt} = -k_{fwd}\,([L\cdot\alpha]\,\beta + [L\cdot\alpha]\,\gamma_c) + k_{11,rev}\,[L\cdot\alpha\cdot\beta] + k_{4,rev}\,[2\cdot\alpha\cdot\gamma_c] + k_{fbnd}\,L\,\alpha - k_{1,rev}\,[L\cdot\alpha]$$

$$\frac{d[L\cdot\beta]}{dt} = -k_{fwd}\,([L\cdot\beta]\,\alpha + [L\cdot\beta]\,\gamma_c) + k_{12,rev}\,[L\cdot\alpha\cdot\beta] + k_{5,rev}\,[L\cdot\beta\cdot\gamma_c] + k_{fbnd}\,L\,\beta - k_{2,rev}\,[L\cdot\beta]$$

$$\frac{d[L\cdot\alpha\cdot\beta]}{dt} = k_{fwd}\,([L\cdot\beta]\,\alpha + [L\cdot\alpha]\,\beta - [L\cdot\alpha\cdot\beta]\,\gamma_c) + k_{10,rev}\,[L\cdot\alpha\cdot\beta\cdot\gamma_c] - k_{11,rev}\,[L\cdot\alpha\cdot\beta] - k_{12,rev}\,[L\cdot\alpha\cdot\beta]$$

$$\frac{d[L\cdot\alpha\cdot\gamma_c]}{dt} = -k_{9,rev}\,[L\cdot\alpha\cdot\beta\cdot\gamma_c] + k_{fwd}\,([L\cdot\alpha]\,\gamma_c - [L\cdot\alpha\cdot\gamma_c]\,\beta) - k_{4,rev}\,[L\cdot\alpha\cdot\gamma_c]$$

$$\frac{d[L\cdot\beta\cdot\gamma_c]}{dt} = k_{8,rev}\,[L\cdot\alpha\cdot\beta\cdot\gamma_c] + k_{fwd}\,([L\cdot\beta]\,\gamma_c - [L\cdot\beta\cdot\gamma_c]\,\alpha) - k_{5,rev}\,[L\cdot\beta\cdot\gamma_c]$$

$$\frac{d[L\cdot\alpha\cdot\beta\cdot\gamma_c]}{dt} = k_{fwd}\,([L\cdot\beta\cdot\gamma_c]\,\alpha + [L\cdot\alpha\cdot\gamma_c]\,\beta + [L\cdot\alpha\cdot\beta]\,\gamma_c) - (k_{8,rev} + k_{9,rev} + k_{10,rev})\,[L\cdot\alpha\cdot\beta\cdot\gamma_c]$$

All above reactions also occur for IL-15, where L, α, and β signify IL-15, IL-2Rα, and IL-2Rβ respectively, and reverse rate parameters are substituted according to Table 1. The ODEs for IL-4 and IL-7 are derived by setting the abundance of α to 0, β representing the private receptor, and L representing the ligand concentration. Table 1 again lists the corresponding rate constants.

Initial values were calculated by assuming steady state in the absence of ligand. Differential equation solving was performed using the SUNDIALS solvers in C++, with a Python interface for all other code (Hindmarsh et al., 2005). Model sensitivities were calculated using the adjoint solution (Cao et al., 2002). Calculating the adjoint requires the partial derivatives of the differential equations both with respect to the species and unknown parameters. Constructing these can be tedious and error prone. Therefore, we calculated these algorithmically using forward-pass autodifferentiation implemented in Adept-2 (Hogan, 2017). A model and sensitivities tolerance of 10^{-9} and 10^{-3}, respectively, were used throughout. We used unit tests for conservation of mass, equilibrium, and detailed balance to ensure model correctness.

Model fitting

We used Markov chain Monte Carlo to fit the unknown parameters in our model using previously published cytokine response data (Gonnord et al., 2018; Ring et al., 2012). Experimental measurements include pSTAT activity under stimulation with varying concentrations of IL-2, −15, −4, and −7 as well as time-course measurements of surface IL-2Rβ upon IL-2 and −15 stimulation. YT-1 human NK cells were used for all datasets involving IL-2 and IL-15. Human PBMC-derived $CD4^+TCR^+CCR7^{high}$ cells were used for all IL-4 and −7 response data. All YT-1 cell experiments were performed both with the wild-type cell line, lacking IL-2Rα, and cells sorted for expression of the receptor. Data from Ring et al. (2012) and Gonnord et al. (2018) can be found in Figure 5 and Figure S3 of each paper, respectively. Measurements of receptor counts at steady state in Gonnord et al. (2018) were used to solve for IL-7Rα, IL-4Rα, and γ_c expression rates in human PBMCs.

Fitting was performed with the Python package PyMC3 (Salvatier et al., 2016). All unknown rate parameters were assumed to have a lognormal distribution with a standard deviation of 0.1; the only exception to these distributions was f_{sort} which was assumed to have a beta distribution with shape parameters of $\alpha = 20$ and $\beta = 40$. Executing this fitting process yielded a distribution of each unknown parameter and a sum of squared error between model prediction and experimental data. The Geweke criterion metric was used to verify fitting convergence for all versions of the model (Figure S2; Geweke, 1992).

Tensor generation and factorization

To perform tensor factorization, we generated a three- (time points × cell types × ligand) or four-dimensional (time points × cell types × concentration × mutein) data tensor of predicted or measured ligand-induced signaling. Before decomposition, the tensor was variance scaled across each cell population. Tensor decomposition was performed using the Python package TensorLy (Kossaifi et al., 2019). Except where indicated otherwise, tensor decomposition was performed using non-negative canonical polyadic decomposition. Where indicated, non-negative Tucker decomposition was used.

Receptor abundance quantitation

Cryopreserved PBMCs (ATCC, PCS-800-011, Lot #81115172) were thawed to room temperature and slowly diluted with 9 mL prewarmed RPMI-1640 medium (GIBCO, 11875-093) supplemented with 10% fetal bovine serum (FBS, Seradigm, 1500-500, Lot #322B15). Media was removed, and cells washed once more with 10 mL warm RPMI-1640 + 10% FBS. Cells were brought to $1.5x10^6$ cells/mL, distributed at 250,000 cells per well in a 96-well V-bottom plate, and allowed to recover 2 hr at 37°C in an incubator at 5% CO2. Cells were then washed twice with PBS + 0.1% BSA (PBSA, GIBCO, 15260-037, Lot #2000843) and suspended in 50 µL PBSA + 10% FBS for 10 min on ice to reduce background binding to IgG.

Antibodies were diluted in PBSA + 10% FBS and cells were stained for 1 hr at 4°C in darkness with a gating panel (Panel 1, Panel 2, Panel 3, or Panel 4) and one anti-receptor antibody, or an equal concentration of matched isotype/fluorochrome control antibody. Stain for CD25 was included in Panel 1 when CD122, CD132, CD127, or CD215 was being measured (CD25 is used to separate T_{reg}s from other CD4+ T cells).

Compensation beads (Simply Cellular Compensation Standard, Bangs Labs, 550, Lot #12970) and quantitation standards (Quantum Simply Cellular anti-Mouse IgG or anti-Rat IgG, Bangs Labs, 815, Lot #13895, 817, Lot #13294) were prepared for compensation

and standard curve. One well was prepared for each fluorophore with 2 μL antibody in 50 μL PBSA and the corresponding beads. Bead standards were incubated for 1 hr at room temperature in the dark.

Both beads and cells were washed twice with PBSA. Cells were suspended in 120 μL per well PBSA, and beads to 50 μL, and analyzed using an IntelliCyt iQue Screener PLUS with VBR configuration (Sartorius) with a sip time of 35 and 30 s for cells and beads, respectively. Antibody number was calculated from fluorescence intensity by subtracting isotype control values from matched receptor stains and calibrated using the two lowest binding quantitation standards. T_{reg} cells could not be gated in the absence of CD25, so CD4+ T cells were used as the isotype control to measure CD25 in T_{reg} populations. Cells were gated (Figure S3), and then measurements were performed using four independent staining procedures over two days. Separately, the analysis was performed with anti-receptor antibodies at 3x normal concentration to verify that receptor binding was saturated. Replicates were summarized by geometric mean.

pSTAT5 measurement in PBMCs

Human PBMCs were thawed, distributed across a 96-well plate, and allowed to recover as described above. IL-2 (R&D Systems, 202-IL-010), IL-2 muteins, or IL-15 (R&D Systems, 247-ILB-025) were diluted in RPMI-1640 without FBS and added to the indicated concentrations. To measure pSTAT5, media was removed, and cells fixed in 100 μL of 10% formalin (Fisher Scientific, SF100-4) for 15 mins at room temperature. Formalin was removed, cells were placed on ice, and cells were gently suspended in 50 μL of cold methanol (−30°C). Cells were stored overnight at −30°C. Cells were then washed twice with PBSA, split into two identical plates, and stained 1 hr at room temperature in darkness using antibody panels 4 and 5 with 50 μL per well. Cells were suspended in 100 μL PBSA per well, and beads to 50 μL, and analyzed on an IntelliCyt iQue Screener PLUS with VBR configuration (Sartorius) using a sip time of 35 s and beads 30 s. Compensation was performed as above. Populations were gated (Figure S3), and the median pSTAT5 level extracted for each population in each well.

Recombinant proteins

IL-2/Fc fusion proteins were expressed using the Expi293 expression system according to manufacturer instructions (Thermo Scientific). Proteins were constructed as human IgG1 Fc fusions at the N- or C terminus to human IL-2 through a (G4S)4 linker. C-terminal fusions omitted the C-terminal lysine residue of human IgG1. The AviTag sequence GLNDIFEAQKIEWHE was included on whichever terminus did not contain IL-2. Fc mutations to prevent dimerization were introduced into the Fc sequence (Ishino et al., 2013). Proteins were purified using MabSelect resin (GE Healthcare). Proteins were biotinylated using BirA enzyme (BPS Biosciences) according to manufacturer instructions, and extensively buffer-exchanged into phosphate buffered saline (PBS) using Amicon 10 kDa spin concentrators (EMD Millipore). The sequence of IL-2Rβ/γ Fc heterodimer was based on a reported active heterodimeric molecule (patent application US20150218260A1), with the addition of (G4S)2 linker between the Fc and each receptor ectodomain. The protein was expressed in the Expi293 system and purified on MabSelect resin as above. IL2-Rα ectodomain was produced with C-terminal 6xHis tag and purified on Nickel-NTA spin columns (QIAGEN) according to manufacturer instructions.

Octet binding assays

Binding affinity was measured on an Octet RED384 (ForteBio). Briefly, biotinylated monomeric IL-2/Fc fusion proteins were uniformly loaded to Streptavidin biosensors (ForteBio) at roughly 10% of saturation point and equilibrated for 10 mins in PBS + 0.1% bovine serum albumin (BSA). Association time was up to 40 mins in IL-2Rβ/γ titrated in 2x steps from 400 nM to 6.25 nM, or IL-2Rα from 25 nM to 20 pM, followed by dissociation in PBS + 0.1% BSA. A zero-concentration control sensor was included in each measurement and used as a reference signal. Assays were performed in quadruplicate across two days. Binding to IL-2Rα did not fit to a simple binding model so equilibrium binding was used to determine the K_D within each assay. Binding to IL-2Rβ/γ fit a 1:1 binding model so on-rate (k_{on}), off-rate (k_{off}) and K_D were determined by fitting to the entire binding curve. Kinetic parameters and K_D were calculated for each assay by averaging all concentrations with detectable binding signal (typically 12.5 nM and above).

QUANTIFICATION AND STATISTICAL ANALYSIS

For each figure, descriptions of pertinent statistical analyses or metrics used, the number of replicates of experiments performed, and the values of confidence intervals can be found in its corresponding figure caption. n indicates the number of times a particular experiment was performed (duplicate, triplicate, etc.) within each figure. All experiments performed using either YT-1 NK cells or hPBMCs were conducted using entirely separate experimental replicates gathered from a single cell line or donor, respectively.

The confidence intervals of model predictions were generated by using 100 draws from the Markov chain generated during the model fitting process to make 100 corresponding dose response predictions. The 10%–90% confidence interval indicates the range from the 10^{th} to 90^{th} percentile of the predicted signaling response magnitude.

For all quantification of cellular species abundances, whether pSTAT5 or receptor amounts, the mean fluorescent intensity (MFI) of flow cytometry data was calculated to determine population-level species abundance.

Experimental and predicted EC_{50}s were estimated by fitting a standard Hill function to the dose-response curves using unbounded non-linear least-squares (Figure 4).

Cell Reports, Volume *35*

Supplemental information

Modeling cell-specific dynamics and regulation of the common gamma chain cytokines

Ali M. Farhat, Adam C. Weiner, Cori Posner, Zoe S. Kim, Brian Orcutt-Jahns, Scott M. Carlson, and Aaron S. Meyer

Supplement

Table S1: **Antibodies used to quantify receptors and cell types. Related to Figure 3.** *Panel 0:* Antibodies for IL-2, IL-15, and IL-7 receptor analysis; *Panel 1:* Antibodies to gate Naïve and Memory T-regulatory and T-helper cells; *Panel 2:* Antibodies to gate NK and CD56bright NK cells; *Panel 3:* Antibodies to gate Naïve and Memory Cytotoxic T cells; *Panel 4:* Antibodies to gate Naïve and Memory T-regulatory, T helper, and Cytotoxic cells, and NK cells for CD127 (IL-7) Quantitation; *Panel 5:* Antibodies to gate Memory and Naïve T-regulatory cells, Memory and Naïve T-helper cells; *Panel 6:* Antibodies to gate NK cells, CD56bright NK cells, and Cytotoxic T cells. CST: Cell Signaling Technology.

Antibody (clone)	Dilution	Fluorophore	Vendor (CAT#)	Panel
CD25 (M-A251)	1:120	Brilliant Violet 421	BioLegend (356114)	0
CD122 (TU27)	1:120	PE/Cy7	BioLegend (339014)	0
CD132 (TUGh4)	1:120	APC	BioLegend (3386)	0
CD215 1st mAb (JM7A4)	1:120	APC	BioLegend (330210)	0
CD215 2nd mAb (151303)	3:100	APC	R&D Systems (FAB1471A)	0
CD127 (A019D5)	1:120	Alexa Fluor 488	BioLegend (351313)	0
Ms IgG1κ (MOPC-21)	1:240	Brilliant Violet 421	BioLegend (400158)	0
Md IgG1κ (MOPC-21)	1:240	PE/Cy7	BioLegend (400126)	0
Rat IgG2Bκ (RTK4530)	1:60	APC	BioLegend (400612)	0
Ms IgG2Bκ (MPC-11)	1:120	APC	BioLegend (400320)	0
Ms IgG2B (133303)	3:100	APC	R&D Systems (IC0041A)	0
Ms IgG1κ (MOPC-21)	1:120	Alexa Fluor 488	BioLegend (400129)	0
CD3 (UCHT1)	1:120	Brilliant Violet 605	BioLegend (300460)	1
CD4 (RPA-T4)	1:120	Brilliant Violet 785	BioLegend (300554)	1
CD127 (A019D5)	1:120	Alexa Fluor 488	BioLegend (351313)	1
CD45RA (HI100)	1:120	PE/Dazzle 594	BioLegend (304146)	1
CD3 (UCHT1)	1:120	Brilliant Violet 605	BioLegend (300460)	2
CD56 (5.1H11)	1:120	PE/Dazzle 594	BioLegend (362544)	2
CD3 (UCHT1)	1:120	Brilliant Violet 605	BioLegend (300460)	3
CD8 (RPA-T8)	1:120	Brilliant Violet 785	BioLegend (301046)	3
CD45RA (HI100)	1:120	PE/Dazzle 594	BioLegend (304146)	3
CD25 (M-A251)	1:120	Brilliant Violet 421	BioLegend (356114)	4
CD3 (UCHT1)	1:120	Brilliant Violet 605	BioLegend (300460)	4
CD4 (RPA-T4)	1:120	Brilliant Violet 785	BioLegend (300554)	4
CD127 (A019D5)	1:120	Alexa Fluor 488	BioLegend (351313)	4
CD45RA (HI100)	1:120	PE/Dazzle 594	BioLegend (304146)	4
CD56 (5.1H11)	1:120	PE/Cy7	BioLegend (362510)	4
CD8 (RPA-T8)	1:120	Alexa Fluor 647	BioLegend (301062)	4
Foxp3 (259D)	1:50	Alexa Fluor 488	BioLegend (320212)	5
CD25 (M-A251)	1:120	Brilliant Violet 421	BioLegend (356114)	5
CD4 (SK3)	1:120	Brilliant Violet 605	BioLegend (344646)	5
CD45RA (HI100)	1:120	PE/Dazzle 594	BioLegend (304146)	5
pSTAT5 (C71E5)	1:120	Alexa Fluor 647	CST (9365)	5
CD3 (UCHT1)	1:120	Brilliant Violet 605	BioLegend (300460)	6
CD8 (RPA-T8)	1:120	Alexa Fluor 647	BioLegend (301062)	6
CD56 (5.1H11)	1:120	Alexa Fluor 488	BioLegend (362518)	6
pSTAT5 (D4737)	1:120	PE	CST (14603)	6

Table S2: **Modified IL-2 ligands and their respective mutations, and Fc conjugations. Related to Figure 6.**

Ligand	Fc Conjugation	Specificity Mutation	Other Mutations
F42Q N-Term	N-Terminus	F42Q	V69A/Q74P/C125S
N88D C-term	C-Terminus	N88D	C125A
R38Q N-term	N-Terminus	R38Q	V69A/Q74P/C125S
V91K C-term	C-Terminus	V91K	C125A
WT C-term	C-Terminus	Wild-type	C125A
WT N-term	N-Terminus	Wild-type	V69A/Q74P/C125S

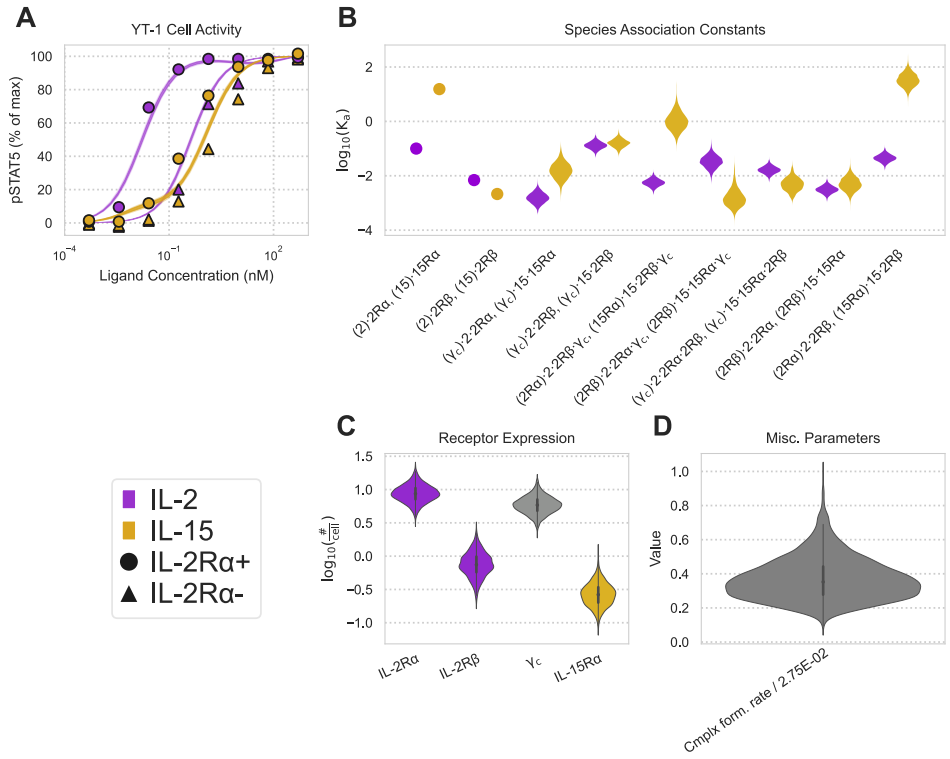

Figure S1: **Model without trafficking fitted to IL-2/-15 dose response. Related to Figure 1.** A) Model without trafficking fit to IL-2 and IL-15 pSTAT5 dose response data (Ring et al., 2012). This model was not fit to the surface IL-2Rβ measurements since no receptors were allowed to internalize from the cell surface (Fig. 1B-D). B) Posterior distributions for the analogous association constants of IL-2 and IL-15. Association constants measured in literature are represented by dots. Association constants are shown for species in parentheses complexing with following species. K_as for (2)·2Rα, (15)·15Rα, (2)·2Rβ, and (15)·2Rβ have units of nM, all other K_as have units of $\# \times \text{cell}^{-1}$. C) Posterior distributions for receptor surface abundance in no-trafficking model. D) Posterior distributions after data fitting for no-trafficking model. C_5, which is a constant in the sigmoidal relationship our model uses to translate active signaling complexes to pSTAT levels, has units of $\# \times \text{cell}^{-1}$, Complex Formation Rate (k_{fwd}) has units of $\text{cell} \times \#^{-1} \times \text{min}^{-1}$.

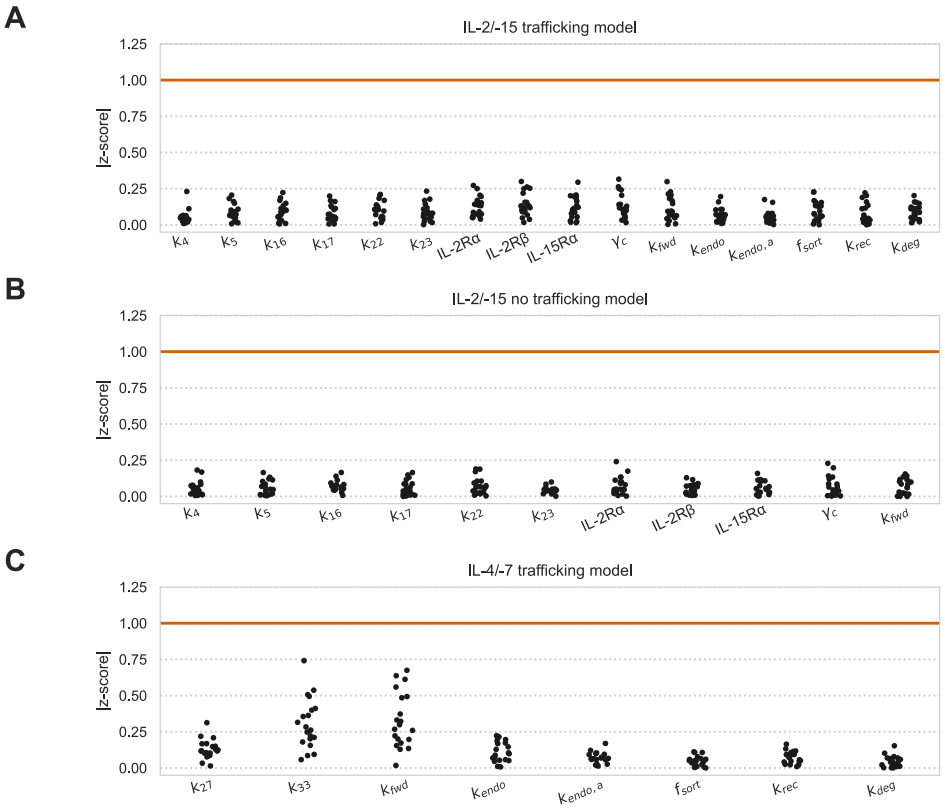

Figure S2: **Geweke criterion scores for model fitting with and without trafficking. Related to Figure 1, 2, 4, and 6.** Geweke criterion z-scores in all subplots were calculated using 20 intervals in the first 10% and last 50% of MCMC chain. Scores of $|z| < 1$ imply fitting convergence. A-B) IL-2/-15 with and without trafficking. C) IL-4/-7 with trafficking (Fig. S1).

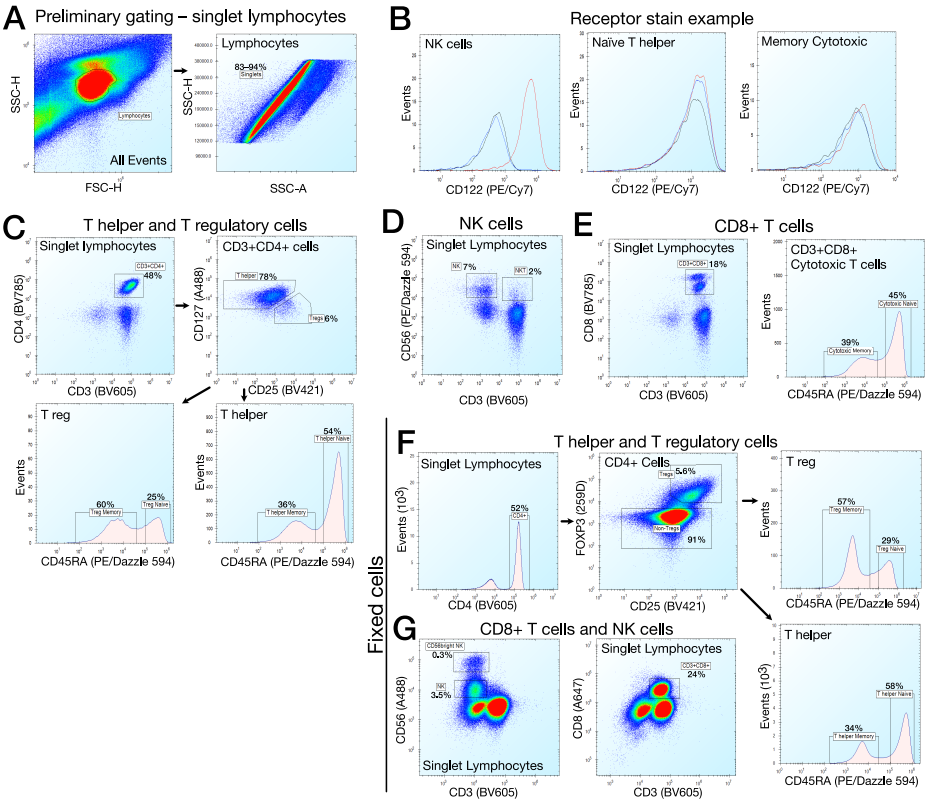

Figure S3: **Receptor quantification and gating of PBMC-derived immune cell types. Related to Figure 3.** A) Preliminary gating for single lyphocytes. B) Example staining for CD122 (red), the corresponding isotype control (blue), and unstained cells (black). C) Gating for live T helper and T regulatory cells during receptor quantification. D) Live cell NK cell gating. E) Live cell CD8+ T cell gating. F) Gating for fixed T helper and T regulatory cells during pSTAT5 quantification. G) Fixed CD8+ T cell and NK cell gating.

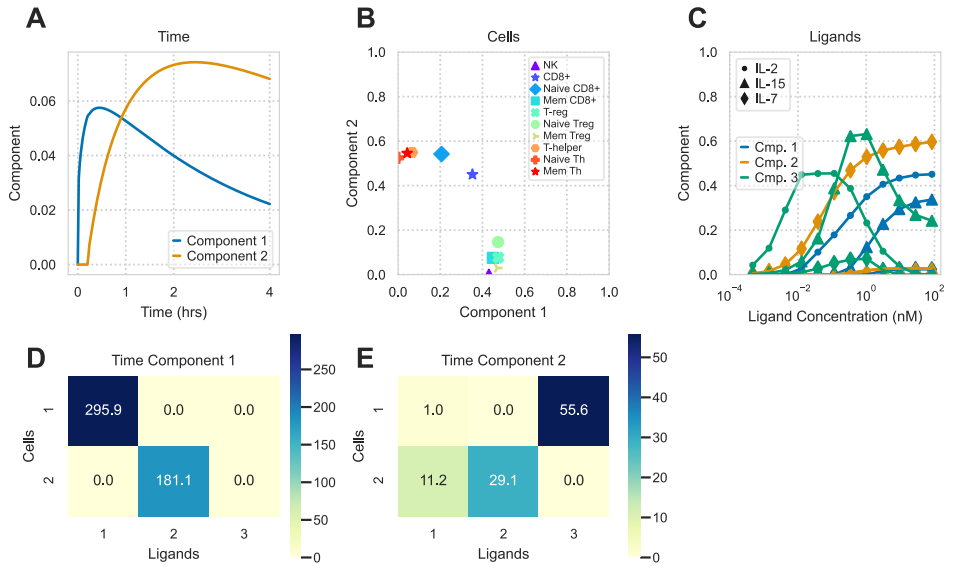

Figure S4: **Tucker factorization of predicted immune cell type responses. Related to Figure 5.** A) Timepoint decomposition plot showing factorization component values against time after decomposing the tensor's first dimension into 2 components. B) Decomposition plot along the second (cell) dimension after decomposing it to 2 components showing the ten cell type values along each component. C) Ligand decomposition plot along the tensor's third dimension after decomposing it into 3 components. D–E) Slices of the Tucker core tensor corresponding to time component 1 (D) and 2 (E).

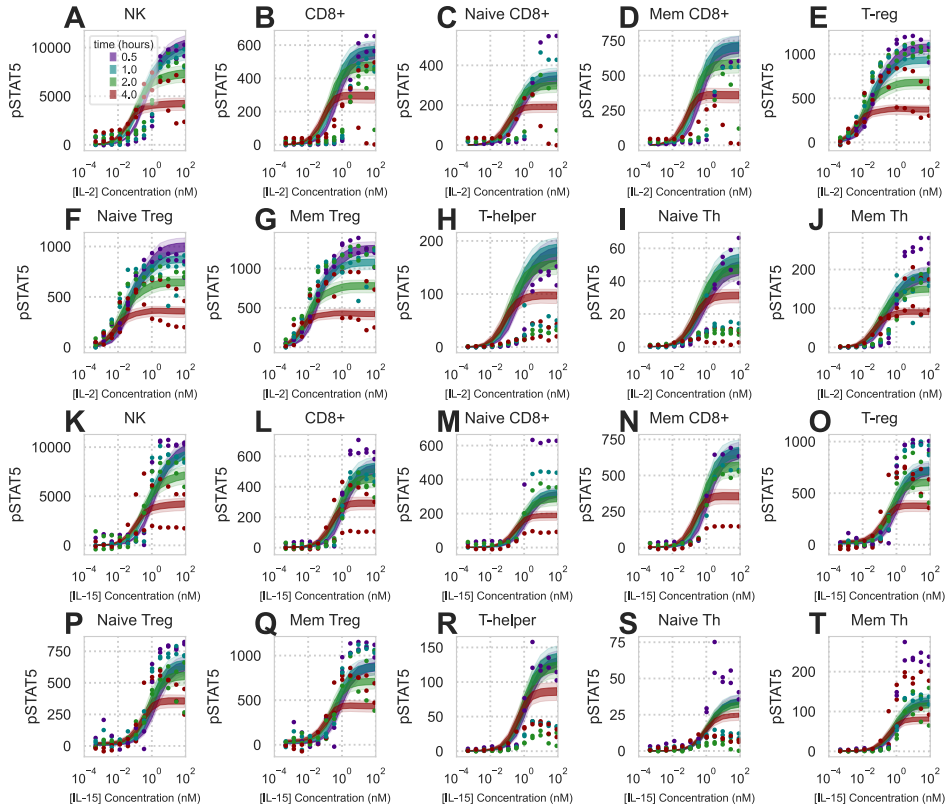

Figure S5: **Full panel of predicted versus actual immune cell type responses. Related to Figure 4.** Dots represent flow cytometry measurements and shaded regions represent 10-90% confidence interval for model predictions. Time of pSTAT5 activity measurement is denoted by color. All cell populations were stimulated with either IL-2 (A-J) or IL-15 (K-T). Experiments were performed in duplicate (N = 2).

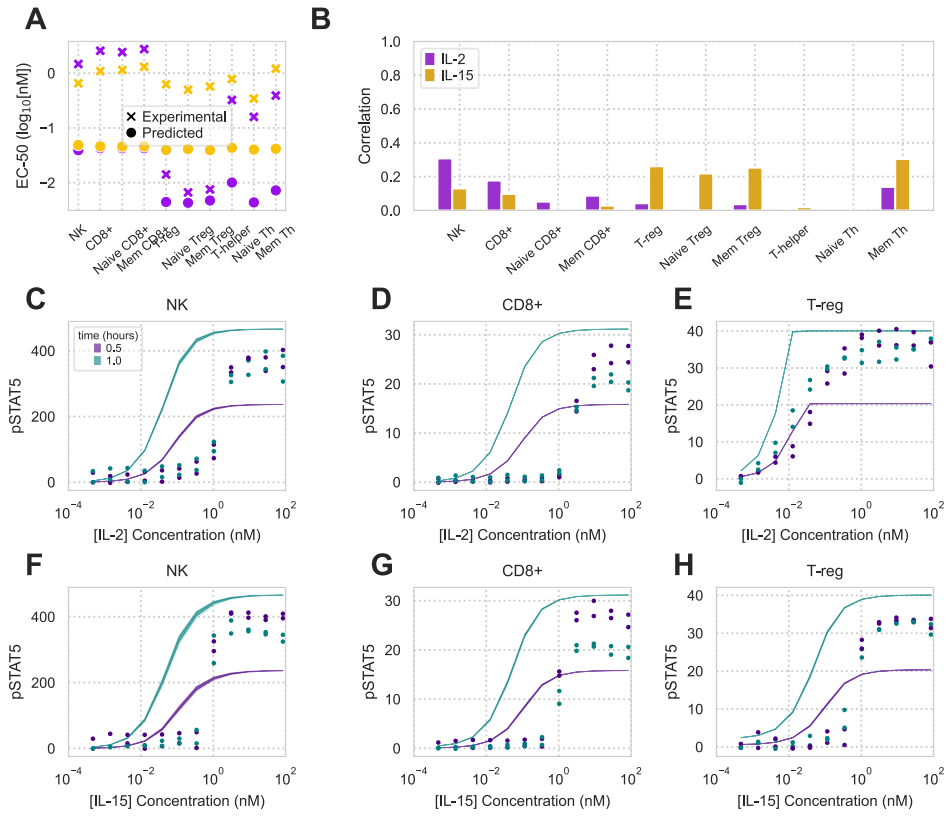

Figure S6: **Model without trafficking is unable to accurately predict PBMC signaling response. Related to Figure 4.** A) Both experimentally-derived and model without trafficking-predicted EC_{50}s of dose response across IL-2/-15 and all 10 cell types. EC_{50}s are shown for 1 hr time point. B) Pearson correlation coefficients between model without trafficking prediction and experimental measurements for all 10 cell populations. C–H) pSTAT5 response to IL-2 (C–E) or IL-15 (F–H) dose responses in NK, CD8+, and T_{reg} cells. Predictions were made using model without trafficking. Experiments were performed in duplicate (N = 2).

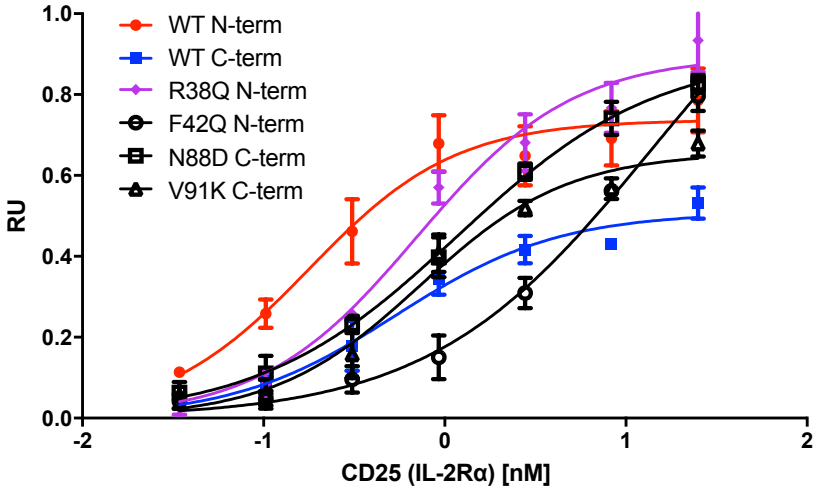

Figure S7: **Cytokine affinity measurements to IL-2Rα. Related to Figure 6.** Binding is quantified in relative units using biolayer interferometry.

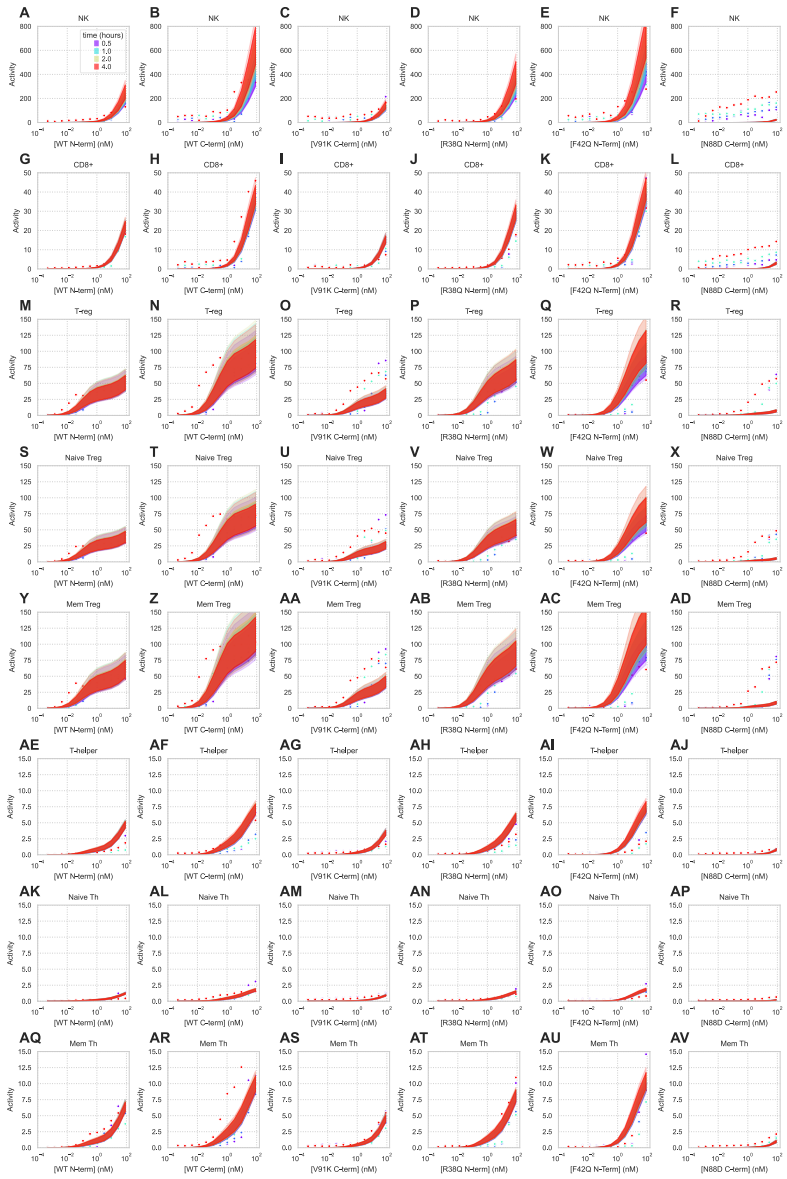

Figure S8: **Full panel of predicted versus actual immune cell type responses to IL-2 muteins. Related to Figure 6.** Dots represent flow cytometry measurements and shaded regions represent 10-90% confidence interval for model predictions. Time of pSTAT5 activity measurement is denoted by color. Cell populations were stimulated with IL-2 muteins of varying IL-2Rα and IL-2Rβ/γ_c binding affinities. Experiments were performed once (N = 1).

Chapter 3:

Multivalent, asymmetric IL-2-Fc fusions provide optimally enhanced T regulatory cell selectivity

Orcutt-Jahns, B.[1], Emmel, P. C.[1], Snyder, E. M.[1], Posner, C.[2], Carlson, S. M.[2], & Meyer, A. S.[1,3,4]

[1]Department of Bioengineering, University of California, Los Angeles, Los Angeles, CA 90095, USA.

[2] Visterra Inc., Waltham, MA 02451

[3]Jonsson Comprehensive Cancer Center, University of California, Los Angeles, Los Angeles, CA 90095, USA.

[4]Eli and Edythe Broad Center of Regenerative Medicine and Stem Cell Research, University of California, Los Angeles, Los Angeles, CA 90095, USA.

IMMUNOLOGY

Multivalent, asymmetric IL-2–Fc fusions show enhanced selectivity for regulatory T cells

Brian T. Orcutt-Jahns[1], Peter C. Emmel[1], Eli M. Snyder[1], Scott D. Taylor[1], Aaron S. Meyer[1,2,3]*

The cytokine interleukin-2 (IL-2) has the potential to treat autoimmune disease but is limited by its modest specificity toward immunosuppressive regulatory T (T_{reg}) cells. IL-2 receptors consist of combinations of α, β, and γ chains of variable affinity and cell specificity. Engineering IL-2 to treat autoimmunity has primarily focused on retaining binding to the relatively T_{reg}-selective, high-affinity receptor while reducing binding to the less selective, low-affinity receptor. However, we found that refining the designs to focus on targeting the high-affinity receptor through avidity effects is key to optimizing T_{reg} selectivity. We profiled the dynamics and dose dependency of signaling responses in primary human immune cells induced by engineered fusions composed of either wild-type IL-2 or mutant forms with altered affinity, valency, and fusion to the antibody Fc region for stability. T_{reg} selectivity and signaling response variations were explained by a model of multivalent binding and dimer-enhanced avidity—a combined measure of the strength, number, and conformation of interaction sites—from which we designed tetravalent IL-2–Fc fusions that had greater T_{reg} selectivity in culture than do current designs. Biasing avidity toward IL2Rα with an asymmetrical multivalent design consisting of one α/β chain–binding and one α chain–binding mutant further enhanced T_{reg} selectivity. Comparative analysis revealed that IL2Rα was the optimal cell surface target for T_{reg} selectivity, indicating that avidity for IL2Rα may be the optimal route to producing IL-2 variants that selectively target T_{regs}.

INTRODUCTION

Cytokines that bind to the common γ-chain (γ_c) receptor, interleukins 2, 4, 7, 9, 15, and 21 (IL-2, IL-4, and so on), are a critical hub in modulating both innate and adaptive immune responses (*1*). Each cytokine in this family binds to the common γ_c receptor alongside a private receptor that is specific for each ligand to induce signaling. These cytokines control the activity of both effector and suppressor immune cell populations. For example, IL-2 can increase the effector functions of $CD8^+$ T cells through the induction of cytotoxic protein expression, as well as promote the suppressive capacity of regulatory T (T_{reg}) cells by inducing the expression of suppressive cytokines and checkpoint proteins (*2*–*4*). Signaling through γ_c family receptors also commonly results in the proliferation of both suppressor and effector cell types; consequently, the γ_c cytokines are an important endogenous and exogenous mechanism for altering the balance of immune cell populations. The importance of these cytokines is observed most extremely from loss-of-function or reduced-activity mutations in γ_c, which subvert T and natural killer (NK) cell maturation (*5*). Disruptive mutations in the private receptors can lead to more selective reductions in cell types, such as T_{regs} in the case of IL2Rα or T cells in that of IL7Rα (*1*). Conversely, activating mutations in these receptors can promote cancers such as B and T cell leukemias (*6*).

The γ_c cytokines have been explored as immunotherapies in a diverse array of disease indications (*7*). The most studied member of the family, IL-2, acts as both as an immunostimulant and immunosuppressant and has been explored as a treatment for diseases ranging from cancer to autoimmunity (*8*–*11*). Its ability to expand T_{reg} populations, particularly at low doses, has great promise as an effective treatment for autoimmune diseases such as graft-versus-host disease and hepatitis-induced vasculitis (*12*, *13*). The efficacy of these IL-2 therapies has been hindered, however, by IL-2's activation of off-target immune populations, which simultaneously reduce therapeutic efficacy and drive toxicities (*14*). Enabling more selective activation of T_{regs} is desired to reduce these detrimental effects. However, this goal has remained elusive; effector and suppressor immune populations have only subtly differing abundances of each IL-2 receptor subunit, and no truly T_{reg}-specific marker has been discovered for targeting purposes (*15*). Reducing IL-2′s affinity for IL2Rβ moderately increases T_{reg} selectivity by increasing IL-2′s reliance on IL2Rα, which is found in greater abundance on T_{regs} (*15*, *16*). However, this increase in selectivity comes at the cost of potency, because IL2Rβ is necessary for signal transduction (*17*). Thus, when targeting T_{regs}, IL-2 therapies have faced a persistent tradeoff between selectivity and potency (*18*).

The challenges involved in engineering cell-selective forms of IL-2 have inspired varied therapeutic designs. As mentioned, the most common approach has been to alter the receptor affinities of IL-2 to weaken its interaction with IL2Rα, IL2Rβ, or both receptors (*19*–*23*). In most cases, the wild-type (WT) cytokine or mutein is fused to an immunoglobulin G (IgG) Fc to take advantage of FcRn-mediated recycling to extend drug half-life. Fc fusion has taken many forms, such as fusion to the cytokine at the N or C terminus, including one or two cytokines per IgG and including or excluding Fc effector functions (*15*). Also used have been so-called immunocytokines that bind to IL-2 and block certain receptor interactions to bias signaling responses (*18*). Cis-targeted IL-2 fusions, such as bispecific antibodies in which a nonfused Fab binds to CD8, have been designed to deliver cytokines to cytotoxic T cells (*24*). However, it is unclear whether this approach can be applied to targeting T_{regs}. Other, more diverse IL-2 engineering

[1]Department of Bioengineering, University of California, Los Angeles, Los Angeles, CA 90095, USA. [2]Jonsson Comprehensive Cancer Center, University of California, Los Angeles, Los Angeles, CA 90095, USA. [3]Eli and Edythe Broad Center of Regenerative Medicine and Stem Cell Research, University of California, Los Angeles, Los Angeles, CA 90095, USA.
*Corresponding author. Email: ameyer@asmlab.org

has also been explored: "Orthogonal" IL-2, which only signals through a synthetic receptor, has shown promise for stimulating ex vivo engineered T_{regs} (*25*); a signaling-deficient IL-2 with high specificity for IL2Rβ that attenuates graft-versus-host disease by inhibiting effector cells' IL-2 signaling has been developed (*26*); and last, mRNA delivery of a T_{reg}-selective IL-2 mutein has been shown to provide better pharmacokinetics by sustaining low amounts of the cytokine (*27*). These varied approaches demonstrate the complex nature of cytokine engineering necessitating systematic design principles.

Here, we systematically profiled the signaling specificity effects of engineered cytokine alterations, including affinity-altering mutations and Fc-fusion formats, to map the current landscape of cell-selective IL-2 designs. Through this systematic evaluation, we identified Fc fusion valency to be an important factor in cell type selectivity. The signaling specificity of all muteins and Fc formats quantitatively matches a multivalent binding model, both between cell types and across cell-to-cell variation within a cell type, indicating that the effect of cytokine multivalency is derived from altered surface receptor binding avidity. Using this model, we then identified that cytokines engineered in higher valency formats are predicted to confer greater specificity toward a variety of immune cell types. These insights were experimentally validated by designing and testing two novel tetravalent IL-2 muteins in both symmetric and asymmetric forms that displayed superior T_{reg} signaling selectivity. The performance of asymmetric, tetravalent IL-2 fusion proteins also demonstrates how bitargeting and asymmetry can decouple targeting from signaling, enabling new therapeutic opportunities. In total, our analysis and experimental findings demonstrate that cytokine valency is an unexplored direction for further enhancing selective signaling responses and that many opportunities for leveraging multivalency engineering exist within the γ_c cytokine family and beyond.

RESULTS

Systematic IL-2 variant profiling reveals multiple determinants of response

To explore how IL-2 mutations affect signaling across immune populations, we stimulated peripheral blood mononuclear cells (PBMCs), collected from a single donor, with 13 IL-2 muteins (Fig. 1, A and B, and table S1). Our panel included several IL-2 muteins previously developed to confer enhanced T_{reg}-selective signaling (*15*, *22*, *23*). In addition to changes in receptor affinities, the muteins included some variation in structural features: Fc fusion at either the C or N terminus, which has been shown to alter receptor interaction kinetics (*15*), and fusion to Fc in both monomeric and dimeric formats. We previously profiled 6 of the 11 IL-2 muteins (*15*); however, we both expanded this previous panel while also adding dimeric Fc fusions, thus greatly expanding the scope of IL-2 engineering approaches surveyed. Our panel includes several muteins previously published or clinically developed for their T_{reg} selectivity—monomeric N88D and dimeric R38Q/H16N were previously developed by Amgen and Otsuka Pharmaceuticals, respectively (*22*). Our panel was also designed to feature IL-2 variants whose affinities for IL2Rα and IL2Rβ span the range of currently available T_{reg}-selective affinity mutants (Fig. 1B).

The panel of IL-2 variants was used to stimulate cells from a single donor at four time points using 12 treatment concentrations. The PBMCs were then stained for canonical cell type markers and phosphorylated signal transducers and activators of transcription 5 (pSTAT5), a commonly used read-out of IL-2 signaling response, allowing us to separate signaling response by cell type. Five different cell types—T_{reg}, helper T (T_{helper}), $CD8^+$, NK, and NK $CD56^{bright}$ (NK^{bright}) cells—were gated and quantified (fig. S1, A to D). T_{reg} and T_{helper} cells were further dissected into low, average, and high IL2Rα abundance by isolating subpopulations using three logarithmically spaced bins (fig. S1J). For a surface-level visualization of the effects of time, cell type, receptor abundance, ligand format, ligand affinity, and concentration, we organized our signaling data into a heatmap (Fig. 1C). The complexity of the data demanded closer examination.

We selectively highlighted several dose-response curves to demonstrate the importance of our comprehensive characterization (Fig. 1, D to O). First, as expected, we found that the affinity with which each IL-2 interacted with receptors divided responses (Fig. 1, D to G); for example, WT IL-2 most potently activated all cell types, as expected given that it bound to IL2Rβ with the greatest affinity (Fig. 1, B and D to G). Valency also had a prominent effect on signaling response; the bivalent Fc fusion form increased sensitivity and potency of response across all cell types.

Temporal dynamics also affected response characteristics (Fig. 1, H to K). For example, we found that C or N terminus Fc-fused IL-2 demonstrated distinct responses in T_{regs} at 1 hour of treatment but shared responses after 4 hours of treatment (Fig. 1, H to K). Temporal effects are likely influenced by receptor-mediated endocytosis of IL-2 receptor subunits and transcriptional changes arising from IL-2 signaling (*28*, *29*).

Last, we found that receptor abundance interacted with cell identity to alter response (Fig. 1, L to O). T_{reg} populations with high amounts of IL2Rα strongly responded to monovalent H16N N terminus, and the bivalent form moderately enhanced this response. However, in the $IL2R\alpha^{lo}$ T_{regs}, the effect of bivalency was even greater; only bivalent H16N induced a substantial response. $IL2R\alpha^{high}$ T_{helper} cells also showed a moderate increase in potency with bivalency, like the $IL2R\alpha^{high}$ T_{regs}, but the $IL2R\alpha^{lo}$ population showed no distinction between the monovalent and bivalent fusions. Thus, immune populations are further subdivided by receptor abundance into subpopulations with distinct cellular responses.

In total, the dynamics of response, cell type, concentration, ligand affinity, Fc fusion valency, and Fc fusion orientation all play roles in determining cellular response. These determinants interact in unique and often counterintuitive ways and thus require a more comprehensive accounting of their effects.

Ligand valency and affinity interact to form unique cell type selectivity profiles

Given the coordinated importance of time, ligand valency, ligand affinity, cell type, and receptor expression, we next sought to focus on how ligand format affected T_{reg} selectivity. The selectivity of IL-2 for specific cell types corresponds closely to its therapeutic potency and potential toxicities (*19*, *21*, *22*, *30*). Therefore, we sought to better understand the relationship between T_{reg} selectivity and ligand properties (Fig. 2, A to I). First, we plotted the ratio of STAT5 phosphorylation (fit by a Hill curve) in T_{regs} to that of off-target cells for each ligand across our concentration range and saw that the shape of each selectivity curve varied substantially for each

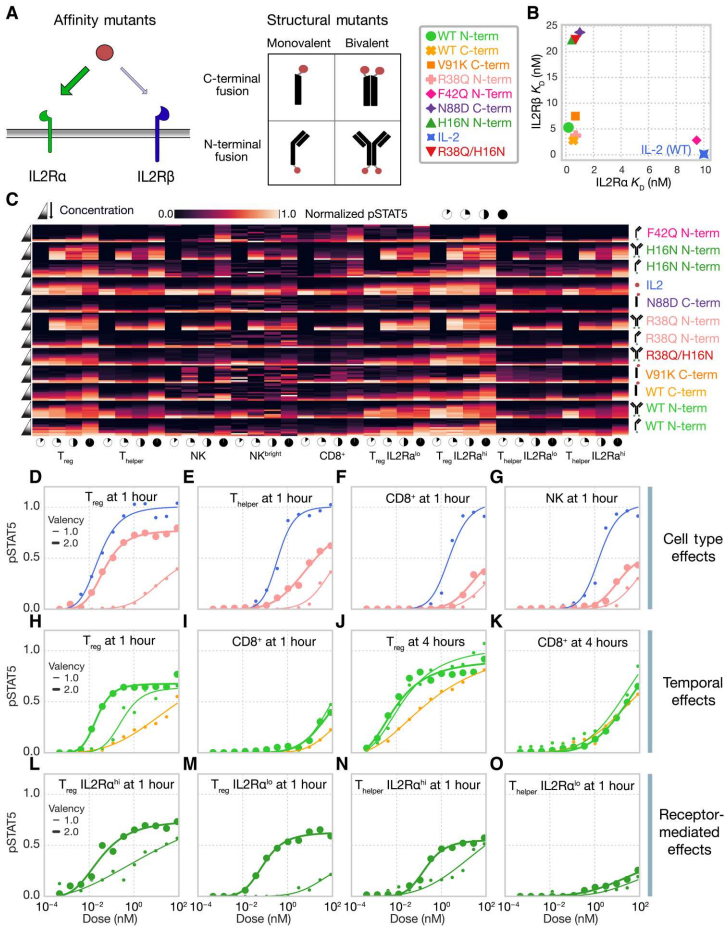

Fig. 1. Systematically profiling IL-2 muteins reveals determinants of response. (**A**) Schematic of affinity and structural mutants explored. (**B**) IL2Rα and IL2Rβ affinities of each IL-2 variant. For affinity assays, two technical replicates were conducted ($N = 2$). (**C**) Heatmap of phosphorylated STAT5 measurements for each cell type, time point, ligand, and concentration. pSTAT5 measurements were normalized to the maximum pSTAT5 observed in response to WT IL-2 for each cell type. (**D** to **O**) STAT5 phosphorylation response curves for immune cells stimulated with select IL-2 muteins. Time points and cell types are indicated in subplot titles. For all signaling assays, PBMCs were collected from one donor, and three technical replicates—meaning independent batches of cells from the single donor—were conducted on independent days ($N = 3$).

ligand and off-target cell type that was considered (Fig. 2, A, B, D, F, and H). T_{reg} selectivity quantified against $CD8^+$, NK, or NK^{bright} cells most prominently separated bivalent from monovalent ligands, with bivalent muteins being most selective for T_{regs} at lower concentrations. The selectivity demonstrated by bivalent muteins at lower doses can also be quantified by observing their lower T_{reg} activation median effective concentration (EC_{50}) values and relatively unchanged off-target EC_{50} values (table S2). Because IL2Rα affinity varied widely between our IL-2 mutants and is a known T_{reg} selectivity regulator, we sought to understand how affinity differences contribute to T_{reg} selectivity. We plotted IL2Rα affinity against the peak T_{reg} selectivity observed across concentrations (Fig. 2, C, E, G, and I). Because of the high abundance of IL2Rα displayed by T_{regs} (fig. S1I), we expected to see a positive correlation between IL2Rα affinity and peak T_{reg} selectivity. However, we saw that this relationship varied in a cell type– and valency-dependent manner. When considering either $CD8^+$ or NK cells, decreasing IL2Rα affinity led to not only decreases in

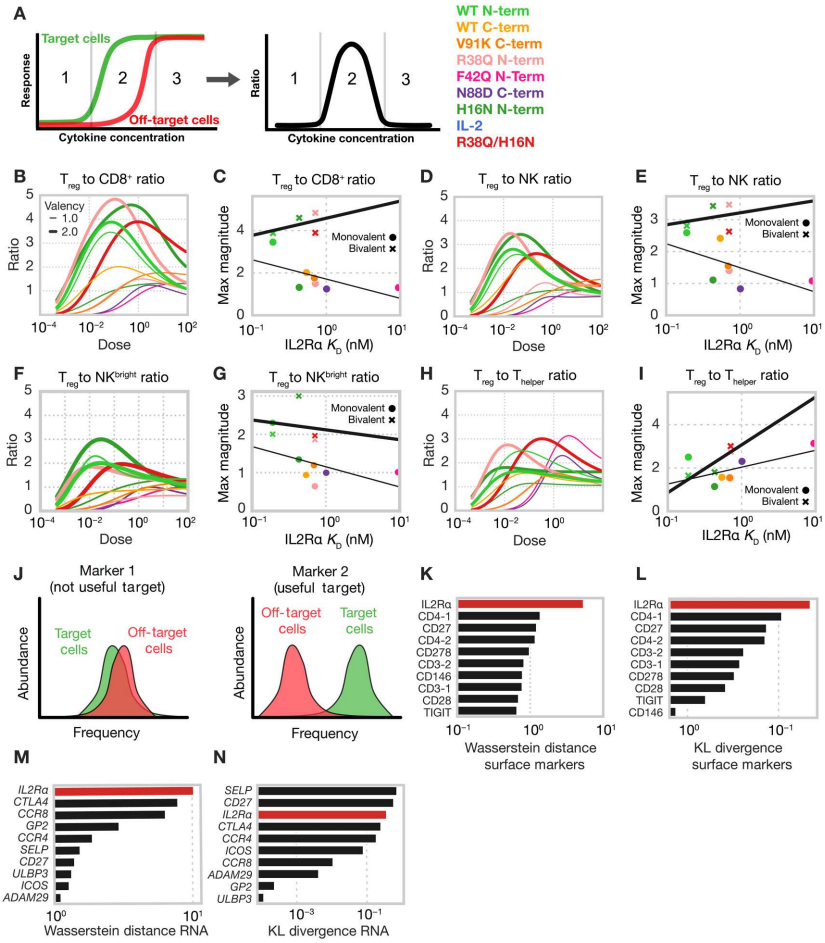

Fig. 2. IL-2 muteins display structural- and affinity-dependent T_{reg} selectivity that cannot be overcome with cis-targeting strategies. (**A**) Schematic describing ratio of activation between target and off-target immune populations. (**B** and **C**) Ratio of T_{reg}-to-$CD8^+$ T cell pSTAT5 dose-response curve at 4 hours (B) and the maximum ratio of signaling (pSTAT5) in T_{regs} to off-target cell type versus IL2Rα affinity (C). (**D** and **E**) As described in (B) and (C), respectively, of T_{regs} to NK cells (D and E), NK^{bright} cells (**F** and **G**), and T_{helper} cells (**H** and **I**). The ratio was defined as the ratio of Hill curves fit to experimental data for target and off-target populations shown in Fig. 1. Lines of best fit were separately fit to monovalent (thin) and bivalent (thick). Signaling data in (B) to (I) were gathered from PBMCs harvested from a single donor, and three technical replicates were conducted ($N = 3$). (**J**) Schematic depicting how useful markers for conferring selectivity are selected. (**K** to **N**) Top sorted Wasserstein distances (K and M) and Kullback-Leibler (KL) divergences (L and N) of surface markers (K and L) and RNA data (M and N) in T_{regs} in the CITE-seq dataset (GSE164378) (*31*).

the peak T_{reg} selectivity of monovalent muteins but also, somewhat unexpectedly, little relationship with the bivalent selectivity peaks (Fig. 2, C, E, and F). When considering T_{helper} populations, which have greater amounts of IL2Rα than $CD8^+$ and NK cells, we observed that decreases in IL2Rα affinity led to increases in maximum selectivity for both monovalent and bivalent muteins (Fig. 2I). Expectedly, the mutein concentration at which the maximum T_{reg} selectivity occurred was higher for ligands with weaker IL2Rα affinity across all cell types (fig. S2, A to D). In total, affinity and valency affected the selectivity profiles across ligand doses in distinct yet intertwined manners. To understand these relationships, a method mapping each of these factors simultaneously is needed.

T_{regs} have limited opportunities for cis-targeting

Whereas IL2Rα is more abundant in T_{regs}, the difference is subtle compared with that of some off-target cells, making selectively targeted activation more challenging (*15*, *18*). Consequently, we wondered whether a cis-targeting strategy—in which IL-2 is fused to a domain binding some other T_{reg}-specific surface marker—would provide even greater selectivity. To explore this possibility, we used a cellular indexing of transcriptomes and epitopes by sequencing (CITE-seq) dataset in which >211,000 human PBMCs were simultaneously analyzed for 228 surface markers coupled with single-cell RNA sequencing (GSE164378) (*31*). Our previous work shows that specificity is conferred by markers expressed at a high ratio between target and off-target cells (Fig. 2J) (*32*). As measures of difference, we calculated the Wasserstein distance and Kullback-Leibler divergence of each surface marker abundance and expression between T_{reg} populations and all off-target PBMCs. These complimentary distance metrics were chosen to reflect two different measures of difference: The Wasserstein distance that is maximized when transforming one distribution to another would require changing the cells to a large degree, whereas the Kullback-Leibler distance is maximized when the overlap between two distributions is minimized. We were surprised to find that IL2Rα was the most differentiating and unique marker on T_{regs} by both proteomic and transcriptomic analyses (Fig. 2, K to N). These results were reinforced by using both a linear and nonlinear classifier to identify which surface markers and transcripts were most informative for T_{reg} classification; this analysis again found that IL2Rα was optimal (fig. S3, A to D). Consequently, we reasoned that binding alternative surface markers would not improve IL-2 T_{reg} selectivity.

Bivalent Fc-cytokine fusions have distinct cell specificity but shared dynamics

Understanding that selectivity for T_{regs} must be derived through engineering binding to the IL-2 receptors, we sought to develop a more complete view of the various structural choices for IL-2 fusion design. Exploring variation in response across cell types and ligand treatments is challenging because of its multidimensional nature. Restricting one's view to a single time point, cell type, or ligand concentration provides only a slice of the picture (Figs. 1 and 2) (*15*, *33*). Dimensionality reduction is a generally effective tool for exploring multidimensional data. However, flattening our signaling data to two dimensions and using principal components analysis failed to help isolate the effects of concentration, ligand properties, time, and cell type (Fig. 3A). Therefore, to better resolve our data, we organized our profiling experiments into a four-dimensional tensor organized according to the ligand used, concentration, treatment duration, and cell type in the profiling. We then factored these data using nonnegative canonical polyadic (CP) decomposition, a technique that represents *n*-dimensional tensors as additively separable patterns, themselves approximated by the outer product of dimension-specific vectors (*34*). We used CP decomposition to derive factors summarizing the influence of each dimension (Fig. 3B). Three components explained roughly 90% of the variance within the dataset (Fig. 3C).

Factorization separated distinct response profiles into separate components and the effect of each dimension (such as time or concentration) into separate factors. For instance, component 1 almost exclusively represented responses to WT cytokines (Fig. 3D), the only ligands that were not Fc-fused, showing a distinct response primarily at high concentrations (Fig. 3E), with broad specificity (Fig. 3F) and a signaling profile peaking at 30 min and then more rapidly decreasing (Fig. 3G). An alternative way to interpret the factorization results is to compare profiles within a single factor. For example, component 1 led to a less sustained profile of signaling response as compared with the other signaling patterns (Fig. 3G).

Components 2 and a combination of components 1 and 3 cleanly separated ligands conjugated in bivalent or monovalent forms, respectively (Fig. 3, D and H). Ligand valency was represented more prominently than differences in receptor affinity between muteins. Component 2 had uniquely high T_{reg} specificity (Fig. 3F) most represented at intermediate concentrations (Fig. 3E). Component 2 was also highly correlated with IL2Rα abundance in subsets of T_{reg} and T_{helper} cells, suggesting that the bivalent molecules' specificity for T_{regs} is mediated by their higher abundance of IL2Rα. Component 3 had a broader cell response (Fig. 3F) and increased monotonically with concentration (Fig. 3E). Despite these strong differences in specificities, both components had nearly identical time dynamics (Fig. 3G). Whereas other ligand variation influenced the potency and selectivity of each ligand, only the bivalent Fc fusions, regardless of their receptor affinities, more highly weighted the T_{reg}-selective component 2 over components 1 and 3, which represented effector cell response (Fig. 3H). In total, these results indicated that mono- and multivalent cytokines shared identical dynamics and that, although Fc fusion and affinity modulation affect response, ligand valency was a critical and prominent determinant of specificity.

Variation in IL-2 responses is explained by a simple multivalent binding model

Having observed that T_{reg} selectivity is prominently enhanced by multivalency, we sought to determine whether cell surface binding on its own could explain these selectivity differences. To do so, we applied a two-step, equilibrium, multivalent binding model to predict IL-2 response, assuming that signaling response was proportional to the amount of active receptor-ligand complexes (Fig. 4A) (*35*). Within the model, ligand binding first occurs with kinetics equivalent to the single binding site, and then subsequent interactions occur proportionally to affinity, adjusted by K_x^*, a cross-linking constant that corrects for differences between monovalent and multivalent interactions. We fit this model to our signaling experiments and evaluated its concordance with the data. The model is very simple, with the cross-linking parameter being the only non-scaling fit parameter; this parameter had an optimum at 1.2×10^{-11} per cell, consistent with that seen for other receptor families (*36*–*38*). Overall, we observed remarkable consistency between predicted and observed responses ($R^2 = 0.85$; fig. S4), and accuracy was maintained when examining data subsets, including individual cell types and ligands (Fig. 4, B and C).

To ensure that our model was not simply capturing a trend toward higher signaling with increasing concentration, we examined our model's accuracy within each concentration (Fig. 4D). Our model did not predict a response at the lowest concentrations because there was little to no response in the data itself but increased in accuracy at concentrations where responses were observed. Last, we examined how the model's accuracy varied within each time point (Fig. 4E); each was predicted with consistent accuracy. Some decrease in model accuracy would be expected, given that longer treatments likely involve various compensatory mechanisms,

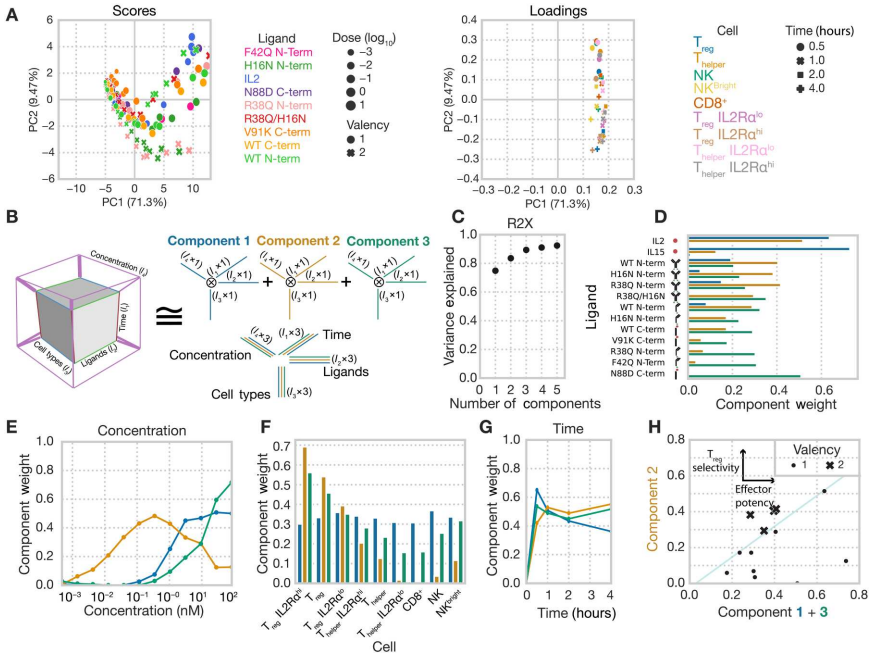

Fig. 3. Tensor-based decomposition reveals unique selectivity defined by fusion valency. (**A**) Principal components analysis scores (left) and loadings (right) of pSTAT5 signaling data. Signaling data were gathered from PBMCs harvested from a single donor, and three technical replicates were conducted ($N = 3$). Principal component (PC) decomposition was performed on signaling data arranged in matrix form, where each dose and ligand combination is included as a row and each cell and time combination is included as a column. (**B**) Schematic representation of nonnegative canonical polyadic (CP) decomposition. Experimental pSTAT5 measurements are arranged in a tensor according to the duration of treatment, ligand used, cytokine concentration, and cell type. CP decomposition then helps to identify and visualize patterns across these dimensions. (**C**) Percent variance reconstructed (R2X) of the signaling dataset versus the number of components used during CP decomposition. (**D**) Component weights for each IL-2 mutant resulting from CP decomposition of the signaling dataset. (**E**) Component weights representing the effect of IL-2 concentration resulting from CP decomposition of the signaling dataset. (**F**) Component weights representing cell type specificity resulting from CP decomposition of the signaling dataset. (**G**) Component weights for the effect of treatment duration resulting from CP decomposition of the signaling dataset. (**H**) Sum of component 1 and 3 weights (off-target signaling) versus component 2 (T_{reg} signaling) weight for each monovalent and bivalent ligand. The thin line is included for visualization purposes only.

such as the degradation or increased transcription of IL-2 receptor subunits (*29*, *39*). In total, multivalent cell surface binding showed quantitative agreement with the pattern of cell type–specific responses to IL-2 muteins, supporting that the specificity enhancement of bivalency is derived from receptor avidity effects and is explained by a simple model of cell surface binding.

Upon finding that our model was broadly predictive of cell type–specific signaling responses, we sought to use our model to understand and visualize how valency and affinity interact to determine T_{reg} selectivity. Here, our model showed that T_{reg} response is strongly governed by IL2Rα affinities and that these effects have an exceptionally strong relationship with valency, particularly at intermediate cytokine doses, whereas NK signaling barely varied across ligands of varying affinities (Fig. 4, F and G). We then used the model to explore how receptor abundance affects multivalent ligand binding (Fig. 4, H and I). Here, theoretical cell populations expressing 10^4 IL2Rα and 10^3 IL2Rβ molecules varied widely in their response to multivalent IL-2 muteins (Fig. 4H), whereas cells expressing very few IL2Rα receptors and the same abundance of IL2Rβ barely varied in their response (Fig. 4I). Therefore, we concluded that multivalent cytokines with high IL2Rα affinities uniquely and selectively target T_{regs} through IL2Rα-mediated avidity effects.

Multivalency provides a general strategy for enhanced signaling selectivity and guides the development of superior IL-2 muteins

Given that a simple binding model accurately predicted cell type–specific responses to IL-2 and that bivalent, Fc-fused IL-2 muteins have favorable specificity properties, we computationally explored to what extent multivalency might be a generally useful strategy. Although monovalent ligand binding scales linearly with receptor abundance, multivalent ligands bind nonlinearly depending on receptor abundance (*40*). Thus, multivalent ligands should be able to selectively target cells with uniquely high expression of certain γ_c family receptors.

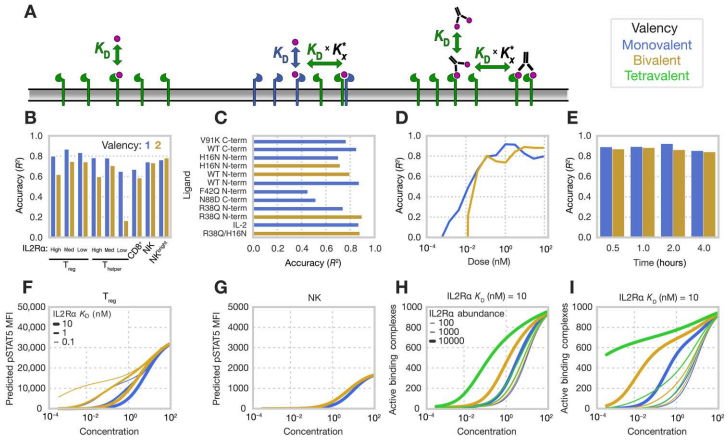

Fig. 4. Responses are predicted by a simple multivalent binding model. (**A**) Schematic of the model. Initial association of multivalent ligands proceeds according to monovalent affinity, and subsequent binding events proceed with that affinity scaled by the K_x^* parameter. Model was fit to the signaling data gathered from PBMCs harvested from a single donor, and three technical replicates were conducted ($N = 3$). Receptor counts used in model simulations for each cell population were measured in PBMCs gathered from a single donor, and four technical replicates were performed ($N = 4$). (**B** and **C**) Model's accuracy subset by cell type (B) and ligand (C) for all monovalent and bivalent IL-2 muteins. (**D** and **E**) Model's accuracy subset by concentration (D) for all ligands and time (E) for all ligands, concentrations, and cell types. All accuracies (B to E) are calculated as a Pearson's correlation R^2 score for experimental cytokine responses at 30 min and 1 hour. (**F** and **G**) Model-predicted pSTAT for T_{regs} (F) and NK cells (G) in response to mono- and bivalent IL-2 ligands with 10 nM IL2Rβ K_D. MFI, mean fluorescent intensity. (**H** and **I**) Predicted number of active signaling complexes (proportional to predicted pSTAT5) formed on cells with 1000 IL2Rβ receptors and varying numbers of IL2Rα for ligands with affinities of 10 nM K_D for IL2Rβ and either 1 nM (F) or 10 nM (I) K_D for IL2Rα.

Valency enhancements are only apparent with coordinated changes in receptor-ligand binding affinities (*32*). Therefore, we optimized the receptor affinities of simulated ligands while varying valency. We first designed IL-2 muteins of varying valency to obtain optimal T_{reg} specificity (Fig. 5A). As expected, ligand valency increased achievable selectivity past that possible using a monovalent cytokine format at any receptor affinities. Muteins of higher valency required reduced IL2Rα affinity to achieve optimal T_{reg} selectivity (Fig. 5B). We then explored whether IL-2 muteins lacking IL2Rα binding could selectively target NK cells, on the basis of their uniquely high expression of IL2Rβ[15], with similar results; IL-2 muteins of higher valency were predicted to be increasingly selective for activation of NK cells, so long as IL2Rβ/γ_c affinity was coordinately decreased (Fig. 5, C and D). Last, we explored whether multivalent IL-7 could be used to target T_{helper}s, because they express high amounts of IL7Rα (fig. S1I). We again found that ligands of higher valency should achieve higher selectivity for these cells but that the benefits of valency were less than the targeting of T_{regs} or NK cells using IL-2 mutants because $CD8^+$ T cells have similar IL7Rα amounts (Fig. 5E). These benefits were again contingent on decreasing IL7Rα affinity at higher valency (Fig. 5F).

To experimentally validate that muteins of higher valency could be engineered to increase T_{reg} selectivity, we expressed and purified Fc fusions of R38Q/H16N IL-2 in monovalent, bivalent, and tetravalent formats (fig. S6). PBMCs from five donors were used to account for patient-to-patient variability. Tetravalent IL-2 was designed by Fc-fusing IL-2 muteins at both the C and N termini and allowing the Fc to dimerize (Fig. 5G). The harvested cells were stimulated for 30 min and stained for cell type markers as well as pSTAT5. R38Q/H16N was selected as the mutant closest to optimal binding affinities in tetravalent form, although further optimization is possible (Figs. 1B and 5B). As predicted, valency increased the responsiveness of both T_{regs} and off-target immune cells at each concentration (fig. S7, A to E). However, the T_{reg} response increase far exceeded that of off-target cells; consequently, tetravalent R38Q/H16N was able to achieve much greater T_{reg} selectivity than bivalent and monovalent formats—two IL-2 fusions with near-optimal selectivity in our initial panel (Fig. 5, H to K).

In total, these results show that valency beyond bivalency has unexplored potential for engineered cytokines with enhanced therapeutic potency and reduced toxicity. Critically, our tetravalent R38Q/H16N far outperformed its lower valency counterparts that already represented state-of-the-art selectivity. These results demonstrate that multivalent complexes can achieve selective cytokine signaling in T_{regs} beyond what is achievable with only changes to receptor affinity. They also show the benefit of mechanistic modeling to guide ligand design, particularly when ligand affinity must be considered together with other parameters such as valency.

Bitargeted IL-2–Fc fusions demonstrate even greater T_{reg} selectivity

Through the CITE-seq data analysis, we found that IL2Rα was the optimal surface target for T_{reg} selectivity (Fig. 2, I to M). This result was further strengthened when we integrated these data with our binding model and ligand optimization approach. We used the model to consider whether WT IL-2 fused to a selective binder for any surface markers could increase T_{reg} selectivity. WT IL-2 fusion to an IL2Rα binder was predicted to enhance T_{reg} selectivity

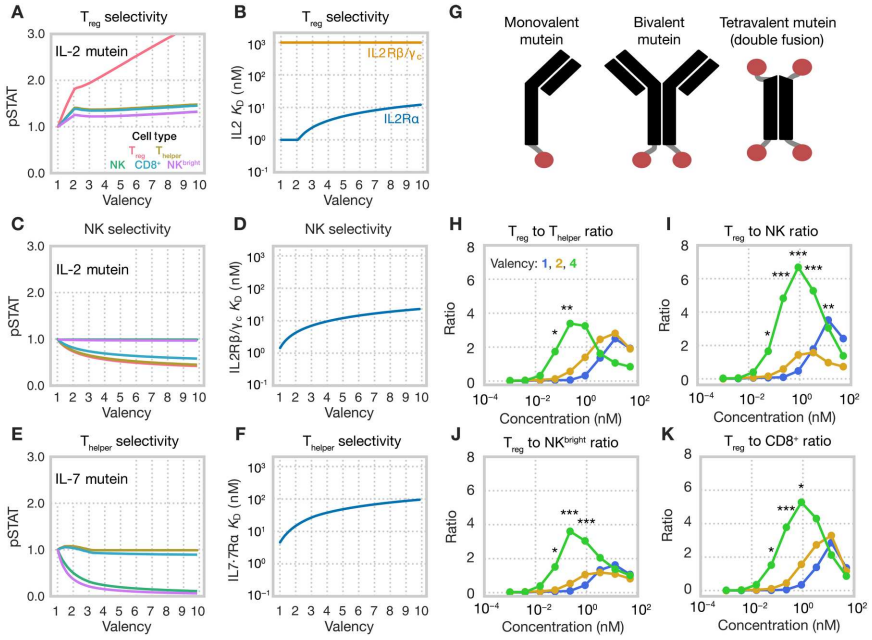

Fig. 5. Multivalency enhances the selectivity of cytokine fusion proteins. (**A** and **B**) Predicted signaling response of T_{regs} in response to a ligand of optimal selectivity at different valencies (A) and optimal receptor-ligand dissociation constants for ligand optimized for selectivity (B). Response predictions were normalized to each population's response for the monovalent case. (**C** and **D**) As described in (A) and (B), respectively, of NK cells (C and D). (**E** and **F**) As described in (A) and (B), respectively, of T_{helper} cells (E and F). Selectivity for T_{reg} and NK cells was derived from IL-2 muteins, and selectivity for T_{helper}s was calculated using IL-7 muteins. During affinity optimization (B, D, and F), mutein affinity for IL2Rα and IL2Rβ/γ_c was allowed to vary for IL-2 muteins, and affinity for IL7Rα was allowed to vary for IL-7 muteins. Affinities were allowed to vary across K_Ds of 10 pM to 1 μM, whereas K_x^* was fixed at its fitting optimum. All optimizations were performed using a concentration of 1 nM. Selectivity was calculated as the ratio of predicted pSTAT5 in target cells to the mean pSTAT5 predicted in off-target cells. Receptor counts used in model simulations for each cell population were measured in PBMCs gathered from a single donor, and four technical replicates were performed ($N = 4$). (**G**) Schematic of multivalent IL-2 mutant design. (**H** to **K**) Ratio of STAT5 phosphorylation in T_{regs} to T_{helper} (H), NK (I), NK^{bright} (J), and $CD8^+$ (K) cells at varying dosages for R38Q/H16N in various valency formats. Dots are representative of the mean of biological replicates. Responses in PBMCs from five donors were included, and two experimental replicates were conducted for each donor ($N = 5$). Statistical significance was determined by comparing the ratios achieved by tetravalent R38Q/H16N to bivalent R38Q/H16N using a Student's *t* test. Here, "*" signifies *P* values < 0.05, "**" signifies *P* values < 0.005, and "***" signifies *P* values < 0.0005. Full ratio plots including experimental error are shown in fig. S7.

over off-target immune cells (Fig. 6, A and B). This was initially unexpected because IL-2 itself binds IL2Rα but indicated to us that multivalent complexes provide the potential opportunity to decouple T_{reg} selectivity (by binding IL2Rα) from cytokine potency.

To decouple cell-selective binding from signaling response, we expressed an asymmetric Fc fusion including both a signaling-competent R38Q/H16N IL-2 and signaling-deficient V91K/D20A/M104V IL-2 with only IL2Rα binding (Fig. 6C and fig. S6). V91K/D20A/M104V IL-2 is reported to effectively eliminate IL2Rβ binding while maintaining IL2Rα interaction (*23*). We henceforth refer to this asymmetric construct as "bitargeted" IL-2 to reflect the inclusion of two IL-2 muteins with separate signaling and targeting roles. To ensure consistent stoichiometry between signaling and non-signaling IL-2, bivalent bitargeted ligand was designed by introducing Fc mutations preventing Fc dimerization (Fig. 6C). Tetravalent bitargeted constructs were predicted to have greater T_{reg} specificity than their non-bitargeted counterparts for any IL2Rβ affinity, using either the IL2Rα affinity of WT or R38Q/H16N (Fig. 6D). We tested our bivalent and tetravalent bitargeted constructs by again stimulating PBMCs gathered from five donors and quantifying their pSTAT5 responses. Both bivalent and tetravalent bitargeted ligands increased or maintained high potency in T_{regs} (fig. S8, A to E). This potency translated to greater T_{reg} selectivity for both bivalent and tetravalent bitargeted forms, both of which outperformed any previously characterized monovalent and bivalent IL-2 fusions and modestly outperformed tetravalent R38Q/H16N (Fig. 6, E to H).

Although both our tetravalent R38Q/H16N molecules and bitargeted constructs were able to target T_{regs} with superior selectivity with respect to T_{helper}, NK, NK^{bright}, and $CD8^+$ cells, principally through the targeting of IL2Rα, we considered whether our molecule could also select for T_{regs} with respect to type 2 innate lymphoid

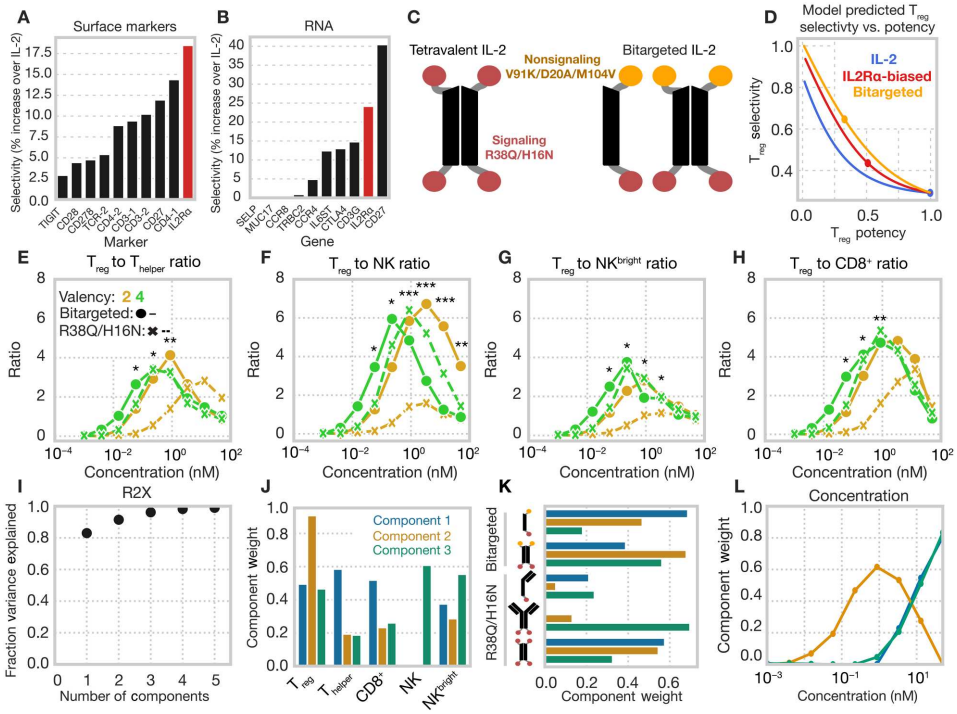

Fig. 6. Asymmetric IL-2 mutants display even greater T_{reg} selectivity. (**A** and **B**) Predicted enhancements to T_{reg} selectivity for IL-2 muteins including a separate targeting domain as calculated using CITE-seq surface marker data (A) or surface-expressed RNA transcripts (B). Selectivity was calculated for T_{regs} against all other PBMC cells as the increase in average T_{reg} to off-target cell binding against WT IL-2 at a simulated concentration of 0.1 nM. Model predicted signaling was predicted on a single-cell basis for cells within the CITE-seq dataset. (**C**) Schematic of asymmetric IL-2 mutant design. (**D**) Predicted normalized T_{reg} selectivity displayed by bivalent WT IL-2, IL2Rα-biased IL-2 (IL2Rα affinity of R38Q/H16N), and bitargeted IL-2 across IL2Rβ affinities. (**E** to **G**) Ratio of STAT5 phosphorylation in T_{regs} to T_{helper} (E), NK (F), NK^{bright} (G), and $CD8^+$ (H) cells at varying concentrations for R38Q/H16N in various valency formats. Dots are representative of mean of experimental replicates. Responses in PBMCs from five donors were included, and two experimental replicates were conducted for each donor. Statistical significance was determined by comparing the ratios achieved by bivalent bitargeted with bivalent R38Q/H16N using a Student's *t* test. Here, "*" signifies *P* values < 0.05, "**" signifies *P* values < 0.005, and "***" signifies *P* values < 0.0005. Full ratio plots including experimental error are shown in fig. S8. (**I** to **L**) Tensor factorization of the signaling responses to R38Q/H16N and bitargeted variants. Experimental pSTAT5 measurements are arranged in a tensor according to the duration of treatment, ligand used, cytokine concentration, and cell type. The results of decomposition of this tensor are shown as percent variance reconstructed (R2X) versus the number of components used (I), component values representing cell type specificity (J), component values for each IL-2 mutant (K), and component values representing the effect of concentration (L).

cells (ILC2s). ILC2s are able to secrete large quantities of inflammatory cytokines such as IL-5 and IL-13, are known to respond to IL-2 through expression of IL2Rα, and have been implicated as a potential source of eosinophilia in low-dose IL-2 therapy. We quantified the abundance of IL2Rα on ILC2s and T_{regs} from four donors and found that both populations expressed nearly identical levels of the receptor (fig. S9H). Thus, neither our nor any other existing approach for targeting T_{regs} through the IL-2 receptors themselves offers superior selectivity against ILC2s.

We again applied nonnegative CP decomposition of the R38Q/H16N and bitargeted ligand signaling responses to summarize our ligand engineering efforts (Fig. 6, I to L). Three components captured >90% of the variation in the data. Here, T_{reg} responses were primarily represented by component 2, T effector cells (T_{eff}s) cell responses by component 1, and NK cell responses by component 3 (Fig. 6J). Valency again determined ligand component 2 weight most potently, with both tetravalent constructs, bitargeted or R38Q/H16N, demonstrating highest component 2 weight. However, whereas the bivalent bitargeted construct demonstrated no NK cell activity (component 3), both tetravalent constructs had some NK activity (Fig. 6K). Thus, our experimental results demonstrate that tradeoffs still exist between T_{reg} potency and selectivity. As before, T_{reg} selectivity was maximized at low and intermediate dosages (Fig. 6L). Despite these tradeoffs, the selectivity demonstrated by both model-guided "cis"-targeting or higher

valency fusion formats greatly improved on the selectivity possible with existing approaches.

DISCUSSION

Here, we systematically explored how ligand properties determine signaling response and specificity across 13 engineered IL-2 variants (Figs. 1 and 2). Our study included clinically relevant muteins alongside variation in Fc fusion format. Dimensionality reduction in tensor form identified how ligand properties alter response, revealing that multivalent cytokines have unique specificity advantages (Fig. 3). Using a multivalent binding model, we uncovered that this unique specificity arises from surface binding avidity effects. Both our analysis using this model and experimental validation indicated that modulating the valency of cytokines may offer T_{reg} selectivity far beyond that achievable through affinity modulation alone (Figs. 4 and 5), and we demonstrated this strategy experimentally by expressing tetravalent IL-2 fusions with greater T_{reg} selectivity than current state-of-the-art monovalent or bivalent affinity muteins. Last, we uncovered that IL2Rα itself is the optimal target for designing T_{reg}-selective binding and that cis-targeting can be designed into multivalent IL-2 fusions through asymmetric tetravalent IL-2 fusions, again improving on signaling selectivity (Fig. 6). In total, our results show that not only do multivalency and cis-targeting of IL2Rα improve T_{reg} selectivity but that these paired strategies represent the only known method for overcoming the selectivity-potency tradeoff faced by T_{reg}-selective muteins (*18*).

Our results have implications for the design of T_{reg}-directed IL-2 therapies, an area of enormous interest for the treatment and management of autoimmune diseases (*22*, *41*). We showed computationally and experimentally that multivalency and bitargeting can enhance IL-2 T_{reg} selectivity for potential use in clinical settings, where IL-2–based therapies have traditionally struggled (*42*). Engineering valency requires precise compensatory adjustments in the ligand affinity; given that we limited our experiments to preexisting muteins, we expect that our selectivity gains might be improved even further by identifying muteins with optimal affinities. Various T_{reg}-selective affinity mutants continue to be published, and many previously developed affinity mutants were not included in our analysis—as we have shown, paired affinity and valency engineering confer selectivity beyond what is achievable in monovalent formats of any affinity; we believe that the approach here will synergize with the continued development of affinity variants (*20*, *27*). Our multivalent and bitargeted designs will additionally need to be tested in vivo to see whether these selectivity gains translate to the in vivo setting (*23*). In the majority of previous studies, the selectivity with which pSTAT5 activity is induced in T_{regs} has consistently translated to selective expansion of T_{regs} in vivo, and thus, we are confident that our mutein's heightened selectivity will translate to such settings (*18*, *21*, *23*, *27*, *43*). T_{reg} selectivity is central to the mechanism of action for these therapies, and so we expect that these benefits to selectivity will improve therapeutic properties in several ways: more potent activation of signaling in T_{regs} without off-target effects may improve the potency of these therapies and the breadth of applications (*18*, *25*, *44*); reduced toxicity may allow for more routine use with minimal patient monitoring (*14*). The superior selectivity offered by engineered multivalent ligands will likely further increase their in vivo pharmacokinetic lifetimes, in turn requiring less frequent dosing, because most drug clearance occurs via receptor-mediated endocytosis in off-target populations (*21*, *27*, *45*, *46*). However, known differences exist in IL-2 receptor expression between humans and mice, so we do not expect that results from murine models would be a reliable indication for the comparative advantages of these molecules (*15*, *16*), and primate studies are outside the scope of the present work.

Heterospecificity, in our case exploited through bitargeting, opens a whole range of new possibilities through its ability to decouple the targeting and signaling properties of cytokine therapy and/or combine synergistic signals. This capability has been demonstrated through bispecific antibodies previously and through the design of cis-targeted cytokine-antibody fusions. However, we showed that, unlike other immune cells, T_{regs} do not express any surface marker more selective than IL2Rα (Fig. 2, I to L). Consequently, there are no alternative targeting options to our approach of using the IL-2 receptors themselves (Fig. 6). Beyond our results, heterospecificity creates opportunities for synergistic receptor agonism. For example, programmed cell death protein 1 (PD-1) cis-targeting with IL-2 increases the stemness of $CD8^+$ T cells and consequently their tumor killing capacity (*47*, *48*). Although IL-2 has been used as a therapy because of its relative T_{reg} selectivity, there is no reason to believe that the cytokine's signaling effects are optimal for enhancing T_{regs}' suppressive activities. With cell therapies where selectivity is not a concern and non-natural cytokine receptors can be introduced, other cytokine signaling such as IL-9 is qualitatively more effective than IL-2 at promoting cytotoxic T cell function (*49*, *50*). Thus, one possibility enabled by bitargeting is potentially plug-and-play combinations of one or more cytokines that are more capable than IL-2 of driving desirable T_{reg} properties and that are made T_{reg}-selective through their fusion to multivalent IL2Rα-targeting complexes (*51*–*53*). More system-level research into the signaling regulation of T_{reg} proliferation and suppressive activities, and comparisons with other cytokines beyond IL-2, is needed to develop these possibilities. Such studies, which will be used to not only identify the optimal signal using functional suppressive assays but also to further improve the selectivity with which that signal is delivered, will justify the translation of such fusion proteins into in vivo disease model studies.

Most generally, our results demonstrate the value of computationally directed biologics design, particularly for fusion constructs incorporating more than one binding moiety. The design of these modular ligands leads to a combinatorial explosion of ligand configurations (*54*). Furthermore, multivalent ligands have several documented effects, including altered signal transduction (*55*, *56*), binding avidity, pharmacokinetics (*57*), and intracellular trafficking (*58*). Although valency has been extensively applied as a means to introduce binding selectivity based on receptor density (*59*, *60*), multiple receptors, ligand subunits with varied targeting, and differences in signaling effects lead to additional complexity. For instance, whereas we found that the contribution of multivalency was explained primarily through avidity effects, bitargeting as a strategy arises through differences in the signaling capacity of IL2Rα versus IL2Rβ. The approach here—computationally designed, multivalent, bitargeted ligands for enhanced therapeutic selectivity—has widespread application to other receptor-ligand pathways, including IL-4/IL-13, bone morphogenic proteins, and the tumor necrosis factor cytokines (*54*, *61*, *62*). There are likely still other design strategies to be found across these many signaling pathway structures.

MATERIALS AND METHODS

Experimental methods

Receptor abundance quantitation, octet binding assays, expression of recombinant bivalent and monovalent IL-2 muteins (Figs. 1 to 4), and measurement of those muteins' signaling in PBMCs were performed as described in (*15*).

Receptor abundance quantitation

Receptor quantitation data were gathered as described previously in (*15*); the preprocessing of fluorescence measurements, population gating, and receptor abundance calculations were performed using these data. To quantify the number of antibodies bound to cells and to standard beads, the fluorescence intensity of isotype controls was subtracted from the signal from matched receptor stains and then calibrated using the two lowest quantitation standards. Cell gating was conducted as shown in fig. S1 (A to H). The geometric means of replicates were calculated to summarize the results.

pSTAT5-based measurement of IL-2 and IL-15 signaling in PBMCs

Cryopreserved PBMCs (American Type Culture Collection, PCS-800-011, lot #81115172) were thawed to room temperature and slowly diluted with 9 ml of prewarmed RPMI 1640 (Corning, 10040CV) supplemented with 10% fetal bovine serum (FBS; VWR, 97068-091, lot# 029K20) and penicillin/streptomycin (Gibco, 15140122). Media were removed, and cells were brought to 3×10^6 cells/ml, distributed at 300,000 cells per well in a 96-well V-bottom plate, and allowed to recover 2 hours at 37°C in an incubator at 5% CO_2. IL-2 (R&D Systems, 202-IL-010) or IL-15 (R&D Systems, 247-ILB-025) were diluted in RPMI 1640 in the absence of FBS. These dilutions were then added to the concentrations indicated. To quantify STAT5 phosphorylation, the media were taken away, and cells were fixed using 100 μl of 10% formalin (Thermo Fisher Scientific, SF100-4) for 15 min at room temperature. Formalin was removed from the cells, and the PBMCs were placed on ice. They were then suspended in 50 μl of cold methanol (−30°C). PBMCs were then kept at −30°C overnight. 0.1% bovine serum albumin (BSA; Sigma-Aldrich, B4287-25G) in PBS (PBSA) was used to wash the cells twice. The cells were then split into two identical plates and stained with fluorescent antibodies for 1 hour at room temperature in darkness using 50 μl of antibody panels 4 and 5 per well. Cells were suspended in 100 μl of PBSA per well and beads to 50 μl and analyzed on an IntelliCyt iQue Screener PLUS with VBR configuration (Sartorius) using a sip time of 35 s and beads 30 s. Compensation of measured fluorescent values was calculated as detailed above. Gating of cell populations was performed as shown in fig. S1, and the median pSTAT5 level was calculated for each population in each well.

Recombinant proteins

The Expi293 expression system was used to express IL-2/Fc fusion proteins. Expression was conducted as prescribed by the manufacturer's instructions (Thermo Fisher Scientific). Proteins were formulated as the Fc of human IgG1 fused at its N or C terminus to human IL-2 using a $(G_4S)_4$ linker. C-terminal lysine residues of human IgG1 were not included in C-terminal fusions. The AviTag sequence GLNDIFEAQKIEWHE was added to the Fc terminus, which did not contain IL-2. Fc mutations that prevented dimerization were introduced into the Fc sequence for monovalent muteins (*63*). MabSelect resin (GE Healthcare) was used to purify protein. Biotinylation of proteins was conducted using BirA enzyme (BPS Biosciences) according to manufacturer's instructions. Extensive buffer exchanging into phosphate-buffered saline (PBS) was conducted using Amicon 10-kDa spin concentrators (EMD Millipore). The sequence that was used to express the IL2Rβ/γ Fc heterodimer was the same as that of a reported, active heterodimeric molecule (patent application US20150218260A1); a $(G_4S)_2$ linker was added between the Fc portion and each receptor ectodomain. The Expi293 system was used to express the protein, which was subsequently purified on MabSelect resin as above. The IL2Rα ectodomain was generated to include a C-terminal 6× His tag and then purified on nickel–nitrilotriacetic acid spin columns (Qiagen) according to manufacturer's instructions.

pSTAT5-based measurement of tetravalent IL-2 signaling in PBMCs

Cryopreserved PBMCs (UCLA Virology Core, sex of donors unknown) were thawed to room temperature and slowly diluted with 9 ml of prewarmed RPMI 1640 (Corning, 10040CV) supplemented with 10% FBS (VWR, 97068-091, lot #029 K20) and penicillin/streptomycin (Gibco, 15140122). Media were removed, and cells were brought to 3×10^6 cells/ml, distributed at 300,000 cells per well in a 96-well V-bottom plate, and allowed to recover 2 hours at 37°C in an incubator at 5% CO_2. IL-2 (Peprotech, 200-02-50 μg) and tetravalent IL-2 (expressed and purified as described below) were diluted in RPMI 1640 without FBS and added to the indicated concentrations. Cells were stained with antibodies from panel 1 described below. To measure pSTAT5, media was removed, and cells were fixed in 100 μl of 4% paraformaldehyde (PFA; Election Microscopy Sciences, 15714) diluted in PBS for 15 min at room temperature.

PFA was removed, and cells were gently suspended in 100 μl of cold methanol (−30°C). Cells were stored overnight at −30°C, then washed twice with PBSA, and stained for 1 hour at room temperature in darkness using antibody panel X with 40 μl per well. Cells were then washed twice with 0.1% PBSA and resuspended in 150 μl of PBSA per well. Cells were analyzed on a BD FACSCelesta flow cytometer. Populations were gated (as shown in fig. S1, A to H), and the median pSTAT5 level was extracted for each population in each well. Wells with fewer than 1000 cells were excluded from analysis (resulted in removal of six wells over five experimental replicates).

Tetravalent IL-2 expression

Proteins were expressed as human IgG1 Fc-fused at the N or C terminus to mutant human IL-2 through a flexible $(G_4S)_4$ linker. C-terminal fusions omitted the C-terminal lysine residue of human IgG1. In monovalent R38Q/H16N variants, Fc mutations to prevent dimerization were introduced into the Fc sequence. In R38Q/H16N variants, each IL-2 fused via the 20–amino acid–long linker to the Fc domain contained R38Q and H16N mutations to reduce the IL-2's affinity with which it binds IL2Rβ. In bitargeted variants, one IL-2 included R38Q/H16N mutations, and the other IL-2 fused to the Fc domain included V91K/D20A/M104V mutations to ablate binding to IL2Rβ. In bivalent bitargeted IL-2, Fc mutations were included to prevent Fc dimerization. Plasmid DNA

prepared by maxi-prep (Qiagen, 12162) was transfected into adherent human embryonic kidney 293 cells using Lipofectamine 3000 (Thermo Fisher Scientific, L3000008) in 15-cm dishes in Dulbecco's modified Eagle's medium (DMEM; Corning, 15017CV) supplemented with GlutaMax (Gibco, 35050061) and 10% FBS. Media were exchanged after 24 hours with fresh DMEM supplemented with GlutaMax and 5% ultra-low IgG FBS (Thermo Fisher Scientific, A3381901). Media were harvested after an additional 72 hours. Media was incubated in the presence of Protein A/G Plus Agarose resin (Santa Cruz Biotechnology, sc-2003) overnight. The following day, the media-resin mixture was centrifuged, and the supernatant was discarded. Resin was washed with PBS five times or until protein was no longer detected in supernatant by ultraviolet-vis using a NanoDrop One Spectrophotometer (Thermo Fisher Scientific, ND-ONE-W). IL-2 was eluted from resin using 0.1 M glycine (pH 2.3) into 2 M tris-HCl (pH 8). IL-2 was then buffer-exchanged into PBS for storage at −80°C. Concentration was determined by BCA assay and confirmed using an IgG1 enzyme-linked immunosorbent assay.

Octet binding assays

An Octet RED384 (ForteBio) was used to measure the binding affinity of each IL-2 mutein. Monomeric, biotintylated IL-2/Fc fusion proteins were loaded to streptavidin biosensors (ForteBio) at roughly 10% of saturation point and allowed to equilibrate for 10 min in PBS + 0.1% BSA. Up to 40 min of association time in IL2Rβ/γ titrated in 2× steps from 400 to 6.25 nM or IL2Rα from 25 nM to 20 pM, which was followed by dissociation in PBS + 0.1% BSA. A zero-concentration sample was included in each measurement and served as a negative control/reference signal. The affinity quantification experiments were performed in quadruplicate across 2 days. Binding of IL-2 to IL2Rα on its own did not fit to a simple binding model; the dissociation constant (K_D) was calculated using equilibrium binding within each assay for this case. IL2Rβ/γ binding data fit a 1:1 binding model; thus, in these cases, on-rate (k_{on}), off-rate (k_{off}), and K_D were determined by fitting to the entire binding curve. The average of each kinetic parameter across all concentrations with detectable binding (typically 12.5 nM and above) was used to calculate K_D.

CD25 measurement in T_{regs} and ILC2s

Cryopreserved PBMCs (UCLA Virology Core, sex of donors unknown) from each donor were thawed to room temperature and slowly diluted with 9 ml of prewarmed RPMI 1640 (Corning, 10040CV) supplemented with 10% FBS (VWR, 97068-091, lot #029 K20) and penicillin/streptomycin (Gibco, 15140122). Media were then removed, and PBMCs were washed with ice-cold 1% BSA (Sigma-Aldrich, B4287-25G) in PBS (PBSA). PBMCs were then stained for 1 hour at 4°C in a cocktail of anti-lineage fluorescein isothiocyanate (FITC; Invitrogen, 22-7778-72), anti-FcεR1 FITC (BioLegend, 334608), anti-CD25 APC/Fire 810 (BioLegend, 356150), anti-CD127 Brilliant Violet 421 (BioLegend, 351310), and anti-CRTH2 Brilliant Violet 605 (BioLegend, 350122) (panel 2 below), all at a dilution of 1:20 in PBSA except for the anti-lineage antibody, which was diluted 1:10. Cells were then washed once with cold PBSA and once with cold PBS and then fixed in 2% PFA at room temperature for 15 min. PFA (Election Microscopy Sciences, 15714) was diluted in PBS for 15 min at room temperature. PFA was then removed, and cells were washed once with PBS. Cells were then resuspended in ice-cold methanol and incubated on ice for 30 min. Cells were then washed with PBS and resuspended in anti-Foxp3 Alexa Fluor 647 (BioLegend, 320114) diluted 1:20 in PBSA for 1 hour. Cells were then washed twice with PBSA before being resuspended in PBSA for analysis on a BD FACSCelesta flow cytometer. Populations were gated as shown in supplementary figures, and the median IL2Rα abundance was extracted for each population.

Statistical analysis

The number of replicates performed for each experimental measurement and the values of confidence intervals are described in corresponding figure captions. N is used to describe the number of times a particular experiment was performed. Flow cytometry experiments performed using the initial panel of monovalent and bivalent cytokines (Figs. 1 to 4) were performed on human peripheral blood mononuclear cells (hPBMCs) and were conducted using separate experimental replicates on cells gathered from a single donor. Each replicate of the flow cytometry signaling experiments in Figs. 5 and 6 was conducted using hPBMCs from different donors. To quantify population-level flow cytometry measurements for both signaling and receptor quantitation experiments, the mean fluorescent intensity of a gated population was measured. Compensation to remove fluorescent spectral overlap was performed for each experimental measurement. Subtraction of either negative controls or cells treated with isotype antibodies was performed on signaling and receptor quantitation data, respectively, to remove background signal. Cells that were measured to display fluorescent intensities above 1,000,000 were excluded from analysis during signaling experiments. Pearson correlation coefficients (R^2) values were used to describe model accuracy when predicting signaling response to IL-2 and IL-2 muteins. The K_x^* parameter was fit with least-squares fitting using the Broyden-Fletcher-Goldfarb-Shanno minimization algorithm as implemented in SciPy.

Antibodies

Antibodies (listed in table S4) used to quantify receptor abundances, as well as to perform initial pSTAT5 response quantification in PBMCs, can be found in (*15*).

Newly created materials

All novel IL-2 muteins were synthesized as described above and contained the mutations as described above. No restrictions on access to these materials are noted.

Binding model

The model was formulated as described in (*35*). The monomer composition of a ligand complex was represented by a vector $\boldsymbol{\theta} = (\theta_1, \theta_2, ..., \theta_{N_L})$, where each θ_i was the fraction of monomer ligand type i out of all monomers on that complex. Let $C_{\boldsymbol{\theta}}$ be the proportion of the $\boldsymbol{\theta}$ complexes in all ligand complexes and Θ be the set of all possible $\boldsymbol{\theta}'$s. $\sum_{\theta \in \Theta} C_\theta = 1$.

The binding between a ligand complex and a cell expressing several types of receptors can be represented by a series of q_{ij}. The relationship between q_{ij}'s and θ_i is given by $\theta_i = q_{i0} + q_{i1} + ... + q_{iN_R}$. Let the vector $\mathbf{q}_i = (q_{i0}, q_{i1}, ..., q_{iN_R})$ and the corresponding $\boldsymbol{\theta}$ of a binding configuration $\mathbf{q}$ be $\boldsymbol{\theta}(\mathbf{q})$. For all i in $\{1,2, ..., N_L\}$, we define $\psi_{ij} = R_{eq,j} K_{a,ij} K_x^*$ where $j = \{1,2, ..., N_R\}$ and $\psi_{i0} = 1$. The relative number of complexes bound to a cell with configuration $\mathbf{q}$ at

equilibrium is

$$v_{\boldsymbol{q},eq} = \frac{L_0 C_{\theta(\boldsymbol{q})}}{K_x^*} \prod_{\substack{i=1 \\ j=0}}^{\substack{i=N_L \\ j=N_R}} \psi_{ij}^{q_{ij}} \prod_{i=1}^{N_L} \binom{\theta_i}{\boldsymbol{q}_i}$$

Then we can calculate the relative amount of bound receptor n as

$$R_{\text{bound},n} = \frac{L_0}{K_x^*} \sum_{\theta \in \Theta} C_\theta \left[\sum_{i=1}^{N_L} \frac{\psi_{in} \theta_i}{\sum_{j=0}^{N_R} \psi_{ij}} \right] \prod_{i=1}^{N_L} \left(\sum_{j=0}^{N_R} \psi_{ij} \right)^{\theta_i}$$

By mass conservation, ($R_{\text{tot},\,n} = R_{\text{eq},\,n} + R_{\text{bound},\,n}$), we can solve $R_{\text{eq},\,n}$ numerically for each type of receptor.

Application of multivalent binding model to IL-2 signaling pathway

Each IL-2 molecule was allowed to bind to one free IL2Rα and one IL2Rβ/γ_c receptor. Initial IL-2–receptor association proceeded with the known kinetics of monomeric ligand-receptor interaction (table S1). Subsequent ligand-receptor binding interactions then proceeded with an association constant proportional to available receptor abundance and affinity multiplied by the scaling constant, K_x^*, as described above. To predict the pSTAT5 response to IL-2 stimulation, we assumed that pSTAT5 is proportional to the amount of IL-2–bound IL2Rβ/γ_c, because complexes that contain these species actively signal through the JAK/STAT pathway. Scaling factors converting from predicted active signaling species to pSTAT5 abundance were fit to experimental data on a per-experiment and cell type basis. A single K_x^* value was fit for all experiments and cell types.

CITE-seq marker selectivity analysis

To assist in identifying possible markers to increase IL-2 selectivity toward T_{regs}, a publicly available CITE-seq dataset containing data gathered from human PBMCs was analyzed (*31*). Only RNA transcripts encoding cell membrane extracellular-facing proteins were included. We first analyzed the data by determining the Wasserstein distance and Kullback-Leibler divergence of markers and RNA measured in T_{regs} against the distribution of these markers displayed by all other cells. We also analyzed the data using a ridge classification model, where all markers and RNA sequences were used by the model to distinguish between T_{regs} and all other cell types.

Markers of interest were then used in conjunction with the binding model to determine whether they could confer selectivity, using the CITE-seq data to inform the number of markers per cell. Conversion factors for calculating marker abundance from CITE-seq marker and mRNA reads were estimated using proportional conversions from the data to previously experimentally determined marker abundances (*15*). Single-cell marker abundances were calculated for 1000 cells at a time, and the ratio of T_{reg} signaling to off-target signaling was calculated. To simulate bispecific binding, two distinct binding domains for each ligand were modeled, one for IL-2, with affinity for IL2Rα and IL2Rβ/γ_c, and the other for the marker of interest. The ligand affinities were varied while defining selectivity as the summed T_{reg} signaling divided by the signaling across all off-target cell populations. After finding IL2Rα to be the optimal epitope for increasing selectivity, we sought to explore the effects of increasing valency by doubling the number of binding domains per ligand.

Tensor factorization

Before decomposition, the signaling response data were background-subtracted and variance-scaled across each cell population. Nonnegative CP decomposition was performed using the Python package TensorLy and using the HALS algorithm with nonnegative SVD initialization (*64*).

Supplementary Materials

This PDF file includes:
Figs. S1 to S9
Tables S1 to S4

Other Supplementary Material for this manuscript includes the following:
MDAR Reproducibility Checklist

REFERENCES AND NOTES

1. W. J. Leonard, J.-X. Lin, J. J. O'Shea, The γ_c family of cytokines: Basic biology to therapeutic Ramifications. *Immunity* **50**, 832–850 (2019).
2. M. L. Janas, P. Groves, N. Kienzle, A. Kelso, IL-2 regulates perforin and granzyme gene expression in CD8$^+$ T cells independently of its effects on survival and proliferation. *J. Immunol.* **175**, 8003–8010 (2005).
3. T. Chinen, A. K. Kannan, A. G. Levine, X. Fan, U. Klein, Y. Zheng, G. Gasteiger, Y. Feng, J. D. Fontenot, A. Y. Rudensky, An essential role for the IL-2 receptor in T_{reg} cell function. *Nat. Immunol.* **17**, 1322–1333 (2016).
4. M. Y. Fan, J. S. Low, N. Tanimine, K. K. Finn, B. Priyadharshini, S. K. Germana, S. M. Kaech, L. A. Turka, Differential roles of IL-2 signaling in developing versus mature Tregs. *Cell Rep.* **25**, 1204–1213.e4 (2018).
5. M. Noguchi, H. Yi, H. M. Rosenblatt, A. H. Filipovich, S. Adelstein, S. S. Modi II, O. W. McBride, W. J. Leonard, Interleukin-2 receptor γ chain mutation results in X-linked severe combined immunodeficiency in humans. *Cell* **73**, 147–157 (1993).
6. P. P. Zenatti, D. Ribeiro, W. Li, L. Zuurbier, M. C. Silva, M. Paganin, J. Tritapoe, J. A. Hixon, A. B. Silveira, B. A. Cardoso, L. M. Sarmento, N. Correia, M. L. Toribio, J. Kobarg, M. Horstmann, R. Pieters, S. R. Brandalise, A. A. Ferrando, J. P. Meijerink, S. K. Durum, J. A. Yunes, J. T. Barata, Oncogenic *IL7R* gain-of-function mutations in childhood T-cell acute lymphoblastic leukemia. *Nat. Genet.* **43**, 932–939 (2011).
7. C. J. Dwyer, H. M. Knochelmann, A. S. Smith, M. M. Wyatt, G. O. R. Rivera, D. C. Arhontoulis, E. Bartee, Z. Li, M. P. Rubinstein, C. M. Paulos, Fueling cancer immunotherapy with common gamma chain cytokines. *Front. Immunol.* **10**, 263 (2019).
8. A. K. Abbas, E. Trotta, D. R. Simeonov, A. Marson, J. A. Bluestone, Revisiting IL-2: Biology and therapeutic prospects. *Sci. Immunol.* **3**, eaat1482 (2018).
9. H. Choudhry, N. Helmi, W. H. Abdulaal, M. Zeyadi, M. A. Zamzami, W. Wu, M. M. Mahmoud, M. K. Warsi, M. Rasool, M. S. Jamal, Prospects of IL-2 in cancer immunotherapy. *Biomed. Res. Int.* **2018**, e9056173 (2018).
10. M. Tahvildari, R. Dana, Low-dose IL-2 therapy in transplantation, autoimmunity, and inflammatory diseases. *J. Immunol.* **203**, 2749–2755 (2019).
11. R. Spolski, P. Li, W. J. Leonard, Biology and regulation of IL-2: From molecular mechanisms to human therapy. *Nat. Rev. Immunol.* **18**, 648–659 (2018).
12. J. Koreth, K.-I. Matsuoka, H. T. Kim, S. M. McDonough, B. Bindra, E. P. Alyea III, P. Armand, C. Cutler, V. T. Ho, N. S. Treister, D. C. Bienfang, S. Prasad, D. Tzachanis, R. M. Joyce, D. E. Avigan, J. H. Antin, J. Ritz, R. J. Soiffer, Interleukin-2 and regulatory T cells in graft-versus-host disease. *N. Engl. J. Med.* **365**, 2055–2066 (2011).
13. D. Saadoun, M. Rosenzwajg, F. Joly, A. Six, F. Carrat, V. Thibault, D. Sene, P. Cacoub, D. Klatzmann, Regulatory T-cell responses to low-dose interleukin-2 in HCV-induced vasculitis. *N. Engl. J. Med.* **365**, 2067–2077 (2011).
14. C. Krieg, S. Létourneau, G. Pantaleo, O. Boyman, Improved IL-2 immunotherapy by selective stimulation of IL-2 receptors on lymphocytes and endothelial cells. *Proc. Natl. Acad. Sci. U.S.A.* **107**, 11906–11911 (2010).

15. A. M. Farhat, A. C. Weiner, C. Posner, Z. S. Kim, B. Orcutt-Jahns, S. M. Carlson, A. S. Meyer, Modeling cell-specific dynamics and regulation of the common gamma chain cytokines. *Cell Rep.* **35**, 109044 (2021).
16. P. Gonnord, B. R. Angermann, K. Sadtler, E. Gombos, P. Chappert, M. Meier-Schellersheim, R. Varma, A hierarchy of affinities between cytokine receptors and the common gamma chain leads to pathway cross-talk. *Sci. Signal.* **11**, eaal1253 (2018).
17. S. Mitra, W. J. Leonard, Biology of IL-2 and its therapeutic modulation: Mechanisms and strategies. *J. Leukoc. Biol.* **103**, 643–655 (2018).
18. D. VanDyke, M. Iglesias, J. Tomala, A. Young, J. Smith, J. A. Perry, E. Gebara, A. R. Cross, L. S. Cheung, A. G. Dykema, B. T. Orcutt-Jahns, T. Henclová, J. Golias, J. Balolong, L. M. Tomasovic, D. Funda, A. S. Meyer, D. M. Pardoll, J. Hester, F. Issa, C. A. Hunter, M. S. Anderson, J. A. Bluestone, G. Raimondi, J. B. Spangler, Engineered human cytokine/antibody fusion proteins expand regulatory T cells and confer autoimmune disease protection. *Cell Rep.* **41**, 111478 (2022).
19. D.-A. Silva, S. Yu, U. Y. Ulge, J. B. Spangler, K. M. Jude, C. Labão-Almeida, L. R. Ali, A. Quijano-Rubio, M. Ruterbusch, I. Leung, T. Biary, S. J. Crowley, E. Marcos, C. D. Walkey, B. D. Weitzner, F. Pardo-Avila, J. Castellanos, L. Carter, L. Stewart, S. R. Riddell, M. Pepper, G. J. L. Bernardes, M. Dougan, K. C. Garcia, D. Baker, De novo design of potent and selective mimics of IL-2 and IL-15. *Nature* **565**, 186–191 (2019).
20. L. Khoryati, M. N. Pham, M. K. Sherve, S. Kumari, K. Cook, J. Pearson, M. Bogdani, D. J. Campbell, M. A. Gavin, An IL-2 mutein engineered to promote expansion of regulatory T cells arrests ongoing autoimmunity in mice. *Sci Immunol.* **5**, eaba5264 (2020).
21. C. J. M. Bell, Y. Sun, U. M. Nowak, J. Clark, S. Howlett, M. L. Pekalski, X. Yang, O. Ast, I. Waldhauer, A. Freimoser-Grundschober, E. Moessner, P. Umana, C. Klein, R. J. Hosse, L. S. Wicker, L. B. Peterson, Sustained in vivo signaling by long-lived IL-2 induces prolonged increases of regulatory T cells. *J. Autoimmun.* **56**, 66–80 (2015).
22. L. B. Peterson, C. J. M. Bell, S. K. Howlett, M. L. Pekalski, K. Brady, H. Hinton, D. Sauter, J. A. Todd, P. Umana, O. Ast, I. Waldhauer, A. Freimoser-Grundschober, E. Moessner, C. Klein, R. J. Hosse, L. S. Wicker, A long-lived IL-2 mutein that selectively activates and expands regulatory T cells as a therapy for autoimmune disease. *J. Autoimmun.* **95**, 1–14 (2018).
23. A. Ghelani, D. Bates, K. Conner, M.-Z. Wu, J. Lu, Y.-L. Hu, C.-M. Li, A. Chaudhry, S. J. Sohn, Defining the threshold IL-2 signal required for induction of selective Treg cell responses using engineered IL-2 muteins. *Front. Immunol.* **11**, 1106 (2020).
24. K. Moynihan, D. Pappas, T. Park, W. Chen, I. Ni, P. Bessette, M. Chin, T. Schumacher, A. Yeung, I. Djuretic, 717 Selective activation of CD8+ T cells by a CD8-targeted IL-2 results in enhanced anti-tumor efficacy and safety. *J. Immunother. Cancer* **9**, 10.1136/jitc-2021-SITC2021.717, (2021).
25. T. Hirai, T. L. Ramos, P.-Y. Lin, F. Simonetta, L. L. Su, L. K. Picton, J. Baker, J.-X. Lin, P. Li, K. Seo, J. K. Lohmeyer, S. Bolivar-Wagers, M. Mavers, W. J. Leonard, B. R. Blazar, K. C. Garcia, R. S. Negrin, Selective expansion of regulatory T cells using an orthogonal IL-2/IL-2 receptor system facilitates transplantation tolerance. *J. Clin. Invest.* **131**, e139991 (2021).
26. S. Mitra, A. M. Ring, S. Amarnath, J. B. Spangler, P. Li, W. Ju, S. Fischer, J. Oh, R. Spolski, K. Weiskopf, H. Kohrt, J. E. Foley, S. Rajagopalan, E. O. Long, D. H. Fowler, T. A. Waldmann, K. C. Garcia, W. J. Leonard, Interleukin-2 activity can be fine tuned with engineered receptor signaling clamps. *Immunity* **42**, 826–838 (2015).
27. S. de Picciotto, N. DeVita, C. J. Hsiao, C. Honan, S.-W. Tse, M. Nguyen, J. D. Ferrari, W. Zheng, B. T. Wipke, E. Huang, Selective activation and expansion of regulatory T cells using lipid encapsulated mRNA encoding a long-acting IL-2 mutein. *Nat. Commun.* **13**, 3866 (2022).
28. O. Feinerman, G. Jentsch, K. E. Tkach, J. W. Coward, M. M. Hathorn, M. W. Sneddon, T. Emonet, K. A. Smith, G. Altan-Bonnet, Single-cell quantification of IL-2 response by effector and regulatory T cells reveals critical plasticity in immune response. *Mol. Syst. Biol.* **6**, 437 (2010).
29. J. W. Lowenthal, H. R. M. Donald, B. J. Iacopetta, Intracellular pathway of interleukin 2 following receptor-mediated endocytosis. *Eur. J. Immunol.* **16**, 1461–1463 (1986).
30. D. Klatzmann, A. K. Abbas, The promise of low-dose interleukin-2 therapy for autoimmune and inflammatory diseases. *Nat. Rev. Immunol.* **15**, 283–294 (2015).
31. Y. Hao, S. Hao, E. Andersen-Nissen, W. M. Mauck III, S. Zheng, A. Butler, M. J. Lee, A. J. Wilk, C. Darby, M. Zager, P. Hoffman, M. Stoeckius, E. Papalexi, E. P. Mimitou, J. Jain, A. Srivastava, T. Stuart, L. M. Fleming, B. Yeung, A. J. Rogers, J. M. McElrath, C. A. Blish, R. Gottardo, P. Smibert, R. Satija, Integrated analysis of multimodal single-cell data. *Cell* **184**, 3573–3587.e29 (2021).
32. Z. C. Tan, B. T. Orcutt-Jahns, A. S. Meyer, A quantitative view of strategies to engineer cell-selective ligand binding. *Integr. Biol.* **13**, 269–282 (2021).
33. Z. C. Tan, M. C. Murphy, H. S. Alpay, S. D. Taylor, A. S. Meyer, Tensor-structured decomposition improves systems serology analysis. *Mol. Syst. Biol.* **17**, e10243 (2021).
34. T. G. Kolda, B. W. Bader, Tensor Decompositions and Applications. *SIAM Rev.* **51**, 455–500 (2009).
35. Z. C. Tan, A. S. Meyer, A general model of multivalent binding with ligands of heterotypic subunits and multiple surface receptors. *Math. Biosci.* **342**, 108714 (2021).
36. R. A. Robinett, N. Guan, A. Lux, M. Biburger, F. Nimmerjahn, A. S. Meyer, Dissecting FcγR regulation through a multivalent binding model. *Cell Syst.* **7**, 41–48.e5 (2018).
37. A. S. Perelson, C. DeLisi, Receptor clustering on a cell surface. I. Theory of receptor cross-linking by ligands bearing two chemically identical functional groups. *Math. Biosci.* **48**, 71–110 (1980).
38. J. D. Stone, J. R. Cochran, L. J. Stern, T-cell activation by soluble MHC oligomers can be described by a two-parameter binding model. *Biophys. J.* **81**, 2547–2557 (2001).
39. S. D. Voss, R. J. Robb, G. Weil-Hillman, J. A. Hank, K. Sugamura, M. Tsudo, P. M. Sondel, Increased expression of the interleukin 2 (IL-2) receptor beta chain (p70) on CD56+ natural killer cells after in vivo IL-2 therapy: P70 expression does not alone predict the level of intermediate affinity IL-2 binding. *J. Exp. Med.* **172**, 1101–1114 (1990).
40. Y. Mazor, K. F. Sachsenmeier, C. Yang, A. Hansen, J. Filderman, K. Mulgrew, H. Wu, W. F. Dall'Acqua, Enhanced tumor-targeting selectivity by modulating bispecific antibody binding affinity and format valence. *Sci. Rep.* **7**, 40098 (2017).
41. C. Ye, D. Brand, S. G. Zheng, Targeting IL-2: An unexpected effect in treating immunological diseases. *Signal Transduct. Target. Ther.* **3**, 2 (2018).
42. J. P. Siegel, R. K. Puri, Interleukin-2 toxicity. *J. Clin. Oncol.* **9**, 694–704 (1991).
43. N. Tchao, K. S. Gorski, T. Yuraszeck, S. J. Sohn, K. Ishida, H. Wong, K. Park, Amg 592 is an investigational IL-2 mutein that induces highly selective expansion of regulatory T cells. *Blood* **130**, 696 (2017).
44. L. E. Buitrago-Molina, J. Pietrek, F. Noyan, J. Schlue, M. P. Manns, H. Wedemeyer, M. Hardtke-Wolenski, E. Jaeckel, Treg-specific IL-2 therapy can reestablish intrahepatic immune regulation in autoimmune hepatitis. *J. Autoimmun.* **117**, 102591 (2021).
45. A. Carr, S. Emery, A. Lloyd, J. Hoy, R. Garsia, M. French, G. Stewart, G. Fyfe, D. A. Cooper, Outpatient continuous intravenous interleukin-2 or subcutaneous, polyethylene glycol-modified interleukin-2 in human immunodeficiency virus-infected patients: A randomized, controlled, multicenter study. Australian IL-2 Study Group. *J. Infect. Dis.* **178**, 992–999 (1998).
46. M. J. Bernett, R. Varma, C. Bonzon, L. Bogaert, R. Rashid, K. Liu, I. W. L. Leung, S. Schubbert, S.-H. Lee, D. C. Kirouac, F. Hua, N. Rodriguez, Y. Kim, K. N. Avery, C. Ardila, N. Hassanzadeh-Kiabi, U. S. Muchhal, S. Y. Chu, G. L. Moore, J. R. Desjarlais, "An IL15/IL15Rα heterodimeric Fc-fusion engineered for reduced potency demonstrates an optimal balance of in vivo activity and exposure," Poster. (2018); https://investors.xencor.com/static-files/1a80b800-5bba-441e-8955-e95dec573d65.
47. M. Hashimoto, K. Araki, M. A. Cardenas, P. Li, R. R. Jadhav, H. T. Kissick, W. H. Hudson, D. J. McGuire, R. C. Obeng, A. Wieland, J. Lee, D. T. McManus, J. L. Ross, S. J. Im, J. Lee, J.-X. Lin, B. Hu, E. E. West, C. D. Scharer, G. J. Freeman, A. H. Sharpe, S. S. Ramalingam, A. Pellerin, V. Teichgräber, W. J. Greenleaf, C. Klein, J. J. Goronzy, P. Umaña, W. J. Leonard, K. A. Smith, R. Ahmed, PD-1 combination therapy with IL-2 modifies $CD8^+$ T cell exhaustion program. *Nature* **610**, 173–181 (2022).
48. L. C. Deak, V. Nicolini, M. Hashimoto, M. Karagianni, P. C. Schwalie, L. Lauener, E. M. Varypataki, M. Richard, E. Bommer, J. Sam, S. Joller, M. Perro, F. Cremasco, L. Kunz, E. Yanguez, T. Hüsser, R. Schlenker, M. Mariani, V. Tosevski, S. Herter, M. Bacac, I. Waldhauer, S. Colombetti, X. Gueripel, S. Wullschleger, M. Tichet, D. Hanahan, H. T. Kissick, S. Leclair, A. Freimoser-Grundschober, S. Seeber, V. Teichgräber, R. Ahmed, C. Klein, P. Umaña, PD-1-cis IL-2R agonism yields better effectors from stem-like CD8+ T cells. *Nature* **610**, 161–172 (2022).
49. A. Kalbasi, M. Siurala, L. L. Su, M. Tariveranmoshabad, L. K. Picton, P. Ravikumar, P. Li, J.-X. Lin, H. Escuin-Ordinas, T. Da, S. V. Kremer, A. L. Sun, S. Castelli, S. Agarwal, J. Scholler, D. Song, P. C. Rommel, E. Radaelli, R. M. Young, W. J. Leonard, A. Ribas, C. H. June, K. C. Garcia, Potentiating adoptive cell therapy using synthetic IL-9 receptors. *Nature* **607**, 360–365 (2022).
50. F. Mo, Z. Yu, P. Li, J. Oh, R. Spolski, L. Zhao, C. R. Glassman, T. N. Yamamoto, Y. Chen, F. M. Golebiowski, D. Hermans, S. Majri-Morrison, L. K. Picton, W. Liao, M. Ren, X. Zhuang, S. Mitra, J.-X. Lin, L. Gattinoni, J. D. Powell, N. P. Restifo, K. C. Garcia, W. J. Leonard, An engineered IL-2 partial agonist promotes $CD8^+$ T cell stemness. *Nature* **597**, 544–548 (2021).
51. W. Elyaman, E. M. Bradshaw, C. Uyttenhove, V. Dardalhon, A. Awasthi, J. Imitola, E. Bettelli, M. Oukka, J. van Snick, J.-C. Renauld, V. K. Kuchroo, S. J. Khoury, IL-9 induces differentiation of T_H17 cells and enhances function of $FoxP3^+$ natural regulatory T cells. *Proc. Natl. Acad. Sci. U.S.A.* **106**, 12885–12890 (2009).
52. D. M. W. Zaiss, J. van Loosdregt, A. Gorlani, C. P. J. Bekker, A. Gröne, M. Sibilia, P. M. P. van Bergen en Henegouwen, R. C. Roovers, P. J. Coffer, A. J. A. M. Sijts, Amphiregulin enhances regulatory T cell-suppressive function via the epidermal growth factor receptor. *Immunity* **38**, 275–284 (2013).
53. J. C. Marie, J. J. Letterio, M. Gavin, A. Y. Rudensky, TGF-β1 maintains suppressor function and Foxp3 expression in $CD4^+CD25^+$ regulatory T cells. *J. Exp. Med.* **201**, 1061–1067 (2005).
54. Y. E. Antebi, J. M. Linton, H. Klumpe, B. Bintu, M. Gong, C. Su, R. M. Cardell, M. B. Elowitz, Combinatorial signal perception in the BMP pathway. *Cell* **170**, 1184–1196.e24 (2017).

55. L. L. Kiessling, J. E. Gestwicki, L. E. Strong, Synthetic multivalent ligands as probes of signal transduction. *Angew. Chem. Int. Ed.* **45**, 2348–2368 (2006).
56. I. Moraga, J. B. Spangler, J. L. Mendoza, M. Gakovic, T. S. Wehrman, P. Krutzik, K. C. Garcia, Synthekines are surrogate cytokine and growth factor agonists that compel signaling through non-natural receptor dimers. *eLife* **6**, e22882 (2017).
57. A. M. Cuesta, N. Sainz-Pastor, J. Bonet, B. Oliva, L. Alvarez-Vallina, Multivalent antibodies: When design surpasses evolution. *Trends Biotechnol.* **28**, 355–362 (2010).
58. S. J. York, L. S. Arneson, W. T. Gregory, N. M. Dahms, S. Kornfeld, The rate of internalization of the mannose 6-phosphate/insulin-like growth factor II receptor is enhanced by multivalent ligand binding. *J. Biol. Chem.* **274**, 1164–1171 (1999).
59. C. M. Csizmar, J. R. Petersburg, T. J. Perry, L. Rozumalski, B. J. Hackel, C. R. Wagner, Multivalent ligand binding to cell membrane antigens: Defining the interplay of affinity, valency, and expression density. *J. Am. Chem. Soc.* **141**, 251–261 (2019).
60. C. B. Carlson, P. Mowery, R. M. Owen, E. C. Dykhuizen, L. L. Kiessling, Selective tumor cell targeting using low-affinity, multivalent interactions. *ACS Chem. Biol.* **2**, 119–127 (2007).
61. A. E. Kelly-Welch, E. M. Hanson, M. R. Boothby, A. D. Keegan, Interleukin-4 and interleukin-13 signaling connections maps. *Science* **300**, 1527–1528 (2003).
62. G. A. Efimov, A. A. Kruglov, Z. V. Khlopchatnikova, F. N. Rozov, V. V. Mokhonov, S. Rose-John, J. Scheller, S. Gordon, M. Stacey, M. S. Drutskaya, S. V. Tillib, S. A. Nedospasov, Cell-type-restricted anti-cytokine therapy: TNF inhibition from one pathogenic source. *Proc. Natl. Acad. Sci. U.S.A.* **113**, 3006–3011 (2016).
63. T. Ishino, M. Wang, L. Mosyak, A. Tam, W. Duan, K. Svenson, A. Joyce, D. M. O'Hara, L. Lin, W. S. Somers, R. Kriz, Engineering a monomeric Fc domain modality by N-glycosylation for the half-life extension of biotherapeutics. *J. Biol. Chem.* **288**, 16529–16537 (2013).
64. J. Kossaifi, Y. Panagakis, A. Anandkumar, M. Pantic, TensorLy: Tensor Learning in Python. arXiv:1610.09555 [cs] (2018).

Acknowledgments: We thank C. Posner for contributing to initial profiling studies that enabled the study. **Funding:** This work was partly supported by startup funds from UCLA Engineering and by NIH U01-AI148119 to A.S.M. **Author contributions:** A.S.M. conceived of the study. A.S.M., B.O.-J., E.M.S., and P.C.E. performed the computational analysis. S.D.T. performed the PBMC experiments with the IL-2 fusion proteins. All authors helped to design experiments and/or analyze the data. All authors contributed to writing the paper. **Competing interests:** A.S.M. has filed a patent PCT/US22/35711 on the use of multivalent cytokines to enhance cell type–selective responses. A.S.M., B.O.-J., and P.C.E. have filed a provisional patent on the use of bitargeting for engineered cytokine responses. All other authors declare that they have no competing interests. **Data and materials availability:** All analyses were implemented in Python v3.10 and can be found at https://doi.org/10.5281/zenodo.8322891, along with all the experimental data. All other data needed to evaluate the conclusions in the paper are present in the paper or the Supplementary Materials.

Submitted 5 December 2022
Resubmitted 26 April 2023
Accepted 21 September 2023
Published 17 October 2023
10.1126/scisignal.adg0699

Science Signaling
AAAS

Supplementary Materials for

Multivalent, asymmetric IL-2-Fc fusions show enhanced selectivity for regulatory T cells

Brian Orcutt-Jahns *et al.*

Corresponding author: Aaron S. Meyer, ameyer@asmlab.org

Sci. Signal. **16**, eadg0699 (2023)
DOI: 10.1126/scisignal.adg0699

The PDF file includes:

Figs. S1 to S9
Tables S1 to S4

Other Supplementary Material for this manuscript includes the following:

MDAR Reproducibility Checklist

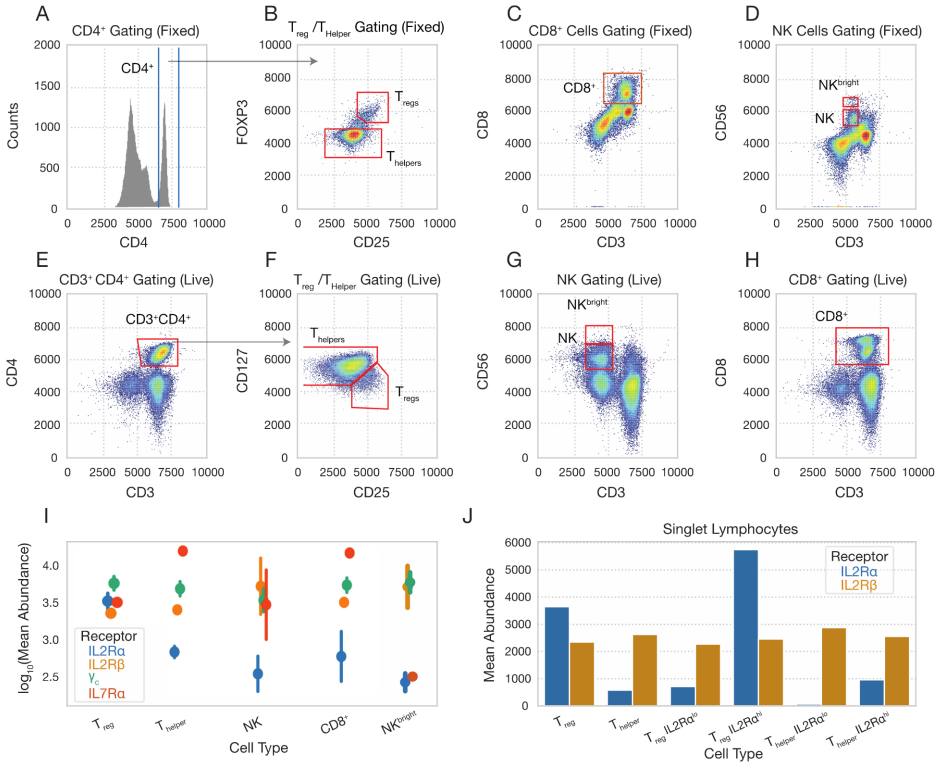

Figure S1: Receptor quantification and gating of PBMC-derived immune cell types. (A and B) Gating for fixed T_{helper} and T_{reg} cells from donor PBMCs during pSTAT5 quantification. **(C and D)** Fixed CD8+ T cell and NK cell gating. **(E and F)** Gating for live T_{helper} and T_{reg} cells during receptor quantification. **(G)** Live cell NK and NK^{bright} cell gating. **(H)** Live cell CD8+ cell gating. **(I)** Receptor quantification for each cell type described in (A to H). Experiments in (A to I) were performed using PBMCs from a human donorand represent 4 experiments. **(J)** IL2Rα and IL2Rβ abundances on IL-2Rα high and low T_{reg} and T_{helper} populations. Cells were binned using three evenly logarithmically spaced separations between 5^{th} and 95^{th} percentile of IL-2Rα abundance.

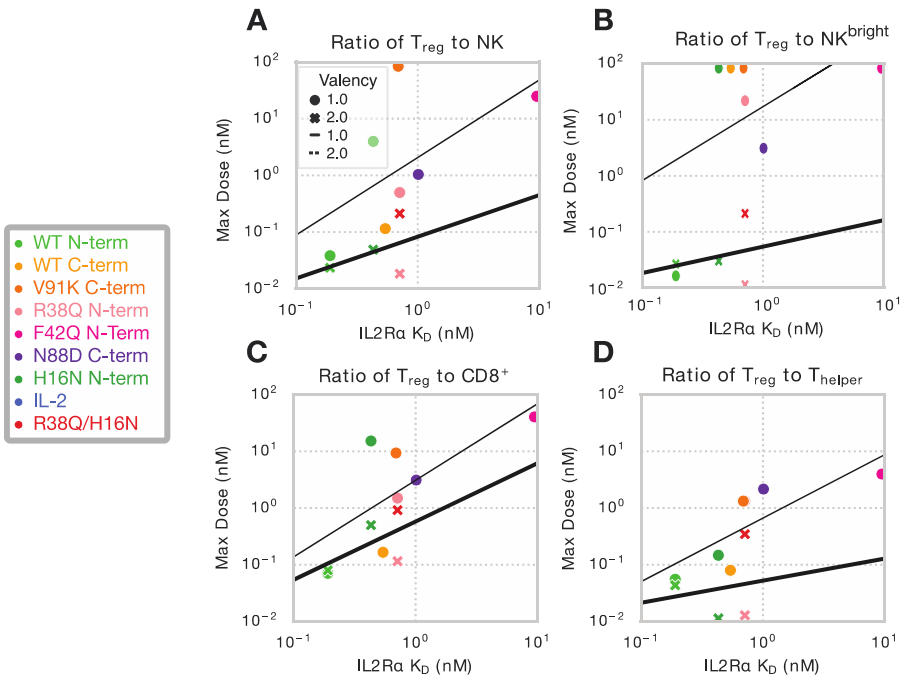

Figure S2: Concentration of optimum ligand selectivity is a function of IL2Rα affinity. (A to D) Location of the concentration at which the ratio of T_{reg} to NK (A), NK^{bright} (B) $CD8^+$ (C), and T_{helper} (D) cell activity, assessed as pSTAT5 abundance, is maximized vs. IL2Rα affinity. Lines were fit to monovalent (thin) and bivalent (thick). Ratios were measured using cells from a human donor, and signaling data represent 3 experiments. Affinity of IL-2 mutants was measured using biolayer interferometry and represent 2 experiments.

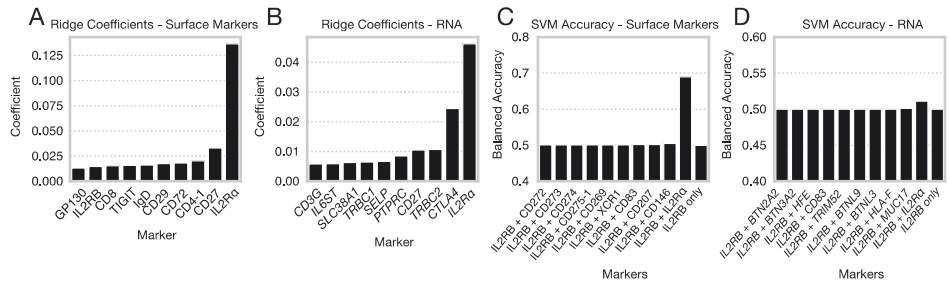

Figure S3: Linear and non-linear classification algorithms identify IL2Rα as the most unique marker on T_{reg} cells. (A and B) Largest marker coefficients determined by fitting a RIDGE-classifier to previously published CITE-seq surface marker data (A) and mRNA data (B) (GSE164378). Model was fit to identify T_{reg}s using a one-vs.-all approach. **(C and D)** Largest T_{reg} identification accuracies of Support Vector Classifier fit using IL2Rβ and one other marker using surface marker (C) and RNA (D) data. Accuracy is reported as Balanced Accuracy.

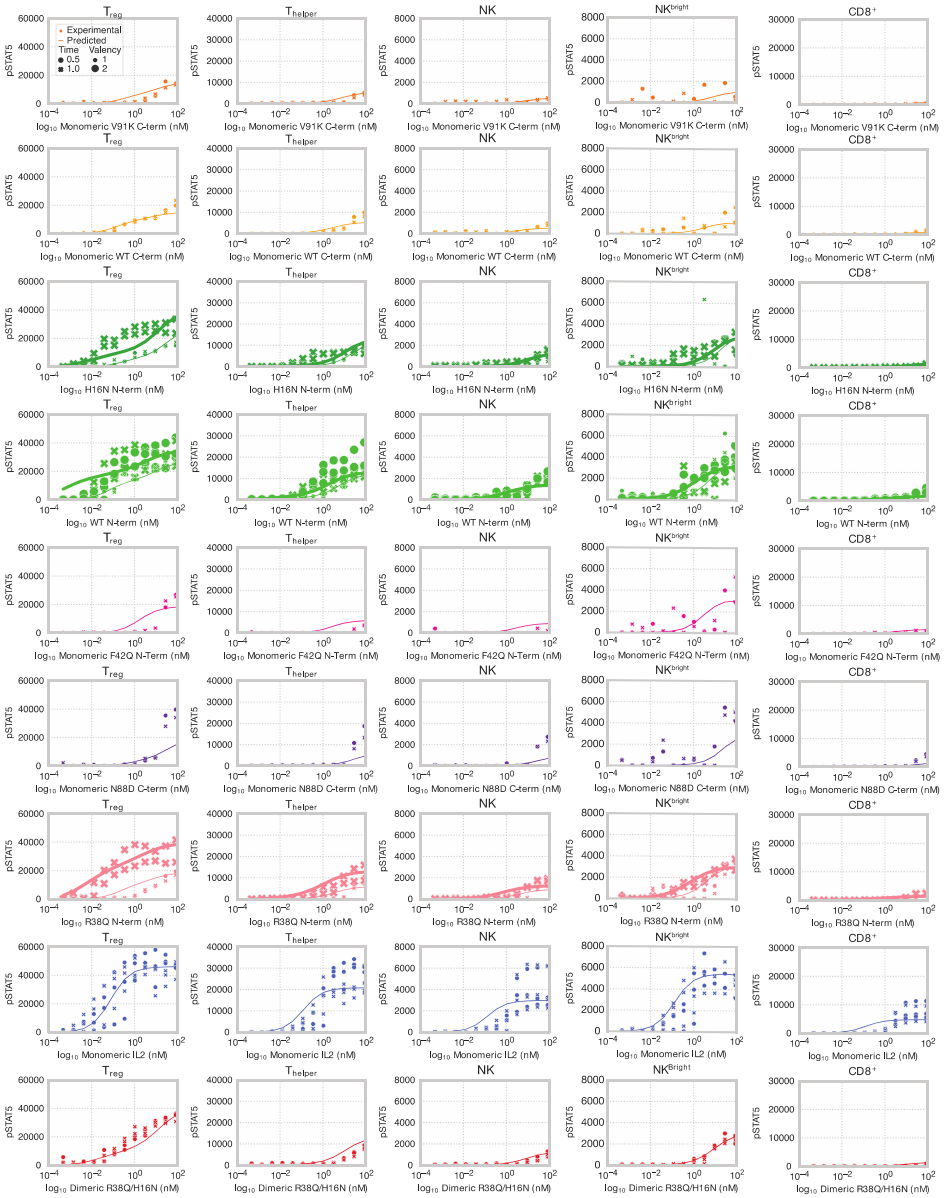

Figure S4: Full panel of predicted versus experimental immune cell-type responses to monomeric and dimeric IL-2 muteins. Dots represent flow cytometry measurements and lines represent pSTAT response predicted by model. Experimental pSTAT measurements are shown for 0.5- and 1-hour timepoints (inset legend, top left). Predictions and experiments are shown for T_{reg}s, T_{helper}s, NK, NK^{bright}, and CD8 cells. Each individual point is representative of one experimental replicate of triplicate experiments.

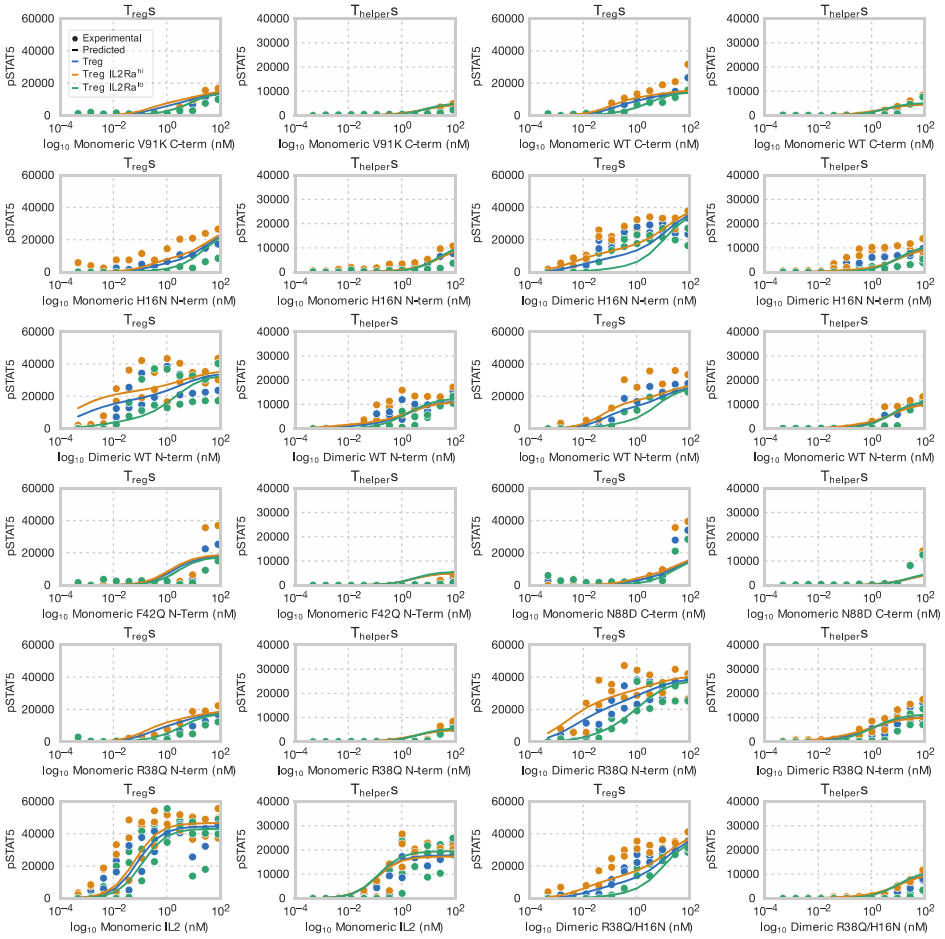

Figure S5: Full panel of predicted versus experimental IL-2Rα high, medium, and low T_{reg} and T_{helper} responses to monomeric and dimeric IL-2 muteins. Dots represent flow cytometry measurements and lines represent pSTAT response predicted by model. Experimental pSTAT measurements are shown for 0.5- and 1-hour timepoints. Predictions and experiments are shown for T_{reg}s, T_{helper}s binned by their IL-2Rα abundances. Each individual point is representative of one of 3 experimental, independently run replicates.

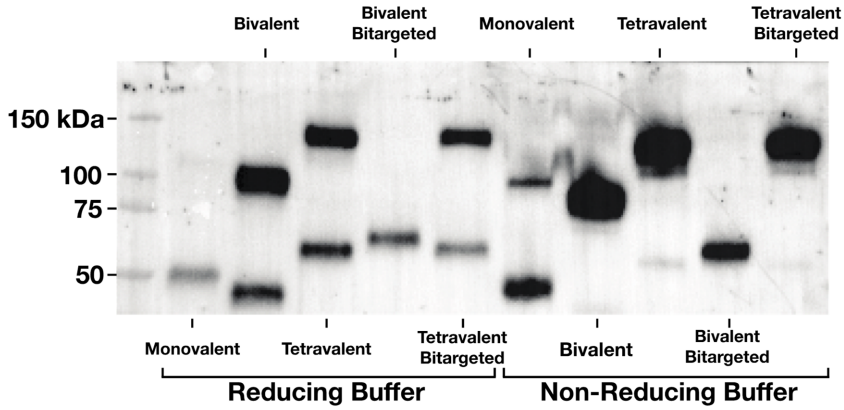

Figure S6: Western blot of multivalent IL-2 constructs. Western blot of monovalent, bivalent, tetravalent R38Q/H16N (lanes 1–3 and 6–8) and bivalent and tetravalent Bitargeted IL-2 (lanes 4–5 and 9–10). Samples in lanes 1–5 were run in reducing buffer, and lanes 6–10 were run in non-reducing buffer. Blot was stained with a primary anti-human-IL-2 antibody. Blots are representative of 2 experiments.

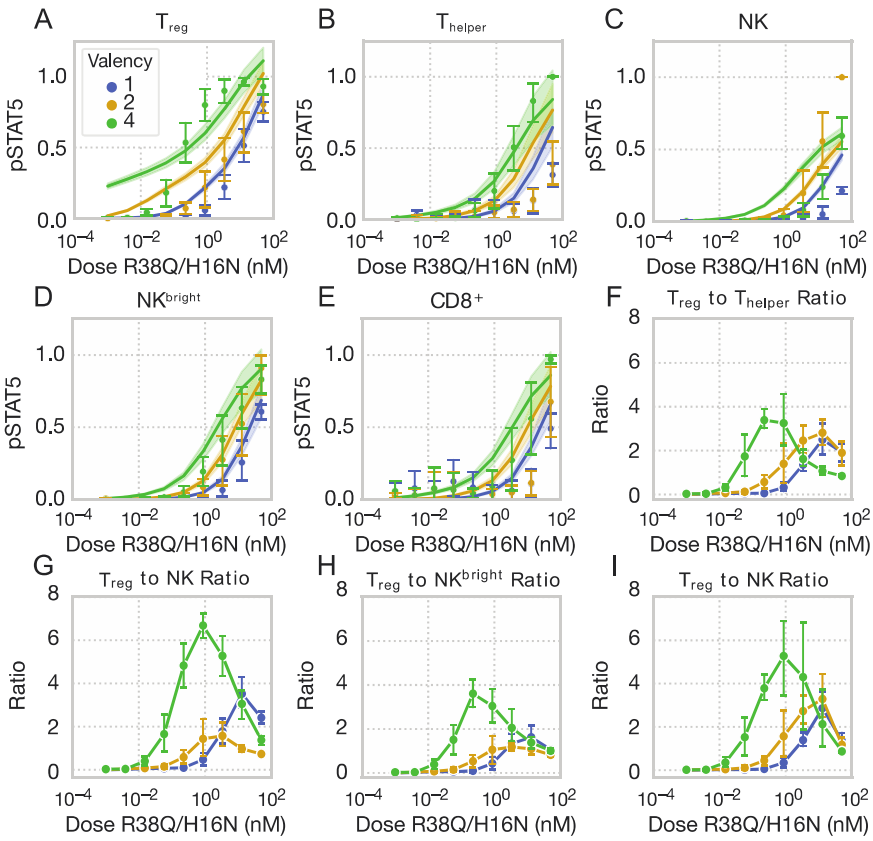

Figure S7: Full panel of predicted and experimental responses to R38Q/H16N multivalent mutants. (A to E) Responses of human T_{reg}s (A), T_{helper}s (B), NK (C), NK^{bright} (D), and $CD8^+$ (E) cells, measured by STAT5 phosphorylation, in response to varying dosages of R38Q/H16N in various valency formats. Cells were stimulated with cytokine for 30 minutes and signaling was normalized to the largest signaling response for each cell type and donor. Points are representative of experimental results (N=5), error bars represent experimental standard deviation, and lines represent model-predicted responses. Shaded regions are indicative of the standard error of prediction when the scalar factor converting between signaling complexes and MFI was fit to multiple experiments. **(F to I)** Ratio of STAT5 phosphorylation in T_{reg}s to T_{helper}s (F), NK cells (G), NK^{bright} (H), and $CD8^+$ (I) cells at varying dosages for R38Q/H16N in various valency formats. Dots are representative of mean of biological replicates. Data show responses in PBMCs from 5 donors, each with two experimental replicates conducted; error bars represent experimental standard deviation.

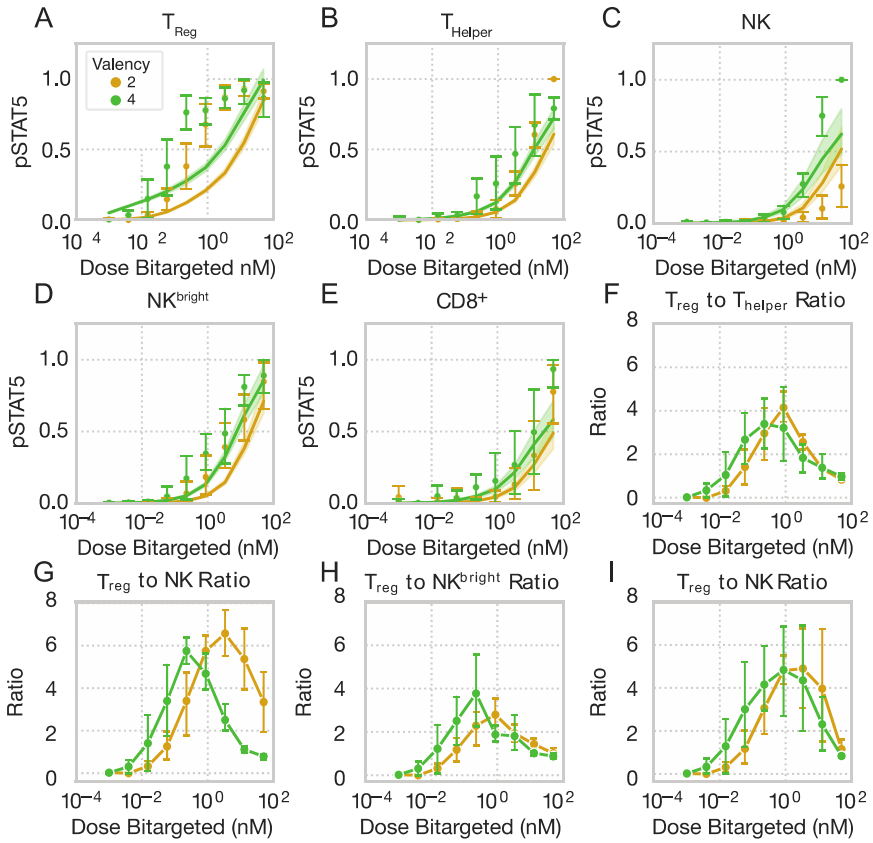

Figure S8: Full panel of predicted and experimental responses to bitargeted, multivalent mutants. (A to E) Responses of human T_{reg}s (A), T_{helper}s (B), NK (C), NK^{bright} (D), and $CD8^+$ (E) cells, measured by STAT5 phosphorylation, in response to varying dosages of Live/Dead IL-2 in various valency formats. Cells were stimulated with cytokine for 30 minutes and signaling was normalized to the largest signaling response for each cell type and donor. Points are representative of experimental results (N=5), error bars represent experimental standard deviation, and lines represent model-predicted responses. Shaded regions are indicative of the standard error of prediction when the scalar factor converting between signaling complexes and MFI was fit to multiple experiments. **(F to I)** Ratio of STAT5 phosphorylation in T_{reg}s to T_{helper}s (F), NK cells (G), NK^{bright} (H), and $CD8^+$ (I) cells at varying dosages for bitargeted in various valency formats. Dots are representative of mean of biological replicates. Data show responses in PBMCs from 5 donors, each with two experimental replicates conducted; error bars represent experimental standard deviation.

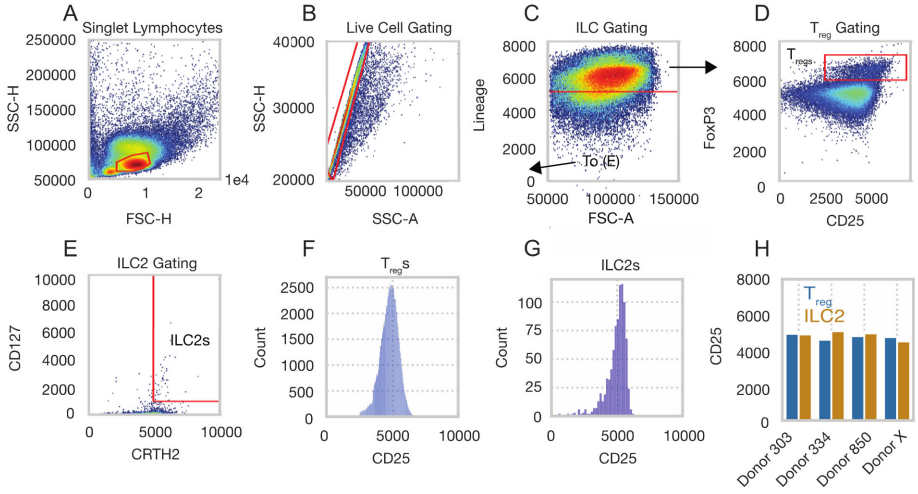

Figure S9: Receptor quantification and gating of PBMC-derived immune cell types. (A to E) Gating for fixed ILC2s and T_{reg} cells from donor PBMCs. **(F and G)** Mean fluorescent intensity (MFI) for T_{reg}s and ILC2s across aggregated across 4 donors. **(H)** MFI of CD25 on T_{reg}s and ILC2s for each donor. In (A to H), one experimental replicate was performed for each of 4 donors.

Ligand	IL2Rα K_D (nM)	IL2Rβ/γ_c K_D (nM)
WT IL-2	10.0	0.133
WT N-term	0.19	5.30
WT C-term	0.54	3.04
V91K C-term	0.69	7.56
R38Q N-term	0.71	4.00
F42Q N-Term	9.48	2.81
N88D C-term	1.01	24.0
H16N N-term	0.43	22.4
R38Q/H16N	0.71	22.4

Table S1. IL-2 variant affinity for IL-2R subunits. PBMCs were stimulated with IL-2 muteins. The affinities of each IL-2 monomeric mutein for IL2Rα and IL2Rβ/γ_c dimer were measured using biolayer interferometry. Two technical replicates of PBMCs collected from a single donor were conducted for each ligand.

Ligand	CD8	NK	NK^{bright}	T_{helper}	T_{reg}
F42Q N-Term (Mono)	N/A	97.0	N/A	N/A	N/A
H16N N-term (Biv)	N/A	N/A	N/A	N/A	N/A
H16N N-term (Mono)	1.3	0.88	0.94	1.1	1.0
IL15 (Mono)	3.6	1.9	0.77	1.2	0.94
IL2 (Mono)	N/A	N/A	19.6	N/A	N/A
N88D C-term (Mono)	N/A	68.1	N/A	N/A	N/A
R38Q N-term (Biv)	N/A	N/A	6.3	37.1	23.3
R38Q N-term (Mono)	N/A	N/A	N/A	79.0	N/A
R38Q/H16N (Biv)	N/A	N/A	14.8	51.9	41.4
V91K C-term (Mono)	N/A	N/A	3.3	0.74	0.30
WT C-term (Mono)	N/A	35.0	17.4	11.3	5.5
WT N-term (Biv)	N/A	97.0	N/A	N/A	N/A
WT N-term (Mono)	N/A	N/A	N/A	N/A	N/A

Table S2: IL-2 variant EC_{50} values for each immune cell subtype. The EC_{50} of each IL-2 mutein for immune cell subtype as determined using STAT5 phosphorylation. All EC_{50} values are reported in nM units and were determined by fitting a Hill function to an experimental dose-response curve. EC_{50} values greater than the dose range tested are reported here as “N/A”. The valency of each ligand is reported next to the ligand’s name (Mono, monovalent; Biv, bivalent). Signaling data was gathered using PBMCs harvested from a single donor, from which 3 independent replicates were performed. Hill curves were fit to all experimental replicates simultaneously for each ligand and cell population. Each experiment was repeated over 4 technical, independent replicates, wherein cells from a single blood draw were split, thawed, and tested on different days.

Name	Insert Sequence
Tetravalent R38Q/H16N	ATGTATAGAATGCAACTGCTCTCCTGCATAGCATTAAGCCTCGCCTTAGTCACTAATAGCGCTCCGAC ATCAAGTAGTACGAAGAAAACACAACTGCAACTTGAGAATCTTCTACTGGATCTCCAGATGATCCTTA ACGGTATCAACAACTATAAGAATCCCAAGTTAACACAAATGTTGACCTTTAAATTCTACATGCCCAAGA AGGCCACAGAATTGAAGCATCTCCAATGTCTTGAGGAAGAGCTGAAACCCCTTGAGGAAGTGTTAAA TCTGGCACAGTCTAAGAACTTTCATCTCCGCCCCAGAGATTTAATATCTAATATCAATGTGATCGTTCT GGAACTGAAGGGTTCAGAAACCACTTTCATGTGCGAGTATGCTGATGAGACAGCCACAATTGTAGAA TTCCTCAACAGGTGGATAACATTCTGCCAGTCCATCATTAGTACATTAACTGGTGGCGGTGGATCAG GGGGAGGCGGATCAGGTGGCGGAGGATCCGGTGGAGGAGGTTCCGATAAGACCCATACTTGTCCA CCGTGTCCAGCTCCAGAATTGTTGGGTGGACCTAGCGTGTTTCTGTTCCCACCCAAGCCCAAAGATA CACTTATGATCAGTCGGACTCCTGAGGTAACGTGCGTGGTAGTGGACGTCAGCCATGAGGACCCAG AGGTCAAATTTAACTGGTATGTTGATGGAGTTGAAGTGCATAACGCCAAAACTAAACCAAGGGAAGAA CAGTACAACTCTACCTATAGAGTGGTTTCCGTACTCACAGTACTGCACCAAGACTGGCTGAACGGAA AAGAATATAAATGTAAGGTGAGCAATAAAGCATTGCCCGCCCCGATCGAGAAAACAATTTCAAAAGCT AAAGGCCAACCGAGAGAACCCCAAGTTTATACCCTTCCACCCTCTCGGGATGAGTTGACCAAGAACC AAGTGTCATTAACTTGTCTGGTGAAGGGATTTTATCCCTCTGACATTGCCGTGGAATGGGAATCCAAC GGTCAGCCGGAAAACAATTATAAAACTACTCCACCCGTCTTAGACTCTGACGGGAGTTTCTTCCTGTA CAGCAAGCTTACAGTAGACAAGTCTCGGTGGCAACAAGGAAACGTCTTCAGCTGTAGCGTCATGCAT GAAGCATTACATAATCACTATACACAAAAGTCTCTGTCACTGTCCCCTGGCGGTGGAGGAGGCAGCG GCGGTGGTGGTTCTGGAGGAGGTGGAAGTGGTGGCGGCGGGAGTGCACCAACTAGCAGTTCCACC AAAAAGACTCAGTTACAGCTCGAAAACCTGCTGCTTGACCTGCAGATGATTCTGAATGGAATAAATAA TTACAAAAACCCTAAGCTCACACAGATGCTTACGTTCAAGTTTTATATGCCAAAGAAGGCTACGGAGC TCAAACACCTGCAATGCTTGGAAGAGGAACTCAAGCCATTGGAAGAGGTTCTGAACCTGGCTCAATC CAAAAATTTCCACCTTAGGCCTAGAGACCTCATCAGCAACATAAACGTTATAGTACTAGAGCTCAAAG GGAGCGAGACGACCTTTATGTGCGAGTACGCCGATGAAACTGCTACCATCGTGGAGTTTTTGAATAG ATGGATCACCTTTTGTCAAAGCATTATATCCACACTTACCTGA
Bivalent R38Q/H16N	ATGTATCGCATGCAACTCTTGTCTTGTATTGCCCTCTCTCTCGCCCTCGTCACGAACTCTGCTCCAAC AAGTAGTTCAACCAAGAAAACCCAATTACAATTGGAAAACTTGCTGCTGGACTTACAGATGATACTTA ACGGCATCAATAACTACAAGAACCCAAAGCTCACACAAATGCTTACATTTAAATTCTATATGCCGAAG AAAGCAACAGAGCTCAAGCATCTCCAATGCCTCGAAGAAGAGTTAAAGCCTCTCGAGGAAGTTCTCA ATCTTGCCCAATCCAAGAACTTTCATCTTAGACCGCGAGATCTGATATCTAATATAAATGTGATTGTCC TTGAACTCAAAGGGTCAGAGACTACTTTCATGTGTGAGTATGCCGATGAGACGGCTACCATCGTGGA GTTCCTCAATAGGTGGATCACGTTTTGCCAAAGCATAATTTCCACCTTGACCGGCGGCGGTGGATCC GGTGGAGGAGGGAGTGGTGGCGGCGGAAGCGGCGGTGGTGGCTCCGATAAAACACACACATGTCC CCCTTGTCCTGCACCAGAACTCCTGGGCGGCCCTTCAGTGTTCCTGTTTCCCCCAAAACCCAAAGAC ACATTGATGATCTCCCGCACTCCTGAGGTGACGTGTGTTGTCGTGGATGTTTCCCATGAAGACCCGG AAGTTAAATTTAACTGGTACGTGGATGGCGTAGAAGTCCATAATGCCAAGACAAAGCCACGGGAAGA GCAGTACAACTCTACCTATCGAGTGGTCTCAGTGTTGACCGTTCTGCACCAAGATTGGCTGAATGGG AAGGAGTATAAGTGTAAGGTTTCAAACAAAGCTCTGCCGGCACCCATTGAAAAGACAATCTCTAAGG CAAAAGGCCAACCAAGAGAGCCACAAGTCTATACGCTGCCCCCTAGCCGGGATGAGCTCACTAAGA ACCAGGTATCTCTCACATGTCTCGTCAAAGGGTTCTATCCATCTGATATCGCAGTGGAATGGGAATCA AATGGACAGCCAGAGAACAATTATAAAACCACTCCACCCGTCCTTGATTCCGACGGGTCCTTCTTCTT ATATTCCAAGTTAACTGTGGATAAATCTCGTTGGCAGCAAGGCAATGTCTTTAGTTGCTCCGTAATGC ATGAAGCGCTCCATAACCATTACACACAGAAGTCACTGTCACTCAGCCCTTAA
Monovalent R38Q/H16N	ATGTACCGAATGCAATTGCTTAGCTGTATTGCCTTGAGTCTCGCACTCGTGACTAACTCAGCCCCCAC CTCATCCAGCACTAAGAAAACGCAGCTGCAACTCGAGAACTTACTGCTTGATCTCCAGATGATTCTCA ACGGCATCAACAATTACAAGAATCCAAAGTTGACACAAATGCTGACCTTTAAATTTTATATGCCAAAGA AGGCCACCGAGCTGAAGCATTTGCAGTGCCTTGAAGAGGAACTTAAACCACTGGAAGAAGTTTTGAA CCTGGCCCAAAGCAAGAACTTCCACTTGAGACCTCGGGATCTGATAAGCAACATTAACGTTATTGTC CTGGAGCTCAAAGGATCAGAAACAACCTTCATGTGTGAATACGCAGATGAGACTGCAACTATTGTAG AGTTTCTGAACCGCTGGATTACCTTCTGCCAGAGCATTATTTCCACACTCACAGGCGGAGGAGGATC AGGCGGCGGCGGTAGCGGCGGAGGAGGAAGCGGAGGAGGCGGCAGTGATAAGACACATACATGT CCACCTTGTCCAGCCCCAGAGCTTTTGGGCGGCCCGTCCGTGTTTCTGTTTCCACCTAAGCCTAAAG ATACATTAATGATCAGCCGGACTCCTGAAGTTACTTGTGTTGTGGTTGATGTCAGTCATGAGGATCCA GAGGTTAAGTTCAACTGGTACGTGGATGGTGTGGAAGTTCACAATGCGAAAACGAAACCACGCGAAG AACAGTATAATAGTACATACCGTGTAGTGAGCGTATTGACTGTGCTCCATCAAGACTGGCTTAATGGC AAAGAATATAAGTGTAAGGTGAGTAACAAAGCGCTCCCCGCACCTATTGAGAAGACGATTAGCAAAG CCAAGGGTCAACCACGCGAACCCCAAGTCTATACACTGCCCCCTTCCCGTGATGAGTTAACCAAGAA TCAAGTCAATCTTACCTGTCTTGTAAAAGGTTTCTACCCGTCTGATATCGCCGTCGAATGGGAGTCTA ATGGCCAACCGGAAAACAACTACAAGACCACACCGCCCGTCCTCGACTCAGATGGGAGTTTCTTCCT GAATAGCACTTTGACAGTGGATAAAAGTCGATGGCAACAGGGGAATGTGTTCTCCTGTAGCGTAATG CATGAGGCTCTGCATAACCATTACACACAGAAATCACTCAGTCTCAGCCCTTAA
Tetravalent bitargeted	ATGTATAGAATGCAACTGCTCTCCTGCATAGCATTAAGCCTCGCCTTAGTCACTAATAGCGCTCCGAC ATCAAGTAGTACGAAGAAAACACAACTGCAACTTGAGAATCTTCTACTGGATCTCCAGATGATCCTTA ACGGTATCAACAACTATAAGAATCCCAAGTTAACACAAATGTTGACCTTTAAATTCTACATGCCCAAGA AGGCCACAGAATTGAAGCATCTCCAATGTCTTGAGGAAGAGCTGAAACCCCTTGAGGAAGTGTTAAA TCTGGCACAGTCTAAGAACTTTCATCTCCGCCCCAGAGATTTAATATCTAATATCAATGTGATCGTTCT GGAACTGAAGGGTTCAGAAACCACTTTCATGTGCGAGTATGCTGATGAGACAGCCACAATTGTAGAA TTCCTCAACAGGTGGATAACATTCTGCCAGTCCATCATTAGTACATTAACTGGTGGCGGTGGATCAG GGGGAGGCGGATCAGGTGGCGGAGGATCCGGTGGAGGAGGTTCCGATAAGACCCATACTTGTCCA

	CCGTGTCCAGCTCCAGAATTGTTGGGTGGACCTAGCGTGTTTCTGTTCCCACCCAAGCCCAAAGATA CACTTATGATCAGTCGGACTCCTGAGGTAACGTGCGTGGTAGTGGACGTCAGCCATGAGGACCCAG AGGTCAAATTTAACTGGTATGTTGATGGAGTTGAAGTGCATAACGCCAAAACTAAACCAAGGGAAGAA CAGTACAACTCTACCTATAGAGTGGTTTCCGTACTCACAGTACTGCACCAAGACTGGCTGAACGGAA AAGAATATAAATGTAAGGTGAGCAATAAAGCATTGCCCGCCCCGATCGAGAAAACAATTTCAAAAGCT AAAGGCCAACCGAGAGAACCCCAAGTTTATACCCTTCCACCCTCTCGGGATGAGTTGACCAAGAACC AAGTGTCATTAACTTGTCTGGTGAAGGGATTTTATCCCTCTGACATTGCCGTGGAATGGGAATCCAAC GGTCAGCCGGAAAACAATTATAAAACTACTCCACCCGTCTTAGACTCTGACGGGAGTTTCTTCCTGTA CAGCAAGCTTACAGTAGACAAGTCTCGGTGGCAACAAGGAAACGTCTTCAGCTGTAGCGTCATGCAT GAAGCATTACATAATCACTATACACAAAAGTCTCTGTCACTGTCCCCTGGTGGAGGAGGCAGCGGCG GTGGTGGTTCTGGAGGAGGTGGAAGTGGTGGCGGCGGGAGTGCACCAACTAGCAGTTCCACCAAA AAGACTCAGTTACAGCTCGAACATCTGCTGCTTGCACTGCAGATGATTCTGAATGGAATAAATAATTA CAAAAACCCTAAGCTCACACGTATGCTTACGTTCAAGTTTTATATGCCAAAGAAGGCTACGGAGCTCA AACACCTGCAATGCTTGGAAGAGGAACTCAAGCCATTGGAAGAGGTTCTGAACCTGGCTCAATCCAA AAATTTCCACCTTAGGCCTAGAGACCTCATCAGCAACATAAACAAGATAGTACTAGAGCTCAAAGGGA GCGAGACGACCTTTGTTTGCGAGTACGCCGATGAAACTGCTACCATCGTGGAGTTTTTGAATAGATG GATCACCTTTTGTCAAAGCATTATATCCACACTTACCTGA
Bivalent bitargeted	ATGTATAGAATGCAACTGCTCTCCTGCATAGCATTAAGCCTCGCCTTAGTCACTAATAGCGCTCCGAC ATCAAGTAGTACGAAGAAAACACAACTGCAACTTGAGAATCTTCTACTGGATCTCCAGATGATCCTTA ACGGTATCAACAACTATAAGAATCCCAAGTTAACACAAATGTTGACCTTTAAATTCTACATGCCCAAGA AGGCCACAGAATTGAAGCATCTCCAATGTCTTGAGGAAGAGCTGAAACCCCTTGAGGAAGTGTTAAA TCTGGCACAGTCTAAGAACTTTCATCTCCGCCCCAGAGATTTAATATCTAATATCAATGTGATCGTTCT GGAACTGAAGGGTTCAGAAACCACTTTCATGTGCGAGTATGCTGATGAGACAGCCACAATTGTAGAA TTCCTCAACAGGTGGATAACATTCTGCCAGTCCATCATTAGTACATTAACTGGTGGCGGTGGATCAG GGGGAGGCGGATCAGGTGGCGGAGGATCCGGTGGAGGAGGTTCCGATAAGACCCATACTTGTCCA CCGTGTCCAGCTCCAGAATTGTTGGGTGGACCTAGCGTGTTTCTGTTCCCACCCAAGCCCAAAGATA CACTTATGATCAGTCGGACTCCTGAGGTAACGTGCGTGGTAGTGGACGTCAGCCATGAGGACCCAG AGGTCAAATTTAACTGGTATGTTGATGGAGTTGAAGTGCATAACGCCAAAACTAAACCAAGGGAAGAA CAGTACAACTCTACCTATAGAGTGGTTTCCGTACTCACAGTACTGCACCAAGACTGGCTGAACGGAA AAGAATATAAATGTAAGGTGAGCAATAAAGCATTGCCCGCCCCGATCGAGAAAACAATTTCAAAAGCT AAAGGCCAACCGAGAGAACCCCAAGTTTATACCCTTCCACCCTCTCGGGATGAGTTGACCAAGAACC AAGTGAATTTAACTTGTCTGGTGAAGGGATTTTATCCCTCTGACATTGCCGTGGAATGGGAATCCAAC GGTCAGCCGGAAAACAATTATAAAACTACTCCACCCGTCTTAGACTCTGACGGGAGTTTCTTCCTGAA TAGCACCCTTACAGTAGACAAGTCTCGGTGGCAACAAGGAAACGTCTTCAGCTGTAGCGTCATGCAT GAAGCATTACATAATCACTATACACAAAAGTCTCTGTCACTGTCCCCTGGTGGAGGAGGCAGCGGCG GTGGTGGTTCTGGAGGAGGTGGAAGTGGTGGCGGCGGGAGTGCACCAACTAGCAGTTCCACCAAA AAGACTCAGTTACAGCTCGAACATCTGCTGCTTGCACTGCAGATGATTCTGAATGGAATAAATAATTA CAAAAACCCTAAGCTCACACGTATGCTTACGTTCAAGTTTTATATGCCAAAGAAGGCTACGGAGCTCA AACACCTGCAATGCTTGGAAGAGGAACTCAAGCCATTGGAAGAGGTTCTGAACCTGGCTCAATCCAA AAATTTCCACCTTAGGCCTAGAGACCTCATCAGCAACATAAACAAGATAGTACTAGAGCTCAAAGGGA GCGAGACGACCTTTGTTTGCGAGTACGCCGATGAAACTGCTACCATCGTGGAGTTTTTGAATAGATG GATCACCTTTTGTCAAAGCATTATATCCACACTTACCTGA

Table S3: DNA sequences for novel IL-2 muteins. DNA sequences used to express novel multivalent IL-2 muteins.

Antibody	Source	Identifiers	Panel
Anti-FoxP3, Pacific Blue	BioLegend	Cat #: 320216; Clone: 206D; RRID: AB_439801	1
Anti-CD3, PerCP-Cy5	BioLegend	Cat #: 300328; Clone: HIT3a; RRID: AB_1575008	1
Anti-CD4, PE	BioLegend	Cat #: 300508; Clone: RPA-T4; RRID: AB_314076	1
Anti-CD8a, Alexa Fluor 488	BioLegend	Cat #: 344716; Clone: SK1; RRID: AB_10549301	1
Anti-CD56, BV605	BioLegend	Cat #: 318334; Clone: GCD56; RRID: AB_2561912	1
Anti-pSTAT5, R718	BD Biosciences	Cat #: BDB566978; Clone: 47; RRID: AB_2869984	1
Anti-CD25, BV786	BD Biosciences	Cat #: 563701; Clone: M-A251; RRID: AB_2744338	1
Anti-CD25, APC-Fire 810	BioLegend	Cat #: 356150; Clone: M-A251; RRID: AB_2876679	2
Anti-CD127, BV421	BioLegend	Cat # 351310 Clone: A019D5; RRID: AB_10960140	2
Lineage Cocktail, FITC	Invitrogen	Cat # 22-7778-72; Clones: UCHT1; HCD14; 3G8; HIB19; 2H7; HCD56; RRID: AB_1311229	2
Anti-CRTH2, BV605	BioLegend	Cat #: 350122; Clone: BM16; RRID: AB_2566760	2
Anti-FoxP3, Alexa 647	BioLegend	Cat # 320114; Clone: 206D; RRID: AB_439754	2
Anti-FcεR1, FITC	Biolegend	Cat # 334608; Clone: AER-37; RRID: AB_1227653	2
Anti-IL-2	R&D Systems	Cat # MAB202-SP; Clone 5334; RRID: AB_2264789	N/A

Table S4: Antibodies. Antibodies used in this study are listed. Those used to quantify receptor abundances, as well as to perform initial pSTAT5 response quantification in PBMCs, are detailed in Farhat *et al.*[15]

Chapter 4:

Engineered human cytokine/antibody fusion proteins elicit targeted expansion of regulatory T cells and confer protection against autoimmune diseases

Van Dyke, D.[1,2], Iglesias, M.[3], Tomala, J.[4], Young, A.[5,6,7,8], Smith, J.[5], Perry, J. A.[9], Gebara, E.[2,10], Cross, A.[11], Cheung, L. S.[12,13], Dykema, A. G.[12,13], **Orcutt-Jahns, B. T.[14],** Henclova, T., Golias, J.[15], Balolong, J.[5], Tomasovic, L.[1,2], Funda, D.[15], Meyer, A. S.[14], Pardoll, D. M.[12,13], Hester, J.[11], Issa, F.[11], Hunter, C. A.[9], Anderson, M. S.[5], Bluestone, J. A.[5,6,16], Raimondi, G.[3], & Spangler, J. S.[1,2,12,13,17.18.19.20]

[1]Department of Chemical and Biomolecular Engineering, Johns Hopkins University, Baltimore, MD 21218, USA
[2]Translational Tissue Engineering Center, Johns Hopkins University School of Medicine, Baltimore, MD 21231, USA
[3]Vascularized Composite Allotransplantation Laboratory, Department of Plastic and Reconstructive Surgery, Johns Hopkins University School of Medicine, Baltimore, MD 21205, USA
[4]Institute of Biotechnology of the Academy of Sciences of the Czech Republic, Vestec 252 50, Czech Republic
[5]Diabetes Center, University of California San Francisco, San Francisco, CA 94143, USA
[6]Sean N. Parker Autoimmune Research Laboratory, University of California San Francisco, San Francisco, CA 94143, USA
[7]Huntsman Cancer Institute, University of Utah Health Sciences Center, Salt Lake City, UT 84112, USA
[8]Department of Pathology, University of Utah School of Medicine, Salt Lake City, UT 84112, USA
[9]Department of Pathobiology, University of Pennsylvania, Philadelphia, PA 19104, USA
[10]Department of Molecular Microbiology and Immunology, Johns Hopkins Bloomberg School of Public Health, Baltimore, MD 21205, USA
[11]Translational Research Immunology Group, Nuffield Department of Surgical Sciences, University of Oxford, Oxford OX3 9DU, UK
[12]Bloomberg-Kimmel Institute for Cancer Immunotherapy, Johns Hopkins University, Baltimore, MD 21231, USA
[13]Sidney Kimmel Comprehensive Cancer Center, Johns Hopkins University, Baltimore, MD 21231, USA
[14]Department of Bioengineering, Jonsson Comprehensive Cancer Center, Eli and Edythe Broad Center of Regenerative Medicine and Stem Cell Research, University of California, Los Angeles, Los Angeles, CA 90095, USA
[15]Institute of Microbiology of the Academy of Sciences of the Czech Republic, Prague 142 20, Czech Republic
[16]Sonoma Biotherapeutics, South San Francisco, CA 94080, USA
[17]Department of Biomedical Engineering, Johns Hopkins University School of Medicine, Baltimore, MD 21205, USA
[18]Department of Oncology, Johns Hopkins University School of Medicine, Baltimore, MD 21231, USA
[19]Department of Ophthalmology, Johns Hopkins University School of Medicine, Baltimore, MD 21287, USA

Cell Reports

Article

Engineered human cytokine/antibody fusion proteins expand regulatory T cells and confer autoimmune disease protection

Graphical abstract

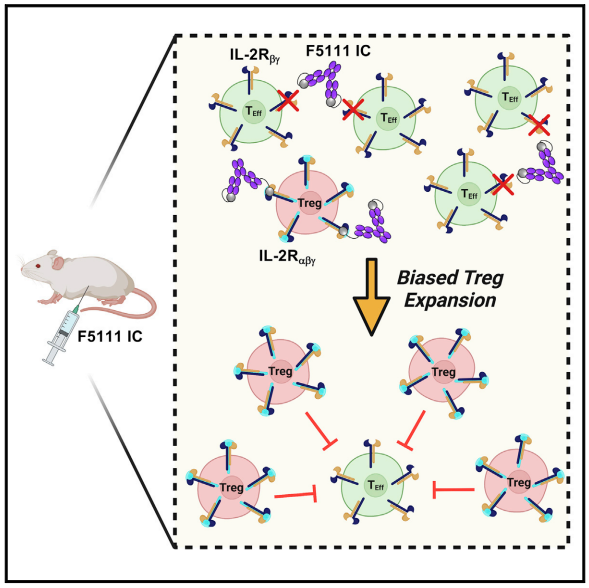

Highlights

- Single-chain human interleukin-2/antibody fusion protein (immunocytokine) is designed
- F5111 immunocytokine promotes biased Treg activation and expansion
- Immunocytokine induces superior Treg bias compared with cytokine/antibody complex
- F5111 immunocytokine confers protection in mouse models of autoimmune diseases

Authors

Derek VanDyke, Marcos Iglesias, Jakub Tomala, ..., Jeffrey A. Bluestone, Giorgio Raimondi, Jamie B. Spangler

Correspondence

jamie.spangler@jhu.edu

In brief

VanDyke et al. engineer a single-chain fusion protein composed of the human interleukin-2 cytokine and the anti-cytokine antibody F5111, which induces biased activation and expansion of regulatory T cells *in vitro* and *in vivo*. This protein confers protection in animal models of colitis and immune checkpoint inhibitor-induced diabetes mellitus.

VanDyke et al., 2022, Cell Reports *41*, 111478
October 18, 2022
https://doi.org/10.1016/j.celrep.2022.111478

CellPress

Cell Reports

CellPress
OPEN ACCESS

Article

Engineered human cytokine/antibody fusion proteins expand regulatory T cells and confer autoimmune disease protection

Derek VanDyke,[1,2] Marcos Iglesias,[3] Jakub Tomala,[4] Arabella Young,[5,6,7,8] Jennifer Smith,[5] Joseph A. Perry,[9] Edward Gebara,[2,10] Amy R. Cross,[11] Laurene S. Cheung,[12,13] Arbor G. Dykema,[12,13] Brian T. Orcutt-Jahns,[14] Tereza Henclová,[4] Jaroslav Golias,[15] Jared Balolong,[5] Luke M. Tomasovic,[1,2] David Funda,[15] Aaron S. Meyer,[14] Drew M. Pardoll,[12,13] Joanna Hester,[11] Fadi Issa,[11] Christopher A. Hunter,[9] Mark S. Anderson,[5] Jeffrey A. Bluestone,[5,6,16] Giorgio Raimondi,[3] and Jamie B. Spangler[1,2,12,13,17,18,19,20,*]

[1]Department of Chemical and Biomolecular Engineering, Johns Hopkins University, Baltimore, MD 21218, USA
[2]Translational Tissue Engineering Center, Johns Hopkins University School of Medicine, Baltimore, MD 21231, USA
[3]Vascularized Composite Allotransplantation Laboratory, Department of Plastic and Reconstructive Surgery, Johns Hopkins University School of Medicine, Baltimore, MD 21205, USA
[4]Institute of Biotechnology of the Academy of Sciences of the Czech Republic, Vestec 252 50, Czech Republic
[5]Diabetes Center, University of California San Francisco, San Francisco, CA 94143, USA
[6]Sean N. Parker Autoimmune Research Laboratory, University of California San Francisco, San Francisco, CA 94143, USA
[7]Huntsman Cancer Institute, University of Utah Health Sciences Center, Salt Lake City, UT 84112, USA
[8]Department of Pathology, University of Utah School of Medicine, Salt Lake City, UT 84112, USA
[9]Department of Pathobiology, University of Pennsylvania, Philadelphia, PA 19104, USA
[10]Department of Molecular Microbiology and Immunology, Johns Hopkins Bloomberg School of Public Health, Baltimore, MD 21205, USA
[11]Translational Research Immunology Group, Nuffield Department of Surgical Sciences, University of Oxford, Oxford OX3 9DU, UK
[12]Bloomberg-Kimmel Institute for Cancer Immunotherapy, Johns Hopkins University, Baltimore, MD 21231, USA
[13]Sidney Kimmel Comprehensive Cancer Center, Johns Hopkins University, Baltimore, MD 21231, USA
[14]Department of Bioengineering, Jonsson Comprehensive Cancer Center, Eli and Edythe Broad Center of Regenerative Medicine and Stem Cell Research, University of California, Los Angeles, Los Angeles, CA 90095, USA
[15]Institute of Microbiology of the Academy of Sciences of the Czech Republic, Prague 142 20, Czech Republic
[16]Sonoma Biotherapeutics, South San Francisco, CA 94080, USA
[17]Department of Biomedical Engineering, Johns Hopkins University School of Medicine, Baltimore, MD 21205, USA
[18]Department of Oncology, Johns Hopkins University School of Medicine, Baltimore, MD 21231, USA
[19]Department of Ophthalmology, Johns Hopkins University School of Medicine, Baltimore, MD 21287, USA
[20]Lead contact
*Correspondence: jamie.spangler@jhu.edu
https://doi.org/10.1016/j.celrep.2022.111478

SUMMARY

Low-dose human interleukin-2 (hIL-2) treatment is used clinically to treat autoimmune disorders due to the cytokine's preferential expansion of immunosuppressive regulatory T cells (Tregs). However, off-target immune cell activation and short serum half-life limit the clinical potential of IL-2 treatment. Recent work showed that complexes comprising hIL-2 and the anti-hIL-2 antibody F5111 overcome these limitations by preferentially stimulating Tregs over immune effector cells. Although promising, therapeutic translation of this approach is complicated by the need to optimize dosing ratios and by the instability of the cytokine/antibody complex. We leverage structural insights to engineer a single-chain hIL-2/F5111 antibody fusion protein, termed F5111 immunocytokine (IC), which potently and selectively activates and expands Tregs. F5111 IC confers protection in mouse models of colitis and checkpoint inhibitor-induced diabetes mellitus. These results provide a roadmap for IC design and establish a Treg-biased immunotherapy that could be clinically translated for autoimmune disease treatment.

INTRODUCTION

Interleukin-2 (IL-2) is a pleiotropic cytokine that regulates key homeostatic functions, including proliferation, survival, and activation of both pro-inflammatory immune effector cells (Effs) (e.g., $CD4^+$/$CD8^+$ effector T cells, natural killer [NK] cells), and anti-inflammatory regulatory T cells (Tregs). IL-2 engages transmembrane receptors to activate signaling through the Janus kinase-signal transducer and activator of transcription (STAT) pathway, which regulates gene expression and functional outcomes (Malek, 2008; Stroud and Wells, 2004; Murray, 2007). IL-2 forms either an intermediate-affinity heterodimeric receptor

complex, comprising the IL-2 receptor-β (IL-2Rβ, CD122) and common gamma (γ_c) (CD132) chains, or a high-affinity heterotrimeric receptor complex, comprising the non-signaling IL-2Rα subunit (also CD25) as well as the IL-2Rβ and γ_c chains (Leonard et al., 1984; Liao et al., 2013; Wang et al., 2005). IL-2Rα is highly expressed on Tregs but virtually absent from naive Effs; thus, Tregs are 100-fold more sensitive to IL-2 (Boyman and Sprent, 2012; Sakaguchi et al., 1995; Taniguchi and Minami, 1993). IL-2Rα expression is also induced in activated Effs, albeit at lower levels, and activated Effs may compete with Tregs for extracellular IL-2 (Baecher-Allan et al., 2001; Höfer et al., 2012; Schmidt et al., 2012). Hence, IL-2 promotes both pro- and anti-inflammatory responses, which has made it an attractive, albeit complex, candidate for immunotherapy.

IL-2 first received FDA approval as a pro-inflammatory agent, wherein high doses are administered to treat metastatic cancers (Alva et al., 2016; Rosenberg, 2014; Sim and Radvanyi, 2014). In contrast, low doses of IL-2 have been used to treat autoimmune conditions, such as diabetes, ulcerative colitis, graft-versus-host disease (GVHD), and allograft rejection. However, low-dose IL-2 strategies are limited by the dangerous off-target effects that result from activation of Effs and by the short serum half-life of IL-2.

Several approaches have been explored to overcome the limitations of IL-2 therapy by biasing cytokine activity (Hernandez et al., 2022), including the design of IL-2 muteins (Peterson et al., 2018; Carmenate et al., 2018; Khoryati et al., 2020; Glassman et al., 2021), PEGylated IL-2 variants (Charych et al., 2016; Dixit et al., 2021; Zhang et al., 2021), and IL-2/IL-2Rα fusion proteins (Hernandez et al., 2021; Lopes et al., 2020; Ward et al., 2018, 2020; Xie et al., 2021). In addition, since IL-15 shares IL-2Rβ and γ_c with the IL-2 receptor but has a distinct α chain (Waldmann, 2006), IL-15 therapies have been designed that preferentially target Effs over IL-2Rα^{High} Tregs (Knudson et al., 2020), for example, the current clinical candidate ALT-803 (Romee et al., 2018; Rubinstein et al., 2006; Wrangle et al., 2018; Xu et al., 2013).

Another approach, pioneered by Boyman et al. (2006), built on seminal work (Finkelman et al., 1993) in developing cytokine/antibody complexes to combine IL-2 with anti-IL-2 antibodies that bias cytokine activity. These complexes increase therapeutic efficacy and reduce toxicity of the cytokine by extending its *in vivo* half-life (Roopenian and Akilesh, 2007) and selectively targeting its functions toward particular immune cell subsets (Arenas-Ramirez et al., 2016; Boyman et al., 2006; De Paula et al., 2020; Karakus et al., 2020; Lee et al., 2020b; Spangler et al., 2015a; Tomala et al., 2009; Trotta et al., 2018; Yokoyama et al., 2018). Trotta et al. (2018) discovered and mechanistically described a human antibody (F5111) against hIL-2 that biases its activities toward Tregs. F5111 sterically blocks hIL-2 binding to IL-2Rβ and also allosterically reduces hIL-2 affinity for IL-2Rα. Receptor activation is gated by hIL-2/antibody dissociation, and interaction of the hIL-2/F5111 complex with IL-2Rα destabilizes cytokine/antibody interactions, leading to selective IL-2Rα^{High} Treg activation. This paradigm resembles the exchange/release mechanism observed for the anti-mouse IL-2 (mIL-2) antibody JES6-1 and the anti-hIL-2 antibody UFKA-20, both of which bias IL-2 toward Tregs (Boyman et al., 2006; Karakus et al., 2020; Spangler et al., 2015a). An affinity matured version of F5111 (F5111.2) preferentially expanded Tregs and ameliorated autoimmune diseases in mice (Trotta et al., 2018). However, clinical translation of cytokine/antibody complexes is complicated by the need for dosing ratio optimization and by IL-2 dissociation, which leads to off-target effects. Moreover, use of a single agent rather than a multi-component mixture facilitates the clinical approval pathway. For instance, investigational new drug-enabling nonhuman primate studies of cytokine/antibody complexes require use of the matched species cytokine, but the antibody may not cross-react with nonhuman primate cytokines.

To overcome the limitations of IL-2/antibody complexes, the cytokine has been genetically fused to anti-IL-2 antibodies (Sahin et al., 2020; Spangler et al., 2018; Tomala et al., 2013). In one example, a single-chain fusion protein (immunocytokine [IC]) comprising mIL-2 and the JES6-1 antibody led to superior autoimmune disease control in mice compared with the mIL-2/JES6-1 complex (Spangler et al., 2018). Here, we designed an IC linking hIL-2 to the F5111 antibody (termed F5111 IC) that preferentially promotes mouse and human Treg activation. By modulating the cytokine/antibody affinity, we developed IC variants with a range of immune activation potencies. The parent F5111 IC was poised at an affinity optimum and showed greater Treg bias than hIL-2/antibody complexes. Finally, we established the therapeutic promise of F5111 IC in mouse models of colitis and immune checkpoint inhibitor-induced diabetes mellitus.

RESULTS

Immunocytokine design and optimization

To advance development of F5111 IC, we first produced the F5111 human immunoglobulin G1 (IgG1) antibody. Binding studies using the yeast surface display platform (Boder and Wittrup, 1997) revealed that recombinantly expressed F5111 bound yeast-displayed hIL-2 with the expected affinity (Trotta et al., 2018), and the antibody did not cross-react with mIL-2 (Figure S1A).

F5111 IC was constructed by tethering hIL-2 to the N terminus of the light chain (LC) of the full-length human F5111 antibody with a flexible linker (Figure 1A). The mechanism of action for biased immune activation by hIL-2/antibody complexes requires cytokine dissociation, and we hypothesized that fusing the cytokine to the antibody could hinder this dissociation through enhanced avidity effects (Spangler et al., 2018). Thus, to reduce the intramolecular cytokine/antibody affinity and enhance hIL-2 release, we formulated the IC using F5111 rather than the affinity matured F5111.2. The hIL-2/F5111 complex structure (Trotta et al., 2018) shows that the F5111 LC N terminus is 43 Å from the hIL-2 C terminus (Figure 1B); therefore our initial design (denoted F5111 IC LN15) used a 15 amino acid $(Gly_4Ser)_3$ linker to enable intramolecular engagement. Constructs with 25 amino acid $(Gly_4Ser)_5$ and 35 amino acid $(Gly_4Ser)_7$ linkers were also designed (F5111 IC LN25 and F5111 IC LN35, respectively). Control IC was constructed by replacing the variable chains of the F5111 IC LN35 construct with those of an irrelevant antibody (Honegger et al., 2005) (Table S1).

ICs were produced in mammalian cells and purified via protein G affinity chromatography and size-exclusion chromatography

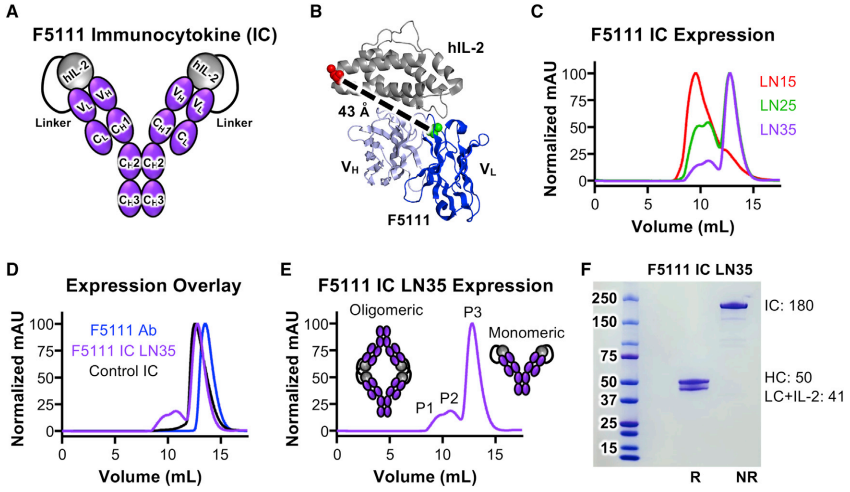

Figure 1. Design and production of F5111 IC

(A) Schematic of F5111 IC design.

(B) Structure of the hIL-2/F5111 complex (PDB: 5UTZ), showing the distance between the C terminus of hIL-2 (red) and the N terminus of the F5111 antibody LC (green).

(C) SEC trace overlay of F5111 ICs.

(D) SEC trace overlay of F5111 antibody (Ab) and ICs.

(E) SEC trace of F5111 IC LN35 with peaks (P1, P2, and P3) denoted.

(F) SDS-PAGE analysis of F5111 IC LN35 P3. R, reducing; NR, non-reducing. Molecular weights (kDa) are indicated on the right. See also Figure S1 and Table S1.

(SEC). Compared with the F5111 antibody, which eluted as a single monodisperse peak, F5111 IC LN15 eluted earlier and showed two broader peaks (Figures 1C and 1D), suggesting possible oligomerization of F5111 IC LN15. Analysis of F5111 IC LN25 and LN35 revealed three peaks (P1, P2, and P3) (Figures 1C–1E). Elution volumes suggested that P1 and P2 contained oligomeric structures, whereas P3 contained monomeric IC (Figures 1D and 1E). Higher-order oligomers likely indicate binding of linked hIL-2 to F5111 on a neighboring IC (intermolecular assembly) rather than intramolecular assembly (Figure 1E), presumably due to linker constraint of intramolecular interaction between hIL-2 and F5111. Indeed, we saw less oligomerization as we increased linker length. Control IC (which does not assemble intramolecularly or intermolecularly) eluted as a single peak that coincided with P3 of F5111 IC LN25 and LN35, further suggesting that P3 represents monomeric IC. SDS-PAGE verified IC purity (Figure 1F). Henceforth, F5111 IC LN25 and F5111 IC LN35 refer to P3 unless otherwise specified. Also, F5111 IC LN15 indicates the majority peak (Figure 1C).

F5111 ICs are intramolecularly assembled and exhibit expected binding properties

To confirm proper assembly and functionality of F5111 ICs, we measured binding to hIL-2, hIL-2Rα, and hIL-2Rβ using bio-layer interferometry. If properly assembled, F5111 IC would not engage hIL-2 since the hIL-2 within the IC is bound to the antibody. F5111 antibody bound to hIL-2 as expected (Trotta et al., 2018), whereas F5111 IC LN15, F5111 IC LN25, and F5111 IC LN35 showed impaired hIL-2 binding (Figures 2A, left, S1C, left, and S1D, left; Table S2), reflecting intramolecular assembly of the ICs. Trace hIL-2 binding to ICs suggested transient exchange between intramolecular and intermolecular interactions. hIL-2 binding decreased as linker length increased, reinforcing that longer linker lengths enhance IC assembly. The three peaks that eluted from F5111 IC LN25 showed similarly impaired hIL-2 binding (Figure S1E, left). As expected, binding was observed between hIL-2 and the hIL-2/F5111 complex (1:1 molar ratio) due to unoccupied sites on F5111 (Figure 2A, left).

We expected F5111 IC to interact with hIL-2Rα since the receptor-binding epitope on hIL-2 is not directly obstructed by the antibody. F5111 ICs with varying linker lengths bound hIL-2Rα with similar affinities, all of which were >2-fold higher than those of free hIL-2 and hIL-2/F5111 complex due to bivalent cytokine presentation (Figures 2A, middle, S1C, middle, and S1D, middle; Table S2). Control IC had a 5-fold higher affinity for hIL-2Rα compared with free IL-2 (Figure 2A, middle; Table S2). A 2-fold lower hIL-2Rα affinity was observed for F5111 IC LN15 compared with F5111 IC LN25 and F5111 IC LN35, likely due to oligomerization. Indeed, among the three peaks of F5111 IC LN25, P3 had the highest and P1 had the lowest IL-2Rα affinity (Figure S1E, middle).

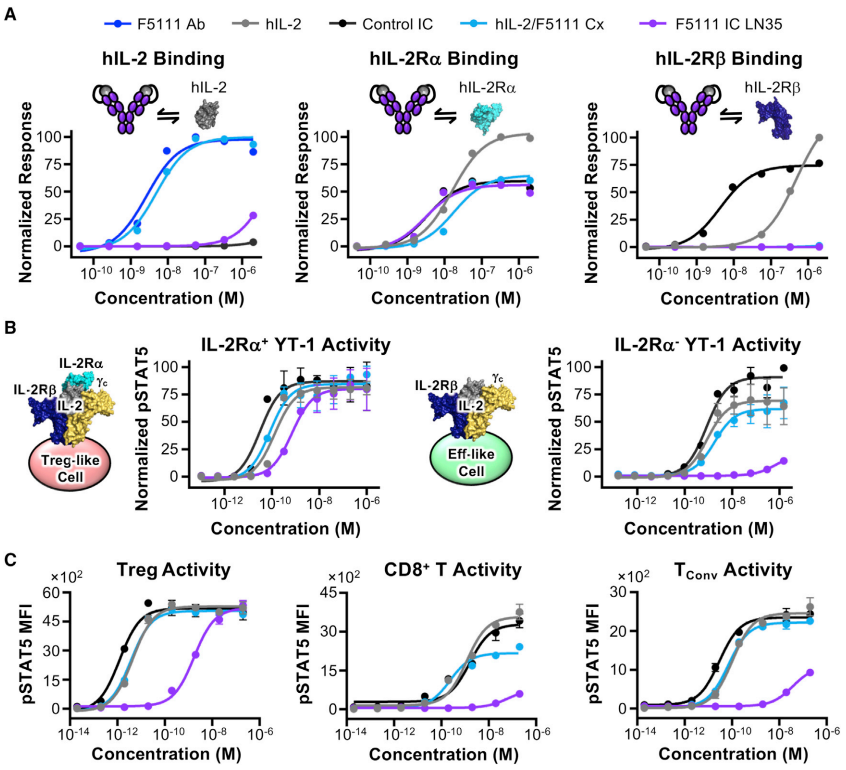

Figure 2. F5111 IC blocks IL-2 binding to IL-2Rβ and biases toward Treg activation

(A) Equilibrium biolayer interferometry-based titrations of F5111 antibody (Ab), hIL-2, control IC, hIL-2/F5111 complex (Cx, 1:1 molar ratio), and F5111 IC LN35 binding to hIL-2 (left), hIL-2Rα (middle), or hIL-2Rβ (right).

(B) STAT5 phosphorylation response of IL-2Rα$^+$ (left) and IL-2Rα$^-$ (right) YT-1 cells stimulated with hIL-2, control IC, hIL-2/F5111 Cx (1:1 molar ratio), or F5111 IC LN35.

(C) STAT5 phosphorylation responses of stimulated human Treg (left), CD8$^+$ T (middle), and T_{Conv} (right) cells. Data represent mean ± SD (n = 3). See also Figures S1 and S2; Tables S2, S3, and S4.

In contrast with hIL-2Rα, hIL-2Rβ should *not* bind F5111 IC since F5111 fully blocks the receptor binding epitope on hIL-2. Control IC had a 100-fold hIL-2Rβ affinity improvement over free hIL-2 due to its bivalency (Figure 2A, right; Table S2). Whereas binding to hIL-2Rβ was completely abolished for hIL-2/F5111 complex (Figure 2A, right; Table S2), F5111 IC LN15 showed similar hIL-2Rβ affinity to free hIL-2 (Figure S1C, right), indicating deficient intramolecular assembly. Lengthening the linker eliminated these issues, as F5111 IC LN25 and F5111 IC LN35 did not engage hIL-2Rβ (Figures 2A, right, S1C, right, and S1D, right; Table S2). F5111 IC LN25 P1 and F5111 IC LN25 P2 bound hIL-2Rβ weakly, whereas F5111 LN25 P3 did not bind hIL-2Rβ (Figure S1E, right). Overall, hIL-2 cytokine and receptor binding studies confirmed proper assembly and function of F5111 ICs.

F5111 ICs demonstrate Treg bias *in vitro*

IL-2-dependent STAT5 phosphorylation (pSTAT5) was assessed on YT-1 human NK cells that either express (Treg-like) or lack (Eff-like) IL-2Rα (Kuziel et al., 1993). ICs were compared with hIL-2/F5111 complex (1:1 molar ratio), and increasing antibody-to-cytokine ratio did not affect signaling potency (Figure S1B; Table S3).

On IL-2Rα$^+$ (Treg-like) cells, F5111 IC LN15, F5111 IC LN25, and F5111 IC LN35 induced robust activation, similar to free hIL-2 and hIL-2/F5111 complex (Figures 2B, left, and S1F; Table S3). Control IC was more potent than free hIL-2 due to its bivalency, whereas F5111 ICs were slightly less potent due to incomplete cytokine/antibody dissociation. On IL-2Rα$^-$ (Eff-like) cells, F5111 IC LN15 was 15-fold less potent than free hIL-2 and control IC, and F5111 IC LN25 and

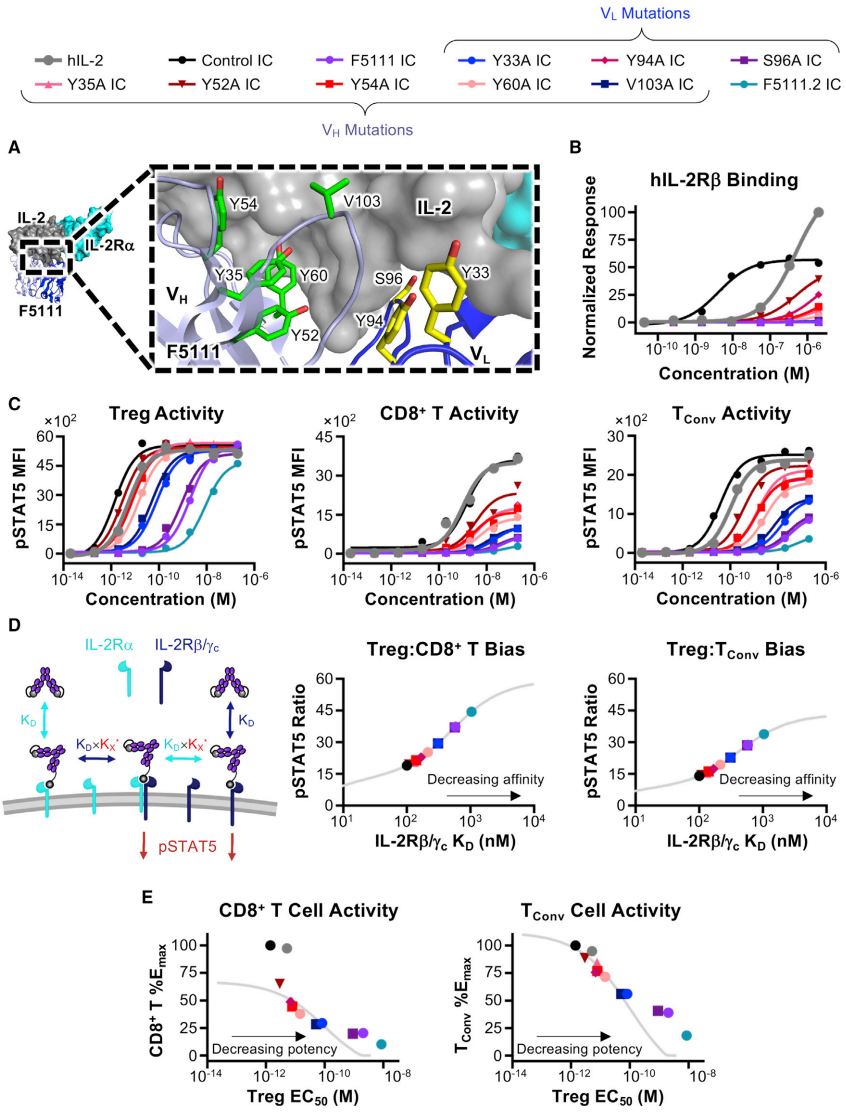

Figure 3. Tuning IC intramolecular affinity modulates Treg bias

(A) hIL-2/F5111 crystal structure (PDB: 5UTZ) with alanine-mutated residues shown in yellow (LC) or green (HC). Human IL-2Rα is overlaid from the IL-2 quaternary complex structure (PDB: 2B5I).

(B) Equilibrium biolayer interferometry-based titrations against hIL-2Rβ.

(legend continued on next page)

F5111 IC LN35 induced little to no activation (Figures 2B, right, and S1G; Table S3). In contrast, hIL-2/F5111 complex was only ~2-fold less potent than free hIL-2 on IL-2Rα$^-$ cells, highlighting the enhanced IL-2Rα$^+$ cell bias of ICs versus the complex. The two peaks of F5111 IC LN15 elicited ~10-fold weaker activation of IL-2Rα$^-$ cells relative to free hIL-2 (Figure S1H, top; Table S3). For F5111 IC LN25, P1 and P2 EC_{50} values were 50- and 100-fold weaker than that of hIL-2, respectively, whereas P3 was >2,000-fold weaker (Figure S1H, bottom; Table S3). All three peaks of F5111 IC LN25 were less active on IL-2Rα$^-$ cells compared with F5111 IC LN15, confirming that increased linker length improved IC assembly. The potencies of F5111 IC LN25 and F5111 IC LN35 on IL-2Rα$^+$ and IL-2Rα$^-$ cells were similar; however, less oligomerization was observed for F5111 IC LN35 (Figure 1B). Thus, we proceeded with F5111 IC LN35, hereafter denoted F5111 IC.

To confirm Treg bias in a mixed cell population, IC activity was interrogated on human peripheral blood mononuclear cells (PBMCs). F5111 IC was less potent than free hIL-2 and IL-2/F5111 complex (~500-fold) as well as control IC (~1,000-fold) on Tregs due to incomplete cytokine/antibody dissociation (Figure 2C, left; Table S4). However, equivalent E_{Max} values were achieved for all constructs. F5111 IC did not activate on CD8$^+$ T cells, as indicated by reduced potency and ~80% reduction in E_{Max} value compared with free hIL-2 and control IC (Figure 2C, middle; Table S4). In contrast, hIL-2/F5111 complex showed improved potency on CD8$^+$ T cells with a milder 35% reduction in E_{Max} relative to free IL-2 and control IC. Similarly, F5111 IC induced little to no activation of conventional CD4$^+$ T cells (T_{Conv}), with 55% lower E_{Max} compared with free hIL-2 and control IC (Figure 2C, right; Table S4). However, hIL-2/F5111 complex activated T_{Conv} cells with similar potency and E_{Max} as free IL-2, presumably due to complex dissociation. Control IC was more potent than free hIL-2 due to bivalency. Collectively, PBMC studies revealed that F5111 IC, but not IL-2/F5111 complex, is strongly biased toward Treg versus Eff activation due to preferential engagement of IL-2Rα^{High} cell subsets.

To understand the more dramatic potency reduction for F5111 IC compared with free hIL-2 on human Tregs compared with IL-2Rα$^+$ YT-1 cells, we quantified IL-2Rα expression on these cells. IL-2Rα mean fluorescence intensity (MFI) on Tregs was only 40-fold greater than the fluorescence minus one (FMO) control, whereas IL-2Rα MFI was 75-fold greater than FMO control for IL-2Rα$^+$ YT-1 cells (Figure S2B, left), indicating that YT-1 cells express more IL-2Rα than Tregs. IL-2Rα MFI levels on CD8$^+$ T, T_{Conv}, and IL-2Rα$^-$ YT-1 cells were close to FMO background (Figure S2B, right). As F5111 IC binding requires IL-2Rα-dependent disruption of the cytokine/antibody interaction, lower expression of IL-2Rα on human primary cells rationalizes the weakened activity of F5111 IC on Tregs.

Tuning IC intramolecular affinity modulates IL-2 receptor binding and Treg bias

Based on our mechanistic understanding of F5111 IC activity, we hypothesized that modulating cytokine/antibody affinity would impact relative engagement of IL-2Rα^{High} versus IL-2Rα^{Low} cells, enabling optimization of IC bias on different cell types with various IL-2Rα expression levels. We conjectured that reducing the IL-2/F5111 interaction affinity would lead to enhanced IL-2 signaling, particularly on human Tregs. Informed by the structure of the IL-2/F5111 complex (Trotta et al., 2018), we rationally designed a panel of eight single-point alanine mutations of the F5111 antibody, including three variable LC (V_L) (Y33, Y94, and S96) and five variable HC (V_H) (Y35, Y52, Y54, Y60, and V103) residues at the cytokine/antibody interface (Figure 3A). Each F5111 variant and the affinity matured F5111.2 antibody (Rondon et al., 2015) were produced as ICs with 35 amino acid linkers (Figure S3A).

Bio-layer interferometry studies showed that F5111 IC variants minimally engaged hIL-2, confirming their intramolecular assembly (Figure S3B; Table S2). All IC variants bound hIL-2Rα with similar affinities, comparable with the parent F5111 IC (Figure S3B; Table S2). All IC variants showed significantly weaker IL-2Rβ binding compared with free hIL-2 and control IC, indicating successful receptor blockade (Figure 3B; Table S2). However, whereas most IC variants completely ablated hIL-2Rβ binding, IC variants Y94A, Y35A, Y52A, Y54A, and Y60A detectably bound hIL-2Rβ at high concentrations, suggesting weaker cytokine/antibody interactions for these clones.

We wondered whether hIL-2Rβ binding differences between IC variants would impact IL-2 signaling bias. In human PBMC studies, all F5111 IC variants either maintained or enhanced Treg potency compared with the parent F5111 antibody (Figure 3C, left; Table S4), indicating that the mutations weakened cytokine/antibody binding, as intended. IC variants were grouped into three cohorts: the "high"-potency group (Y94A, Y35A, Y52A, Y54A, and Y60A ICs), which were of similar potency to control IC; the "intermediate"-potency group (Y33A and V103A ICs), which were ~50-fold weaker than control IC; and the "low"-potency group (parent F5111 IC and the S96A IC), which were ~1,000-fold weaker than control IC. F5111.2 IC impaired the Treg potency (>6,000-fold weaker than control IC) due to reduced cytokine/antibody dissociation. As anticipated, weakened cytokine/antibody affinity also potentiated the activity of F5111 IC variants on both CD8$^+$ T cells (Figure 3C, middle; Table S4) and T_{Conv} cells (Figure 3C, right; Table S4). However, all IC variants showed impaired Eff activation compared with free hIL-2 and control IC, meaning they retained some Treg bias. IC variants with the highest Treg potencies led to the most potent CD8$^+$ T and T_{Conv} cell activation, and F5111.2 IC, which was the least potent on Tregs, elicited the weakest Eff activation. Moreover, signaling potency on both Treg and Effs was directly correlated with extent of hIL-2Rβ engagement, as anticipated.

(C) STAT5 phosphorylation responses of stimulated human Treg (left), CD8$^+$ T (middle), and T_{Conv} (right) cells.
(D) Schematic of multivalent binding model (left). Predicted Treg:CD8$^+$ T (middle) and Treg:T_{Conv} (right) pSTAT5 ratios for ICs at 10 pM concentration are plotted against predicted IL2Rβ/γ_c K_D (nM).
(E) Predicted (lines) and experimental (points) percent control IC pSTAT5 E_{Max} on CD8$^+$ T (left) or T_{Conv} (right) cells plotted against the predicted (lines) or experimental (points) pSTAT5 EC_{50} on Tregs for each IC. See also Figure S3; Tables S2 and S4.

F5111 IC variants represent a panel of IL-2Rα "probes," as illustrated by IL-2Rα MFI analysis within the activated cell populations for various immune cell subsets. At saturating concentrations, the mean IL-2Rα MFIs of activated Tregs were similar following treatment with all F5111 ICs except for the significantly less potent F5111.2 IC (Figure S3C, left). This finding suggests that Treg cell IL-2Rα expression is sufficient to induce cytokine/antibody dissociation for all F5111 ICs other than F5111.2 IC, which requires more IL-2Rα to induce cytokine/antibody dissociation. On $CD8^+$ T and T_{Conv} cells, ICs that induced more potent activation required lower levels of IL-2Rα to stimulate IL-2 signaling (Figure S3C, middle and right).

To further explore the relationship between cytokine/antibody affinity and Treg bias of ICs we developed a multivalent binding model that predicts F5111 IC signaling properties in specific immune cell subsets based on receptor affinity (Figure 3D, left). This model accurately predicted activities of the IC variants (Figures S3D–S3F) and inferred hIL-2Rβ/γ_c affinities (Figures S3G and S3H), which we could not measure experimentally since IC variants did not reach binding saturation. We plotted the predicted affinity of each IC against the predicted Treg:$CD8^+$ T and Treg:T_{Conv} pSTAT5 MFI ratios at a fixed concentration (Figure 3D, middle and right). As IC affinity toward hIL-2Rβ/γ_c decreased, Treg bias increased. Bias resulted from attenuated signaling on both $CD8^+$ T and T_{Conv} cells but was also accompanied by decreased activation of Tregs (Figures 3C and 3E), illustrating the trade-off between Treg activation and selectivity. We selected three IC variants for further analysis that improved Treg potency while minimizing Eff activation (Y60A, Y33A, and V103A ICs).

To improve their therapeutic potential, we introduced the N297A mutation into the Fc region of all ICs. This mutation prevents glycosylation, which significantly impairs Fc γ receptor binding and thus reduces antibody effector functions (Delidakis et al., 2022; Mimura et al., 2000, 2001; Saunders, 2019; Tao et al., 1993; Wang et al., 2018). Bio-layer interferometry studies showed no differences in hIL-2, hIL-2Rα, and hIL-2Rβ binding between F5111 IC with and without the N297A mutation (Figure S4A; Table S2). Human PBMC signaling assays confirmed that N297A mutation did not affect the activity of control IC, F5111 IC, or IC variants (Figures S4B and S4C; Table S4). Thus, IC will hereafter denote the IC with the N297A mutation unless otherwise indicated.

Parent F5111 IC maximizes Treg expansion bias

We sought to determine whether the *in vitro* IL-2 signaling bias of our engineered ICs toward activation of Tregs would translate into selective expansion of Tregs in mice. We first evaluated IC potencies on splenocytes isolated from non-obese diabetic (NOD) mice. IC activation trends on mouse primary cells were similar to those on human PBMCs (Figures S4C and S4D; Tables S4 and S5), albeit with weaker potency due to the lower affinity of hIL-2 for mIL-2 versus hIL-2 receptors (Spangler et al., 2015a).

To inform *in vivo* dosing, we plotted *in vitro* Treg:$CD8^+$ T and Treg:T_{Conv} pSTAT5 MFI ratios as a function of IC concentration (Figure S4E). Each IC variant exhibited a unique optimum concentration and maximum level of Treg bias, and variants that were more potent on Tregs had lower optimum concentrations and higher magnitude biases.

NOD mice were treated with each IC and immune cell subset expansion was evaluated in harvested spleens (Figure S5A). Y33A IC, V103A IC, and Y60A IC showed significant Treg bias (Figure 4A), but remarkably, the parent F5111 IC led to the most biased Treg expansion among the ICs tested, indicating that the optimum hIL-2/antibody affinity for Treg bias corresponded to that of the parent F5111 IC. This is visualized by plotting the Treg:$CD8^+$ T cell ratio against Treg potency for each IC (Figure 4B; Table S4). If Treg activity is weak (as for F5111.2 IC), no activity is observed on any immune cell subset. If the Treg activity is too potent (as for control IC), all immune cell subsets are activated, confounding Treg bias. The optimum Treg EC_{50} lies between these extrema, and F5111 IC is close to this optimum. Non-negative matrix factorization was performed using a two-component analysis, revealing that F5111 IC had equivalent Treg specificity IC variants while maintaining inhibition of Eff activation (Figure 4C).

We also evaluated our panel of IC variants in a humanized mouse model. BALB/c $Rag2^{-/-}$ $\gamma_c^{-/-}$ $H2^d$ mice engrafted with human PBMC were treated with ICs and immune cell subset expansion in the peritoneum was measured. In contrast to NOD mouse results, optimal Treg expansion bias was observed for Y60A IC and Y33A IC (Figure S4F), which have weaker cytokine/antibody affinity than the parent F5111 IC. Thus, the optimal Treg-promoting therapy may vary between mice and humans.

To assess the impact of Fc effector function on IC-induced Treg expansion, we compared immune activation by the IC with and without the N297A mutation. F5111 IC with the N297A mutation (impaired Fc effector function) led to significantly more Treg bias and >3-fold more Treg expansion (Figure S5B); thus we elected to employ F5111 IC with impaired Fc effector function in mouse models of disease.

F5111 IC exhibits greater Treg bias than hIL-2/F5111.2 complex

We hypothesized that the IC could have stability improvements over cytokine/antibody complexes; thus, we compared the previously reported lead IL-2/antibody complex (hIL-2/F5111.2 complex) (Trotta et al., 2018) to our lead construct (F5111 IC). The N297A mutation was installed in the F5111.2 antibody for consistency with F5111 IC. Bio-layer interferometry studies showed that the F5111.2 antibody and hIL-2/F5111.2 complex (1:1 molar ratio) bound to hIL-2, whereas F5111 IC and control IC had little to no hIL-2 binding (Figure S5C, left; Table S2). hIL-2/F5111.2 complex bound hIL-2Rα with ∼18-fold weaker affinity than F5111 IC and control IC and ∼3-fold weaker affinity than free hIL-2 (Figure S5C, middle; Table S2), consistent with previous data (Trotta et al., 2018). Both hIL-2/F5111.2 complex and F5111 IC fully blocked binding to hIL-2Rβ (Figure S5C, right; Table S2).

On human Tregs, F5111 IC and hIL-2/F5111.2 complex (1:1 molar ratio) were ∼1,700- and ∼10-fold weaker than control IC on Tregs, respectively (Figure 5A, left; Table S4). On $CD8^+$ T cells, F5111 IC and hIL-2/F5111.2 reduced the E_{Max} by 85% and 80%, respectively, relative to control IC (Figure 5A, middle; Table S4). On T_{Conv} cells, F5111 IC was ∼1,000-fold weaker with a 60% reduction in E_{Max}, whereas hIL-2/F5111.2 complex

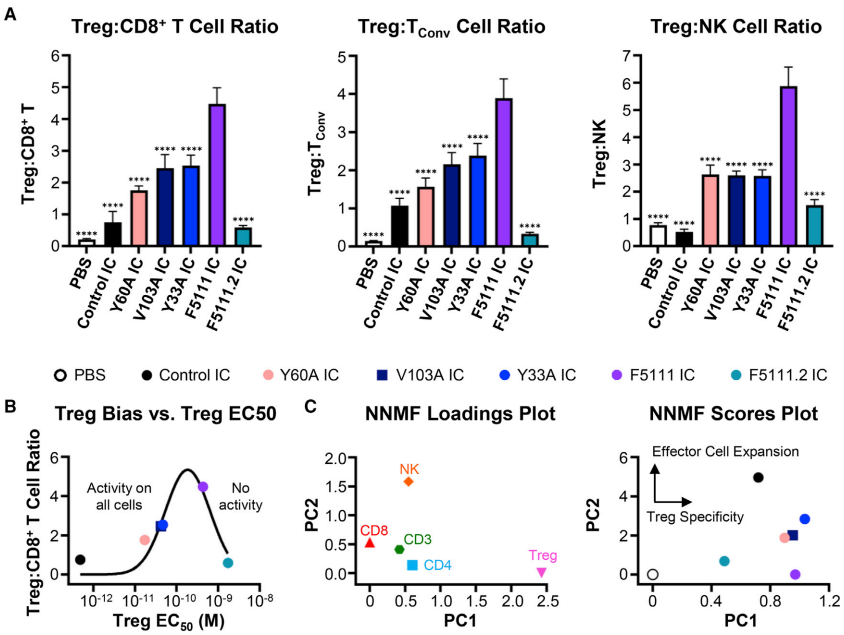

Figure 4. Parent F5111 IC induces maximum Treg expansion bias

(A) Treg:CD8$^+$ T (left), Treg:T_{Conv} (middle), and Treg:NK (right) cell ratios in NOD mice spleens after four daily treatments with PBS (n = 4) or 8.2 μg (1.5 μg IL-2 equivalence) control IC (n = 4), Y60A IC (n = 5), V103A IC (n = 4), Y33A IC (n = 4), F5111 IC (n = 5), or F5111.2 IC (n = 4). Data represent mean + SD. Statistical significance compared with F5111 IC is shown (all data in Table S6).

(B) Plot of Treg:CD8$^+$ T cell *in vivo* expansion ratio versus pSTAT5 EC_{50} on human Tregs (Figure S4C, left; Table S4). Data were fit to a Gaussian distribution.

(C) Non-negative matrix factorization (NNMF) loadings plot (left) and scores plot (right) of *in vivo* cell subset expansion studies in NOD mice. *p ≤ 0.05, **p ≤ 0.01, ***p ≤ 0.001, ****p ≤ 0.0001. See also Figures S4 and S5.

was ~7-fold weaker with a 50% reduction in E_{Max} relative to control IC (Figure 5A, middle; Table S4).

NOD mouse studies showed that both F5111 IC and hIL-2/F5111.2 complex (2:1 cytokine:antibody molar ratio) led to 15-fold increases in the total number of Tregs compared with untreated mice, and induced 3-fold more Treg expansion than control IC (Figure 5B). F5111 IC and hIL-2/F111.2 complex treatment also led to significantly less CD8$^+$ T, T_{Conv}, and NK cell expansion compared with control IC, with the IC inducing less Eff expansion than the complex (Figure 5B). Both F5111 IC and hIL-2/F5111.2 complex elevated expression of forkhead box P3 (FOXP3) within the Treg population compared with control IC, with the IC inducing significantly more FOXP3 expression than the complex (Figure 5C). In addition, F5111 IC and hIL-2/F5111.2 complex increased IL-2Rα expression on Treg, CD8$^+$ T, and T_{Conv} cells relative to control IC (Figure 5C). Both F5111 IC and hIL-2/F5111.2 complex augmented the Treg:CD8$^+$ T, Treg:T_{Conv}, and Treg:NK cell ratios compared with control IC, with the IC eliciting significantly more bias than the complex (Figure 5D). Notably, F5111 IC treatment resulted in >80% Tregs within the CD4$^+$ population, a massive expansion over the 10% Treg proportion observed in saline-treated mice (Figure 5E). F5111 IC treatment also significantly increased the percentage of Ki-67$^+$ (proliferating) Tregs and lowered the percentage of Ki-67$^+$ CD8$^+$ T, T_{Conv}, and NK cells compared with hIL-2/F5111.2 complex and control IC (Figure 5F). Taken together, our *in vivo* data showcase the Treg-biasing capacity of F5111 IC, and demonstrate its superiority to cytokine/antibody complex.

F5111 IC induces durable expansion of functional Tregs

Dose dependence studies of F5111 IC-induced Treg expansion showed that Treg frequency within the CD4$^+$ T cell population was consistent down to a dose of 0.5 μg IL-2 equivalence (Figure S5D). Kinetic studies revealed that Treg percentage within the CD4$^+$ population was highest 1 day after the final of four daily F5111 IC doses, and the percentage declined monotonically for each subsequent time point but still remained elevated after 1 week (Figures 6A and 6B). Similarly, maximum Treg bias was observed 1 day after the last dose, and bias was mostly gone after 5 days (Figure 6C). Serum levels of F5111 IC in C57BL/6 mice followed a two-phase decay with a fast half-life of ~5 min and a slow half-life of 35 h (Figure 6D).

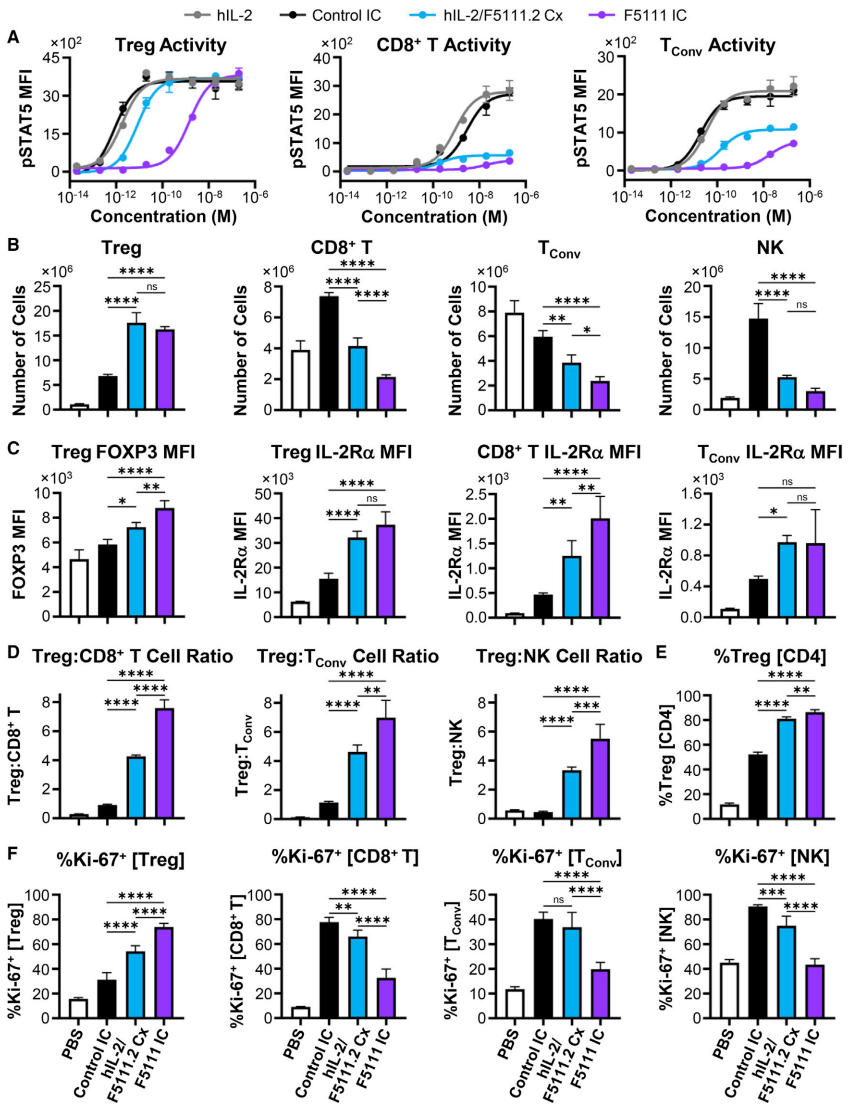

Figure 5. F5111 IC shows greater Treg bias than hIL-2/F5111.2 complex

(A) pSTAT5 response of stimulated human Treg (left), $CD8^+$ T (middle), and T_{Conv} (right) cells. hIL-2/F5111.2 complex (Cx) was at a 1:1 molar ratio.

(B–E) NOD mice (n = 4 per group) were treated daily for 4 days with PBS, 1.5 μg hIL-2 with 6.6 μg F5111.2 antibody (1:2 molar ratio), or 8.2 μg (1.5 μg IL-2 equivalence) control IC or F5111 IC.

(B) Number of Treg, $CD8^+$ T, T_{Conv}, and NK cells.

(C) MFI of FOXP3 within Tregs (left) and IL-2Rα MFI within Treg, $CD8^+$ T, and T_{Conv} cells.

(legend continued on next page)

To characterize the functional properties of Tregs expanded by F5111 IC, we conducted a suppression assay using Tregs isolated from C57BL/6 CD45.1 RFP-FOXP3 mice treated with either saline or F5111 IC. Compared with Tregs isolated from saline-treated mice, Tregs expanded by F5111 IC had equivalent suppressive capacity against naive T_{Conv} cells from C57BL/6 CD45.2 mice. (Figure 6E). We also assessed the phenotype of F5111 IC-expanded Tregs from C57BL/6 mice and found significantly increased numbers of conventional Tregs (cTregs) ($CD4^+FOXP3^+IL\text{-}2R\alpha^{High}BCL\text{-}2^{High}$) but not effector Tregs ($CD4^+FOXP3^+IL\text{-}2R\alpha^{Low}BCL\text{-}2^{Low}$) (Figure 6F). Interestingly, control IC treatment resulted in a reduced number of cTregs compared with saline-treated mice, whereas eTreg numbers were not affected. This aligns with the mechanism of F5111 IC, which biases the molecule toward immune cell subsets with high levels of IL-2Rα.

F5111 IC treatment does not impair immune response to infection

A potential concern for therapeutic administration of a Treg-promoting agent, such as F5111 IC, is that it may interfere with T cell-mediated clearance of infection (Belkaid and Tarbell, 2009; Belkaid et al., 2006; Oldenhove et al., 2009; Sacks and Anderson, 2004). We therefore probed the effects of F5111 IC in a mouse model of toxoplasmosis. Treatment with either F5111 IC or control IC following *Toxoplasma gondii* infection conferred protection against disease-associated weight loss compared with saline treatment (Figure 6G), and no significant differences were observed in lung parasite burden (Figure 6H). Control IC and F5111 IC led to similar changes in parasite burden in the liver relative to saline treatment. Histological analysis of immune-mediated liver pathology in control IC-treated mice showed exacerbated leukophilia and necrosis compared with saline-treated mice (Figure S5E). Interestingly, despite similar parasite burden to control IC-treated animals, F5111 IC-treated mice showed an overall reduction in immunopathological changes compared with saline-treated mice (Figure S5E). Importantly, F5111 IC and control IC behaved similarly in this model even though F5111 IC significantly increased Treg numbers (Figure S5F) and skewed ratios of Tregs to both $T\text{-}bet^+Tetramer^+$ $CD8^+$ T cells (Figure 6I) and $T\text{-}bet^+Tetramer^+$ $CD4^+$ T_{Conv} cells (Figure S5G). Expanded Tregs showed evidence of active proliferation (Figure S5H) and upregulation of IL-2Rα (Figure S5I). Overall, this study suggests that, although F5111 IC promotes Treg expansion, it does not impair infection clearance.

F5111 IC efficacy in a mouse colitis model

To evaluate the potential for F5111 IC to prevent autoimmune disease development, we assessed its performance as a prophylactic treatment in a mouse dextran sulfate sodium (DSS)-induced mouse colitis model (Chassaing et al., 2014; Cooper et al., 1993; Okayasu et al., 1990; Spangler et al., 2015a, 2018) (Figure 7A). Both F5111 IC and hIL-2/F5111.2 complex significantly reduced the severity of weight loss and led to decreased disease activity scores on day 15 compared with saline and control IC treatment (Figures 7B, 7C, S6A, and S6B). Relative to control mice without DSS exposure, mice treated with F5111 IC and hIL-2/F5111.2 complex exhibited a less significant colon length reduction compared with mice treated with saline or control IC (Figure 7D). Colon histology analysis revealed that both F5111 IC and hIL-2/F5111.2 complex treatment led to reduced histopathological scores compared with control IC and saline treatment (Figures 7E and S6C). Overall, this colitis model illustrated the capacity of F5111 IC to confer protection against autoimmune disease pathogenesis.

F5111 IC is protective in a mouse model of immune checkpoint inhibitor-induced diabetes mellitus

To further evaluate the therapeutic potential for F5111 IC, we examined its performance in a mouse model of immune checkpoint inhibitor-induced diabetes mellitus (Ansari et al., 2003; Fife et al., 2006; Hu et al., 2020). This model mimics the etiology of a current clinical concern, in which cancer patients treated with immunotherapies are at risk of developing immune-related adverse events, including diabetes (Quandt et al., 2021; Stamatouli et al., 2018; Young et al., 2018). NOD mice were treated with saline, control IC, or F5111 IC, and then administered anti-mouse PD-1 antibody to induce disease (Figure 7F). Saline-treated mice began developing diabetes on day 12, whereas a proportion of control IC-treated mice showed accelerated diabetes onset starting on day 4 (Figures 7G and 7H). In contrast, all mice treated with F5111 IC remained diabetes free until day 22. On day 44 (before onset of spontaneous disease in the control group that did not receive anti-PD-1), 60% of mice treated with F5111 IC were diabetes free, whereas only 10% of mice in the saline-treated group were diabetes free. Disease-free survival was found to be significantly improved for F5111 IC-treated but not control IC-treated mice compared with saline-treated mice. To further assess the durability of F5111 IC therapy in this model, we performed a similar study over 175 days (Figure S6D). F5111 IC led to significant long-term protection compared with saline in immune checkpoint inhibitor-treated mice, as no additional animals developed diabetes after day 31 (Figures S6E and S6F). Control mice that did not receive anti-PD-1 antibody began developing spontaneous diabetes on day 50 and, by day 157, all mice had disease. These studies highlight that the biased Treg expansion induced by F5111 IC is protective in preventing the onset of immune checkpoint inhibitor-induced diabetes in mice and hint that therapy may also help prevent spontaneous diabetes onset in NOD mice.

DISCUSSION

Biased cytokines are of great interest as therapeutics due to their potential to harness the power of natural proteins and precisely

(D) Treg:$CD8^+$ T (left), Treg:T_{Conv} (middle), and Treg:NK cell (right) ratios.
(E) Percent Tregs within the $CD4^+$ T cell population.
(F) Percent Ki-67^+ cells within Treg, $CD8^+$ T, T_{Conv}, and NK cells from NOD mice (n = 5 per group) treated as in (B–E). Data represent mean ± SD. Statistical significance between control IC, hIL-2/F5111.2 Cx, and F5111 IC shown. *p ≤ 0.05, **p ≤ 0.01, ***p ≤ 0.001, ****p ≤ 0.0001. See also Figure S5; Table S4.

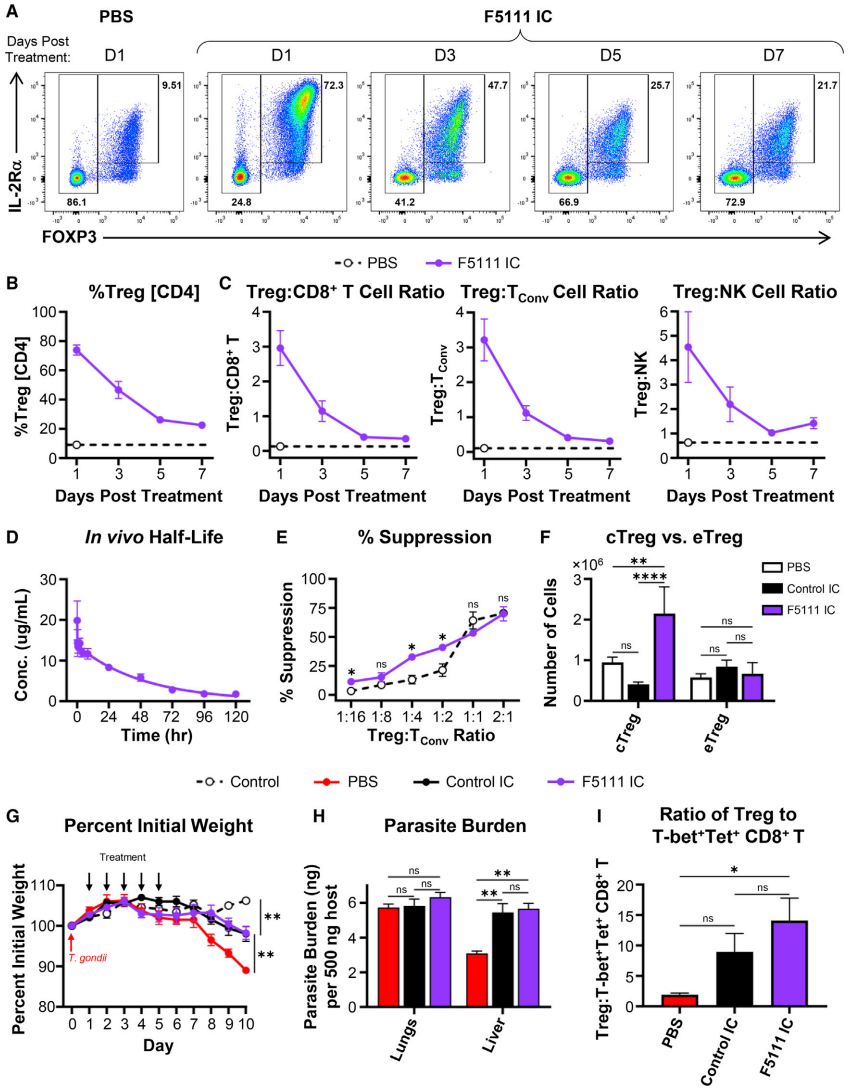

Figure 6. F5111 IC expands functional Tregs without compromising infection immunity

(A–C) C57BL/6 mice (n = 3 per group) were treated daily for 4 days (intraperitoneally) with PBS or 8.2 μg F5111 IC (1.5 μg IL-2 equivalence) and spleens were harvested at the indicated times.

(A) Representative flow plots showing Treg percentage and IL-2Rα versus FOXP3 levels in $CD4^+$ T cells at the indicated times. (B) Percent Tregs within $CD4^+$ T cells at the indicated times. (C) Treg:$CD8^+$ T (left), Treg:T_{Conv} (middle), and Treg:NK (right) at the indicated times. Dashed lines show baseline values for the PBS-treated cohort harvested 1 day after the last dose.

(D) Serum half-life of F5111 IC in C57BL/6 mice (n = 5) treated retro-orbitally with 2 mg/kg F5111 IC (~0.4 mg/kg IL-2 equivalence).

(legend continued on next page)

regulate their biological effects (Spangler et al., 2015b). Ongoing efforts in cytokine targeting include mutein engineering (Peterson et al., 2018; Carmenate et al., 2018; Khoryati et al., 2020; Glassman et al., 2021), selective PEG-ylation (Charych et al., 2016; Dixit et al., 2021; Zhang et al., 2021), and cytokine/antibody complex design (Arenas-Ramirez et al., 2016; Boyman et al., 2006; De Paula et al., 2020; Karakus et al., 2020; Lee et al., 2020b; Spangler et al., 2015a; Tomala et al., 2009; Trotta et al., 2018; Yokoyama et al., 2018). Here, we built upon a Treg-biasing anti-hIL-2 antibody (Trotta et al., 2018) and engineered a single-chain hIL-2/antibody fusion protein (F5111 IC). Compared with hIL-2/antibody complexes, our IC benefits from extended serum half-life, enhanced stability, and reduced counterproductive activation of Effs. Also, the single-chain format results in a stoichiometrically balanced cytokine-to-antibody ratio and streamlines the clinical development pathway. Indeed, F5111 IC induced a more pronounced Treg bias compared with hIL-2/F5111.2 complex.

Tethering IL-2 to an anti-IL-2 antibody enhances the apparent affinity of the cytokine/antibody interaction (Spangler et al., 2018). However, the mechanism of action for biased immune activation by hIL-2/F5111.2 complex requires cytokine/antibody dissociation. We speculated that the strengthened hIL-2/F5111.2 interaction in the context of the IC would hinder cytokine dissociation, rationalizing our choice to use the weaker affinity F5111 antibody in our IC. In fact, when the F5111.2 antibody was formatted as an IC, Treg activation was severely impaired. Thus, although hIL-2/F5111.2 complex led to enhanced Treg bias compared with the hIL-2/F5111 complex, F5111 outperformed F5111.2 when formatted as ICs.

Based on this finding, as well as the differential IL-2Rα expression patterns between mouse and human immune cells, we designed a panel of F5111 IC variants with varying cytokine/antibody affinities and consequent IL-2 receptor interaction properties. Although cellular studies showed increased Treg activation potency for IC variants, this improved activity was accompanied by increased potency on Effs. The IL-2Rα affinities of IC variants were identical, and discrepancies in IL-2Rβ affinities drove differential immune cell subset engagement. Furthermore, IL-2Rα expression levels were lower within $CD8^+$ T and T_{Conv} cell populations activated by IC variants with higher Treg potencies, indicating that these ICs have a lower threshold for activation in the presence of IL-2Rα. Insights from our affinity modulation studies thus provide a roadmap for designing biased IL-2 therapies.

We deployed our IC variants *in vivo*, and a clear cytokine/antibody affinity optimum emerged for the parent F5111 IC, balancing activation of Tregs with concurrent stimulation of Effs. The Treg EC_{50} for F5111 IC was poised at an optimum; enhanced activity on Tregs confounded bias by activating Effs as well, whereas attenuated activity on Tregs led to poor stimulation of all cell types. Importantly, IL-2 receptor expression levels differ between human and mouse cells, and the affinities of receptor subunits toward hIL-2 also vary across species (Spangler et al., 2015a). We observed that the optimal IC variant for biased Treg expansion in humanized mice differed from that in immunocompetent mice, suggesting the possibility for designing patient-specific treatments to address IL-2 receptor level heterogeneity.

F5111 IC design efforts emphasized the importance of optimizing linker length. Shorter linker lengths hindered intramolecular assembly of the cytokine and antibody, driving intermolecular interactions that resulted in higher-order oligomers. Moreover, IC variants with higher Treg potencies eluted as broad single peaks by SEC, whereas F5111.2 IC eluted as a single peak at the expected molecular weight for the monomeric IC, suggesting that stronger cytokine/antibody interactions reduce IC oligomerization. Direct comparison of ICs with intact versus impaired effector function capabilities showed that curbing antibody effector function is critical for avoiding Treg depletion via antibody-dependent cellular cytotoxicity (Saunders, 2019; Wang et al., 2018). Collectively, these findings will guide future IL-2 IC design, and use of the modular hIgG1 scaffold enables extension of the IC approach to other cytokines.

In vivo studies showed that F5111 IC improves autoimmune disease outcomes in mice, without compromising pathogen clearance. This represents an important translational achievement for the application of hIL-2-based therapies in autoimmune disease treatment, which is hindered by the cytokine's short half-life, dosing complications, off-target effects, and toxicity. Deployment of an IL-2-based therapy in a mouse model of immune checkpoint inhibitor-induced diabetes showed that F5111 IC confers long-term protection against drug-induced disease and continues to protect mice even when control mice develop spontaneous disease. F5111 IC had the reverse effect of control IC, which accelerated disease development, likely due to stimulation of Effs. Acceleration of diabetes onset resonates with previous reports that IL-2 and untethered IL-2/antibody complexes can exacerbate disease pathogenesis (Dong et al., 2021; Tang et al., 2008; Wesley et al., 2010), highlighting the safety, selectivity, and efficacy advantages for our IC. Our therapeutic approach could be extended to additional autoimmune conditions, including multiple sclerosis, systemic lupus erythematosus, and GVHD (Klatzmann and Abbas, 2015; Koreth et al., 2011; Webster et al., 2009), and it could also be leveraged to suppress anti-drug immune responses or to prevent immune-related adverse events in cancer patients (June et al., 2017; Kang et al., 2021; Quandt et al., 2021; Stamatouli et al., 2018).

(E) C57BL/6 CD45.1 RFP-FOXP3 mice were treated daily for 4 days with PBS (n = 3) or 6.2 μg F5111 IC (1.125 μg IL-2 equivalence, n = 2). Percent proliferation suppression of T_{Conv} cells from untreated C57BL/6 CD45.2 mice (n = 5) by titrating ratios of Tregs from spleens of treated mice is shown.
(F) C57BL/6 mice (n = 5 per group) were dosed on days 0, 2, and 4 with PBS or 8.2 μg (1.5 μg IL-2 equivalence) control IC or F5111 IC. Spleens were harvested on day 6. Number of cTregs ($CD4^+FOXP3^+IL\text{-}2R\alpha^{High}BCL\text{-}2^{High}$) and effector (eTregs) ($CD4^+FOXP3^+IL\text{-}2R\alpha^{Low}BCL\text{-}2^{Low}$) are shown.
(G–I) C57BL/6 mice were administered 25 cysts of *T. gondii* on day 0. The control group was not given cysts. Starting on day 1, mice were treated daily for 5 days with PBS (control, n = 5; PBS, n = 4) or 8.2 μg (1.5 μg IL-2 equivalence) control IC (n = 5) or F5111 IC (n = 5). Mice were sacrificed on day 10. (G) Mouse weight. (H) Parasite burden. (I) Treg:T-bet$^+$Tetramer (Tet)$^+$ $CD8^+$ T cell ratio in the spleen. (G–I) Mean ± SEM. All other data are mean ± SD. Statistical significance in percent initial weight on day 10 compared with F5111 IC is shown. *p ≤ 0.05, **p ≤ 0.01, ***p ≤ 0.001, ****p ≤ 0.0001. See also Figure S5.

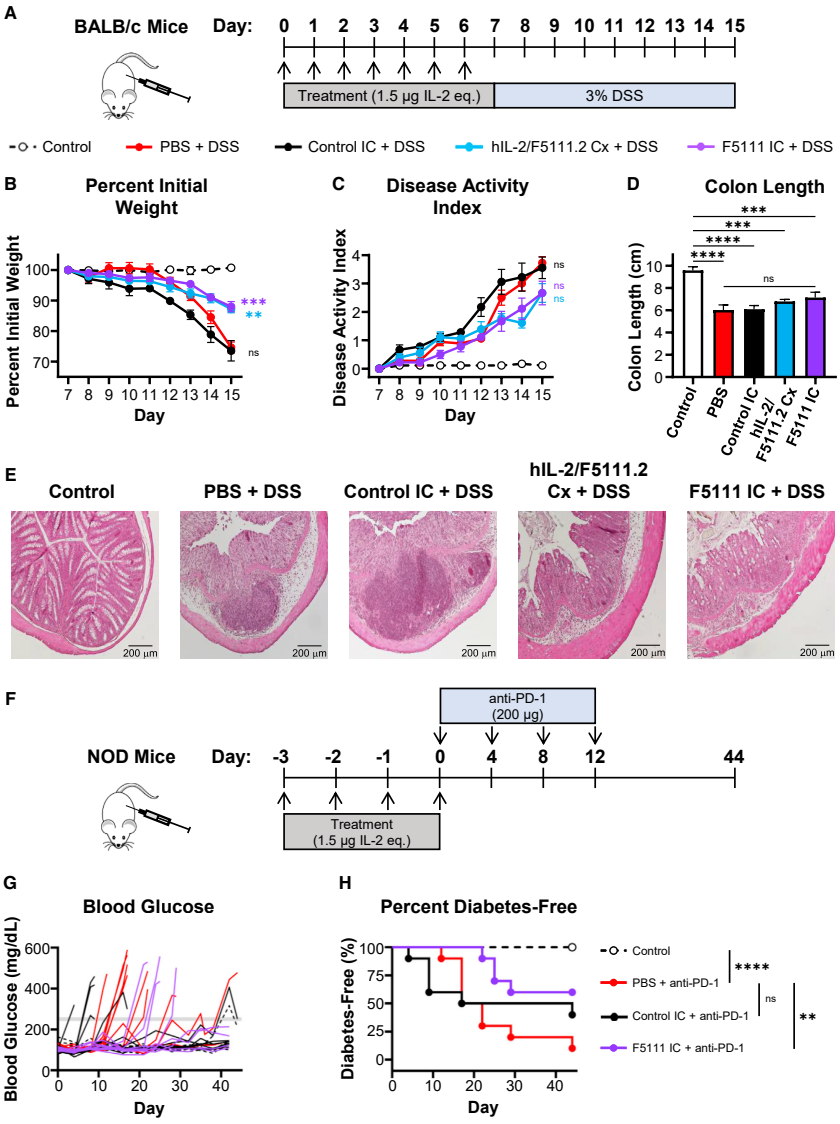

Figure 7. F5111 IC confers protection in mouse models of autoimmune disease

(A) BALB/c mice (n = 6 per group) were treated daily for 7 days with PBS (control and PBS), 1.5 μg hIL-2 complexed with 6.6 μg F5111.2 antibody (1:2 molar ratio, hIL-2/F5111.2 Cx), or 8.2 μg (1.5 μg IL-2 equivalence) control IC or F5111 IC. Beginning on day 7, all groups except disease-free control received 3% DSS in their drinking water.

(B) Weight change.

(C) Disease activity index (DAI).

(legend continued on next page)

F5111 IC biases the activity of IL-2 while also extending its serum half-life; however, it does not target IL-2 toward specific tissues. Several recent approaches have been taken to target IL-2 and other cytokines to specific locations, such as the tumor microenvironment (Hutmacher et al., 2019; Mortara et al., 2018; Ongaro et al., 2020; Silver et al., 2021). Our approach could be integrated with these emerging technologies to bias the local immune microenvironment and enhance therapy. In addition, F5111 could be incorporated with antigen-specific immune-activating technologies to enable targeted activation of disease-protective Tregs. Overall, this work presents a stable, off-the-shelf Treg-expanding agent with potential applications as a research tool and for therapeutic design.

Limitations of the study

Certain limitations need to be addressed in future studies of F5111 IC to advance clinical translation. Mechanistic experiments will consider the comparative effects of F5111 IC on various Treg subsets. For instance, detection of Helios and Neuropilin-1 could be used to interrogate the expansion and survival of thymically versus peripherally derived Tregs (Weiss et al., 2012; Yadav et al., 2012). Additional phenotyping and RNA sequencing studies are also needed to compare the functional activity of F5111 IC-expanded Tregs relative to endogenous Tregs. It will also be important to characterize Treg persistence in disease models to better understand the long-term effects of F5111 IC.

We note that autoimmune disease models in this study used prophylactic treatment strategies due to the rapid onset of pathogenesis. Although there is evidence that preventative treatment can be effective in delaying development of type 1 diabetes (Herold et al., 2019) and that prophylactic therapy could offer benefit in rheumatoid arthritis (Dekkers et al., 2017), such early interventions are not always possible. Thus, future work will explore autoimmune disease reversal. We plan to demonstrate generality of F5111 IC through testing in additional contexts, such as GVHD and allograft rejection models and the experimental autoimmune encephalomyelitis model of multiple sclerosis. Furthermore, although the DSS colitis model has been widely used to evaluate IL-2-based therapies (Abo et al., 2019; Lee et al., 2020a; Sagiv et al., 2009; Spangler et al., 2015a), colitis can also be induced in immunodeficient mice lacking T and B cells using this model (Dieleman et al., 1994; Strober et al., 2002). Therefore, it will be important to demonstrate the clinical potential of F5111 IC in other colitis models, such as the chronic T cell transfer model or 2,4,6-trinitrobenzene sulfonic acid-induced colitis.

Finally, to advance clinical development of F5111 IC, it will be important to address developability considerations. For instance, further optimization of sequence and/or linker length may be needed to increase IC purity and yield. Also, it will be critical to benchmark our molecule against other IL-2-based therapies and Treg-biased molecules. Collectively, downstream studies of the activity, therapeutic efficacy, and biophysical properties of F5111 IC will offer valuable insight into its mechanistic activities and support therapeutic translation.

STAR★METHODS

Detailed methods are provided in the online version of this paper and include the following:

- KEY RESOURCES TABLE
- RESOURCE AVAILABILITY
  - Lead contact
  - Materials availability
  - Data and code availability
- EXPERIMENTAL MODEL AND SUBJECT DETAILS
  - Cell lines
  - Human PBMCs
  - Mice
- METHOD DETAILS
  - Protein purification and expression
  - Yeast surface binding studies
  - Bio-layer interferometry binding measurements
  - YT-1 human NK cell activation studies
  - Human PBMC and mouse splenocyte activation studies
  - Quantification of IL-2Rα expression levels
  - Development of a multivalent binding model for IC signaling
  - Immune cell subset expansion studies in NOD mice
  - Non-negative matrix factorization of immune cell subset expansion studies in NOD mice
  - Immune cell subset expansion studies in humanized mice
  - Immune cell subset expansion study dose titrations
  - Immune cell subset expansion study kinetics
  - Pharmacokinetic study
  - *In vitro* Treg suppression assay
  - Comparison of cTreg versus eTreg expansion
  - *Toxoplasma gondii* infection mouse model
  - DSS–induced colitis mouse model
  - Immune checkpoint inhibitor-induced diabetes mellitus mouse model
- QUANTIFICATION AND STATISTICAL ANALYSIS

SUPPLEMENTAL INFORMATION

Supplemental information can be found online at https://doi.org/10.1016/j.celrep.2022.111478.

(D) Colon lengths on day 15 (n = 6 PBS, Cx, F5111 IC, control; n = 5 control IC).
(E) H&E-stained colons from treated mice (n = 5 control, control IC; n = 6 PBS, Cx, F5111 IC). Scale bar, 200 μm. (B–D) Mean ± SEM. Weight change and DAI plots show significance of control IC-, Cx-, and F5111 IC-treated mice versus PBS-treated mice on day 15. Colon length plot shows significance compared with control group and between PBS- and F5111 IC-treated mice.
(F–H) NOD mice (n = 10 per group) were treated with PBS (control and PBS) or 8.2 μg (1.5 μg IL-2 equivalence) control IC or F5111 IC.
(G) Blood glucose concentrations. The gray line indicates the 250 mg/dL threshold.
(H) Percent diabetes-free mice. Statistical significance compared with mice treated with PBS + anti-PD-1 is shown. *p ≤ 0.05, **p ≤ 0.01, ***p ≤ 0.001, ****p ≤ 0.0001. See also Figure S6.

ACKNOWLEDGMENTS

The authors acknowledge funding from the NIH (K99CA246061, U01AI148119, R01AI125563, R01AI41158, and R01EB029455), DOD (W81XWH-18-1-0735, W81WH-21-1-0892, and W81XWH-21-1-0891), JDRF (1-INO-2020-923-A-N), Czech Science Foundation (20-13029S), Institute of Biotechnology of the Czech Academy of Sciences (RVO 86652036), EU Horizon project ReSHAPE, and the Mark Foundation for Cancer Research. We acknowledge the Czech Centre for Phenogenomics at the Institute of Molecular Genetics (RVO 68378050 and MEYS CR LM2018126). D.V. is an ARCS Foundation Metro-Washington Chapter Scholar and NSF Graduate Research Fellowship Program awardee. A.R.C. is an Oxford-Bristol Myers Squibb Fellow. F.I. is a Wellcome Trust CRCD Fellow (211122/Z/8). The graphical abstract and Figure 3C were created with Biorender.com.

AUTHOR CONTRIBUTIONS

D.V. and J.B.S. conceived and oversaw the project. D.V., M.I., J.T., T.H., J.G., A.Y., J.S., J.B., J.A.P., E.G., A.R.C., L.S.C., A.G.D., B.T.O.-J., and L.M.T. designed, executed, and analyzed the experiments. D.F., A.S.M., D.M.P., J.H., F.I., C.A.H., M.S.A., J.A.B., G.R., and J.B.S. oversaw experiments and analysis. D.V. and J.B.S. wrote the manuscript with input from all authors.

DECLARATION OF INTERESTS

Johns Hopkins University has filed intellectual property on technologies herein with J.B.S. and D.V. as inventors (WO2020264318A1).

INCLUSION AND DIVERSITY

We support inclusive, diverse, and equitable conduct of research.

Received: May 23, 2022
Revised: August 2, 2022
Accepted: September 20, 2022
Published: October 18, 2022

REFERENCES

Abo, H., Flannigan, K.L., Geem, D., Ngo, V.L., Harusato, A., and Denning, T.L. (2019). Combined IL-2 immunocomplex and anti-IL-5 mAb treatment expands Foxp3+ Treg cells in the absence of Eosinophilia and ameliorates experimental colitis. Front. Immunol. *10*, 459.

Alva, A., Daniels, G.A., Wong, M.K.K., Kaufman, H.L., Morse, M.A., McDermott, D.F., Clark, J.I., Agarwala, S.S., Miletello, G., Logan, T.F., et al. (2016). Contemporary experience with high-dose interleukin-2 therapy and impact on survival in patients with metastatic melanoma and metastatic renal cell carcinoma. Cancer Immunol. Immunother. *65*, 1533–1544. https://doi.org/10.1007/s00262-016-1910-x.

Ansari, M.J.I., Salama, A.D., Chitnis, T., Smith, R.N., Yagita, H., Akiba, H., Yamazaki, T., Azuma, M., Iwai, H., Khoury, S.J., et al. (2003). The programmed death-1 (PD-1) pathway regulates autoimmune diabetes in nonobese diabetic (NOD) mice. J. Exp. Med. *198*, 63–69. https://doi.org/10.1084/jem.20022125.

Arenas-Ramirez, N., Zou, C., Popp, S., Zingg, D., Brannetti, B., Wirth, E., Calzascia, T., Kovarik, J., Sommer, L., Zenke, G., et al. (2016). Improved cancer immunotherapy by a CD25-mimobody conferring selectivity to human interleukin-2. Sci. Transl. Med. *8*, 367ra166. https://doi.org/10.1126/scitranslmed.aag3187.

Baecher-Allan, C., Brown, J.A., Freeman, G.J., and Hafler, D.A. (2001). CD4+CD25high regulatory cells in human peripheral blood. J. Immunol. *167*, 1245–1253. https://doi.org/10.4049/jimmunol.167.3.1245.

Belkaid, Y., and Tarbell, K. (2009). Regulatory T cells in the control of host-microorganism interactions. Annu. Rev. Immunol. *27*, 551–589. https://doi.org/10.1146/annurev.immunol.021908.132723.

Belkaid, Y., Blank, R.B., and Suffia, I. (2006). Natural regulatory T cells and parasites: a common quest for host homeostasis. Immunol. Rev. *212*, 287–300. https://doi.org/10.1111/j.0105-2896.2006.00409.x.

Boder, E.T., and Wittrup, K.D. (1997). Yeast surface display for screening combinatorial polypeptide libraries. Nat. Biotechnol. *15*, 553–557. https://doi.org/10.1038/nbt0697-553.

Boyman, O., and Sprent, J. (2012). The role of interleukin-2 during homeostasis and activation of the immune system. Nat. Rev. Immunol. *12*, 180–190. https://doi.org/10.1038/nri3156.

Boyman, O., Kovar, M., Rubinstein, M.P., Surh, C.D., and Sprent, J. (2006). Selective stimulation of T cell subsets with antibody-cytokine immune complexes. Science *311*, 1924–1927. https://doi.org/10.1126/science.1122927.

Carmenate, T., Ortíz, Y., Enamorado, M., García-Martínez, K., Avellanet, J., Moreno, E., Graça, L., and León, K. (2018). Blocking IL-2 signal in vivo with an IL-2 antagonist reduces tumor growth through the control of regulatory T cells. J. Immunol. *200*, 3475–3484. https://doi.org/10.4049/jimmunol.1700433.

Charych, D.H., Hoch, U., Langowski, J.L., Lee, S.R., Addepalli, M.K., Kirk, P.B., Sheng, D., Liu, X., Sims, P.W., VanderVeen, L.A., et al. (2016). NKTR-214, an engineered cytokine with biased IL2 receptor binding, increased tumor exposure, and marked efficacy in mouse tumor models. Clin. Cancer Res. *22*, 680–690. https://doi.org/10.1158/1078-0432.CCR-15-1631.

Chassaing, B., Aitken, J.D., Malleshappa, M., and Vijay-Kumar, M. (2014). Dextran sulfate sodium (DSS)-Induced colitis in mice. Curr. Protoc. Immunol. *104*, 15.25.1–15.25.14. https://doi.org/10.1002/0471142735.im1525s104.

Collison, L.W., and Vignali, D.A.A. (2011). In vitro Treg suppression assays. Methods Mol. Biol. *707*, 21–37. https://doi.org/10.1007/978-1-61737-979-6_2.

Cooper, H.S., Murthy, S.N., Shah, R.S., and Sedergran, D.J. (1993). Clinicopathologic study of dextran sulfate sodium experimental murine colitis. Lab. Invest. *69*, 238–249.

De Paula, V.S., Jude, K.M., Nerli, S., Glassman, C.R., Garcia, K.C., and Sgourakis, N.G. (2020). Interleukin-2 druggability is modulated by global conformational transitions controlled by a helical capping switch. Proc. Natl. Acad. Sci. USA *117*, 7183–7192. https://doi.org/10.1073/pnas.2000419117.

Dekkers, J.S., Schoones, J.W., Huizinga, T.W., Toes, R.E., and van der Helm-van Mil, A.H. (2017). Possibilities for preventive treatment in rheumatoid arthritis? Lessons from experimental animal models of arthritis: a systematic literature review and meta-analysis. Ann. Rheum. Dis. *76*, 458–467. https://doi.org/10.1136/annrheumdis-2016-209830.

Delidakis, G., Kim, J.E., George, K., and Georgiou, G. (2022). Improving antibody therapeutics by manipulating the Fc domain: immunological and structural considerations. Annu. Rev. Biomed. Eng. *24*, 249–274. https://doi.org/10.1146/annurev-bioeng-082721-024500.

Dieleman, L.A., Ridwan, B.U., Tennyson, G.S., Beagley, K.W., Bucy, R.P., and Elson, C.O. (1994). Dextran sulfate sodium-induced colitis occurs in severe combined immunodeficient mice. Gastroenterology *107*, 1643–1652. https://doi.org/10.1016/0016-5085(94)90803-6.

Dixit, N., Fanton, C., Langowski, J.L., Kirksey, Y., Kirk, P., Chang, T., Cetz, J., Dixit, V., Kim, G., Kuo, P., et al. (2021). NKTR-358: a novel regulatory T-cell stimulator that selectively stimulates expansion and suppressive function of regulatory T cells for the treatment of autoimmune and inflammatory diseases. J. Transl. Autoimmun. *4*, 100103. https://doi.org/10.1016/j.jtauto.2021.100103.

Dong, S., Hiam-Galvez, K.J., Mowery, C.T., Herold, K.C., Gitelman, S.E., Esensten, J.H., Liu, W., Lares, A.P., Leinbach, A.S., Lee, M., et al. (2021). The effect of low-dose IL-2 and Treg adoptive cell therapy in patients with type 1 diabetes. JCI Insight *6*, e147474. https://doi.org/10.1172/jci.insight.147474.

Farhat, A.M., Weiner, A.C., Posner, C., Kim, Z.S., Orcutt-Jahns, B., Carlson, S.M., and Meyer, A.S. (2021). Modeling cell-specific dynamics and regulation of the common gamma chain cytokines. Cell Rep. *35*, 109044. https://doi.org/10.1016/j.celrep.2021.109044.

Fife, B.T., Guleria, I., Gubbels Bupp, M., Eagar, T.N., Tang, Q., Bour-Jordan, H., Yagita, H., Azuma, M., Sayegh, M.H., and Bluestone, J.A. (2006). Insulin-induced remission in new-onset NOD mice is maintained by the PD-1–PD-L1 pathway. J. Exp. Med. *203*, 2737–2747. https://doi.org/10.1084/jem.20061577.

Finkelman, F.D., Madden, K.B., Morris, S.C., Holmes, J.M., Boiani, N., Katona, I.M., and Maliszewski, C.R. (1993). Anti-cytokine antibodies as carrier proteins. Prolongation of in vivo effects of exogenous cytokines by injection of cytokine-anti-cytokine antibody complexes. J. Immunol. *151*, 1235–1244.

Glassman, C.R., Su, L., Majri-Morrison, S.S., Winkelmann, H., Mo, F., Li, P., Pérez-Cruz, M., Ho, P.P., Koliesnik, I., Nagy, N., et al. (2021). Calibration of cell-intrinsic interleukin-2 response thresholds guides design of a regulatory T cell biased agonist. eLife *10*, e65777. https://doi.org/10.7554/eLife.65777.

Grover, H.S., Blanchard, N., Gonzalez, F., Chan, S., Robey, E.A., and Shastri, N. (2012). The toxoplasma gondii peptide AS15 Elicits CD4 T cells that can control parasite burden. Infect. Immun. *80*, 3279–3288. https://doi.org/10.1128/IAI.00425-12.

Hernandez, R., Toomer, K.H., Põder, J., Santos Savio, A., Hsiung, S., and Malek, T.R. (2021). Sustained IL-2R signaling of limited duration by high-dose mIL-2/mCD25 fusion protein amplifies tumor-reactive CD8+ T cells to enhance antitumor immunity. Cancer Immunol. Immunother. *70*, 909–921. https://doi.org/10.1007/s00262-020-02722-5.

Hernandez, R., Põder, J., LaPorte, K.M., and Malek, T.R. (2022). Engineering IL-2 for immunotherapy of autoimmunity and cancer. Nat. Rev. Immunol. *72*, 281–311. https://doi.org/10.1038/s41577-022-00680-w.

Herold, K.C., Bundy, B.N., Long, S.A., Bluestone, J.A., DiMeglio, L.A., Dufort, M.J., Gitelman, S.E., Gottlieb, P.A., Krischer, J.P., Linsley, P.S., et al. (2019). An anti-CD3 antibody, teplizumab, in relatives at risk for type 1 diabetes. N. Engl. J. Med. *381*, 603–613. https://doi.org/10.1056/NEJMoa1902226.

Höfer, T., Krichevsky, O., and Altan-Bonnet, G. (2012). Competition for IL-2 between regulatory and effector T cells to chisel immune responses. Front. Immunol. *3*, 268. https://doi.org/10.3389/fimmu.2012.00268.

Honegger, A., Spinelli, S., Cambillau, C., and Plückthun, A. (2005). A mutation designed to alter crystal packing permits structural analysis of a tight-binding fluorescein–scFv complex. Protein Sci. *14*, 2537–2549. https://doi.org/10.1110/ps.051520605.

Hu, H., Zakharov, P.N., Peterson, O.J., and Unanue, E.R. (2020). Cytocidal macrophages in symbiosis with CD4 and CD8 T cells cause acute diabetes following checkpoint blockade of PD-1 in NOD mice. Proc. Natl. Acad. Sci. USA *117*, 31319–31330. https://doi.org/10.1073/pnas.2019743117.

Hutmacher, C., Gonzalo Núñez, N., Liuzzi, A.R., Becher, B., and Neri, D. (2019). Targeted delivery of IL2 to the tumor stroma potentiates the action of immune checkpoint inhibitors by preferential activation of NK and CD8+ T cells. Cancer Immunol. Res. *7*, 572–583. https://doi.org/10.1158/2326-6066.CIR-18-0566.

June, C.H., Warshauer, J.T., and Bluestone, J.A. (2017). Is autoimmunity the Achilles' heel of cancer immunotherapy? Nat. Med. *23*, 540–547. https://doi.org/10.1038/nm.4321.

Kang, J.H., Bluestone, J.A., and Young, A. (2021). Predicting and preventing immune checkpoint inhibitor toxicity: targeting cytokines. Trends Immunol. *42*, 293–311. https://doi.org/10.1016/j.it.2021.02.006.

Karakus, U., Sahin, D., Mittl, P.R.E., Mooij, P., Koopman, G., and Boyman, O. (2020). Receptor-gated IL-2 delivery by an anti-human IL-2 antibody activates regulatory T cells in three different species. Sci. Transl. Med. *12*, eabb9283. https://doi.org/10.1126/scitranslmed.abb9283.

Khoryati, L., Pham, M.N., Sherve, M., Kumari, S., Cook, K., Pearson, J., Bogdani, M., Campbell, D.J., and Gavin, M.A. (2020). An IL-2 mutein engineered to promote expansion of regulatory T cells arrests ongoing autoimmunity in mice. Sci. Immunol. *5*, eaba5264. https://doi.org/10.1126/sciimmunol.aba5264.

Klatzmann, D., and Abbas, A.K. (2015). The promise of low-dose interleukin-2 therapy for autoimmune and inflammatory diseases. Nat. Rev. Immunol. *15*, 283–294. https://doi.org/10.1038/nri3823.

Knudson, K.M., Hodge, J.W., Schlom, J., and Gameiro, S.R. (2020). Rationale for IL-15 superagonists in cancer immunotherapy. Expert Opin. Biol. Ther. *20*, 705–709. https://doi.org/10.1080/14712598.2020.1738379.

Koreth, J., Matsuoka, K.i., Kim, H.T., McDonough, S.M., Bindra, B., Alyea, E.P., Armand, P., Cutler, C., Ho, V.T., Treister, N.S., et al. (2011). Interleukin-2 and regulatory T cells in graft-versus-host disease. N. Engl. J. Med. *365*, 2055–2066. https://doi.org/10.1056/NEJMoa1108188.

Kuziel, W.A., Ju, G., Grdina, T.A., and Greene, W.C. (1993). Unexpected effects of the IL-2 receptor alpha subunit on high affinity IL-2 receptor assembly and function detected with a mutant IL-2 analog. J. Immunol. *150*, 3357–3365.

Lee, H., Son, Y.S., Lee, M.-O., Ryu, J.-W., Park, K., Kwon, O., Jung, K.B., Kim, K., Ryu, T.Y., Baek, A., et al. (2020a). Low-dose interleukin-2 alleviates dextran sodium sulfate-induced colitis in mice by recovering intestinal integrity and inhibiting AKT-dependent pathways. Theranostics *10*, 5048–5063. https://doi.org/10.7150/thno.41534.

Lee, J.-Y., Lee, E., Hong, S.-W., Kim, D., Eunju, O., Sprent, J., Im, S.-H., Lee, Y.J., and Surh, C.D. (2020b). TCB2, a new anti-human interleukin-2 antibody, facilitates heterodimeric IL-2 receptor signaling and improves anti-tumor immunity. Oncoimmunology *9*, 1681869. https://doi.org/10.1080/2162402X.2019.1681869.

Leonard, W.J., Depper, J.M., Crabtree, G.R., Rudikoff, S., Pumphrey, J., Robb, R.J., Krönke, M., Svetlik, P.B., Peffer, N.J., and Waldmann, T.A. (1984). Molecular cloning and expression of cDNAs for the human interleukin-2 receptor. Nature *311*, 626–631. https://doi.org/10.1038/311626a0.

Liao, W., Lin, J.-X., and Leonard, W.J. (2013). Interleukin-2 at the crossroads of effector responses, tolerance, and immunotherapy. Immunity *38*, 13–25. https://doi.org/10.1016/j.immuni.2013.01.004.

Lin, M.-H., Chen, T.-C., Kuo, T.T., Tseng, C.-C., and Tseng, C.-P. (2000). Real-time PCR for quantitative detection of toxoplasma gondii. J. Clin. Microbiol. *38*, 4121–4125.

Lopes, J.E., Fisher, J.L., Flick, H.L., Wang, C., Sun, L., Ernstoff, M.S., Alvarez, J.C., and Losey, H.C. (2020). ALKS 4230: a novel engineered IL-2 fusion protein with an improved cellular selectivity profile for cancer immunotherapy. J. Immunother. Cancer *8*, e000673. https://doi.org/10.1136/jitc-2020-000673.

Malek, T.R. (2008). The biology of interleukin-2. Annu. Rev. Immunol. *26*, 453–479. https://doi.org/10.1146/annurev.immunol.26.021607.090357.

Mimura, Y., Church, S., Ghirlando, R., Ashton, P.R., Dong, S., Goodall, M., Lund, J., and Jefferis, R. (2000). The influence of glycosylation on the thermal stability and effector function expression of human IgG1-Fc: properties of a series of truncated glycoforms. Mol. Immunol. *37*, 697–706. https://doi.org/10.1016/S0161-5890(00)00105-X.

Mimura, Y., Sondermann, P., Ghirlando, R., Lund, J., Young, S.P., Goodall, M., and Jefferis, R. (2001). Role of oligosaccharide residues of IgG1-Fc in FcγRIIb binding. J. Biol. Chem. *276*, 45539–45547. https://doi.org/10.1074/jbc.M107478200.

Mortara, L., Balza, E., Bruno, A., Poggi, A., Orecchia, P., and Carnemolla, B. (2018). Anti-cancer therapies employing IL-2 cytokine tumor targeting: contribution of innate, adaptive and immunosuppressive cells in the anti-tumor efficacy. Front. Immunol. *9*, 2905. https://doi.org/10.3389/fimmu.2018.02905.

Murray, P.J. (2007). The JAK-STAT signaling pathway: input and output integration. J. Immunol. *178*, 2623–2629. https://doi.org/10.4049/jimmunol.178.5.2623.

Okayasu, I., Hatakeyama, S., Yamada, M., Ohkusa, T., Inagaki, Y., and Nakaya, R. (1990). A novel method in the induction of reliable experimental acute and chronic ulcerative colitis in mice. Gastroenterology *98*, 694–702. https://doi.org/10.1016/0016-5085(90)90290-h.

Oldenhove, G., Bouladoux, N., Wohlfert, E.A., Hall, J.A., Chou, D., Dos Santos, L., O'Brien, S., Blank, R., Lamb, E., Natarajan, S., et al. (2009). Decrease of Foxp3+ Treg cell number and acquisition of effector cell phenotype during lethal infection. Immunity *31*, 772–786. https://doi.org/10.1016/j.immuni.2009.10.001.

Ongaro, T., Gouyou, B., Stringhini, M., Corbellari, R., Neri, D., and Villa, A. (2020). A novel format for recombinant antibody-interleukin-2 fusion proteins exhibits superior tumor-targeting properties in vivo. Oncotarget *11*, 3698–3711. https://doi.org/10.18632/oncotarget.27726.

Pedregosa, F., Varoquaux, G., Gramfort, A., Michel, V., Thirion, B., Grisel, O., Blondel, M., Prettenhofer, P., Weiss, R., Dubourg, V., et al. (2011). Scikit-learn: machine learning in Python. J. Mach. Learn. Res. *12*, 2825–2830. https://doi.org/10.5555/1953048.2078195.

Peterson, L.B., Bell, C.J.M., Howlett, S.K., Pekalski, M.L., Brady, K., Hinton, H., Sauter, D., Todd, J.A., Umana, P., Ast, O., et al. (2018). A long-lived IL-2 mutein that selectively activates and expands regulatory T cells as a therapy for autoimmune disease. J. Autoimmun. *95*, 1–14. https://doi.org/10.1016/j.jaut.2018.10.017.

Quandt, Z., Young, A., Perdigoto, A.L., Herold, K.C., and Anderson, M.S. (2021). Autoimmune Endocrinopathies: an emerging complication of immune checkpoint inhibitors. Annu. Rev. Med. *72*, 313–330. https://doi.org/10.1146/annurev-med-050219-034237.

Romee, R., Cooley, S., Berrien-Elliott, M.M., Westervelt, P., Verneris, M.R., Wagner, J.E., Weisdorf, D.J., Blazar, B.R., Ustun, C., DeFor, T.E., et al. (2018). First-in-human phase 1 clinical study of the IL-15 superagonist complex ALT-803 to treat relapse after transplantation. Blood *131*, 2515–2527. https://doi.org/10.1182/blood-2017-12-823757.

Rondon, I.J., CRELLIN, N.K., Bessette, P., Trotta, E., and Bluestone, J.A. (2015). Anti-IL-2 Antibodies and Compositions and Uses Thereof.

Roopenian, D.C., and Akilesh, S. (2007). FcRn: the neonatal Fc receptor comes of age. Nat. Rev. Immunol. *7*, 715–725. https://doi.org/10.1038/nri2155.

Rosenberg, S.A. (2014). IL-2: the first effective immunotherapy for human cancer. J. Immunol. *192*, 5451–5458. https://doi.org/10.4049/jimmunol.1490019.

Rubinstein, M.P., Kovar, M., Purton, J.F., Cho, J.-H., Boyman, O., Surh, C.D., and Sprent, J. (2006). Converting IL-15 to a superagonist by binding to soluble IL-15R{alpha. Proc. Natl. Acad. Sci. USA *103*, 9166–9171. https://doi.org/10.1073/pnas.0600240103.

Sacks, D., and Anderson, C. (2004). Re-examination of the immunosuppressive mechanisms mediating non-cure of Leishmania infection in mice. Immunol. Rev. *201*, 225–238. https://doi.org/10.1111/j.0105-2896.2004.00185.x.

Sagiv, Y., Kaminitz, A., Lorberboum-Galski, H., Askenasy, N., and Yarkoni, S. (2009). A fusion protein composed of IL-2 and caspase-3 ameliorates the outcome of experimental inflammatory colitis. Ann. N. Y. Acad. Sci. *1173*, 791–797. https://doi.org/10.1111/j.1749-6632.2009.04877.x.

Sahin, D., Arenas-Ramirez, N., Rath, M., Karakus, U., Hümbelin, M., van Gogh, M., Borsig, L., and Boyman, O. (2020). An IL-2-grafted antibody immunotherapy with potent efficacy against metastatic cancer. Nat. Commun. *11*, 6440. https://doi.org/10.1038/s41467-020-20220-1.

Sakaguchi, S., Sakaguchi, N., Asano, M., Itoh, M., and Toda, M. (1995). Immunologic self-tolerance maintained by activated T cells expressing IL-2 receptor alpha-chains (CD25). Breakdown of a single mechanism of self-tolerance causes various autoimmune diseases. J. Immunol. *155*, 1151–1164.

Saunders, K.O. (2019). Conceptual approaches to modulating antibody effector functions and circulation half-life. Front. Immunol. *10*, 1296. https://doi.org/10.3389/fimmu.2019.01296.

Schmidt, A., Oberle, N., and Krammer, P.H. (2012). Molecular mechanisms of treg-mediated T cell suppression. Front. Immunol. *3*, 51. https://doi.org/10.3389/fimmu.2012.00051.

Silver, A.B., Leonard, E.K., Gould, J.R., and Spangler, J.B. (2021). Engineered antibody fusion proteins for targeted disease therapy. Trends Pharmacol. Sci. *42*, 1064–1081. https://doi.org/10.1016/j.tips.2021.09.009.

Sim, G.C., and Radvanyi, L. (2014). The IL-2 cytokine family in cancer immunotherapy. Cytokine Growth Factor Rev. *25*, 377–390. https://doi.org/10.1016/j.cytogfr.2014.07.018.

Spangler, J.B., Tomala, J., Luca, V.C., Jude, K.M., Dong, S., Ring, A.M., Votavova, P., Pepper, M., Kovar, M., and Garcia, K.C. (2015a). Antibodies to Interleukin-2 elicit selective T cell subset potentiation through distinct conformational mechanisms. Immunity *42*, 815–825. https://doi.org/10.1016/j.immuni.2015.04.015.

Spangler, J.B., Moraga, I., Mendoza, J.L., and Garcia, K.C. (2015b). Insights into cytokine–receptor interactions from cytokine engineering. Annu. Rev. Immunol. *33*, 139–167. https://doi.org/10.1146/annurev-immunol-032713-120211.

Spangler, J.B., Trotta, E., Tomala, J., Peck, A., Young, T.A., Savvides, C.S., Silveria, S., Votavova, P., Salafsky, J., Pande, V.S., et al. (2018). Engineering a single-agent cytokine/antibody fusion that selectively expands regulatory T cells for autoimmune disease therapy. J. Immunol. *201*, 2094–2106. https://doi.org/10.4049/jimmunol.1800578.

Stamatouli, A.M., Quandt, Z., Perdigoto, A.L., Clark, P.L., Kluger, H., Weiss, S.A., Gettinger, S., Sznol, M., Young, A., Rushakoff, R., et al. (2018). Collateral damage: insulin-dependent diabetes induced with checkpoint inhibitors. Diabetes *67*, 1471–1480. https://doi.org/10.2337/dbi18-0002.

Strober, W., Fuss, I.J., and Blumberg, R.S. (2002). The immunology of mucosal models of inflammation. Annu. Rev. Immunol. *20*, 495–549. https://doi.org/10.1146/annurev.immunol.20.100301.064816.

Stroud, R.M., and Wells, J.A. (2004). Mechanistic diversity of cytokine receptor signaling across cell membranes. Sci. STKE *2004*, re7. https://doi.org/10.1126/stke.2312004re7.

Tan, Z.C., and Meyer, A.S. (2021). A general model of multivalent binding with ligands of heterotypic subunits and multiple surface receptors. Math. Biosci. *342*, 108714. https://doi.org/10.1016/j.mbs.2021.108714.

Tang, Q., Adams, J.Y., Penaranda, C., Melli, K., Piaggio, E., Sgouroudis, E., Piccirillo, C.A., Salomon, B.L., and Bluestone, J.A. (2008). Central role of a defective interleukin-2 production in triggering islet autoimmune destruction. Immunity *28*, 687–697. https://doi.org/10.1016/j.immuni.2008.03.016.

Taniguchi, T., and Minami, Y. (1993). The IL-2IL-2 receptor system: a current overview. Cell *73*, 5–8. https://doi.org/10.1016/0092-8674(93)90152-G.

Tao, M.H., Smith, R.I., and Morrison, S.L. (1993). Structural features of human immunoglobulin G that determine isotype-specific differences in complement activation. J. Exp. Med. *178*, 661–667. https://doi.org/10.1084/jem.178.2.661.

Tomala, J., and Spangler, J.B. (2020). Characterization of immune cell subset expansion in response to therapeutic treatment in mice. Methods Mol. Biol. *2111*, 101–114. https://doi.org/10.1007/978-1-0716-0266-9_9.

Tomala, J., Chmelova, H., Mrkvan, T., Rihova, B., and Kovar, M. (2009). In vivo expansion of activated naive CD8+ T cells and NK cells driven by complexes of IL-2 and anti-IL-2 monoclonal antibody as novel approach of cancer immunotherapy. J. Immunol. *183*, 4904–4912. https://doi.org/10.4049/jimmunol.0900284.

Tomala, J., Kovarova, J., Kabesova, M., Votavova, P., Chmelova, H., Dvorakova, B., Rihova, B., and Kovar, M. (2013). Chimera of IL-2 linked to light chain of anti-IL-2 mAb mimics IL-2/anti-IL-2 mAb complexes both structurally and functionally. ACS Chem. Biol. *8*, 871–876. https://doi.org/10.1021/cb3007242.

Trotta, E., Bessette, P.H., Silveria, S.L., Ely, L.K., Jude, K.M., Le, D.T., Holst, C.R., Coyle, A., Potempa, M., Lanier, L.L., et al. (2018). A human anti-IL-2 antibody that potentiates regulatory T cells by a structure-based mechanism. Nat. Med. *24*, 1005–1014. https://doi.org/10.1038/s41591-018-0070-2.

Waldmann, T.A. (2006). The biology of interleukin-2 and interleukin-15: implications for cancer therapy and vaccine design. Nat. Rev. Immunol. *6*, 595–601. https://doi.org/10.1038/nri1901.

Wang, X., Rickert, M., and Garcia, K.C. (2005). Structure of the quaternary complex of interleukin-2 with its a, b, and gc receptors. Science *310*, 1159–1163. https://doi.org/10.1126/science.1117893.

Wang, X., Mathieu, M., and Brezski, R.J. (2018). IgG Fc engineering to modulate antibody effector functions. Protein Cell *9*, 63–73. https://doi.org/10.1007/s13238-017-0473-8.

Ward, N.C., Yu, A., Moro, A., Ban, Y., Chen, X., Hsiung, S., Keegan, J., Arbanas, J.M., Loubeau, M., Thankappan, A., et al. (2018). IL-2/CD25: a long-acting fusion protein that promotes immune tolerance by selectively targeting the IL-2 receptor on regulatory T cells. J. Immunol. *201*, 2579–2592. https://doi.org/10.4049/jimmunol.1800907.

Ward, N.C., Lui, J.B., Hernandez, R., Yu, L., Struthers, M., Xie, J., Santos Savio, A., Dwyer, C.J., Hsiung, S., Yu, A., and Malek, T.R. (2020). Persistent IL-2 receptor signaling by IL-2/CD25 fusion protein controls diabetes in NOD mice by multiple mechanisms. Diabetes *69*, 2400–2413. https://doi.org/10.2337/db20-0186.

Webster, K.E., Walters, S., Kohler, R.E., Mrkvan, T., Boyman, O., Surh, C.D., Grey, S.T., and Sprent, J. (2009). In vivo expansion of T reg cells with IL-2-mAb complexes: induction of resistance to EAE and long-term acceptance of islet allografts without immunosuppression. J. Exp. Med. *206*, 751–760. https://doi.org/10.1084/jem.20082824.

Weiss, J.M., Bilate, A.M., Gobert, M., Ding, Y., Curotto de Lafaille, M.A., Parkhurst, C.N., Xiong, H., Dolpady, J., Frey, A.B., Ruocco, M.G., et al. (2012). Neuropilin 1 is expressed on thymus-derived natural regulatory T cells, but not mucosa-generated induced Foxp3+ T reg cells. J. Exp. Med. *209*, 1723–1742. https://doi.org/10.1084/jem.20120914.

Wesley, J.D., Sather, B.D., Perdue, N.R., Ziegler, S.F., and Campbell, D.J. (2010). Cellular requirements for diabetes induction in DO11.10xRIPmOVA mice. J. Immunol. *185*, 4760–4768. https://doi.org/10.4049/jimmunol.1000820.

Wilson, D.C., Grotenbreg, G.M., Liu, K., Zhao, Y., Frickel, E.-M., Gubbels, M.-J., Ploegh, H.L., and Yap, G.S. (2010). Differential regulation of effector- and central-memory responses to toxoplasma gondii infection by IL-12 revealed by tracking of tgd057-specific CD8+ T cells. PLoS Pathog. *6*, e1000815. https://doi.org/10.1371/journal.ppat.1000815.

Wrangle, J.M., Velcheti, V., Patel, M.R., Garrett-Mayer, E., Hill, E.G., Ravenel, J.G., Miller, J.S., Farhad, M., Anderton, K., Lindsey, K., et al. (2018). ALT-803, an IL-15 superagonist, in combination with nivolumab in patients with metastatic non-small cell lung cancer: a non-randomised, open-label, phase 1b trial. Lancet Oncol. *19*, 694–704. https://doi.org/10.1016/S1470-2045(18)30148-7.

Xie, J.H., Zhang, Y., Loubeau, M., Mangan, P., Heimrich, E., Tovar, C., Zhou, X., Madia, P., Doyle, M., Dudhgaonkar, S., et al. (2021). Mouse IL-2/CD25 fusion protein induces regulatory T cell expansion and immune suppression in preclinical models of systemic Lupus erythematosus. J. Immunol. *207*, 34–43. https://doi.org/10.4049/jimmunol.2100078.

Xu, W., Jones, M., Liu, B., Zhu, X., Johnson, C.B., Edwards, A.C., Kong, L., Jeng, E.K., Han, K., Marcus, W.D., et al. (2013). Efficacy and mechanism-of-action of a novel superagonist interleukin-15: interleukin-15 receptor αSu/Fc fusion complex in syngeneic murine models of multiple myeloma. Cancer Res. *73*, 3075–3086. https://doi.org/10.1158/0008-5472.CAN-12-2357.

Yadav, M., Louvet, C., Davini, D., Gardner, J.M., Martinez-Llordella, M., Bailey-Bucktrout, S., Anthony, B.A., Sverdrup, F.M., Head, R., Kuster, D.J., et al. (2012). Neuropilin-1 distinguishes natural and inducible regulatory T cells among regulatory T cell subsets in vivo. J. Exp. Med. *209*, 1713–1722. https://doi.org/10.1084/jem.20120822.

Yodoi, J., Teshigawara, K., Nikaido, T., Fukui, K., Noma, T., Honjo, T., Takigawa, M., Sasaki, M., Minato, N., and Tsudo, M. (1985). TCGF (IL 2)-receptor inducing factor(s). I. Regulation of IL 2 receptor on a natural killer-like cell line (YT cells). J. Immunol. *134*, 1623–1630.

Yokoyama, Y., Iwasaki, T., Kitano, S., Satake, A., Nomura, S., Furukawa, T., Matsui, K., and Sano, H. (2018). IL-2-Anti-IL-2 monoclonal antibody immune complexes inhibit collagen-induced arthritis by augmenting regulatory T cell functions. J. Immunol. *201*, 1899–1906. https://doi.org/10.4049/jimmunol.1701502.

Young, A., Quandt, Z., and Bluestone, J.A. (2018). The balancing Act between cancer immunity and autoimmunity in response to immunotherapy. Cancer Immunol. Res. *6*, 1445–1452. https://doi.org/10.1158/2326-6066.CIR-18-0487.

Zhang, B., Sun, J., Wang, Y., Ji, D., Yuan, Y., Li, S., Sun, Y., Hou, Y., Li, P., Zhao, L., et al. (2021). Site-specific PEGylation of interleukin-2 enhances immunosuppression via the sustained activation of regulatory T cells. Nat. Biomed. Eng. *5*, 1288–1305. https://doi.org/10.1038/s41551-021-00797-8.

STAR★METHODS

KEY RESOURCES TABLE

REAGENT or RESOURCE	SOURCE	IDENTIFIER
Antibodies		
F5111 Antibody	This manuscript; see Table S1	N/A
F5111.2 Antibody (N297A)	This manuscript; see Table S1	N/A
Trastuzumab Antibody	This manuscript	N/A
Anti-human IgG Fc APC [HP6017]	BioLegend	Cat# 409306; RRID: AB_11149491
Anti-mouse/human phospho-STAT5 AlexaFluor 647 [pY694]	BD Biosciences	Cat# 562076; RRID: AB_11154412
Anti-human CD3 APC-eFluor780 [UCHT1]	ThermoFisher Scientific	Cat# 47-0038-42; RRID: AB_1272042
Anti-human CD4 PerCP-Cy5.5 [SK3]	BD Biosciences	Cat# 341654; RRID: AB_400452
Anti-human CD8 BV605 [SK1]	BioLegend	Cat# 344742; RRID: AB_2566513
Anti-human IL-2Rα BV421 [M-A251]	BD Biosciences	Cat# 562442; RRID: AB_11154578
Anti-human FOXP3 PE [236A/E7]	BD Biosciences	Cat# 560852; RRID: AB_10563418
Anti-human CD127 AlexaFluor 488 [eBioRDR5]	ThermoFisher Scientific	Cat# 53-1278-42; RRID: AB_2744750
Anti-mouse CD3 BV510 [145-2C11]	BioLegend	Cat# 100353; RRID: AB_2565879
Anti-mouse CD4 APC-eF780 [RM4-5]	ThermoFisher Scientific	Cat# 47-0042-82; RRID: AB_1272183
Anti-mouse CD8a AlexaFluor 488 [53-6.7]	BD Biosciences	Cat# 557668; RRID: AB_396780
Anti-mouse IL-2Rα PE [PC61.5]	ThermoFisher Scientific	Cat# 12-0251-83; RRID: AB_465608
Anti-mouse FOXP3 eFluor450 [FJK-16s]	ThermoFisher Scientific	Cat# 48-5773-82; RRID: AB_1518812
Anti-human CD4 PerCP-Cy5.5 [SK3]	BD Biosciences	Cat# 566316; RRID: AB_2739678
Anti-mouse CD4 eFluor450 [RM4-5]	ThermoFisher Scientific	Cat# 48-0042-82; RRID: AB_1272194
Anti-mouse CD49b PE-Cy7 [DX5]	BioLegend	Cat# 108922; RRID: AB_2561460
Anti-mouse CD16/32 [2.4G2]	BD Biosciences	Cat# 553142; RRID: AB_394657
Anti-mouse FOXP3 APC [FJK-16s]	ThermoFisher Scientific	Cat# 17-5773-82; RRID: AB_469457
Anti-mouse CD8a BV570 [53-6.7]	BioLegend	Cat# 100739; RRID: AB_10897645
Anti-mouse Ki-67 AlexaFluor 488 [16A8]	BioLegend	Cat# 652417; RRID: AB_2564236
Anti-mouse CD44 PerCP-Cy5.5 [IM7]	ThermoFisher Scientific	Cat# 45-0441-82; RRID: AB_925746
Anti-mouse/human Helios PE/Dazzle 594 [22F6]	BioLegend	Cat# 137231; RRID: AB_2565796
Anti-mouse CD45 APC-Cy7 [QA17A26]	BioLegend	Cat# 157617; RRID: AB_2890720
Anti-mouse TER-119 APC-Cy7 [TER-119]	BioLegend	Cat# 116223; RRID: AB_2137788
Anti-human CD3 BV605[OKT3]	BioLegend	Cat# 317321; RRID: AB_11126166
Anti-human CD56 PE [TULY56]	ThermoFisher Scientific	Cat# 12-0566-41; RRID: AB_2572562
Anti-human CD4 PE-eFluor610 [RPA-T4]	ThermoFisher Scientific	Cat# 61-0049-42; RRID: AB_2574522
Anti-human CD8 BV711 [SK1]	BioLegend	Cat# 344733; RRID: AB_2565242
Anti-human IL-2Rα PE-Cy7 [M-A251]	BD Biosciences	Cat# 557741; RRID: AB_396847
Anti-human FOXP3 AlexaFluor 647 [259D]	BioLegend	Cat# 320214; RRID: AB_492984
Anti-human Ki-67 FITC [20Raj1]	ThermoFisher Scientific	Cat# 11-5699-42; RRID: AB_10687464
Anti-mouse CD45 PerCP-Cy5.5 [30-F11]	BioLegend	Cat# 103132; RRID: AB_893340
Anti-mouse CD3 BV605 [17A2]	BioLegend	Cat# 100237; RRID: AB_2562039
Anti-mouse CD4 APC [GK1.5]	BioLegend	Cat# 100411; RRID: AB_312696
Anti-mouse CD8a BV786 [53-6.7]	BD Biosciences	Cat# 563332; RRID: AB_2721167
Anti-mouse IL-2Rα BV421 [7D4]	BD Biosciences	Cat# 564571; RRID: AB_2738849
Anti-mouse FOXP3 FITC [FJK-16s]	ThermoFisher Scientific	Cat# 11-5773-82; RRID: AB_465243
Anti-mouse NK-1.1 PerCP-Cy5.5 [PK136]	BioLegend	Cat# 108727; RRID: AB_2132706
Anti-mouse CD45.1 APC-Cy7 [A20]	BioLegend	Cat# 110716; RRID: AB_313505

(*Continued on next page*)

Continued

REAGENT or RESOURCE	SOURCE	IDENTIFIER
Anti-mouse CD45.2 PerCP-Cy5.5 [104]	BioLegend	Cat# 109828; RRID: AB_893350
Anti-mouse CD62L PE [MEL-14]	BioLegend	Cat# 104408; RRID: AB_313095
Anti-mouse CD44 AlexaFluor 700 [IM7]	BioLegend	Cat# 103026; RRID: AB_493713
Anti-mouse CD16/32 [2.4G2]	Bio X Cell	Cat# BP0307; RRID: AB_2736987
Rat IgG Isotype Control	ThermoFisher Scientific	Cat# 10700; RRID: AB_2610661
Anti-mouse CD4 BUV563 [GK1.5]	BD Biosciences	Cat# 612923; RRID: AB_2870208
Anti-mouse CD8a BUV615 [53-6.7]	BD Biosciences	Cat# 613004; RRID: AB_2870272
Anti-mouse CD11a BUV805 [2D7]	BD Biosciences	Cat# 741919; RRID: AB_2871232
Anti-mouse IL-2Rα BV785 [PC61]	BioLegend	Cat# 102051; RRID: AB_2564131
Anti-mouse CD27 BV650 [LG.3A10]	BioLegend	Cat# 124233; RRID: AB_2687192
Anti-mouse CD44 BV570 [IM7]	BioLegend	Cat# 103037; RRID: AB_10900641
Anti-mouse CD69 BUV737 [H1.2F3]	BD Biosciences	Cat# 612793; RRID: AB_2870120
Anti-mouse CD122 BUV661 [TM-β1]	BD Biosciences	Cat# 741493; RRID: AB_2870951
Anti-mouse KLRG1 BUV395 [2F1]	BD Biosciences	Cat# 740279; RRID: AB_2740018
Anti-mouse ICOS APC/Fire 750 [C398.4A]	BioLegend	Cat# 313536; RRID: AB_2632923
Anti-mouse PD-1 BV421 [29F.1A12]	BioLegend	Cat# 135218; RRID: AB_2561447
Anti-mouse BCL-2 AlexaFluor 647 [BCL/10C4]	BioLegend	Cat# 633510; RRID: AB_2274702
Anti-mouse CD3 BV570 [17A2]	BioLegend	Cat# 100249; RRID: AB_2734148
Anti-mouse CTLA-4 APC-R700 [UC10-4F10-11]	BD Biosciences	Cat# 565778; RRID: AB_2739350
Anti-mouse FOXP3 PE-Cy5.5 [FJK-16s]	ThermoFisher Scientific	Cat# 35-5773-82; RRID: AB_11218094
Anti-mouse Ki-67 AlexaFluor 488 [B56]	BD Biosciences	Cat# 558616; RRID: AB_647087
Anti-mouse T-bet PE-Cy5 [4B10]	ThermoFisher Scientific	Cat# 15-5825-82; RRID: AB_2815071
Anti-mouse CXCR3 BV650 [CXCR3-173]	BioLegend	Cat# 126531; RRID: AB_2563160
Anti-mouse NK-1.1 BV711 [PK136]	BioLegend	Cat# 108745; RRID: AB_2563286
Anti-mouse NKp46 BV605 [29A1.4]	BioLegend	Cat# 137619; RRID: AB_2562452
Anti-mouse PD-1 [RMP1-14]	Bio X Cell	Cat# BE0146; RRID: AB_10949053
Bacterial and virus strains		
One Shot™ MAX Efficiency™ DH5α-T1R Competent Cells	ThermoFisher Scientific	Cat# 12297016
Biological samples		
Human PBMCs	Anne Arundel Medical Blood Donor Center; NHS Blood and Transport	N/A
Chemicals, peptides, and recombinant proteins		
Polyethylenimine, Linear, MW 25000, Transfection Grade (PEI 25K™)	Polysciences	Cat# 23966
OptiPRO™ SFM	ThermoFisher Scientific	Cat# 12309019
FreeStyle™ 293 Expression Medium	ThermoFisher Scientific	Cat# 12338018
Pierce™ Protein G Agarose	ThermoFisher Scientific	Cat# 20397
F5111 IC LN15	This manuscript; see Table S1	N/A
F5111 IC LN25	This manuscript; see Table S1	N/A
F5111 IC LN35	This manuscript; see Table S1	N/A
F5111 IC LN35 (Y35A)	This manuscript; see Table S1	N/A
F5111 IC LN35 (Y52A)	This manuscript; see Table S1	N/A
F5111 IC LN35 (Y54A)	This manuscript; see Table S1	N/A
F5111 IC LN35 (Y60A)	This manuscript; see Table S1	N/A
F5111 IC LN35 (V103A)	This manuscript; see Table S1	N/A
F5111 IC LN35 (Y33A)	This manuscript; see Table S1	N/A
F5111 IC LN35 (Y94A)	This manuscript; see Table S1	N/A

(*Continued on next page*)

Continued

REAGENT or RESOURCE	SOURCE	IDENTIFIER
F5111 IC LN35 (S96A)	This manuscript; see Table S1	N/A
F5111.2 IC LN35	This manuscript; see Table S1	N/A
Control (FITC-E2) IC LN35	This manuscript; see Table S1	N/A
F5111 IC LN35 (N297A)	This manuscript; see Table S1	N/A
F5111 IC LN35 (Y60A, N297A)	This manuscript; see Table S1	N/A
F5111 IC LN35 (V103A, N297A)	This manuscript; see Table S1	N/A
F5111 IC LN35 (Y33A, N297A)	This manuscript; see Table S1	N/A
F5111.2 IC LN35 (N297A)	This manuscript; see Table S1	N/A
Control (FITC-E2) IC LN35 (N297A)	This manuscript; see Table S1	N/A
Human IL-2	This manuscript	N/A
Biotinylated human IL-2	This manuscript	N/A
Biotinylated human IL-2Rα	This manuscript	N/A
Biotinylated human IL-2Rβ	This manuscript	N/A
Ni-NTA Agarose	Qiagen	Cat# 30210
16% Paraformaldehyde (formaldehyde) aqueous solution	Electron Microscopy Science	Cat# 15710
Ficoll® Paque Plus	MilliporeSigma	Cat# GE17-1440-02
ACK Lysing Buffer	Quality Biological	Cat# 118-156-101
LIVE/DEAD™ Fixable Blue Dead Cell Stain Kit	ThermoFisher Scientific	Cat# L34961
eBioscience™ Fixable Viability Dye eFluor™ 780	ThermoFisher Scientific	Cat# 65-0865-18
Violet Proliferation Dye 450	BD Biosciences	Cat# 562158
Zombie NIR™ Fixable Viability Kit	BioLegend	Cat# 423105
NHS-Rhodamine (5/6-carboxy-tetramethyl-rhodamine succinimidyl ester), mixed isomer	ThermoFisher Scientific	Cat# 46406
CD4 (L3T4) MicroBeads, mouse	Miltenyi	Cat# 130-117-043
CellTrace™ Violet Cell Proliferation Kit	ThermoFisher Scientific	Cat# C34571
Dynabeads™ Mouse T-Activator CD3/CD28 for T-Cell Expansion and Activation	ThermoFisher Scientific	Cat# 11452D
Ghost Dye™ Violet 510	Tonbo Biosciences	Cat# 13-0870-T100
Tetramer H2k(b) Tgd057 PE: SVLAFRRL	NIH Tetramer Core Facility; Wilson et al., 2010	N/A
Tetramer I-A(b) AS15 PE: AVEIHRPVPGTAPPS	NIH Tetramer Core Facility; Grover et al., 2012	N/A
Power SYBR™ Green PCR Master Mix	ThermoFisher Scientific	Cat# 4368577
Dextran sulfate sodium salt, colitis grade (36,000–50,000)	MP Biomedicals	Cat# 160110; Lot# S5036
Critical commercial assays		
BirA biotin-protein ligase standard reaction kit	Avidity	Cat# BirA500
Octet® Streptavidin (SA) Biosensor	Sartorius	Cat# 18-5019
Transcription Factor Phospho Buffer Set	BD Biosciences	Cat# 565575
eBioscience™ Foxp3/Transcription Factor Staining Buffer Set	ThermoFisher Scientific	Cat# 00-5523-00
DNeasy Blood & Tissue Kit	Qiagen	Cat# 69506
Experimental models: Cell lines		
FreeStyle™ 293-F Cells	ThermoFisher Scientific	Cat# R79007
YT-1 Human NK Cells	Yodoi et al., 1985	N/A
IL-2Rα$^+$ YT-1 Human NK Cells	Kuziel et al., 1993	N/A

(*Continued on next page*)

Continued

REAGENT or RESOURCE	SOURCE	IDENTIFIER
Experimental models: Organisms/strains		
Mouse: NOD/ShiLt	The Jackson Laboratory	Strain #:001976; RRID: IMSR_JAX:001976
Mouse: BALB/c Rag2$^{-/-}$ $\gamma_c^{-/-}$ H2^d (BRG)	The Jackson Laboratory	Strain #: 014593 RRID: IMSR_JAX:014593
Mouse: C57BL/6	The Jackson Laboratory	Strain #:000664; RRID: IMSR_JAX:000664
Mouse: C57BL/6 CD45.1	The Jackson Laboratory	Strain #:002014; RRID: IMSR_JAX:002014
Mouse: C57BL/6 FOXP3-IRES-mRFP	The Jackson Laboratory	Strain #:008374; RRID: IMSR_JAX:008374
Mouse: C57BL/6 CD45.1; RFP-FOXP3 mice	This manuscript; CD45.1 mice were bred in house to FoxP3-RFP mice to homozygosity and maintained at Johns Hopkins University Cancer Research Building 1 use facility	N/A
Mouse: C57BL/6	Taconic Biosciences	Model: B6-M
Toxoplasma gondii – ME49 strain	N/A	N/A
Mouse: CBA/Ca	The Jackson Laboratory	Strain #: 000654 RRID: IMSR_JAX:000654
Mouse: BALB/c	Purchased from Charles River Laboratories and bred at Czech Centre for Phenogenomics	Strain: 028
Oligonucleotides		
qPCR primer: TCCCCTCTGCTGGCGAAAAGT (*Toxoplasma gondii* forward)	This manuscript; Lin et al., 2000	N/A
qPCR primer: AGCGTTCGTGGTCAACTATCGATTG (*Toxoplasma gondii* reverse)	This manuscript; Lin et al., 2000	N/A
Recombinant DNA		
Human IL-2 sequence	GenBank	GenBank: X00695.1
Mouse IL-2 sequence	GenBank	GenBank: X01772.1
pCT3CBN	Derived from pCT302 (Boder and Wittrup, 1997)	N/A
pCT3CBN_hIL2 (Yeast display vector for human IL-2)	This manuscript	N/A
pCT3CBN_mIL2 (Yeast display vector for mouse IL-2)	This manuscript	N/A
F5111 V_H and V_L sequence	Rondon et al., 2015	N/A
F5111.2 V_H and V_L sequence	Rondon et al., 2015	N/A
FITC-E2 V_H and V_L sequence	Honegger et al., 2005	N/A
Human IgG1 constant heavy chain sequence	ImMunoGeneTics (IMGT)	IMGT: J00228
Human IgG1 constant lambda chain sequence	ImMunoGeneTics (IMGT)	IMGT: J00253
Human IL-2Rα sequence (1–217)	GenBank	GenBank: X01057.1
Human IL-2Rβ sequence (1–214)	GenBank	GenBank: M26062.1
gWiz High Expression Blank Vector	Genlantis	P000200
gWiz_F5111_Ab_HC (Expression vector for F5111 heavy chain)	This manuscript	N/A
gWiz_F5111_Ab_LC (Expression vector for F5111 light chain)	This manuscript	N/A
gWiz_F5111.2_Ab_HC (Expression vector for F5111.2 heavy chain)	This manuscript	N/A
gWiz_F5111.2_Ab_LC (Expression vector for F5111.2 light chain)	This manuscript	N/A

(*Continued on next page*)

Continued

REAGENT or RESOURCE	SOURCE	IDENTIFIER
gWiz_F5111_IC_LN15_LC (Expression vector for human IL-2 linked to F5111 light chain with a 15 amino acid linker)	This manuscript	N/A
gWiz_F5111_IC_LN25_LC (Expression vector for human IL-2 linked to F5111 light chain with a 25 amino acid linker)	This manuscript	N/A
gWiz_F5111_IC_LN35_LC (Expression vector for human IL-2 linked to F5111 light chain with a 35 amino acid linker)	This manuscript	N/A
gWiz_F5111_Ab_HC_Y35A (Expression vector for F5111 heavy chain with Y35A mutation)	This manuscript	N/A
gWiz_F5111_Ab_HC_Y52A (Expression vector for F5111 heavy chain with Y52A mutation)	This manuscript	N/A
gWiz_F5111_Ab_HC_Y54A (Expression vector for F5111 heavy chain with Y54A mutation)	This manuscript	N/A
gWiz_F5111_Ab_HC_Y60A (Expression vector for F5111 heavy chain with Y60A mutation)	This manuscript	N/A
gWiz_F5111_Ab_HC_V103A (Expression vector for F5111 heavy chain with V103A mutation)	This manuscript	N/A
gWiz_F5111_IC_LN35_LC_Y33A (Expression vector for human IL-2 linked to F5111 Y33A mutant light chain with a 35 amino acid linker)	This manuscript	N/A
gWiz_F5111_IC_LN35_LC_Y94A (Expression vector for human IL-2 linked to F5111 Y94A mutant light chain with a 35 amino acid linker)	This manuscript	N/A
gWiz_F5111_IC_LN35_LC_S96A (Expression vector for human IL-2 linked to F5111 S96A mutant light chain with a 35 amino acid linker)	This manuscript	N/A
gWiz_F5111.2_IC_LN35_LC (Expression vector for human IL-2 linked to F5111.2 light chain with a 35 amino acid linker)	This manuscript	N/A
gWiz_Control_IC_HC (Expression vector for FITC-E2 heavy chain)	This manuscript	N/A
gWiz_Control_IC_LN35_LC (Expression vector for human IL-2 linked to FITC-E2 light chain with 35 amino acid linker)	This manuscript	N/A
gWiz_F5111_Ab_HC_N297A (Expression vector for F5111 heavy chain with N297A mutation)	This manuscript	N/A
gWiz_F5111.2_Ab_HC (Expression vector for F5111.2 heavy chain with N297A mutation)	This manuscript	N/A
gWiz_F5111_Ab_HC_Y60A_N297A (Expression vector for F5111 heavy chain with Y60A and N297A mutations)	This manuscript	N/A
gWiz_F5111_Ab_HC_V103A_N297A (Expression vector for F5111 heavy chain with V103A and N297A mutations)	This manuscript	N/A
gWiz_Control_IC_HC_N297A (Expression vector for FITC-E2 heavy chain with N297A)	This manuscript	N/A
gWiz_hIL2 (Expression vector for human IL-2)	This manuscript	N/A
gWiz_hIL2_BH3 (Expression vector for human IL-2 with BH3 tag for biotinylation)	This manuscript	N/A
gWiz_hIL2Ra_BH3 (Expression vector for human IL-2Rα residues 1–217 with BH3 tag for biotinylation)	This manuscript	N/A

(*Continued on next page*)

Continued		
REAGENT or RESOURCE	SOURCE	IDENTIFIER
gWiz_hIL2Rb_BH3 (Expression vector for human IL-2Rβ residues 1–214 with BH3 tag for biotinylation)	This manuscript	N/A
gWiz_Trastuzumab_HC (Expression vector for trastuzumab heavy chain)	This manuscript	N/A
gWiz_Trastuzumab_LC (Expression vector for trastuzumab light chain)	This manuscript	N/A
Software and algorithms		
GraphPad Prism 8.4.3	GraphPad	https://www.graphpad.com/
FlowJo v10.7.1	FlowJo, LLC	https://www.flowjo.com/solutions/flowjo
PyMOL v2.3.2	PyMOL	https://pymol.org/2/
BioRender	BioRender	https://biorender.com/

RESOURCE AVAILABILITY

Lead contact

Further information and requests for resources and reagents should be directed to and will be fulfilled by the lead contact, Jamie Spangler (jamie.spangler@jhu.edu).

Materials availability

Reagent generated in this study will be made available on request, but we may require a completed Materials Transfer Agreement.

Data and code availability

- All data reported in this paper will be shared by the lead contact upon request.
- This paper does not report original code.
- Any additional information required to reanalyze the data reported in this paper is available from the lead contact upon request.

EXPERIMENTAL MODEL AND SUBJECT DETAILS

Cell lines

HEK 293F cells (ThermoFisher Scientific) were cultivated in Freestyle 293 Expression Medium (ThermoFisher Scientific) supplemented with 2 U/mL penicillin-streptomycin (Gibco). Unmodified YT-1 (Yodoi et al., 1985) and IL-2Rα^+ (Kuziel et al., 1993) YT-1 human NK cells were cultured in RPMI complete medium (RPMI 1640 medium supplemented with 10% FBS, 2 mM L-glutamine, 1× minimum non-essential amino acids, 1 mM sodium pyruvate, 25 mM HEPES, and 100 U/mL penicillin-streptomycin [Gibco]). All cell lines were maintained at 37°C in a humidified atmosphere with 5% CO_2.

Human PBMCs

For *in vitro* studies containing human PBMCs, leukopaks containing de-identified whole blood were obtained from Anne Arundel Medical Blood Donor Center (Anne Arundel, Maryland, USA). For the immune cell subset expansion studies in humanized mice, PBMCs were isolated from leukocyte cones from de-identified healthy volunteers (NHS Blood and Transport, UK). Human tissue samples taken by NHS Blood and Transport with informed consent and ethical approval from the Oxfordshire Research Ethics Committee, study number 07/H0605/130.

Mice

Female NOD/ShiLt and both male and female C57BL/6 mice were purchased from The Jackson Laboratory unless otherwise specified. Mice were used at 8 weeks of age. Animals were housed in specific pathogen-free conditions and experiments conducted in accordance with National Institutes of Health guidelines, and approval by the Johns Hopkins University Animal Care and Use Committee.

For the immune cell subset expansion studies in humanized mice, male BRG mice were obtained from The Jackson Laboratory and were maintained under specific pathogen-free conditions in the Biomedical Services Unit of the University of Oxford (Oxford, United Kingdom). Mice were used at 8 weeks of age. All experiments in this study were performed using protocols approved by the Committee on Animal Care and Ethical Review at the University of Oxford and in accordance with the UK Animals (Scientific Procedures) Act 1986.

For the *in vitro* Treg suppression assay, both male and female C57BL/6 CD45.1 and C57BL/6 FOXP3-IRES-mRFP mice were purchased from The Jackson Laboratory. For the C57BL/6 CD45.1; RFP-FOXP3 mice, C57BL/6 CD45.1 and C57BL/6 FOXP3-IRES-mRFP mice were bred in house to homozygosity and maintained. 8-week-old female C57BL/6 CD45.1; RFP-FOXP3 mice were used for all studies. All mice were housed and bred under specific pathogen-free conditions at Johns Hopkins University Animal Care and Use Facility in Cancer Research Building I. The Institutional Animal Care and Use Facility at Johns Hopkins University approved all animal experiments.

For the comparison of cTreg versus eTreg expansion and the *Toxoplasma gondii* infection mouse model, 6-week-old male C57BL/6 mice were purchased from Taconic Biosciences (Rensselaer, NY, USA) and kept in the University of Pennsylvania Department of Pathobiology vivarium until they reached 8–9 weeks of age for experimental use. CBA/Ca mice were purchased from the Jackson Laboratory and maintained kept in the University of Pennsylvania Department of Pathobiology vivarium. Mice housed in the University of Pennsylvania Department of Pathobiology vivarium were maintained under institutional guidelines of 12-hour light/dark cycles, temperature ranges of 68–77°F and humidity ranging from 35–55%. Ethical oversight of all animal use in this study was approved by the University of Pennsylvania Institutional Animal Care and Use Committee.

For the DSS-induced colitis mouse model, female BALB/c mice were acquired from the colony kept at the Czech Centre for Phenogenomics, Prague, Czech Republic. Mice were used at 8 weeks of age. They were housed and handled according to the institutional committee guidelines with free access to food and water. Animal experiments were approved by the Animal Care and Use Committee of the Institute of Molecular Genetics and were in agreement with local legal requirements and ethical guidelines.

For the immune checkpoint inhibitor-induced diabetes mellitus mouse model, female NOD/ShiLtJ mice were purchased from the Jackson Laboratory and maintained in the UCSF specific pathogen-free animal facility in accordance with guidelines established by the Institutional Animal Care and Use Committee and Laboratory Animal Resource Center. Mice were used at 8 weeks of age.

METHOD DETAILS

Protein purification and expression

The published VH and VL sequences of F5111 (Trotta et al., 2018) were used to formulate the recombinant F5111 antibody on the human IgG1 lambda isotype platform. The heavy chain (HC) and LC of the F5111 antibody were separately cloned into the gWiz vector (Genlantis). Antibodies were expressed recombinantly in HEK 293F cells via transient co-transfection of plasmids encoding the HC and LC. HC and LC plasmids were titrated in small-scale co-transfection tests to determine optimal ratios for large-scale expression. HEK 293F cells were grown to 1.2×10^6 cells/mL and diluted to 1.0×10^6 cells/mL. Midiprepped DNA (1 mg total of HC and LC plasmids per liter of cells) and 2 mg per liter of cells of polyethyleneimine (PEI, Polysciences) were independently diluted to 0.05 and 0.1 mg/mL in OptiPro medium (ThermoFisher Scientific), respectively, and incubated at room temperature for 15 minutes. Equal volumes of DNA and PEI were mixed and incubated at room temperature for an additional 15 minutes. Subsequently, the diluted HEK 293F cells and 40 mL/L of DNA/PEI mixture were added to a shaking flask and incubated at 37°C and 5% CO_2 with rotation at 125 rpm for 5 days. Secreted antibodies were purified from cell supernatants 5 days post-transfection via protein G agarose (ThermoFisher Scientific) affinity chromatography followed by SEC on a Superdex 200 Increase 10/300 GL column (GE Healthcare) on a fast protein liquid chromatography (FPLC) instrument, equilibrated in HEPES-buffered saline (HBS, 150 mM NaCl in 10 mM HEPES pH 7.3). Purity (>99%) was verified by SDS-PAGE analysis.

For F5111 IC production, the hIL-2 cytokine (residues 1–133) was fused at the N-terminus of the F5111 antibody LC, connected by either a flexible 15-amino acid $(Gly_4Ser)_3$ linker (F5111 IC LN15), a 25-amino acid $(Gly_4Ser)_5$ linker (F5111 IC LN25), or a 35-amino acid $(Gly_4Ser)_7$ linker (F5111 IC LN35). We prepared a plasmid encoding the hIL-2-fused F5111 LC into the gWiz vector (Genlantis). ICs were expressed and purified via transient co-transfection of HEK 293F cells with the F5111 HC and the hIL-2-fused F5111 LC plasmids, as described for the F5111 antibody. F5111 IC variants (all with a 35-amino acid linker) were generated in the same manner, with the indicated single-point mutation in either the HC or the hIL-2 fused LC construct. The following single-point mutations were made to the V_H sequence: Y35A, Y52A, Y54A, Y60A, and V103A. The following single-point mutations were made to the V_L sequence: Y33A, Y94A, and S96A. The sequence for the F5111.2 antibody and F5111.2 IC constructs was obtained from the following patent: (Rondon et al., 2015).

The Control IC was generated in the same manner as described for F5111 IC. Published VH and VL sequences of the FITC-E2 antibody (Honegger et al., 2005) were used to formulate the recombinant Control IC on the human IgG1 lambda isotype platform. hIL-2 (residues 1–133) was fused at the N-terminus of the LC, connected by a 35-amino acid $(Gly_4Ser)_7$ linker. Separate plasmids were constructed in the gWiz vector (Genlantis) encoding the Control HC and the hIL-2-fused Control LC. The Control IC was expressed via transient co-transfection of HEK 293F cells with the HC and hIL-2-fused LC plasmids. Purification proceeded as described for the F5111 antibody.

Antibody or IC constructs with Fc effector function knocked out were generated in the same manner as above, using a HC plasmid with the N297A mutation (Mimura et al., 2000, 2001; Saunders, 2019; Tao et al., 1993; Wang et al., 2018). In all studies, the F5111.2 antibody includes the N297A mutation. All *in vivo* studies were performed with constructs with Fc effector function knocked out unless otherwise noted.

The hIL-2 cytokine (residues 1–133) was cloned into the gWiz vector (Genlantis) with a C-terminal hexahistidine tag. Protein was expressed via transient transfection of HEK 293F cells, as detailed for antibody constructs, and purified via Ni-NTA affinity chromatography followed by SEC using a Superdex 200 Increase 10/300 GL column (GE Healthcare) on an FPLC instrument, equilibrated in HBS. Purity (>99%) was verified by SDS-PAGE analysis.

For expression of biotinylated hIL-2, and the extracellular domains of the hIL-2Rα (residues 1–217) and hIL-2Rβ (residues 1–214) receptor subunits sequences were cloned into the gWiz vector (Genlantis) with a C-terminal biotin acceptor peptide (BAP)-GLNDIFEAQKIEWHE followed by a hexahistidine tag. Proteins were expressed and purified via Ni-NTA affinity chromatography and then biotinylated with the soluble BirA ligase enzyme in 0.5 mM Bicine pH 8.3, 100 mM ATP, 100 mM magnesium acetate, and 500 mM biotin (Avidity). Excess biotin was removed by SEC on a Superdex 200 Increase 10/300 column (GE Healthcare) on an FPLC instrument, equilibrated in HBS. Complete biotinylation was verified via SDS-PAGE streptavidin shift assay.

Yeast surface binding studies

For binding studies on yeast, hIL-2 (residues 1–133) or mIL-2 (residues 1–149) were cloned into the pCT3CBN yeast display vector (a variant of pCT302 (Boder and Wittrup, 1997) with an N-terminal yeast agglutinin protein (Aga2) fusion followed by a 3C protease site, a C-terminal myc epitope tag, and BamHI/NotI gene-flanking restriction sites). After induction for 48 hours, 1×10^5 cells of IL-2-displaying yeast per well were transferred to a 96-well plate and incubated in PBE (PBS with 0.1% BSA and 1 mM EDTA) containing serial dilutions of recombinant F5111 antibody for 2 hours at room temperature. Cells were then washed and stained with anti-human IgG Fc APC (HP6017, BioLegend 409306, 1:50) in PBE for 15 minutes at 4°C. After a final wash, cells were analyzed for antibody binding using a CytoFLEX flow cytometer (Beckman Coulter). Background-subtracted and normalized binding curves were fitted to a first-order binding model, and K_D values were determined using GraphPad Prism. Studies were performed three times with similar results.

Bio-layer interferometry binding measurements

Binding studies were performed using bio-layer interferometry on an OctetRED96® bio-layer interferometry instrument (Molecular Devices). Biotinylated hIL-2, hIL-2Rα, and hIL-2Rβ were immobilized to streptavidin-coated biosensors (Sartorius) in 0.45 μm filtered PBSA (PBS pH 7.2 containing 0.1% BSA). hIL-2 and hIL-2Rβ were immobilized at a concentration of 50 nM for 120 seconds and hIL-2Rα was immobilized at a concentration of 100 nM for 120 seconds. Once baseline measurements were collected in PBSA, binding kinetics were measured by submerging the biosensors in wells containing serial dilutions of the appropriate analyte for 300 seconds (association) followed by submerging the biosensor in wells containing only PBSA for 600 seconds (dissociation). hIL-2/F5111 or hIL-2/F5111.2 complexes were formed by incubating a 1:1 molar ratio of the F5111 antibody to hIL-2 for 60 minutes at 37°C and then diluting to the appropriate concentration. An irrelevant protein (the monoclonal antibody trastuzumab) was immobilized to a reference streptavidin biosensor for subtraction of non-specific binding. Tips were regenerated in 0.1 M glycine pH 2.7. Data was visualized and processed using the Octet® Data Analysis software version 7.1 (Molecular Devices). Equilibrium titration curve fitting and equilibrium dissociation constant (K_D) value determination was implemented using GraphPad Prism, assuming all binding interactions to be first order. Experiments were reproduced two times with similar results.

YT-1 human NK cell activation studies

Approximately 2×10^5 IL-2Rα$^+$ YT-1 or IL-2Rα$^-$ YT-1 cells were plated in each well of a 96-well plate and resuspended in 20 μL of RPMI complete medium containing serial dilutions of either hIL-2, hIL-2/F5111 complexes, or IC. hIL-2/F5111 complexes were formed by incubating a 1:1 molar ratio of the F5111 antibody to hIL-2 for 60 minutes at 37°C and then diluting to the appropriate concentration. Cells were stimulated for 20 minutes at 37°C and immediately fixed by addition of paraformaldehyde (Electron Microscopy Sciences) to a final concentration of 1.5% and incubated for 10 minutes at room temperature. Permeabilization of cells was achieved by resuspension in 200 μL of ice-cold 100% methanol (MilliporeSigma) for 30 minutes at 4°C. Fixed and permeabilized cells were washed twice with PBSA and incubated with anti-pSTAT5 AlexaFluor 647 (pY694, BD Biosciences 562076, 1:50) diluted in 20 μL of PBSA for 2 hours at room temperature. Cells were then washed twice in PBSA and analyzed on a CytoFLEX flow cytometer (BeckmanCoulter). Dose-response curves were fitted to a logistic model and maximum values (E_{Max}) and half maximal effective concentration (EC_{50}) values were calculated using GraphPad Prism data analysis software after subtraction of the MFI of unstimulated cells and normalization to the maximum signal intensity. Experiments were conducted in triplicate and performed at least twice with similar results.

Human PBMC and mouse splenocyte activation studies

For IL-2 induced pSTAT5 assays in human PBMCs, leukopaks containing de-identified whole blood were obtained from Anne Arundel Medical Blood Donor Center (Anne Arundel, Maryland, USA). Human PBMCs were isolated from whole blood by density gradient centrifugation using a standard Ficoll gradient (Ficoll Paque, MilliporeSigma) according to the manufacturer's protocol. PBMCs were subjected to ACK red blood cell lysis (Quality Biological) and resuspended in PBS. Approximately 2×10^6 cells/well were then plated into 96-well plate, pelleted, and resuspended in 40 μL of RPMI complete medium containing serial dilutions of the appropriate treatment. hIL-2/antibody complexes were formed by incubating a 1:1 molar ratio of hIL-2 to either the F5111 or F5111.2 antibody for 60 minutes at 37°C and then diluting to the appropriate concentration. Cells were stimulated for 20 minutes at 37°C and immediately fixed by addition of 160 μL of 1× TFP Fix/Perm buffer (Transcription Factor Phospho Buffer Set, BD Biosciences) and incubated at

4°C for 50 minutes. 40 μL 1× TFP Perm/Wash buffer (Transcription Factor Phospho Buffer Set, BD Biosciences) was then added to each well, and cells were then pelleted and washed again with 200 μL of 1× TFP Perm/Wash buffer. Permeabilization was achieved by resuspending the cells in 150 μL of Perm Buffer III (BD Biosciences) and incubating for 30 minutes at 4°C. Cells were then washed with 200 μL of 1× TFP Perm/Wash buffer and then resuspended in 50 μL of 1× TFP Perm/Wash buffer containing the following antibodies: anti-human CD3 APC-eFlour780 (UCHT1, ThermoFisher Scientific 47-0038-42, 1:50), anti-human CD4 PerCp-Cy5.5 (SK3, BD Biosciences 341654, 1:20), anti-human CD8 BV605 (SK1, BioLegend 344742, 1:50), anti-human IL-2Rα BV421 (M-A251, BD Biosciences 562442, 1:100), anti-human FOXP3 PE (236A/E7, BD Biosciences 560852, 1:50), anti-pSTAT5 AlexaFluor 647 (pY694, BD Biosciences 562076, 1:50), and anti-human CD127 Alexa Fluor 488 (eBioRDR5, ThermoFisher Scientific 53-1278-42, 1:50). Cells were incubated for 2 hours at room temperature and then washed twice with PBSA. Data were collected on a BD Biosciences LSRII flow cytometer (Becton Dickinson) and analyzed using FlowJo software (FlowJo, LLC). Tregs were gated as $CD3^+CD4^+IL\text{-}2R\alpha^{High}FOXP3^{High}$ cells, $CD8^+$ T cells were gated as $CD3^+CD8^+$ cells, and T_{Conv} cells were gated as $CD3^+CD4^+FOXP3^-$ cells. pSTAT5 dose-response curves were fitted to a logistic model and E_{Max} and EC_{50} values were calculated using GraphPad Prism data analysis software after subtraction of the MFI of unstimulated cells and normalization to the maximum signal intensity. Unless otherwise specified, PBMC activation experiments were conducted in triplicate and performed at least twice using PBMCs from independent donors.

For IL-2-induced pSTAT5 assays in murine lymphocytes, spleens from female NOD/ShiLtJ mice (The Jackson Laboratory) were collected and processed into a single-cell suspension followed by ACK red blood cell lysis (Quality Biological). Cells were seeded at 2×10^6 cells/well into a 96-well plate, and the same protocol as for PBMC studies was followed using a different panel of antibodies: anti-mouse CD3 BV510 (145-2C11, BioLegend 100353, 1:100), anti-mouse CD4 APC-eF780 (RM4-5, ThermoFisher Scientific 47-0042-82, 1:100), anti-mouse CD8a AlexaFluor 488 (53-6.7, BD Biosciences 557668, 1:50), anti-mouse IL-2Rα PE (PC61.5, ThermoFisher Scientific 12-0251-83, 1:100), anti-mouse FOXP3 eFlour450 (FJK-16s, ThermoFisher Scientific 48-5773-82, 1:50), and anti-pSTAT5 Alexa Fluor 647 (pY694, BD Biosciences 562076, 1:50). Mouse splenocyte activation studies were conducted in triplicate.

Quantification of IL-2Rα expression levels

Human PBMCs were isolated as described in the section "human PBMC and mouse splenocyte activation studies." Approximately 2×10^6 human PBMCs/well or 0.2×10^6 YT-1 cells/well were resuspended in 50 μL of PBS containing LIVE/DEAD™ Fixable Blue Dead Cell Stain Kit (ThermoFisher Scientific L34961, 1:1000) and stained for 15 minutes at 4°C. Cells were washed with PBSA, resuspended in 40 μL of RPMI, and then fixed by addition of 160 μL of 1× TFP Fix/Perm buffer (Transcription Factor Phospho Buffer Set, BD Biosciences) and incubated at 4°C for 50 minutes. 40 μL 1× TFP Perm/Wash buffer (Transcription Factor Phospho Buffer Set, BD Biosciences) was then added to each well, and cells were then pelleted and washed again with 200 μL of 1× TFP Perm/Wash buffer. Permeabilization was achieved by resuspending the cells in 150 μL of Perm Buffer III (BD Biosciences) and incubating for 30 minutes at 4°C. Cells were then washed with 200 μL of 1× TFP Perm/Wash buffer and resuspended in 50 μL of 1× TFP Perm/Wash buffer containing the following antibodies: anti-human CD3 APC-eFlour780 (UCHT1, ThermoFisher Scientific 47-0038-42, 1:50), anti-human CD4 PerCp-Cy5.5 (SK3, BD Biosciences 566316, 1:100), anti-human CD8 BV605 (SK1, BioLegend 344742, 1:50), anti-human IL-2Rα BV421 (M-A251, BD Biosciences 562442, 1:100), and anti-human FOXP3 PE (236A/E7, BD Biosciences 560852, 1:50). For the IL-2Rα FMO control, the same panel was used minus the addition of anti-human IL-2Rα BV421. Cells were incubated for 2 hours at room temperature and then washed twice with PBSA. Data were collected on a BD Biosciences LSRII flow cytometer (Becton Dickinson) and analyzed using FlowJo software (FlowJo, LLC). Staining was conducted in triplicate and performed twice using PBMCs from independent donors.

Development of a multivalent binding model for IC signaling

The multivalent binding model used to predict cell type-specific signaling response to ICs was formulated as described in Tan et al. (Tan and Meyer, 2021). Each IL-2 molecule within the IC was assumed to bind to one free IL-2Rα and one IL-2Rβ/γ_c receptor; therefore, bivalent ICs were allowed to bind up to two IL-2Rα and IL-2Rβ/γ_c receptors each. Initial IL-2-IL-2Rα association was modeled as proceeding with the experimentally determined kinetics of monomeric ligand-receptor interaction. The affinities with which each IC initially interacted with IL-2Rβ/γ_c receptor dimer were inferred by fitting the binding model to our experimental *in vitro* pSTAT5 signaling data as described below, using least-squares fitting. Subsequent ligand-receptor binding interactions were modeled with an association constant proportional to the free receptor abundance and the monomeric affinity of receptor-ligand interaction multiplied by the scaling constant, K_x^*. A single K_x^* value was fit for all experiments and cell types when we fit our model to our *in vitro* pSTAT5 signaling data. To predict pSTAT5 response to IL-2 stimulation, we assumed that pSTAT5 is proportional to the amount of IL-2-bound IL-2Rβ/γ_c, as complexes which contain these species actively signal through the JAK/STAT pathway. Scaling factors converting from predicted active signaling species to pSTAT5 abundance were fit to experimental data on a per-experiment and cell type basis. The abundance of each IL-2 receptor subunit on each cell type was assumed to be equal to previously published experimental human PBMC receptor quantitation data (Farhat et al., 2021).

Immune cell subset expansion studies in NOD mice

For immune cell expansion studies in NOD mice (Tomala and Spangler, 2020), 8-week-old female NOD/ShiLtJ mice (4–5 mice per group, The Jackson Laboratory) were injected intraperitoneally (*i.p.*) for 4 consecutive days (Days 0, 1, 2, 3) with either 200 μL of

PBS or the indicated treatment diluted in 200 μL of PBS. ICs were dosed at 8.2 μg per day (1.5 μg hIL-2 equivalence) and hIL-2/F5111.2 antibody complexes were formed by preincubating 1.5 μg hIL-2 with 6.6 μg F5111.2 antibody (1:2 antibody to cytokine molar ratio) in PBS for 60 min at 37°C. Mice were sacrificed 24 hours after the last dose (Day 4) by cervical dislocation, and spleens were harvested. Single-cell suspensions were prepared by mechanical homogenization and then subjected ACK red blood cell lysis (Quality Biological) and resuspended in PBS. Absolute count of splenocytes was assessed for each spleen. Approximately 2×10^6 cells were used per sample. To assess viability, cells were resuspended in 50 μL of PBS containing eBioscience Fixable Viability Dye eFluor780 (ThermoFisher Scientific 65-0865-18, 1:2000) and stained for 15 minutes at 4°C. Cells were then washed with PBSA and resuspended in 50 μL of PBSA containing the following antibodies: anti-mouse CD3 BV510 (145-2C11, BioLegend 100353, 1:50), anti-mouse CD4 eFluor450 (RM4-5, ThermoFisher Scientific 48-0042-82, 1:100), anti-mouse CD8a AlexaFluor 488 (53-6.7, BD Biosciences 557668, 1:50), anti-mouse IL-2Rα PE (PC61.5, ThermoFisher Scientific 12-0251-83, 1:100), anti-mouse CD49b PE-Cy7 (DX5, BioLegend 108992, 1:100), and anti-mouse CD16/CD32 (2.4G2, BD Biosciences 553142, 1:100). Cells were stained for 30 minutes at 4°C. Cells were then washed with PBSA and resuspended in 200 μL of 1× eBioscience Fixation/Permeabilization buffer (ThermoFisher Scientific) and incubated for 45 minutes at 4°C. 800 μL of 1× eBioscience Permeabilization buffer (ThermoFisher Scientific) was then added to each tube. Cells were subsequently resuspended in 50 μL of 1× eBioscience Permeabilization buffer containing anti-mouse FOXP3 APC (FJK-16s, ThermoFisher Scientific 17-5733-82, 1:80) and incubated for 45 minutes at 4°C. After a final wash and resuspension in PBSA, data were collected on a BD Biosciences LSRII flow cytometer (Becton Dickinson) and analyzed using FlowJo software (FlowJo, LLC). Tregs were gated as $CD3^+CD4^+IL\text{-}2R\alpha^{High}FOXP3^{High}$ cells, $CD8^+$ T cells were gated as $CD3^+CD8^+$ cells, T_{Conv} cells were gated as $CD3^+CD4^+FOXP3^-$ cells, and NK cells were gated as $CD3^-CD49b^+$ cells. Statistical significance was determined by one-way ANOVA with Tukey post hoc test. Experiments were performed at least twice with similar results.

To quantify cell proliferation the same procedure as above was followed using the following panel: eBioscience Fixable Viability Dye eFluor780 (ThermoFisher Scientific 65-0865-18, 1:2000), CD3 BV510 (145-2C11, BioLegend 100353, 1:50), anti-mouse CD4 eFluor450 (RM4-5, ThermoFisher Scientific 48-0042-82, 1:100), anti-mouse CD8a BV570 (53-6.7, BioLegend 100739, 1:100), anti-mouse IL-2Rα PE (PC61.5, ThermoFisher Scientific 12-0251-83, 1:100), anti-mouse CD49b PE-Cy7 (DX5, BioLegend 108992, 1:100), anti-mouse CD16/CD32 (2.4G2, BD Biosciences 553142, 1:100), anti-mouse FOXP3 APC (FJK-16s, ThermoFisher Scientific 17-5733-82, 1:80), anti-mouse Ki-67 AlexaFluor 488 (16A8, BioLegend 652417, 1:100), anti-mouse CD44 PerCP-Cy5.5 (IM7, ThermoFisher Scientific 45-0441-82, 1:100), and anti-mouse Helios PE/Dazzle 594 (22F6, BioLegend 137231, 1:100). Statistical significance was determined by one-way ANOVA with Tukey post hoc test. Experiments were performed at least twice with similar results.

Non-negative matrix factorization of immune cell subset expansion studies in NOD mice

The *in vivo* proliferative responses induced by the ICs were visualized using non-negative matrix factorization as implemented in scikit-learn (Pedregosa et al., 2011). The replicate average number of cells measured in NOD mice after treatment with each complex or IC was assembled. The log of the experimentally determined cell number was then taken, and number of each cell type measured during control (PBS) trials was subtracted from all other experimental measurements to obtain the log-fold changes in cell counts induced by each ligand in relation to the control trial. Non-negative matrix factorization with two components was subsequently performed on the processed matrix of cellular expansion data.

Immune cell subset expansion studies in humanized mice

Human PBMCs (NHS Blood and Transport) were dyed with Violet Proliferation Dye 450 (BD Biosciences) before *i.p.* injection into 8-week-old male BRG mice (The Jackson Laboratory). Mice received 5×10^6 PBMCs on day 0 and on day 1 received a single *i.p.* dose of either PBS (n = 6) or 8.2 μg (1.5 μg IL-2 equivalence) Y60A IC (n = 5), Y33A IC (n = 4), F5111 IC (n = 4), or F5111.2 IC (n = 5). Mice were sacrificed on day 4 and the PBMCs were retrieved by peritoneal lavage for flow cytometry analysis.

Cell were stained with Zombie NIR Fixable Dye (BioLegend 423105, 1:8000), anti-mouse CD45 APC-Cy7 (QA17A26, BioLegend 157617, 1:400), anti-mouse TER-119 APC-Cy7 (TER-119, BioLegend 116223, 1:400), anti-human CD3 BV605 (OKT3, BioLegend 317321, 1:200), anti-human CD56 PE (TULY56, ThermoFisher Scientific 12-0566-41, 1:200), anti-human CD4 PE-eFluor610 (RPA-T4, ThermoFisher Scientific 61-0049-42, 1:200), anti-human CD8 BV711 (SK1, BioLegend 344733, 1:200), anti-human IL-2Rα PE-Cy7 (M-A251, BD Biosciences 557741, 1:200), anti-human FOXP3 (259D, BioLegend 320214, 1:200), and anti-human Ki-67 FITC (20Rag1, ThermoFisher Scientific, 1:200). The eBioscience Foxp3/Transcription Factor Staining Buffer Set (ThermoFisher Scientific) was used for intracellular staining following the manufacturers protocol. Samples were collected on an Attune NxT flow cytometer and analyzed using FlowJo software (FlowJo, LLC). Tregs were gated as $CD3^+CD4^+IL\text{-}2R\alpha^{High}FOXP3^{High}$ cells, $CD8^+$ T cells were gated as $CD3^+CD8^+$ cells, and T_{Conv} cells were gated as $CD3^+CD4^+FOXP3^-$ cells. Murine cell populations ($mCD45^+mTER\text{-}119^+$) were excluded from the gating. Statistical significance was determined by one-way ANOVA with Tukey post hoc test. The experiment was performed twice with similar results.

Immune cell subset expansion study dose titrations

8-week-old female C57BL/6 mice (2 mice per group, The Jackson Laboratory) were administered either 200 μL of PBS or increasing doses of F5111 diluted in 200 μL of PBS via *i.p.* injection daily for 4 days. The doses of F5111 IC used were 0.91 μg (0.167 μg IL-2 equivalence), 2.7 μg (0.5 μg IL-2 equivalence), 4.1 μg (0.75 μg IL-2 equivalence), 6.2 μg (1.125 μg IL-2 equivalence), and 8.2 μg (1.5 μg

IL-2 equivalence). Mice were euthanized 24 hours after the last dose and spleens were harvested. Splenocytes were isolated by mechanical dissociation through 100 μm filters and subjected to ACK red blood cell lysis buffer. Cells were stained with anti-mouse CD45 PerCP-Cy5.5 (30-F11, BioLegend 103132, 1:1200), anti-mouse CD3 BV605 (17A2, BioLegend 100237, 1:80), anti-mouse CD4 APC (GK1.5, BioLegend 100411, 1:3200), anti-mouse CD8a BV786 (53-6.7, BD Biosciences 563332, 1:400), anti-mouse IL-2Rα BV421 (7D4, BD 564571, 1:200). Transcription Factor Phospho Buffer Set (BD) was used for intracellular staining following the manufacturers protocol and then stained with anti-mouse FOXP3 FITC (FJK-16s, ThermoFisher Scientific 11-5773-82, 1:200). Samples were acquired on a BD Celesta and analyzed using FlowJo (FlowJo, LLC). Tregs were gated as $CD45^+CD3^+CD4^+IL\text{-}2R\alpha^{High}FOXP3^{High}$ cells. Statistical significance was determined by one-way ANOVA with Tukey post hoc test.

Immune cell subset expansion study kinetics

8-week-old male C57BL/6 mice (3 mice per group, The Jackson Laboratory) were administered *i.p.* injections for 4 consecutive days (Days −3, −2, −1, 0) containing either 200 μL of PBS or 8.2 μg F5111 IC (1.5 μg hIL-2 equivalence) diluted in 200 μL of PBS. Spleens from the PBS-treated group were harvested one day post-treatment (Day 1). Spleens from the F5111 IC treated mice were harvested 1, 3, 5, and 7 days post-treatment (3 mice per harvest). The same protocol was implemented as described for the "Immune cell subset expansion studies in NOD mice" with the substitution of the following antibody panel: anti-mouse CD3 BV510 (145-2C11, BioLegend 100353, 1:100), anti-mouse NK-1.1 PerCp-Cy5.5 (PK136, BioLegend 108727, 1:100), anti-mouse CD4 eFluor450 (RM4-5, ThermoFisher Scientific 48-0042-82, 1:100), anti-mouse CD8a AlexaFluor 488 (53-6.7, BD Biosciences 557668, 1:100), anti-mouse IL-2Rα PE (PC61.5, ThermoFisher Scientific 12-0251-83, 1:100), anti-mouse FOXP3 APC (FJK-16s, ThermoFisher Scientific 17-5733-82, 1:80), and anti-mouse CD16/CD32 (2.4G2, BD Biosciences 553142, 1:100). Tregs were gated as $CD3^+CD4^+IL\text{-}2R\alpha^{High}FOXP3^{High}$ cells, $CD8^+$ T cells were gated as $CD3^+CD8^+$ cells, T_{Conv} cells were gated as $CD3^+CD4^+FOXP3^-$ cells, and NK cells were gated as $CD3^-NK\text{-}1.1^+$ cells.

Pharmacokinetic study

F5111 IC was labeled using 10-fold molar excess of N-hydroxysuccinimide (NHS)-Rhodamine (ThermoFisher Scientific), following the manufacturer's protocol. Non-reacted NHS-rhodamine was removed by SEC on a Superdex 200 Increase 10/300 GL column (GE Healthcare), equilibrated in HBS. Protein concentration and degree of labeling were calculated according to the manufacturer's protocol.

Prior to treatment, a small volume of blood was collected from the tail vein of 8-week-old male C57BL/6 mice (5 mice, The Jackson Laboratory). Mice were then administered retro-orbital injections of 2 mg/kg (∼0.36 mg/kg hIL-2 equivalence, ∼10 μg hIL-2 total/mouse) F5111 IC diluted in 200 μL of PBS. Blood was collected from the tail vein of each mouse at 5 minutes, 20 minutes, 40 minutes, 1 hour, 2 hours, 4 hours, 8 hours, 24 hours, 48 hours, 72 hours, 96 hours, and 120 hours. At each time point, blood was collected in EDTA-coated tubes and centrifuged at 500×g for 5 minutes. The plasma was collected and stored at 4°C for later analysis. After all samples were collected, the plasma was diluted in PBS (1:10 dilution), and 100 μL of diluted sample was added to a 96 well black clear-bottom plate. Fluorescence (Excitation/Emission: 540/590 nm) was measured on a BioTek Synergy 2 instrument, and blood samples collected before treatment were used for background subtraction. Standard curves were generated from fluorescent measurements of rhodamine-labeled F5111 IC at concentrations ranging from 3 μg/mL to 0.023 μg/mL (2-fold dilutions) and this standard curve was used to determine protein concentration of the collected samples. Serum half-life was calculated using a two-phase decay model in GraphPad Prism.

In vitro Treg suppression assay

8-week-old female C57BL/6 CD45.1; RFP-FOXP3 mice (The Jackson Laboratory) were treated with either 200 μL of PBS (n = 3) or 6.2 μg F5111 IC in 200 μL of PBS (n = 2) *i.p.* every day for 4 days. 24 hours after the last dose, Tregs were isolated from spleens from each group for the Treg suppression assay. Spleens from female C57BL/6 CD45.2 mice (n = 5) were taken for isolation of T_{Conv} cells.

Pooled mouse spleens were digested and CD4 cells were positively selected from all mouse groups (Miltenyi, 130-117-043). $CD4^+$ cell suspensions were stained with either a Treg isolation panel: anti-mouse CD45.1 APC-Cy7 (A20, BioLegend 110716, 1:400), anti-mouse CD45.2 PerCp-Cy5.5 (104, BioLegend 109828, 1:400), anti-mouse CD4 APC (GK1.5, BioLegend 100411, 1:3200), anti-mouse CD8a BV786 (53-6.7, BD 563332, 1:400), anti-mouse IL-2Rα BV421 (7D4, BD 564571, 1:200), or a T_{Conv} isolation panel: anti-mouse CD45.1 APC-Cy7 (A20, BioLegend 110716, 1:400), anti-mouse CD45.2 PerCp-Cy5.5 (104, BioLegend 109828, 1:400), anti-mouse CD4 APC (GK1.5, BioLegend 100411, 1:3200), anti-mouse CD8a BV786 (53-6.7, BD 563332, 1:400), anti-mouse IL-2Rα BV421 (7D4, BD 564571, 1:200), anti-mouse CD62L PE (MEL-14, BioLegend 104408, 1:200), and anti-mouse CD44 AlexaFluor 700 (IM7, BioLegend 103026, 1:400). $CD45.1^+CD4^+CD8^-IL\text{-}2R\alpha^{High}RFP\text{-}FOXP3^+$ Tregs were sorted from F5111 treated and PBS treated mice. $CD45.2^+CD4^+CD8^-IL\text{-}2R\alpha^-CD62L^{High}CD44^{Low}$ naïve T_{Conv} cells were sorted for effector cells. Cell sorting occurred on a BD FACSAria™.

For division tracking, T_{Conv} cells were labeled with CellTrace™ Violet (CTV, ThermoFisher Scientific) by incubating cells for 16 minutes at 37°C at a cell density of 10^6/mL in PBSA. Cells were vortexed every 4 minutes of staining. Reaction was quenched in ice cold RPMI 1640 medium (Invitrogen) with 10% FBS (MilliporeSigma).

Cells were cultured in RPMI 1640 medium (Invitrogen) supplemented with non-essential amino acids (Gibco), 1 mM sodium pyruvate (MilliporeSigma), 10 mM HEPES (Gibco), 100 U/mL Penicillin, 100 μg/mL streptomycin (Quality Biologic), 50 μM

2-mercaptoethanol (Gibco), 2 mM L-glutamine (Gibco) and 10% FBS (MilliporeSigma). Cells were incubated at 37°C in 5% CO_2. The Treg suppression assay was performed as follows: 50,000 T_{Conv} cells were co-cultured with a varying ratio of Tregs in 96-well U-bottom plate. Anti-CD3/anti-CD28 coated microbeads (Dynabeads Mouse T Activator, ThermoFisher Scientific, 11452D) were added at a 1:2 (bead: cell) ratio with final number of cells in each well. Proliferation was analyzed by flow cytometry done on a BD FACSCelesta™ after 4 days. Cells were washed in PBS and stained with anti-mouse CD45.1 APC-Cy7 (A20, BioLegend 110716, 1:400) and anti-mouse CD45.2 PerCp-Cy5.5 (104, BioLegend 109828, 1:400) to differentiate T_{Conv} cells from Tregs. A minimum number of 20,000 $CD45.2^+CTV^+$ cells were collected and analyzed with FlowJo software (FlowJo, LLC). The percent suppression is calculated using the following formula: ((%CTV^- of T_{Conv} cells alone - %CTV^- of T_{Conv} cells treated with Treg)/%CTV^- of T_{Conv} cells alone)*100 (Collison and Vignali, 2011). CTV is gated on unstimulated T_{Conv} with all divisions beyond unstimulated condition considered CTV^-. Experiment was conducted with technical replicates and repeated twice with similar results. Statistical significance at each ratio was determined by two-tailed unpaired Student *t* test.

Comparison of cTreg versus eTreg expansion

8-week-old male C57BL/6 mice (5 mice per group, Taconic Biosciences) were injected *i.p.* every 48 hours (days 0, 2, and 4) with either 200 μL of 1× Dulbecco's PBS (DPBS, Corning) or 8.2 μg (1.5 μg IL-2 equivalence) Control IC or F5111 IC diluted in 200 μL of 1× DPBS. The mice were sacrificed on day 6 and their splenocytes were harvested for analysis via flow cytometry. Splenocyte single cell suspensions were isolated by mechanically processing harvested spleens through 70 μm nylon filters. The suspensions were spun down at 300×g for 5 minutes, and then resuspended in 1 mL of lysis buffer (0.846% solution of NH_4Cl) for 5 minutes to lyse red blood cells. The cells were then washed in 10 mL of complete RPMI and then resuspended to $30e^6$ cells/mL on ice for staining.

$5e^6$ cells per sample were placed in a 96 well round bottom plate and washed with ice cold 1× DPBS. The cells were resuspended in 50 μL of Ghost Dye™ Violet 510 viability dye (Tonbo Biosciences 13-0870-T100, 1:200) reconstituted in 1× DPBS for 20 minutes on ice and then washed in 0.2% FACS buffer (1× DPBS, 2 g/L BSA, 0.5 M EDTA). The cells were then resuspended in 50 μL of volume of 0.2% FACS buffer containing anti-mouse CD16/CD32 (2.4G2, Bio X Cell BP0307, 1 μg/mL) and rat IgG Isotype Control (ThermoFisher Scientific 10700, 1:200) for 30 minutes on ice. The cells were washed in 0.2% FACS buffer, and then incubated for 30 minutes on ice in 50 μL volume of antibody cocktail composed of: anti-mouse CD4 BUV563 (GK1.5, BD Biosciences 612923, 1:200), anti-mouse CD8a BUV615 (53-6.7, BD Biosciences 613004, 1:200), anti-mouse CD11a BUV805 (2D7, BD Biosciences 741919, 1:200), anti-mouse IL-2Rα BV785 (PC61, BioLegend 102051, 1:200), anti-mouse CD27 BV650 (LG.3A10, BioLegend 124233, 1:200), anti-mouse CD44 BV570 (1M7, BioLegend 103037, 1:100), anti-mouse CD69 BUV737 (H1.2F3, BD Biosciences 612793, 1:200), anti-mouse IL-2Rβ BUV661 (TM-β1, BD Biosciences 741493, 1:200), anti-mouse KLRG1 BUV395 (2F1, BD Biosciences 740279, 1:300), anti-mouse ICOS APC/Fire 750 (C398.4A , BioLegend 313536, 1:200), and anti-mouse PD-1 BV421 (29F.1A12, BioLegend 135218, 1:250) in 0.2% FACS buffer supplemented with Brilliant Stain Buffer (BD Biosciences, 1:10). The cells were washed in 0.2% FACS buffer and re-suspended in 100 μL 1× eBioscience Fixation/Permeabilization buffer (ThermoFisher Scientific) for 4 hours at 4ºC. The cells were then washed twice in 1× eBioscience Permeabilization buffer (ThermoFisher Scientific), and then resuspended in 50 μL of 1× eBioscience Permeabilization buffer containing: anti-mouse BCL-2 AlexaFluor 647 (BCL/10C4, BioLegend 633510, 1:200), anti-mouse CD3 BV750 (17A2, BioLegend 100249, 1:200), anti-mouse CTLA-4 APC-R700 (UC10-4F10-11, BD Biosciences 565778, 1:300), anti-mouse FOXP3 PE-Cy5.5 (FJK-16s, ThermoFisher Scientific 35-5773-82, 1:200), anti-mouse Helios PE/Dazzle 594 (22F6, BioLegend 137231, 1:200), anti-mouse Ki-67 AlexaFluor 488 (B56, BD Biosciences 558616, 1:400), and anti-mouse T-bet PE-Cy5 (4B10, ThermoFisher Scientific 15-5825-82, 1:200) for 2 hours at 4ºC. The cells were then washed with 1× eBioscience Permeabilization buffer twice, and then resuspended in 500 μL 0.2% FACS buffer for flow cytometric analysis. Fluorescence minus one (FMOs) controls and individual single color controls and were created using pooled remaining splenocytes and were prepared simultaneously with experimental samples. The prepared and stained cells were analyzed using a FACS Symphony A5 (BD Biosciences) running BD FACSDiva v9.0 (BD Biosciences). Raw flow cytometry data was compensated and analyzed using FlowJo (FlowJo, LLC). cTregs were gated as $CD4^+FOXP3^+IL\text{-}2R\alpha^{High}BCL\text{-}2^{High}$ and eTregs were gated as $CD4^+FOXP3^+IL\text{-}2R\alpha^{Low}BCL\text{-}2^{Low}$. Statistical significance was determined separately for cTregs and eTregs by one-way ANOVA with a Tukey post hoc test.

Toxoplasma gondii infection mouse model

ME49 strain *Toxoplasma gondii* cysts were obtained from neural tissue harvested from chronically infected CBA/Ca mice (The Jackson Laboratory) and resuspended to 125 cysts/mL in 1× DPBS (Corning). Cohorts of male C57BL/6 mice (5 mice per group, Taconic Biosciences) were infected via *i.p.* injection at 8–9 weeks of age using 200 μL of diluted ME49 cysts for an infection dose of 25 cysts/mouse. The disease-free control group did not receive ME49 cysts and instead received an injection of 1× DPBS. Mice were then injected *i.p.* with either 200 μL of 1× DPBS (control group and PBS) or 8.2 μg (1.5 μg IL-2 equivalence) Control IC or F5111 IC diluted in 200 μL of 1× DPBS every 24 hours after infection on days 1, 2, 3, 4, and 5. The mice were sacrificed on day 10 of infection, and splenocytes were harvested for analysis via flow cytometry, the right lateral lobe of the lungs and liver were frozen at −80°C for DNA isolation, and the left lateral lobe of the liver was stored in 10% buffered formalin (Jansen Pharmaceuticals) for histological analysis.

The staining and flow cytometry analysis was performed as described in the "Comparison of cTreg versus eTreg expansion" methods except anti-mouse CD27 was excluded and the following antibodies were added to the panel: anti-mouse CXCR3 BV650 (CXCR3-173, BioLegend 126531, 1:150), anti-mouse NK-1.1 BV711 (PK136, BioLegend 108245, 1:300), and anti-mouse NKp46 BV605 (29A1.4, BioLegend 137619, 1:300). Additionally, toxoplasma-specific tetramers for $CD4^+$ (Tetramer I-A(b) AS15

PE, NIH, AVEIHRPVPGTAPPS, 1:400) and $CD8^+$ (Tetramer H2k(b) Tgd057 PE, NIH, SVLAFRRL, 1:400) T cells were included. Tregs were gated as $CD3^+CD4^+IL\text{-}2R\alpha^{High}FOXP3^{High}$ cells, $CD8^+$ T cells were gated as $CD3^+CD8^+$ cells, and T_{Conv} cells were gated as $CD3^+CD4^+FOXP3^-$ cells.

Harvested left lateral liver lobes were kept submerged in 10% buffered formalin for 48 hours then mounted in paraffin, cut, and hematoxylin and eosin (H&E) stained by the University of Pennsylvania Comparative Pathology Core.

Total DNA was isolated from frozen sections of the liver, heart, and lungs using a DNeasy Blood and Tissue Kit (Qiagen) according to manufacturer protocol. Isolated DNA concentration was quantified via NanoDrop spectrophotometry (ThermoFisher Scientific) and then individual samples were diluted in DNase/RNase-free distilled water (ThermoFisher Scientific) to equivalent concentrations for qPCR analysis (lungs 40 ng/μL, livers 50 ng/μL). Parasite DNA quantity was assessed in triplicate from the individual prepared DNA samples via qPCR using toxoplasma specific primers: (forward) 5′-TCCCCTCTGCTGGCGAAAAGT-3′ and (reverse) 5′-AGCGTTCGTGGTCAACTATCGATTG-3′ with Power SYBR Green master mix (ThermoFisher Scientific). The reaction conditions for the qPCR were: holding phase of 2 minutes at 50°C, and then 10 minutes at 95°C (occurs only once); followed by 50 cycles of PCR phases of 15 seconds at 95°C, and 1 minute at 60°C. The qPCR reaction was performed on a ViiA 7 Real-Time PCR system operating ViiA 7™ Software. Analysis of parasite qPCR data was performed in Microsoft Excel version 2202 (Build 14931.20120).

Statistical significance was determined by one-way ANOVA with Tukey post hoc test. The experiment was performed twice with similar results.

DSS–induced colitis mouse model

Female, 8-week-old, BALB/c mice (6 mice per group, Czech Centre for Phenogenomics) were injected *i.p.* daily for 7 days (days 0–6) with either 200 μL of PBS (control group and PBS) or 8.2 μg (1.5 μg hIL-2 equivalence) Control IC or F5111 IC diluted in 200 μL of PBS. For the complex, 1.5 μg hIL-2 was complexed with 6.6 μg F5111.2 antibody (1:2 antibody to cytokine molar ratio) in 200 μL of PBS for 60 min at 37°C. Beginning on day 7, all groups except for the disease-free control group were administered 3% DSS (MW = 36,000–50,000; MP Biomedicals) in their drinking water to induce colitis. Mice weight, stool consistency, and rectal bleeding were measured daily and scores were assigned for each category (Cooper et al., 1993). The weight loss score was calculated based on initial weight as follows: 0 (<1% weight loss); 1 (1–5% weight loss); 2 (5–10% weight loss); 3 (10–20% weight loss); 4 (>20% weight loss). Stool consistency was scored as follows: 0 (normal stool); 2 (loose stool); 4 (diarrhea/liquid stool). Rectal bleeding was scored as follows: 0 (no presence of blood); 4 (blood observed). The disease activity index was calculated as the average of the weight loss, stool consistency, and rectal bleeding. On day 15, mice were sacrificed and entire colons were removed (from cecum to anus). Colon length was measured, and shortening was used as an indirect marker of pathological inflammation. Distal colon sections were fixed in Carnoy's solution and embedded in paraffin. Histological scoring of paraffin-embedded and hematoxylin and eosin-stained transversal colon sections was implemented in a blinded manner using a weighted score, ranging from 0 (no signs of inflammation) to 4 (severe inflammation). Statistical significance was determined by one-way ANOVA with Tukey post hoc test. The experiment was performed two times with similar results.

Immune checkpoint inhibitor-induced diabetes mellitus mouse model

8-week-old female NOD/ShiLtJ mice (the Jackson Laboratory) were treated *i.p.* with either 200 μL of PBS (control group and PBS) or 8.2 μg (1.5 μg IL-2 equivalence) Control IC or F5111 IC diluted in 200 μL of PBS from day −3 to 0 prior to initiating anti-PD-1 treatment. Starting on day 0 (4 hours after the last IC treatment), mice were treated *i.p.* every 4 days with either PBS (control group) or 200 μg anti-PD-1 antibody (clone RMP1-14, Bio X Cell) for a total of four or five doses. Non-fasting blood glucose was monitored by using a OneTouch® Ultra® 2 glucometer. Diabetes onset was considered to have occurred when non-fasting blood glucose concentration exceeded 250 mg/dL for two consecutive measurements. Statistical significance was determined by pairwise comparisons using the Log-rank (Mantel-Cox) test.

QUANTIFICATION AND STATISTICAL ANALYSIS

All statistical analysis was performed using GraphPad Prism. The number of replicates, number of mice, definition of center, dispersion and precision measures, and type of analysis performed is described in each of the above sections where applicable. $p \leq 0.05$ was considered significant for all experiments (*$p \leq 0.05$, **$p \leq 0.01$, ***$p \leq 0.001$, ****$p \leq 0.0001$). Significance between all groups is not always shown in figures, for full analysis see Table S6.

Cell Reports, Volume *41*

Supplemental information

Engineered human cytokine/antibody fusion proteins expand regulatory T cells and confer autoimmune disease protection

Derek VanDyke, Marcos Iglesias, Jakub Tomala, Arabella Young, Jennifer Smith, Joseph A. Perry, Edward Gebara, Amy R. Cross, Laurene S. Cheung, Arbor G. Dykema, Brian T. Orcutt-Jahns, Tereza Henclová, Jaroslav Golias, Jared Balolong, Luke M. Tomasovic, David Funda, Aaron S. Meyer, Drew M. Pardoll, Joanna Hester, Fadi Issa, Christopher A. Hunter, Mark S. Anderson, Jeffrey A. Bluestone, Giorgio Raimondi, and Jamie B. Spangler

Figure S1

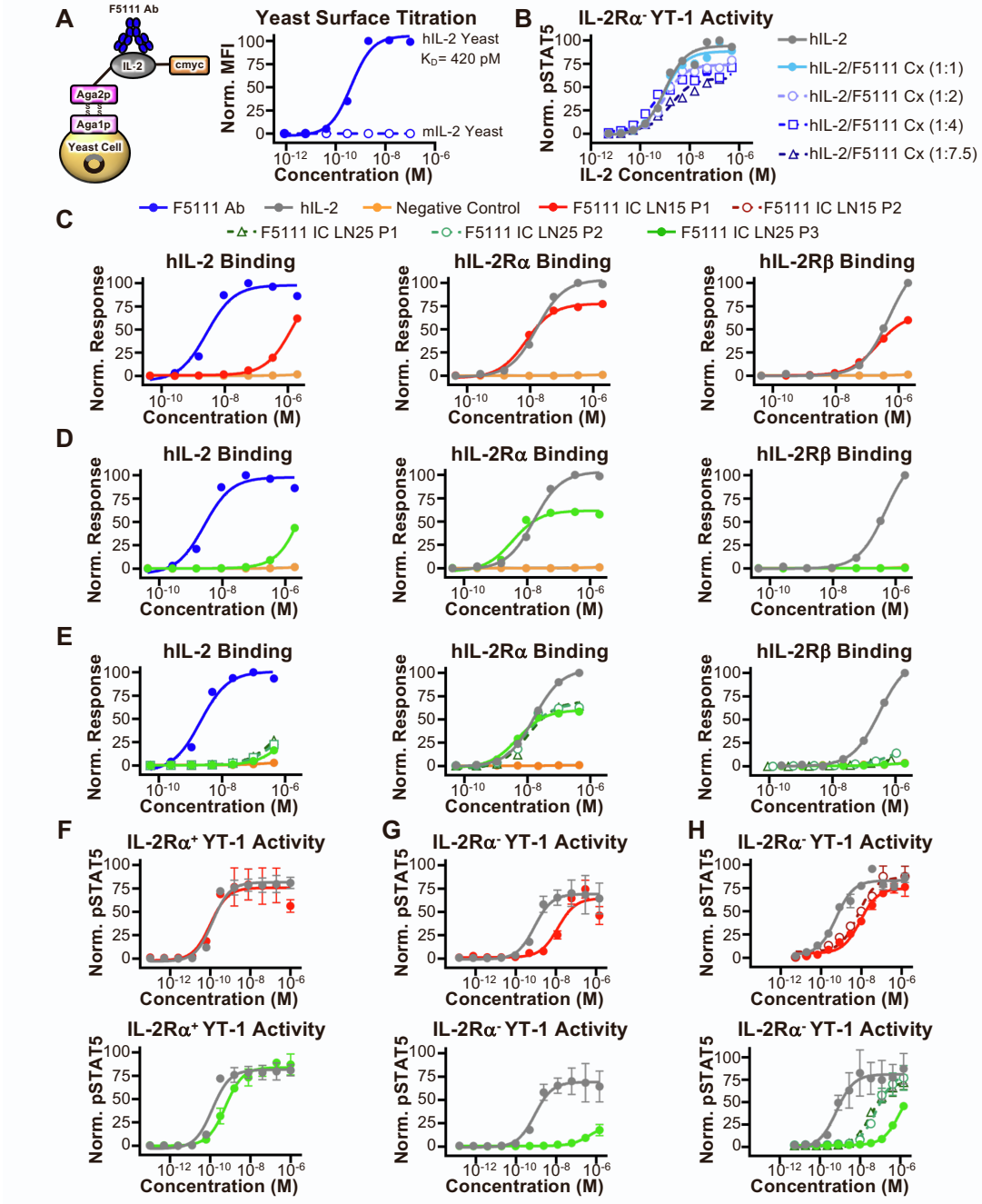
A
F5111 Ab
IL-2
cmyc
Aga2p
Aga1p
Yeast Cell
Yeast Surface Titration
Norm. MFI
hIL-2 Yeast
K_D= 420 pM
mIL-2 Yeast
Concentration (M)
B
IL-2Rα- YT-1 Activity
Norm. pSTAT5
hIL-2
hIL-2/F5111 Cx (1:1)
hIL-2/F5111 Cx (1:2)
hIL-2/F5111 Cx (1:4)
hIL-2/F5111 Cx (1:7.5)
IL-2 Concentration (M)
C
F5111 Ab
hIL-2
Negative Control
F5111 IC LN15 P1
F5111 IC LN15 P2
F5111 IC LN25 P1
F5111 IC LN25 P2
F5111 IC LN25 P3
hIL-2 Binding
hIL-2Rα Binding
hIL-2Rβ Binding
Norm. Response
Concentration (M)
D
E
F
IL-2Rα+ YT-1 Activity
G
IL-2Rα- YT-1 Activity
H

Figure S1. Increasing IC linker length improves Treg bias. Related to Figures 1 and 2. **(A)** Binding of the F5111 antibody (Ab) to yeast-displayed hIL-2 or mIL-2. Fitted equilibrium dissociation constant (K_D) is shown. **(B)** STAT5 phosphorylation response of IL-2Rα^- YT-1 human NK cells stimulated with either hIL-2 or hIL-2/F5111 complex (Cx) at varying molar ratios of cytokine to antibody. **(C-E)** Equilibrium biolayer interferometry-based titrations of hIL-2, F5111 antibody (Ab), Negative Control (trastuzumab), F5111 IC LN15 P1, and F5111 IC LN25 P1, P2, and P3 binding to immobilized hIL-2 (left), immobilized hIL-2Rα (middle), and immobilized hIL-2Rβ (right). **(F)** STAT5 phosphorylation response of IL-2Rα^+ YT-1 human NK cells stimulated with either hIL-2, F5111 IC LN15 P1 (top), or F5111 IC LN25 P3 (bottom). **(G)** STAT5 phosphorylation response of IL-2Rα^- YT-1 human NK cells stimulated with either hIL-2, F5111 IC LN15 P1 (top), or F5111 IC LN25 P3 (bottom). **(H)** STAT5 phosphorylation response of IL-2Rα^- YT-1 human NK cells stimulated with either hIL-2, F5111 IC LN15 P1 and P2 (top), or F5111 IC LN25 P1, P2, and P3 (bottom). Data in **(F-H)** represent mean ± SD (n=3). See also **Tables S2 and S3**.

Figure S2

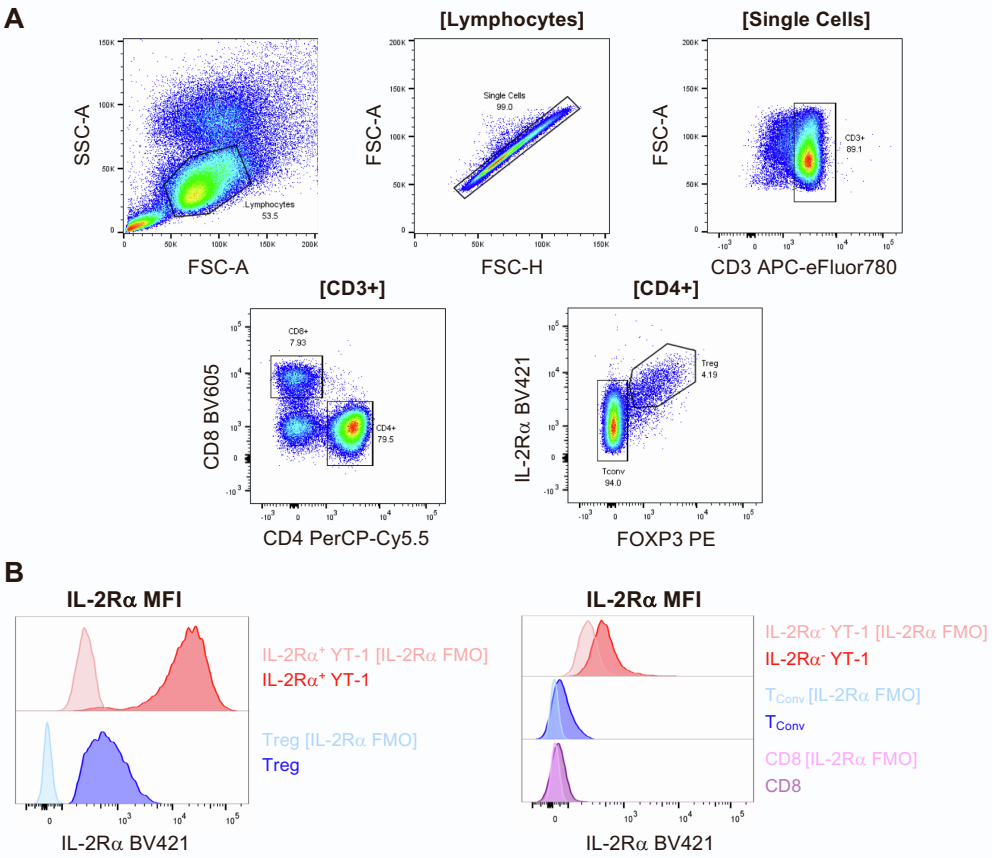

Figure S2. IL-2Rα⁺ YT-1 cells express higher levels of IL-2Rα than human Tregs. Related to Figures 2, 3, and 5. (A) Representative flow cytometry plots illustrating the gating strategy used for human PBMCs. **(B)** Representative histograms illustrating IL-2Rα MFI of IL-2Rα⁺ YT-1 cells and human Tregs (left) and IL-2Rα⁻ YT-1 cells, human CD8⁺ T cells, and human T_{Conv} cells (right) as compared to the IL-2Rα fluorescence minus one (FMO) controls.

Figure S3

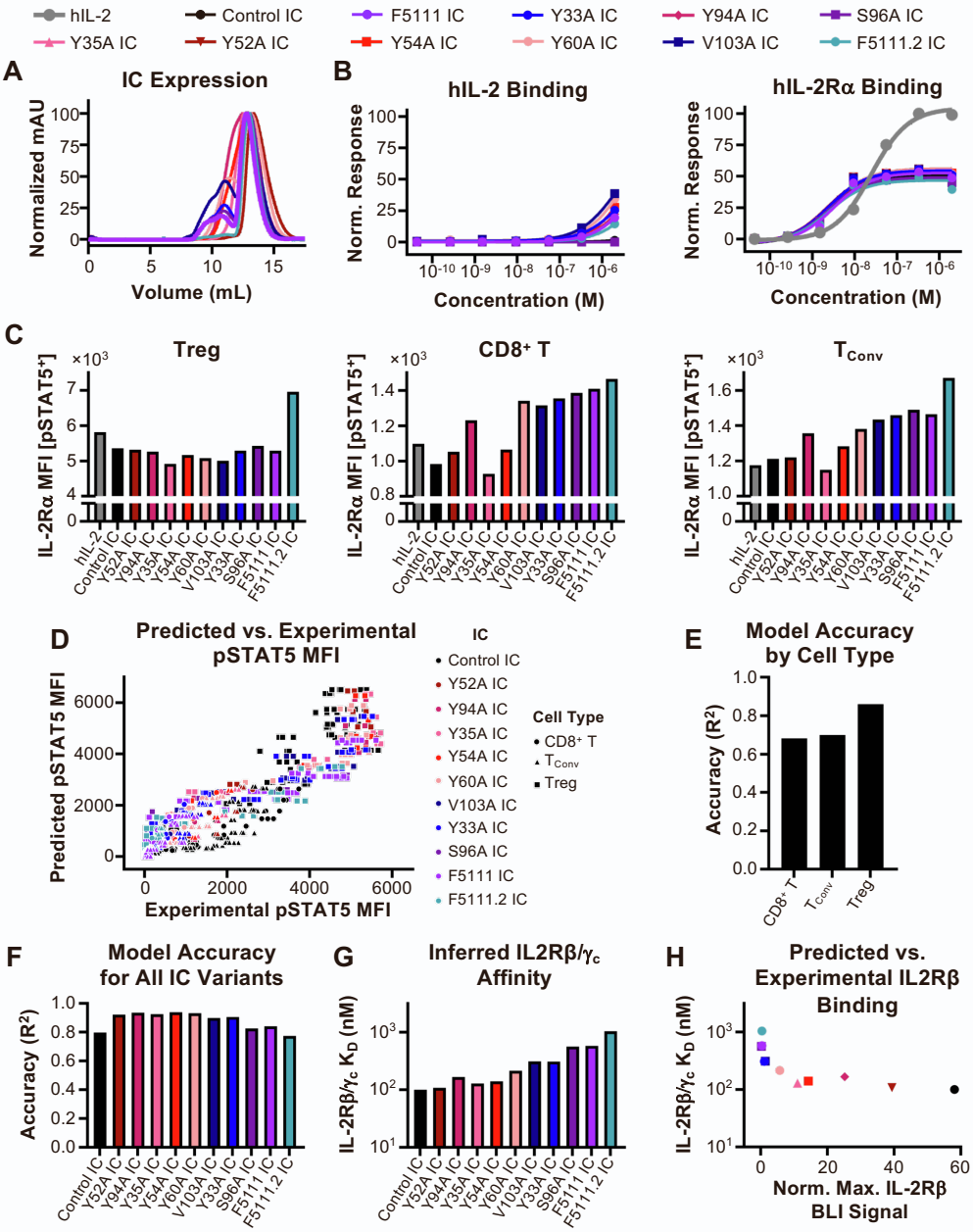
hIL-2
Control IC
F5111 IC
Y33A IC
Y94A IC
S96A IC
Y35A IC
Y52A IC
Y54A IC
Y60A IC
V103A IC
F5111.2 IC
A
IC Expression
Normalized mAU
Volume (mL)
B
hIL-2 Binding
Norm. Response
Concentration (M)
hIL-2Rα Binding
Norm. Response
Concentration (M)
C
Treg
CD8+ T
TConv
IL-2Rα MFI [pSTAT5+]
D
Predicted vs. Experimental pSTAT5 MFI
Predicted pSTAT5 MFI
Experimental pSTAT5 MFI
IC
Cell Type
CD8+ T
TConv
Treg
E
Model Accuracy by Cell Type
Accuracy (R2)
F
Model Accuracy for All IC Variants
Accuracy (R2)
G
Inferred IL2Rβ/γc Affinity
IL-2Rβ/γc KD (nM)
H
Predicted vs. Experimental IL2Rβ Binding
IL-2Rβ/γc KD (nM)
Norm. Max. IL-2Rβ BLI Signal

Figure S3. Characterization of F5111 IC variants. Related to Figures 3 and 4. (A) Overlay of SEC traces for F5111 IC variants. **(B)** Equilibrium biolayer interferometry-based titrations of hIL-2, Control IC, and F5111 IC variants binding to immobilized hIL-2 (left) and immobilized hIL-2Rα (right). Binding to immobilized hIL-2 was normalized based on the binding of the F5111.2 antibody (**Figure S5C, left**). **(C)** IL-2Rα MFI within the $pSTAT5^+$ population of Treg (left), $CD8^+$ T (middle), and T_{Conv} (right) cell populations within human PBMCs stimulated with either hIL-2, Control IC, or F5111 IC variants at treatment concentrations of 2 nM (left) and 200 nM (middle and right). **(D)** Predicted vs. experimentally measured pSTAT5 MFI for all cell types, ICs, and concentrations modeled. Each point represents a single experimental measurement (n=1). **(E)** Model accuracy delineated by cell type for all ICs. **(F)** Model accuracy delineated by treatment for all ICs. Accuracies are calculated as a Pearson's correlation R^2. **(G)** Inferred IL2Rβ/γ_c equilibrium dissociation constants (K_D, nM) for each IC. **(H)** Inferred IL2Rβ/γ_c equilibrium dissociation constants (K_D, nM) compared to the maximum normalized IL2Rβ biolayer interferometry (BLI) signal experimentally measured for each IC. See also **Table S2**.

Figure S4

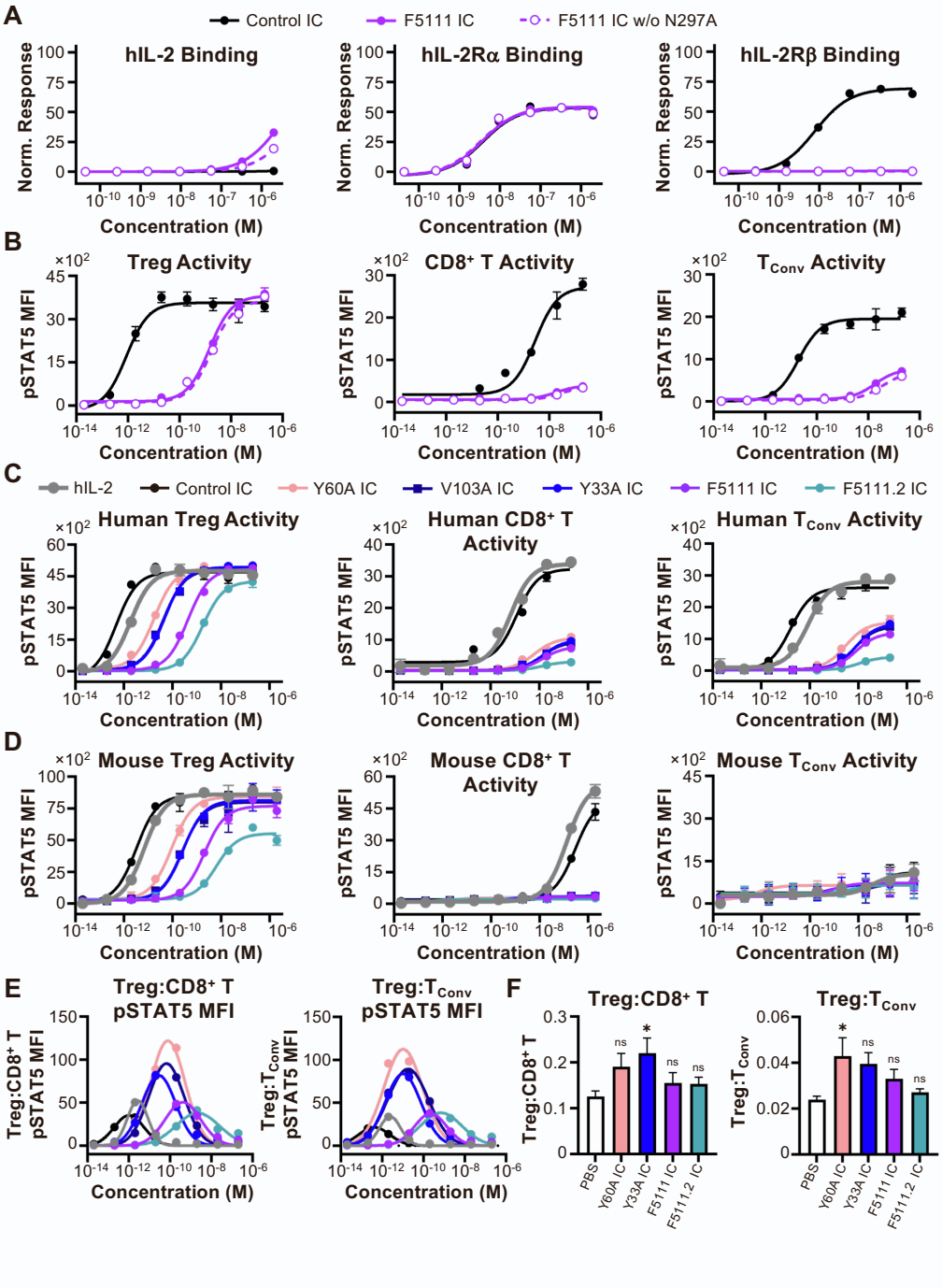
A
Control IC
F5111 IC
F5111 IC w/o N297A
hIL-2 Binding
hIL-2Rα Binding
hIL-2Rβ Binding
Norm. Response
Concentration (M)
B
Treg Activity
CD8⁺ T Activity
T_Conv Activity
pSTAT5 MFI
C
hIL-2
Control IC
Y60A IC
V103A IC
Y33A IC
F5111 IC
F5111.2 IC
Human Treg Activity
Human CD8⁺ T Activity
Human T_Conv Activity
D
Mouse Treg Activity
Mouse CD8⁺ T Activity
Mouse T_Conv Activity
E
Treg:CD8⁺ T pSTAT5 MFI
Treg:T_Conv pSTAT5 MFI
F
Treg:CD8⁺ T
Treg:T_Conv
PBS
Y60A IC
Y33A IC
F5111 IC
F5111.2 IC
ns
*

Figure S4. The N297A mutation does not impact *in vitro* function and IC variants modulate Treg bias *in vitro* and *in vivo*. Related to Figures 3 and 4. (A) Equilibrium biolayer interferometry-based titrations of Control IC, F5111 IC, and F5111 IC without the N297A mutation (w/o N297A, intact effector function) binding to immobilized hIL-2 (left), immobilized hIL-2Rα (middle), and immobilized hIL-2Rβ (right). Binding to immobilized hIL-2 was normalized based on the binding of the F5111.2 antibody (**Figure S5C, left**). **(B)** STAT5 phosphorylation response of Treg (left), $CD8^+$ T (middle), and T_{Conv} (right) cell populations from human PBMCs stimulated with either Control IC, F5111 IC, or F5111 IC w/o N297A. Data represent mean ± SD (n=3). **(C)** STAT5 phosphorylation response of Treg (left), $CD8^+$ T (middle), and T_{Conv} (right) cell populations within human PBMCs stimulated with either hIL-2, Control IC, Y60A IC, V103A IC, Y33A IC, F5111 IC, or F5111.2 IC (all with N297A mutation). Data represent mean ± SD (n=3). **(D)** STAT5 phosphorylation response of Treg (left), $CD8^+$ T (middle), and T_{Conv} (right) cells isolated from spleens of NOD mice and stimulated with either hIL-2, Control IC, Y60A IC, V103A IC, Y33A IC, F5111 IC, or F5111.2 IC (all with N297A mutation). Data represent mean ± SD (n=3). **(E)** Average pSTAT5 MFI ratio of human Treg:$CD8^+$ T (left) and human Treg:T_{Conv} (right) for each IC determined at each stimulation concentration from the experiment shown in **(C)**. **(F)** BRG mice were administered 5×10^6 human PBMCs (*i.p.*) on day 0 and then on day 1 were treated (*i.p.*) with either PBS (n=6) or 8.2 µg (1.5 µg IL-2 equivalence) Y60A IC (n=5), Y33A IC (n=4), F5111 IC (n=4), or F5111.2 IC (n=5). Cells were collected by lavage from the peritoneum on day 4 and ratios of human Treg:$CD8^+$ T (left) and Treg:T_{Conv} (right) were evaluated. Data represent mean + SEM. Statistical significance was determined by one-way ANOVA with a Tukey post hoc test. Only statistical significance compared to PBS is shown on the plots. All statistical data are provided in **Table S6**. *P≤0.05, **P≤0.01, ***P≤0.001, ****P≤0.0001. See also **Tables S2, S4, and S5**.

Figure S5

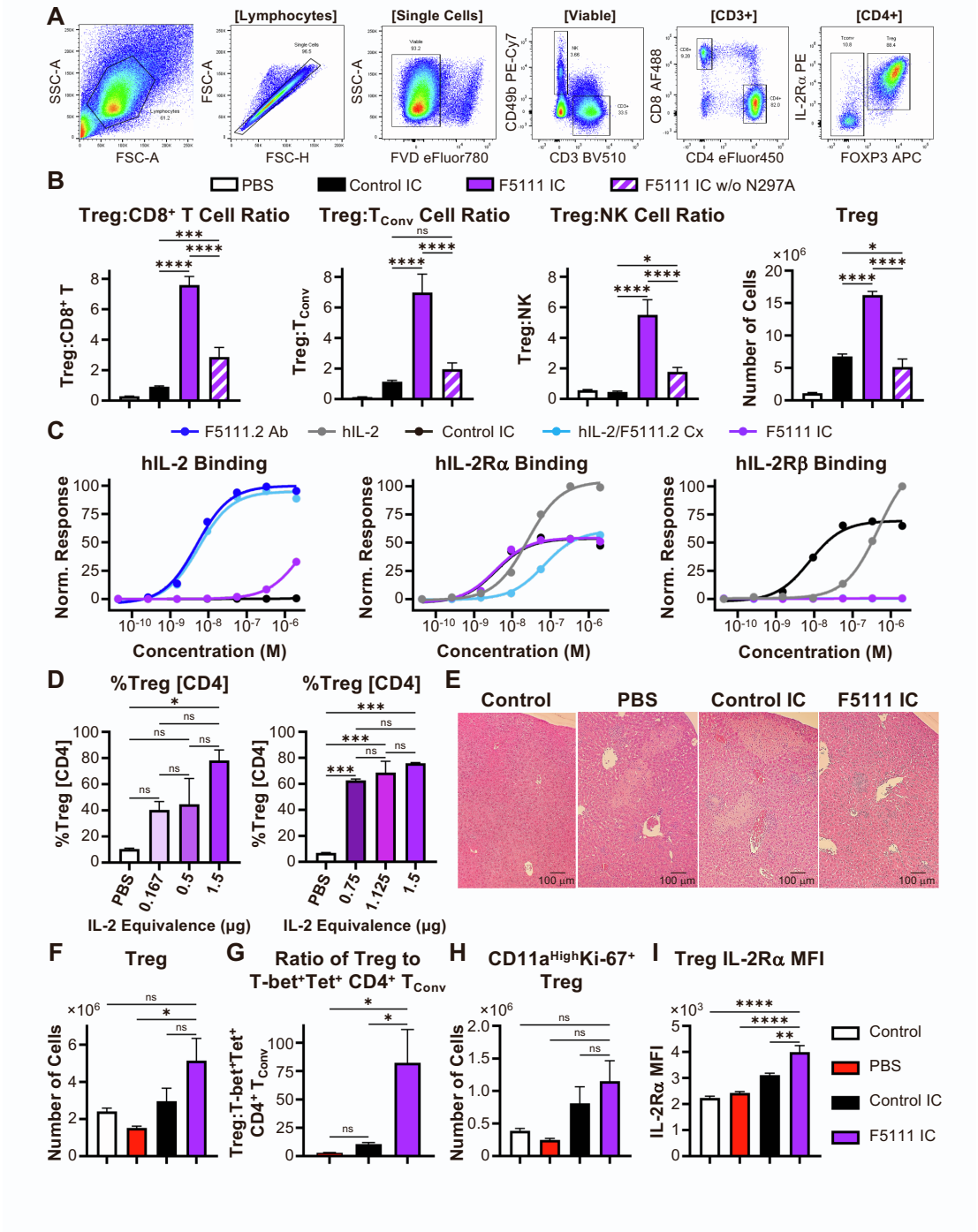
A
[Lymphocytes]
[Single Cells]
[Viable]
[CD3+]
[CD4+]
SSC-A
FSC-A
FSC-H
FVD eFluor780
CD49b PE-Cy7
CD3 BV510
CD8 AF488
CD4 eFluor450
IL-2Rα PE
FOXP3 APC
B
PBS
Control IC
F5111 IC
F5111 IC w/o N297A
Treg:CD8⁺ T Cell Ratio
Treg:T_Conv Cell Ratio
Treg:NK Cell Ratio
Treg
Number of Cells
C
F5111.2 Ab
hIL-2
Control IC
hIL-2/F5111.2 Cx
F5111 IC
hIL-2 Binding
hIL-2Rα Binding
hIL-2Rβ Binding
Norm. Response
Concentration (M)
D
%Treg [CD4]
IL-2 Equivalence (μg)
E
Control
PBS
Control IC
F5111 IC
100 μm
F
Treg
G
Ratio of Treg to T-bet⁺Tet⁺ CD4⁺ T_Conv
H
CD11a^HighKi-67⁺ Treg
I
Treg IL-2Rα MFI
IL-2Rα MFI
Control
PBS
Control IC
F5111 IC

Figure S5. *In vivo* characterization of F5111 IC. Related to Figures 4-6. (A) Representative flow cytometry plots illustrating the gating strategy used for NOD mouse immune cell subset expansion studies. **(B)** Ratios of Treg to $CD8^+$ T cells (left), Treg to T_{Conv} cells (middle), and Treg to NK cells (right) in spleens harvested from NOD mice (n=4 per group) treated daily for four days (*i.p.*) with either PBS or 8.2 µg (1.5 µg IL-2 equivalence) Control IC, F5111 IC, or F5111 IC without the N297A mutation (w/o N297A, intact effector function). Data represent mean + SD. Statistical significance was determined by one-way ANOVA with a Tukey post hoc test. Significance is shown between Control IC and F5111 IC with and without the N297A mutation. **(C)** Equilibrium biolayer interferometry-based titrations of F5111.2 antibody (Ab), hIL-2, Control IC, hIL-2/F5111.2 complex (Cx, 1:1 molar ratio), and F5111 IC binding to immobilized hIL-2 (left), immobilized hIL-2Rα (middle), and immobilized hIL-2Rβ (right). **(D)** C57BL/6 mice (n=2 per group) were treated daily for 4 days (*i.p.*) with either PBS or varying dosages of F5111 IC: 0.91 µg (0.167 µg IL-2 equivalence); 2.7 µg (0.5 µg IL-2 equivalence); 4.1 µg (0.75 µg IL-2 equivalence); 6.2 µg (1.125 µg IL-2 equivalence); or 8.2 µg (1.5 µg IL-2 equivalence). Spleens were harvested 24 hours after the last dose. Percent of Tregs within the $CD4^+$ T cell population is shown. Data represent mean + SD. Statistical significance was determined by one-way ANOVA with a Tukey post hoc test. **(E-I)** C57BL/6 mice were administered (*i.p.*) 25 cysts of the ME-49 strain of *Toxoplasma gondii* (*T. gondii*) on day 0. Control group designates disease-free mice that were not given cysts. Starting on day 1, mice were treated daily for 5 days (*i.p.*) with either PBS (Control, n=5; PBS, n=4) or 8.2 µg (1.5 µg IL-2 equivalence) Control IC (n=5) or F5111 IC (n=5). Mice were sacrificed on day 10. **(E)** Representative H&E staining of harvested mouse livers. Scale bar, 100 µm. **(F)** Total number of Tregs in harvested spleen. **(G)** Ratio of Tregs to T-bet$^+$Tetramer (Tet)$^+$ $CD4^+$ T_{Conv} cells in harvested mouse spleen. **(H)** Total number of $CD11a^{High}$Ki-67^+ Tregs in harvested mouse spleen. **(I)** IL-2Rα MFI of Tregs in harvested mouse spleen. Data in **(F-I)** represent mean + SEM. Statistical significance in **(F-I)** was determined by one-way ANOVA with a Tukey post hoc test. Significance compared to F5111 IC is shown. All statistical data are provided in **Table S6**. *P≤0.05, **P≤0.01, ***P≤0.001, ****P≤0.0001. See also **Table S2**.

Figure S6

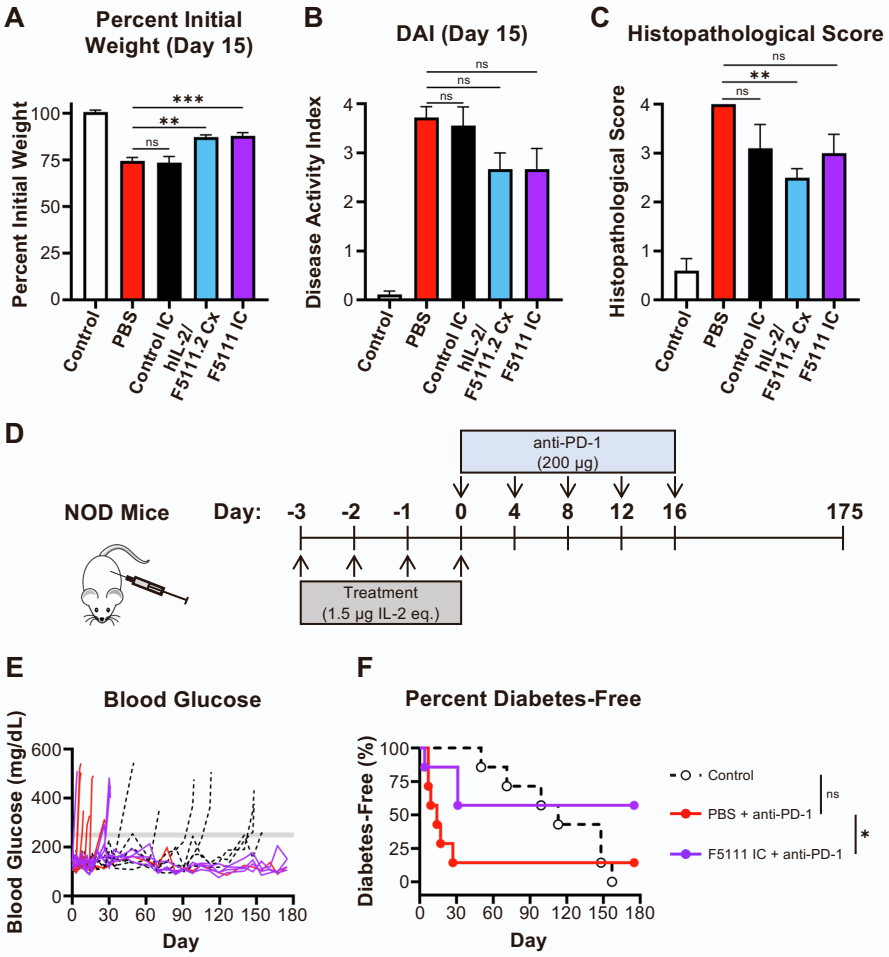
A
Percent Initial Weight (Day 15)
Percent Initial Weight
100
75
50
25
0
***
**
ns
Control
PBS
Control IC
hIL-2/ F5111.2 Cx
F5111 IC
B
DAI (Day 15)
Disease Activity Index
4
3
2
1
0
ns
ns
ns
Control
PBS
Control IC
hIL-2/ F5111.2 Cx
F5111 IC
C
Histopathological Score
Histopathological Score
4
3
2
1
0
ns
**
ns
Control
PBS
Control IC
hIL-2/ F5111.2 Cx
F5111 IC
D
anti-PD-1 (200 µg)
NOD Mice
Day:
-3
-2
-1
0
4
8
12
16
175
Treatment (1.5 µg IL-2 eq.)
E
Blood Glucose
Blood Glucose (mg/dL)
600
400
200
0
0
30
60
90
120
150
180
Day
F
Percent Diabetes-Free
Diabetes-Free (%)
100
75
50
25
0
0
30
60
90
120
150
180
Day
Control
PBS + anti-PD-1
F5111 IC + anti-PD-1
ns
*

Figure S6. Evaluation of F5111 IC in mouse models of autoimmune disease. Related to Figure 7. (A-C) BALB/c mice (n=6 per group) were treated daily for 7 days (*i.p.*) with either PBS (Control and PBS), 1.5 μg hIL-2 complexed with 6.6 μg F5111.2 antibody (1:2 molar ratio, hIL-2/F5111.2 Cx), or 8.2 μg (1.5 μg IL-2 equivalence) Control IC or F5111 IC. Beginning on day 7, all groups except for the disease-free cohort (Control) were administered 3% DSS in their drinking water. Mice were sacrificed on day 15. **(A)** Weight change on day 15. **(B)** Disease activity index (DAI) on day 15. **(C)** Histopathology scores for H&E stained colons (n=5 Control, Control IC; n=6 PBS, Cx, F5111 IC). Data represent mean ± SEM. Statistical significance was determined by one-way ANOVA with a Tukey post hoc test. All plots show significance of Control IC, Cx, and F5111 IC treated mice versus PBS treated mice. **(D-F)** 8-week-old NOD mice (n=7 per group) were treated daily for 4 days (*i.p.*, days -3, -2, -1, 0) with either PBS (Control and PBS) or 8.2 μg (1.5 μg IL-2 equivalence) F5111 IC. Starting on day 0 (4 hours after the last IC dose), mice were administered anti-PD-1 antibody (200 μg) every 4 days until day 16. Control group designates mice that did not receive anti-PD-1 antibody. **(E)** Blood glucose concentrations over the study. The threshold 250 mg/dL value is indicated by the gray line. **(F)** Percent diabetes-free mice. Statistical significance was determined by pairwise comparisons using the Log-rank (Mantel-Cox) test. Statistical significance compared to mice treated with PBS + anti-PD-1 is shown. All statistical data are provided in **Table S6**. *P≤0.05, **P≤0.01, ***P≤0.001, ****P≤0.0001.

Table S1. Antibody and IC sequences. Related to Figures 1 and 3.

Construct	Amino Acid Sequence Signal sequence – V_H or V_L – human IgG1 C_H1, C_H2, and C_H3 – hIL-2 – Linker – human Lambda C_L
F5111 Heavy Chain (Single-point alanine mutations) (N297A)	METDTLLLWVLLLWVPGSTGDQLQLQESGPGLVKPSQTLSLTCTVSGGSISSGGYYWSWIR QHPGKGLEWIGYIYYSGSTYYNPSLKSRVTISVDTSKNQFSLKLSSVTAADTAVYYCARTPTV TGDWFDPWGRGTLVTVSSASTKGPSVFPLAPSSKSTSGGTAALGCLVKDYFPEPVTVSWN SGALTSGVHTFPAVLQSSGLYSLSSVVTVPSSSLGTQTYICNVNHKPSNTKVDKKVEPKSCD KTHTCPPCPAPELLGGPSVFLFPPKPKDTLMISRTPEVTCVVVDVSHEDPEVKFNWYVDGVE VHNAKTKPREEQYNSTYRVVSVLTVLHQDWLNGKEYKCKVSNKALPAPIEKTISKAKGQPRE PQVYTLPPSREEMTKNQVSLTCLVKGFYPSDIAVEWESNGQPENNYKTTPPVLDSDGSFFL YSKLTVDKSRWQQGNVFSCSVMHEALHNHYTQKSLSLSPGK
F5111 Light Chain	MRVPAQLLGLLLLWLPGARCGSNFMLTQPHSVSESPGKTVTISCTRSSGSIASNYVQWYQQ RPGSSPTTVIYEDNQRPSGVPDRFSGSIDSSSNSASLTISGLKTEDEADYYCQSYDSSNVVF GGGTKLTVLGQPKAAPSVTLFPPSSEELQANKATLVCLISDFYPGAVTVAWKADSSPVKAGV ETTTPSKQSNNKYAASSYLSLTPEQWKSHRSYSCQVTHEGSTVEKTVAPTECS
F5111 Light Chain + hIL-2 **LN15:** X = 3 **LN25:** X = 5 **LN35:** X = 7 (Single-point alanine mutations)	MYRMQLLSCIALSLALVTNSAPTSSSTKKTQLQLEHLLLDLQMILNGINNYKNPKLTRMLTFKF YMPKKATELKHLQCLEEELKPLEEVLNLAQSKNFHLRPRDLISNINVIVLELKGSETTFMCEYA DETATIVEFLNRWITFCQSIISTLT(GGGGS)$_X$NFMLTQPHSVSESPGKTVTISCTRSSGSIASN YVQWYQQRPGSSPTTVIYEDNQRPSGVPDRFSGSIDSSSNSASLTISGLKTEDEADYYCQS YDSSNVVFGGGTKLTVLGQPKAAPSVTLFPPSSEELQANKATLVCLISDFYPGAVTVAWKAD SSPVKAGVETTTPSKQSNNKYAASSYLSLTPEQWKSHRSYSCQVTHEGSTVEKTVAPTECS
Control IC Heavy Chain (N297A)	METDTLLLWVLLLWVPGSTGDQVQLVESGGNLVQPGGSLRLSCAASGFTFGSFSMSWVRQ APGGGLEWVAGLSARSSLTHYADSVKGRFTISRDNAKNSVYLQMNSLRVEDTAVYYCARRS YDSSGYWGHFYSYMDVWGQGTLVTVSASTKGPSVFPLAPSSKSTSGGTAALGCLVKDYFP EPVTVSWNSGALTSGVHTFPAVLQSSGLYSLSSVVTVPSSSLGTQTYICNVNHKPSNTKVDK KVEPKSCDKTHTCPPCPAPELLGGPSVFLFPPKPKDTLMISRTPEVTCVVVDVSHEDPEVKF NWYVDGVEVHNAKTKPREEQYNSTYRVVSVLTVLHQDWLNGKEYKCKVSNKALPAPIEKTI SKAKGQPREPQVYTLPPSREEMTKNQVSLTCLVKGFYPSDIAVEWESNGQPENNYKTTPPV LDSDGSFFLYSKLTVDKSRWQQGNVFSCSVMHEALHNHYTQKSLSLSPGK
Control IC Light Chain + hIL-2	MYRMQLLSCIALSLALVTNSAPTSSSTKKTQLQLEHLLLDLQMILNGINNYKNPKLTRMLTFKF YMPKKATELKHLQCLEEELKPLEEVLNLAQSKNFHLRPRDLISNINVIVLELKGSETTFMCEYA DETATIVEFLNRWITFCQSIISTLTGGGGSGGGGSGGGGSGGGGSGGGGSGGGGSGGGG SSVLTQPSSVSAAPGQKVTISCSGSTSNIGNNYVSWYQQHPGKAPKLMIYDVSKRPSGVPD RFSGSKSGNSASLDISGLQSEDEADYYCAAWDDSLSEFLFGTGTKLTVLGGQPKAAPSVTLF PPSSEELQANKATLVCLISDFYPGAVTVAWKADSSPVKAGVETTTPSKQSNNKYAASSYLSL TPEQWKSHRSYSCQVTHEGSTVEKTVAPTECS
F5111.2 Heavy Chain (N297A)	METDTLLLWVLLLWVPGSTGDQLQLQESGPGLVKPSQTLSLTCTVSGGSISSGGYYWSWIR QHPGKGLEWIGYIYKSGSAYYSPSLKSRVTISVDTSKNQFSLKLSSVTAADTAVYYCARTPTV TGDWFDPWGRGTLVTVSSASTKGPSVFPLAPSSKSTSGGTAALGCLVKDYFPEPVTVSWN SGALTSGVHTFPAVLQSSGLYSLSSVVTVPSSSLGTQTYICNVNHKPSNTKVDKKVEPKSCD KTHTCPPCPAPELLGGPSVFLFPPKPKDTLMISRTPEVTCVVVDVSHEDPEVKFNWYVDGVE VHNAKTKPREEQYNSTYRVVSVLTVLHQDWLNGKEYKCKVSNKALPAPIEKTISKAKGQPRE PQVYTLPPSREEMTKNQVSLTCLVKGFYPSDIAVEWESNGQPENNYKTTPPVLDSDGSFFL YSKLTVDKSRWQQGNVFSCSVMHEALHNHYTQKSLSLSPGK
F5111.2 Light Chain	MRVPAQLLGLLLLWLPGARCGSNFMLTQPHSVSESPGKTVTISCTRSSGSIASNYVQWYQQ RPGSSPTTVIYEDNQRPSGVPDRFSGSIDSSSNSASLTISGLKTEDEADYYCQTYDSIDVYFG GGTKLTVLGQPKAAPSVTLFPPSSEELQANKATLVCLISDFYPGAVTVAWKADSSPVKAGVE TTTPSKQSNNKYAASSYLSLTPEQWKSHRSYSCQVTHEGSTVEKTVAPTECS
F5111.2 Light Chain + hIL-2	MYRMQLLSCIALSLALVTNSAPTSSSTKKTQLQLEHLLLDLQMILNGINNYKNPKLTRMLTFKF YMPKKATELKHLQCLEEELKPLEEVLNLAQSKNFHLRPRDLISNINVIVLELKGSETTFMCEYA DETATIVEFLNRWITFCQSIISTLTGGGGSGGGGSGGGGSGGGGSGGGGSGGGGSGGGG SNFMLTQPHSVSESPGKTVTISCTRSSGSIASNYVQWYQQRPGSSPTTVIYEDNQRPSGVP DRFSGSIDSSSNSASLTISGLKTEDEADYYCQTYDSIDVYFGGGTKLTVLGQPKAAPSVTLFP PSSEELQANKATLVCLISDFYPGAVTVAWKADSSPVKAGVETTTPSKQSNNKYAASSYLSLT PEQWKSHRSYSCQVTHEGSTVEKTVAPTECS

Table S2. Equilibrium K_D values from biolayer interferometry studies. Related to Figures 2 and 3.

Treatment	Equilibrium K_D (nM)			Figure
	hIL-2	hIL-2Rα	hIL-2Rβ	
F5111 Ab	2.7	-	-	2A, S1C, S1D
hIL-2	-	16	480	2A, S1C, S1D
Control IC	-	3.4	4.4	2A
hIL-2/F5111 Complex	4.8	18	>2000	2A
F5111 IC LN35	>2000	3.0	>2000	2A
hIL-2	-	25	470	3B, S3B, S5C
Control IC	-	2.5	4.1	3B, S3B
F5111 IC	>2000	3.2	>2000	3B, S3B, S4A
Y33A IC	>2000	2.6	>2000	3B, S3B
Y94A IC	>2000	2.2	>2000	3B, S3B
S96A IC	>2000	2.5	>2000	3B, S3B
Y35A IC	>2000	2.5	>2000	3B, S3B
Y52A IC	>2000	2.8	500	3B, S3B
Y54A IC	>2000	2.8	>2000	3B, S3B
Y60A IC	>2000	2.7	>2000	3B, S3B
V103A IC	>2000	2.4	>2000	3B, S3B
F5111.2 IC	>2000	2.4	>2000	3B, S3B
F5111 IC LN15	>2000	7.5	210	S1C
F5111 IC LN25	>2000	3.4	>2000	S1D
F5111 Ab	2.1	-	-	S1E
hIL-2	-	16	310	S1E
F5111 IC LN25 P1	>2000	11	>700	S1E
F5111 IC LN25 P2	>2000	8.1	>1000	S1E
F5111 IC LN25 P3	>2000	4.8	>2000	S1E
Control IC + N297A	-	3.8	7.7	S4A, S5C
F5111 IC + N297A	>2000	3.6	>2000	S4A, S5C
F5111.2 Ab + N297A	4.9	-	-	S5C
hIL-2/F5111.2 Complex	5.6	68	>2000	S5C

Table S3. EC_{50} and E_{Max} Values from YT-1 cell activation studies. Related to Figure 2.

Treatment	EC_{50} (nM)		Normalized E_{Max}		Figure
	IL-2Rα$^+$	IL-2Rα$^-$	IL-2Rα$^+$	IL-2Rα$^-$	
hIL-2	0.13	0.88	82	69	2B, S1F, S1G
Control IC	0.031	0.83	87	91	2B
hIL-2/F5111 Complex	0.081	1.8	85	62	2B
F5111 IC LN35	0.70	>2000	80	21	2B
hIL-2	-	0.98	-	94	S1B
hIL-2:F5111 = 1:1	-	0.91	-	88	S1B
hIL-2:F5111 = 1:2	-	0.89	-	74	S1B
hIL-2:F5111 = 1:4	-	0.35	-	64	S1B
hIL-2:F5111 = 1:7.5	-	1.7	-	60	S1B
F5111 IC LN15	0.10	13	76	65	S1F, S1G
F5111 IC LN25	0.58	>2000	84	23	S1F, S1G
hIL-2	-	0.57	-	83	S1H (top)
F5111 IC LN15 P1	-	8.9	-	75	S1H
F5111 IC LN15 P2	-	6.9	-	87	S1H
hIL-2	-	0.68	-	81	S1H (bottom)
F5111 IC LN25 P1	-	37	-	73	S1H
F5111 IC LN25 P2	-	69	-	82	S1H
F5111 IC LN25 P3	-	>2000	-	76	S1H

Table S4. EC_{50} and E_{Max} values from human PBMC activation studies. Related to Figures 2, 3, and 5.

Treatment	EC_{50} (pM)			E_{Max} (pSTAT5 MFI)			Figure
	Treg	$CD8^+$ T	T_{Conv}	Treg	$CD8^+$ T	T_{Conv}	
hIL-2	4.5	1200	110	5300	3600	2500	2C
Control IC	1.3	1600	30	5200	3300	2400	2C
hIL-2/F5111 Complex	3.7	240	70	5100	2200	2200	2C
F5111 IC LN35	1700	6.1e4	3.7e4	5200	760	1100	2C
hIL-2	5.2	1000	110	5300	3500	2400	3C
Control IC	1.4	1500	39	5600	3600	2500	3C
F5111 IC	2100	5.0e4	3.4e4	5500	740	980	3C
Y33A IC	81	2.2e4	1.5e4	5300	1100	1400	3C
Y94A IC	6.9	4300	1200	5400	1800	1900	3C
S96A IC	910	3.3e4	2.6e4	5100	710	1000	3C
Y35A IC	7.7	4100	1400	5700	1800	2100	3C
Y52A IC	2.9	3500	360	5500	2300	2200	3C
Y54A IC	7.8	3000	1300	5500	1600	1900	3C
Y60A IC	15	5300	2900	5400	1400	1800	3C
V103A IC	51	1.3e4	7400	5300	1000	1400	3C
F5111.2 IC	8600	>2.0e5	>2.0e5	4700	370	460	3C
hIL-2	1.8	890	35	3700	2800	2100	5A
Control IC + N297A	0.87	2900	19	3600	2700	2000	5A, S4B
F5111 IC + N297A	1500	1.8e4	1.8e4	3800	400	770	5A, S4B
hIL-2/F5111.2 Complex	8.2	190	140	3700	570	1100	5A
F5111 IC w/o N297A	1700	3.2e4	3.4e4	3600	380	700	S4B
hIL-2	1.9	660	84	4800	3400	2800	S4C
Control IC + N297A	0.48	1200	16	4700	3200	2600	S4C
Y60A IC + N297A	17	6300	2900	4900	1100	1500	S4C
V103A IC + N297A	42	1.3e4	7200	4800	950	1400	S4C
Y33A IC + N297A	47	1.5e4	8000	4900	1000	1500	S4C
F5111 IC + N297A	440	1.8e4	7900	4900	790	1200	S4C
F5111.2 IC + N297A	1800	1.3e4	1.1e4	4300	310	430	S4C

Table S5. EC_{50} and E_{Max} values from mouse splenocyte activation studies. Related to Figures 3 and 4.

Treatment	EC_{50} (pM)			E_{Max} (pSTAT5 MFI)			Figure
	Treg	$CD8^+$ T	T_{Conv}	Treg	$CD8^+$ T	T_{Conv}	
hIL-2	6.8	1.3e5	-	8600	5700	1000	S4D
Control IC + N297A	3.2	2.9e5	-	8600	4900	1100	S4D
Y60A IC + N297A	93	>2e6	-	8400	280	650	S4D
V103A IC + N297A	260	>2e6	-	8000	370	720	S4D
Y33A IC + N297A	270	>2e6	-	8100	340	680	S4D
F5111 IC + N297A	2100	>2e6	-	7700	320	720	S4D
F5111.2 IC + N297A	6300	>2e6	-	5500	220	660	S4D

SIGNIFICANCE OF THE DISSERTATION

The work described within this dissertation contains results significant to not only the development of more effective interleukin-2 (IL-2) based therapies, but more generally to the development of superior cytokine-based medicines. Our initial, generalist approach to generating quantitative guidelines for the development of cytokines with increased cell type-selectivity revealed the potential benefits of simultaneous optimization of multiple aspects of a cytokine's design. Often when engineering cytokines with the goal of increasing their selectivities, researchers rely on engineering the affinity with which a cytokine binds to its cognate receptors alone. However, in contrast to this more common approach, we found that by altering a ligand's affinity, valency, and specificity simultaneously and in a quantitatively informed manner, cytokines with far greater selectivity for target cells than those designed with affinity alterations alone could be produced. This study also demonstrated the importance of thoroughly characterizing the receptor abundances of target and off-target populations, as the appropriate design of cytokine agents were inevitably determined by this landscape. We then specifically analyzed the gamma-chain family of cytokines using an ordinary differential equation model. Using this highly parameterized modeling approach, we generated a litany of novel insights; we were able to infer the dynamics of the many previously uncharacterized receptor-receptor and receptor-cytokine interactions which occur during gamma-chain cytokine signaling cascades, demonstrate the oft-overlooked critical importance of receptor trafficking during cytokine signaling activities, and quantify the full range of how affinity alterations could be wielded to increase the selectivity with which monovalent IL-2 signals. Next, we used a combination of data-driven and mechanistic modeling approaches to reveal how valency plays a governing role in determining Fc-fused IL-2's signaling activities, and then characterize its

effects mechanistically. Using these results as a guide, we then generated multivalent Fc-fused IL-2 mutants with selectivity for regulatory cells superior to those demonstrated by state-of-the-art affinity mutants. These combined findings showed that valency engineering, a yet largely unexplored axis of cytokine engineering, can be exploited to more effectively exploit relative differences in receptor abundances of target and off-target populations and thus dramatically enhance the selectivity of engineered cytokine constructs. Finally, we leveraged mechanistic modeling approaches to characterize the signaling activity of next-generation IL-2 immunocytokines and were able to generate insights as to the parameters which determined the *in vitro* performance of affinity engineered variants. These results better characterized the mechanisms by which engineered IL-2 mutants could expand suppressive populations *in vivo* and helped spur the selection and development of mutants which effectively ameliorated autoimmunity across several models of disease. In total these studies have, from the ground up, expanded our understanding of cytokine engineering generally, our fine-grained understanding of IL-2 signaling pathway dynamics, and our understanding of the tools we have at our disposal to better design IL-2 and cytokine-based therapeutics. Using approaches which incorporated and relied heavily upon the application of computational techniques, we have generated quantitative perspectives on each of these topics and shown that such perspectives can be leveraged to generate significant improvements in the design of cytokine-based medicines in both *in vitro* and *in vivo* experimental settings. Thus, the work in this dissertation represents a critical step away from traditional, qualitatively informed cytokine engineering, and towards more efficacious and efficient computationally guided design efforts.

More broadly, when considered together, the studies contained within this dissertation

represents a model for the rational selection and application of modeling techniques in biological applications. The selection of the correct modeling approach must be informed by a combination of one's objectives in modeling a system, as well as the data and domain knowledge already available to answer that question. For example, when studying a well characterized system, one might elect to use a detailed ordinary differential equation model, which allows a modeler to leverage available domain knowledge aided in the extensive parameterization required of such a model, and in turn grants deep insight into the mechanisms and dynamics governing that system. When attempting to study a family of systems more generally, it is beneficial to select modeling approaches which carefully leverage intelligently imposed assumptions that in turn allow the model to generalize efficiently. While it is important to understand what benefits a computational approach affords you, it is of equal importance for a modeler to understand the limitations of a given modeling technique; for example, insights derived from data-driven modes should generally not be used to draw conclusions about yet-uncharacterized systems, as such models are molded entirely by what data they are fit to and are thus generally ill-suited to out-of-set prediction. Such principles guided the selection of each approach leveraged within this dissertation. Furthermore, the benefits of considerate selection and application of modeling techniques are evident throughout each study as manifested in the efficacy of the insights we generated using such approaches; we found that our computational findings consistently translated well into the physical realm.

We plan to use the work contained within this dissertation as a springboard to design cytokine therapeutics which flexibly deliver cytokine signals in a cell type-selective manner. By studying the transcriptomic programs induced by various cytokines, identifying which may most

effectively induce desirable activity in target cells, and using the computational methods described in this to design molecules which selectively deliver those signals, we may be able to design medicines which better galvanize regulatory T cells into highly suppressive states, and thus generate better treatments for autoimmune diseases.